

https://dspace.org/

Engineering robust photonic quantum states for quantum communication and information

Nape, Isaac Mphele

2022

https://hdl.handle.net/10539/34548

Downloaded from a DSpace repository. https://dspace.org/

Engineering robust photonic quantum states for quantum communication and information

Isaac Mphele Nape

A Thesis submitted to the Faculty of Science
in partial fulfillment of the requirements for the Degree of
Doctor of Philosophy

School of Physics
University of Witwatersrand



WITS
UNIVERSITY

Supervisor: Andrew Forbes
28 February 2022

Declaration

I declare that this Dissertation is my own, unaided work. It is being submitted for the Degree of Doctor of Philosophy at the University of the Witwatersrand, Johannesburg. It has not been submitted before for any degree or examination at any other University.



(Signature of candidate)

28 day of February 20 22 in Johannesburg

Abstract

Quantum communication and information processing with photons achieves the overarching goals of transferring, encrypting, and processing digital information using machinery provided by fundamental physics principles that are established in quantum mechanics. In the last decade, the field has matured rapidly, from being the bedrock of simple demonstrations of quantum key distribution protocols with typical polarisation qubits that have two dimensional ($d = 2$) alphabets to now overseeing accelerated developments with high dimensional encoding using alternative photonic degrees of freedom (DOFs) that span larger Hilbert spaces of dimensions $d > 2$. Excitingly, the transverse spatial DOF of light offers an infinite encoding alphabet. While spatial modes may be transported over most propagation media, i.e. free-space, optical fiber and underwater channels, they are easily perturbed by various noise mechanisms, e.g., rapidly varying refractive index profiles, diffraction, mode dependent loss, inhibiting their performance in practical applications. Most potential approaches for undoing these deleterious effects require full knowledge of the channel dynamics or the state evolution. In relation to the latter we can highlight the following challenges for transverse spatial mode encoding that are prevalent in the field: i) the internal modal scattering due to the perturbations from a quantum channel for spatial modes can be difficult to predict; ii) and when possible, accurate characterisation methods are required before the effects of the channel can be undone; iii) in higher dimensions, characterising quantum states become increasing difficult due to the quadratic scaling of the number of measurements with respect to the dimensions.

In this Thesis we tackle these issues by engineering techniques for creating, controlling and characterising photons that are subject to a diverse range of perturbative

channels. For channels, that cause diffraction induced losses, we tailor non-diffracting higher dimensional vectorial photon fields, that have coupled polarisation and azimuthal spatial components, modulated with self-healing radial profiles. We show that these fields can be used to transmit secure quantum information in the presence of disturbances. We overcome the scattering effects of optical media with spatially varying refractive index, by invoking channel state duality and the invariance of non-separable states to unitary channels, but in locally entangled vectorial photon fields. This approach enables us to devise a procedure for undoing the effects of a channel in order to preserve information encoded in spatial modes. This method advances the use of so called classical entanglement in quantum and classical optics. Next, we develop a technique that manipulates heterogeneous channels to deliver multiple hybrid non-locally entangled states using a single mode fiber channel. The nonlocal hybrid entanglement between the polarisation and high dimensional spatial modes of two spatially separated photons is used as main resource. Lastly, we develop a novel technique for characterising high dimensional quantum states that are affected by white noise. The procedure involves the use of conditional measurements that return crucial information about the underlying states' occupied dimensions and purity. We demonstrate the feasibility and adaptability of our approach using photons that have nonlocal entanglement between their transverse spatial modes of orbital angular momentum, and separately using the pixel position basis.

Acknowledgments

To my supervisor: Distinguished Prof. Andrew Forbes, thank you for all the valuable advice, guidence and encouragement. You have been instrumental in my training. You have taught me not to work for the bare minimum but rather to do far better than is expected. I also want to thank you for giving me the opportunity to travel around the world and learn from other experts in our field.

To my seniors: Dr. Adam Valles, Dr. Bienvenue Ndagano, Dr. Carmelo. Rosales-guzman, Dr. Valeria Rodríguez-Fajardo, Dr. Najmeh TabeBordbar and Dr. Wagner Tavares Buono: The work in this dissertation would not be successfully conducted without your valuable nurturing;

To my colleges and team mates: you are all such wonderful people to work with. I have learned the value of friendship and teamwork through all of you.

To our collaborators: Dr. Eileen Otte, Dr. Feng Zhu and Dr. Jun Liu, you all made my visits in Germany, Scotland and China hospitable, respectively. I would like to thank your group leaders Prof. Cornelia Denz, Prof. Jian Wang and Prof. Jonathan Leach for allowing me to work in their labs and also giving me an excellent experience outside South Africa.

Family and friends: thank you for your continuous support and encouragement. It has really brought me far.

Funders: Lastly, I would like to acknowledge the University of the Witwatersrand, the joint Council of Scientific and Industrial Research (CSIR) and Department of Science and Technology (DST)-Interbursary Support (IBS), the National Laser center (NLC) and the SPIE optics society for their financial assistance.

Contents

Declaration i

Abstract ii

Acknowledgments iv

List of Figures ix

List of Tables xii

Publications xiii

1 Introduction 1

1.1 Qubits . . . 3

1.1.1 Polarisation modes . . . 6

1.2 Qudits . . . 7

1.2.1 High dimensional states . . . 7

1.2.2 High dimensional spatial modes with orbital angular momentum 9

1.2.3 High dimensional hybrid polarisation modes . . . 13

1.3 Two photon states in high dimensions . . . 15

1.3.1 Entangled states . . . 16

1.3.2 Nonlocal hybrid entanglement and classical hybrid entanglement 19

1.4 Quantum channels . . . 20

1.5 Outline . . . 24

2 Self healing quantum communication through obstructions 26

2.1 Introduction . . . 27

2.2 Self-healing Bessel modes . . . 28

2.2.1 Non-diffracting information basis . . . 29

2.3 Methods . . . 32

2.3.1 Single photon heralding . . . 32

2.3.2 Tailoring the desired spatial profile . . . 34

2.3.3 Generation and detection . . . 34

2.3.4 Scattering probability . . . 36

2.4 Experimental set-up . . . 37

2.4.1 Procedure and analysis . . . 38

2.5 Results and Discussion . . . 40

2.5.1 Experimental results . . . 40

2.5.2 Discussion . . . 42

2.6 Conclusion . . . 44

3 A single vector beam can be used to charactersise turbulence channels 46

3.0.1 Introduction . . . 47

3.1 Concepts . . . 48

3.1.1 Nonseparable vector modes . . . 48

3.1.2 Vector mode propagation through turbulence from the perspective of quantum mechanics . . . 52

3.2 Methods . . . 55

3.2.1 Experimental set-up . . . 55

3.2.2 Vector quality factor measurement . . . 56

3.3 Results . . . 57

3.3.1 Propagation of vector modes through turbulence . . . 57

3.4 Discussion . . . 60

3.5 Conclusion . . . 61

4 Unraveling the invariance of vectorial photon fields in unitary channels 62

4.1 Introduction . . . 63

4.2 Concepts . . . 64

4.2.1 Vectorial light and unitary channels . . . 64

4.3 Methods . . . 68

4.3.1 Vector beam generation . . . 68

4.4 Non-separability measurements . . . 69

4.4.1 Adjusted basis measurement . . . 71

4.5 Experiment and Results . . . 72

4.5.1 Experimental demonstration: the tilted lens. . . . 72

4.5.2 The role of measurement . . . 75

4.5.3 Reversing turbulence distortions . . . 78

4.6 Discussion and Conclusion . . . 80

5 Transporting multiple hybrid entangled states through optical fibers 82

5.1 Introduction . . . 83

5.2 Concept and principle . . . 85

5.3 Methods . . . 88

5.3.1 The experiment . . . 88

5.3.2 Characterisation . . . 90

5.4 Results . . . 92

5.4.1 A hybrid quantum eraser . . . 94

5.5 Discussion and Conclusion . . . 97

6 Quantifiying Dimensionality and Purity in High Dimensional Entanglement 99

6.1 Introduction . . . 100

6.2 Implementation . . . 101

6.2.1 Concept . . . 101

6.3 Methods . . . 107

6.3.1 High dimensional state projections . . . 107
6.3.2 Experimental setup. . . . 109
6.3.3 Optimal purity and dimensionality calculation . . . 109
6.4 Results . . . 110
6.4.1 Orbital angular momentum basis measurements . . . 110
6.4.2 Pixel basis measurements. . . . 113
6.5 Discussion . . . 114

7 Conclusions 118
7.1 Concluding remarks . . . 118
7.2 Future work . . . 122

A Scattering probability of OAM in turbulence 124

B Synthesis of turbulence 126

C Supplementary material: invariant vectorial photon fields 129
C.1 Transmitting vector beams through unitary single sided channels . . . 129
C.2 Nonseparability of the transformed vector mode . . . 131
C.3 Undoing the effects of the channel . . . 132
C.4 Examples with a titled lens . . . 134
C.5 Titled lens mapping . . . 136
C.5.1 Wave optics description . . . 138
C.6 Basis dependent and basis independent non-separability measurements 139
C.6.1 Basis independent non-separability . . . 139
C.6.2 Basis dependent non-separability . . . 141
C.7 Basis independent VQF propagation of uncertainty . . . 143
C.8 Stokes Parameters . . . 143

D Supporting data for multi-mode SMF fiber channel 147
D.0.1 Modal spectrum data after the two meter fiber . . . 147
D.0.2 Supporting density matrix reconstruction data . . . 147

D.0.3 Supporting quantum eraser data 148
D.0.4 Tabulated concurrence and fidelity data 149

E **151**

E.1 Dimensionality of Pure States 151
E.2 High dimensional state projections 153
E.3 Decomposition of Entangled Photons 155
E.4 Detection Probability 157
E.5 Visibility for Different Spectra 160
E.6 Visibility of Mixed States 161
E.7 Visibility of Separable States 163
E.8 Verification of the Technique 164
E.9 Simulations in the Pixel Basis 165
E.10 Quantum State Fidelity and Schmidt Rank 166
E.11 Measurements in the Pixel Basis 167
E.12 Comparison to State-of-the-art 168

List of Figures

1-1 BlochSphere 4
1-2 Spatial profiles of LG modes 9
1-3 OAM Bloch sphere 12
1-4 Higher order Poincaresphere 14
1-5 Effects of quantum channels on photons 20

2-1 Polarisation profiles of self-healing modes. 30
2-2 QKD elements for self-healing vector modes. 32
2-3 Experimental setup for heralded self healing photons. 37
2-4 Photon count rates. 39
2-5 Crosstalk measurements. 41
2-6 Security analysis. 42

3-1 Vector modes in turbulence 49
3-2 Experimental setup for VQF measurements. 50
3-3 Modal spectrum in turbulence. 52
3-4 Experimental validation 58

4-1 Concept of vectorial fields undergoing a unitary transformation. . . . 65
4-2 Vectorial light through a tilted lens. 66
4-3 Impact of scattering across multiple subspaces. 67
4-4 The unitary channel mapping and its inversion. 73
4-5 The choice of measurement basis. 76
4-6 Unravelling turbulence. 78

5-1 Concept of multi-dimensional entanglement 84
5-2 Experimental setup schematic and modal spectrum 86
5-3 State reconstruction of multiple hybrid states 88
5-4 Hybrid state Bell violations. 94
5-5 Quantum eraser experiment on the channel 95

6-1 Concept of dimensionality measurement 102
6-2 Visibility, dimensionality and purity extraction. 105
6-3 Experimental visibilities 111
6-4 Pixels basis results 115

B-1 Turbulence characterisation. 126

C-1 Basis dependent measurement for tilted lens with input mode of $\ell = 1$. 142
C-2 Basis dependent measurement for tilted lens with input mode of $\ell = 4$. 142
C-3 Stokes parameters through a tilted lens. 144
C-4 Stokes Parameters of corrected modes 146
C-5 Stokes parameters in turbulence 146

D-1 Spectral decomposition of the hybrid channel. 148
D-2 Experimental tomography measurements. 149
D-3 Bell-inequality and quantum eraser measurements. 150

E-1 Modal spectrum shapes. 152
E-2 Modal decomposition of the state projectors 156
E-3 Detection probability vs relative orientation and dimensionality. . . . 157
E-4 Visibility of entangled pure states with differing spectral shapes. . . . 158
E-5 Impact of purity and dimensionality on visibility 169
E-6 Simulations for the pixel basis 170
E-7 Dimensionality witness comparison 171
E-8 Dimensionality and purity measurements in the pixels basis 172

List of Tables

1.1 Eigenvalues and eigenvectors of the Pauli matrices. 6

2.1 Wave-plate orientation angles 36
2.2 Security parameters for the channel 43

3.1 Analysis of vector modes in turbulence 59

6.1 Purity and dimensionality measurements 113

C.1 VQF of selected subspace. 132
C.2 Decomposition of LG modes into HG modes. 137
C.3 Modal decomposition of LG after a tilted lens transformation. 138
C.4 VQF Values and errors. 145

D.1 Fidelity and concurrence values. 149

E.1 Dimensionality and purity measurements in the OAM basis. 165
E.2 Measurement scaling with dimensions 168

Publications

Contributed patents

A. Forbes, B. Ndagano, **I. Nape**, M. Cox, and C. Rosales-guzman, "Method and system for hybrid classical-quantum communication," Dec. 26 2019. US. Patent App. 16/480,008.

Peer reviewed articles

1. **I. Nape**, V. Rodri´guez-Fajardo, F. Zhu, H.-C. Huang, J. Leach, and A. Forbes, "Measuring dimensionality and purity of high-dimensional entangled states," Nature Communications, vol. 12, no. 5159, pp. 1–8, 2021.

2. **I. Nape**, K. Singh, A. Klug, W. Buono, C. Rosales-Guzm´an, S. Franke-Arnold, A. Dudley, and A. Forbes, "Revealing the invariance of vectorial structured light in perturbing media," arXiv preprint arXiv:2108.13890, 2021.

3. A. Klug, **I. Nape**, and A. Forbes, "The orbital angular momentum of a turbulent atmosphere and its impact on propagating structured light fields," New Journal of Physics, vol. 23, p. 093012, 2021.

4. **I. Nape**, N. Mashaba, N. Mphuthi, S. Jayakumar, S. Bhattacharya, and A. Forbes, "Vector-mode decay in atmospheric turbulence: An analysis inspired by quantum mechanics," Physical Review Applied, vol. 15, no. 3, p. 034030, 2021.

5. B. Sephton, A. Vall´es, **I. Nape**, M. A. Cox, F. Steinlechner, T. Konrad, J. P. Torres, F. S. Roux, and A. Forbes, "High-dimensional spatial teleportation enabled by nonlinear optics," arXiv preprint arXiv:2111.13624, 2021.

6. Y. Shen, **I. Nape**, X. Yang, X. Fu, M. Gong, D. Naidoo, and A. Forbes, "Creation and control of high-dimensional multi-partite classically entangled light," Light: Science & Applications, vol. 10, no. 50, pp. 1–10, 2021.

7. J. Liu, **I. Nape**, Q. Wang, A. Vall´es, J. Wang, and A. Forbes, "Multidimensional entanglement transport through single-mode fiber," Sci Adv, vol. 6, no. 4, p. eaay0837, 2020.

8. **I. Nape**, B. Sephton, Y.-W. Huang, A. Vall´es, C.-W. Qiu, A. Ambrosio, F. Capasso, and A. Forbes, "Enhancing the modal purity of orbital angular momentum photons," APL Photonics, vol. 5, no. 7, p. 070802, 2020.

9. A. Forbes and **I. Nape**, "A scramble to preserve entanglement," Nature Physics, vol. 16, no. 11, pp. 1091–1092, 2020.

10. M. de Oliveira, **I. Nape**, J. Pinnell, N. TabeBordbar, and A. Forbes, "Experimental high-dimensional quantum secret sharing with spin-orbit-structured photons," Physical Review A, vol. 101, no. 4, p. 042303, 2020.

11. A. Manthalkar, **I. Nape**, N. T. Bordbar, C. Rosales-Guzm´an, S. Bhattacharya, A. Forbes, and A. Dudley, "All-digital stokes polarimetry with a digital micromirror device," Optics Letters, vol. 45, no. 8, pp. 2319–2322, 2020.

12. A. Forbes and **I. Nape**, "Quantum mechanics with patterns of light: Progress in high dimensional and multidimensional entanglement with structured light," AVS Quantum Science, vol. 1, no. 1, p. 011701, 2019.

13. J. Pinnell, **I. Nape**, M. de Oliveira, N. TabeBordbar, and A. Forbes, "Experimental demonstration of 11-dimensional 10-party quantum secret sharing," Laser & Photonics Reviews, vol. 14, no. 9, p. 2000012, 2020.

14. M. A. Cox, N. Mphuthi, **I. Nape**, N. Mashaba, L. Cheng, and A. Forbes, "Structured light in turbulence," IEEE Journal of Selected Topics in Quantum Electronics, vol. 27, no. 2, pp. 1–21, 2020.

15. E. Otte, **I. Nape**, C. Rosales-Guzm´an, C. Denz, A. Forbes, and B. Ndagano, "High-dimensional cryptography with spatial modes of light: tutorial," JOSA B, vol. 37, no. 11, pp. A309–A323, 2020.

16. J. Pinnell, **I. Nape**, B. Sephton, M. A. Cox, V. Rodr´ıguez-Fajardo, and A. Forbes, "Modal analysis of structured light with spatial light modulators: a practical tutorial," JOSA A, vol. 37, no. 11, pp. C146–C160, 2020.

17. E. Toninelli, B. Ndagano, A. Vall´es, B. Sephton, **I. Nape**, A. Ambrosio, F. Capasso, M. J. Padgett, and A. Forbes, "Concepts in quantum state tomography and classical implementation with intense light: a tutorial," Advances in Optics and Photonics, vol. 11, no. 1, pp. 67–134, 2019.

18. **I. Nape**, E. Otte, A. Vall´es, C. Rosales-Guzm´an, F. Cardano, C. Denz, and A. Forbes, "Self-healing high-dimensional quantum key distribution using hybrid spin-orbit bessel states," Optics express, vol. 26, no. 21, pp. 26946–26960, 2018.

19. E. Otte, **I. Nape**, C. Rosales-Guzm´an, A. Vall´es, C. Denz, and A. Forbes, "Recovery of nonseparability in self-healing vector bessel beams," Physical Review A, vol. 98, no. 5, p. 053818, 2018.

20. B. Ndagano, **I. Nape**, M. A. Cox, C. Rosales-Guzman, and A. Forbes, "Creation and detection of vector vortex modes for classical and quantum communication," Journal of Lightwave Technology, vol. 36, no. 2, pp. 292–301, 2018.

Conference papers

1. **I. Nape**, J. Liu, Q. Wang, A. Valles, J. Wang, and A. Forbes, "Transmitting multiple hybrid entangled states using a conventional single mode fiber," in

Laser Science, pp. JTh4A–31, Optical Society of America, 2020.

2. **I. Nape**, V. Rodr´ıguez-Fajardo, H.-C. Huang, and A. Forbes, "Measuring high dimensional entanglement using fractional orbital angular momentum.," in Frontiers in Optics, pp. FW7C–8, Optical Society of America, 2020.

3. K. Singh, **I. Nape**, A. Manthalkar, N. Tabebordbar, C. Rosales-Guzm´an, S. Bhattacharya, A. Forbes, and A. Dudley, "Polarization reconstruction with a digital micro-mirror device," in Laser Beam Shaping XX, vol. 11486, p. 1148609, International Society for Optics and Photonics, 2020.

4. A. Vall´es, **I. Nape**, J. Liu, Q. Wang, J. Wang, and A. Forbes, "Multidimensional spatial entanglement transfer through our existing fiber optic network," in Optical Manipulation and Structured Materials Conference 2020, vol. 11522, p. 1152218, International Society for Optics and Photonics, 2020.

5. M. de Oliveira, J. Pinnell, **I. Nape**, N. TabeBordbar, and A. Forbes, "Realising high-dimensional quantum secret sharing with structured photons," in Quantum Communications and Quantum Imaging XVIII, vol. 11507, p. 1150709, International Society for Optics and Photonics, 2020.

6. V. Rod´rıguez-Fajardo, S. Scholes, R. Kara, J. Pinnell, C. Rosales-Guzm´an, N. Mashaba, **I. Nape**, and A. Forbes, "Controlling light with dmds," in 2020 International Conference Laser Optics (ICLO), pp. 1–1, IEEE, 2020.

7. J. Pinnell, I. M. Nape, M. De Oliveira, N. Tabebordbar, and A. Forbes, "Quantum secret sharing with twisted light," in Complex Light and Optical Forces XV, vol. 11701, p. 117010K, International Society for Optics and Photonics,2021.

8. Y. Shen, Z. Wang, X. Yang, **I. Nape**, D. Naidoo, X. Fu, and A. Forbes, "Classically entangled vectorial structured light towards multiple degrees of freedom and higher dimensions," in CLEO: Science and Innovations, pp. STh1B–1, Optical Society of America, 2021.

Conference Presentations

1. **I. Nape**, V. Rodr´ıguez-Fajardo, F. Zhu, HC. Huang, J. Leach, A. Forbes, "A method for characterising high dimensional entangled states", Student Conference on Optics and Photonics, India, 2021.

2. **I. Nape**, V. Rodr´ıguez-Fajardo, F. Zhu, HC. Huang, J. Leach, A. Forbes, "Quantitative measurements of the purity and dimensionality of high dimensional entagled states", Annual conference of the South African Institute of Physics, South Africa, 2021.

3. **I. Nape**, N. Mashaba, N. Mphuthi, S. Jayakumar, S. Bhattacharya, A. Forbes, "Characterising laser beams through turbulence using vector beams and a simple quantum trick", Annual conference of the South African Institute of Physics, South Africa, 2021.

4. **I. Nape**, V. Rodr´ıguez-Fajardo, F. Zhu, HC. Huang, J. Leach, A. Forbes, "Measuring the dimensionality of twisted modes", Photon 2020 by the Institute of Physics (IOP), United Kingdom, 2020.

5. **I. Nape**, E. Otte, J. Liu., A. Vall´es, Q. Wang, J. Wang, C. Rosales-guzman, C. Denz and A. Forbes, "Reaching high dimensions by spinning and twisting photons", Quantum Africa (5) Conference, Stellenbosch, South Africa, 2019.

6. **I. Nape**, E. Otte, J. Liu., A. Vall´es, Q. Wang, J. Wang, C. Rosales-guzman, C. Denz and A. Forbes,"Hybrid entanglement for quantum information processing", at the Intentional conference on orbital angular momentum , Ottawa, Canada, 2019.

7. **I. Nape**, E. Otte, J. Liu., A. Vall´es, Q. Wang, J. Wang, C. Rosales-guzman, C. Denz and A. Forbes "Self-healing locally entangled modes for secure communication", at the 2nd International OSA Network of Students (IONS) South Africa, South Africa, 2018.

Chapter 1

Introduction

Initial developments in quantum mechanics unveiled several intriguing features about the fundamental nature of quantum systems that make them distinct from their classical counterparts. For example, the most non-classical manifestation of quantum correlations, i.e. entanglement, was discovered indirectly when Einstein, Podolsky, and Rosen (EPR) [1] attempted to expose the incompleteness of quantum mechanics by demonstrating that two particle systems with space-like separation can remain correlated, therefore violating local hidden variable theories. It took several decades of theoretical studies (see Ref. [2] for a concise review) and convincing experimental validation [3], to prove that quantum entanglement, though paradoxical, is a fundamental aspect of nature. Another, intriguing feature of quantum systems that has no classical equivalent is captured in the no-cloning theorem [4], preventing the creation of exact copies of quantum states. Today, these intriguing properties, among many others, serve as constituent elements of rapidly advancing technologies in quantum communication, computing and information science that offer a variety of solutions for digital information transmission, storage and processing.

While quantum computation harnesses the superposition principle and entanglement for executing computational algorithms and calculations, quantum communication on the other hand offers solutions for secure information transmission over long distances. A topical sub-field of quantum communication is quantum cryptography [5–7], where single photons are used to generate encryption keys in a provably

secure manner instead of relying on computationally difficult algorithms that may fail with advancing computing power. Reaching long transmission distances as well as maintaining high information capacities and communication speeds is at the core of quantum communication research. Photons are favoured in this area as opposed to other elementary particles (protons, electrons, neutrons), because they couple weakly with the environment and have the highest propagation speeds.

Initially, numerous newly developed quantum communication protocols, e.g., quantum key distribution (QKD) [8], superdense coding [9], quantum teleportation [10], entanglement swapping [11], quantum secret sharing (QSS) [12] and some fundamental test of quantum mechanics, e.g., early demonstrations of Bell inequality violations [13], quantum erasures [14], etc., were demonstrated with photon polarisation qubits having a two digit alphabet with dimensions of $d = 2$. For this reason, accessing higher dimensions ($d > 2$) using transverse spatial mode is topical since spatial modes offer the benefit of increasing the information capacity of photonic quantum communication protocols [15–17], overcoming the capacity limit imposed by polarisation encoding. Transverse spatial modes are receiving much attention, with some demonstrations of quantum encryption (QKD and QSS) ranging from $d = 4$ [18, 19], $d = 7$ [20, 21], $d = 8$ [22] and $d = 11$ [23] dimensions. Current research efforts are focused on deploying spatial modes in practical scenarios. However, spatial modes are sensitive to numerous decay mechanisms (or perturbations) in the environment, therefore limiting their performance. The perturbations can include spatially dependent phase variations [24, 25], optical diffraction [26] and environmental noise [27], known to scramble information in quantum channels.

In this chapter, we introduce the qubit (two-dimensional states) and transition to qudits (high dimensional states). We draw our attention to the spatial degree of freedom (DOF) of light together with polarisation modes and focus on how both DOFs can be used to increase the encoding dimensions of photons in single and two photon states. Subsequently, we discuss some of the challenges that come with deploying spatial mode encoding in practical quantum channels and finally provide an outline of each chapter in the thesis.

1.1 Qubits

Discrete quantum states can be expressed as elements of the Hilbert space; an inner product vector space $\mathcal{H}$, that can be spanned by an orthonormal computational basis, $\mathcal{B}_d$, where the subscript d, is the number of unique elements corresponding to the dimensions of the vector space. Moreover, the basis, $\mathcal{B}_d$, is complete because any state on the Hilbert space can be expanded in terms of its elements. The simplest example of a Hilbert space for discrete quantum states is the two dimensional qubit space. For qubits, we can construct vectors, $|0\rangle = \begin{pmatrix} 1 \\ 0 \end{pmatrix}$ and $|1\rangle = \begin{pmatrix} 0 \\ 1 \end{pmatrix}$, which form our basis. Note that $\mathcal{B}_d$ is not unique, e.g., from our computational basis, we can create another basis, $\{|+\rangle = 1/\sqrt{2}\,(|0\rangle + |1\rangle)\,, |-\rangle = 1/\sqrt{2}\,(|0\rangle - |1\rangle)\}$, that can also span the qubit vector space. Accordingly, any qubit state can be expanded in terms of the basis vectors. For example, using our initial basis vectors, $\{|0\rangle\,, |1\rangle\}$, i.e. the computational basis, any state can be expressed as

$$|\Psi\rangle = a\,|0\rangle + b\,|1\rangle\,, \tag{1.1}$$

$$= \begin{pmatrix} a \\ b \end{pmatrix}, \tag{1.2}$$

where a and b are complex coefficients that determine the state $|\Psi\rangle$. Since $|\,\langle\Psi|\Psi\rangle\,|^2 = 1$, the coefficients must satisfy $|a|^2 + |b|^2 = 1$. Physically, $|a|^2$ and $|b|^2$ are the probabilities of obtaining the states $|0\rangle$ and $|1\rangle$, respectively. We can represent qubits on a three dimensional sphere, called the Bloch sphere (shown in Fig. 1-1(a)), where states are parameterised by angles θ and χ. We can express Eq. (1.2) using these parameters according to the mapping

$$|\Psi\rangle = \cos(\theta/2)\,|0\rangle + \sin(\theta/2)e^{-i\chi}\,|1\rangle\,. \tag{1.3}$$

Here θ, the zenith angle controls the relative weighting between the basis states in the computational basis while χ determines the relative phases. A photon with the

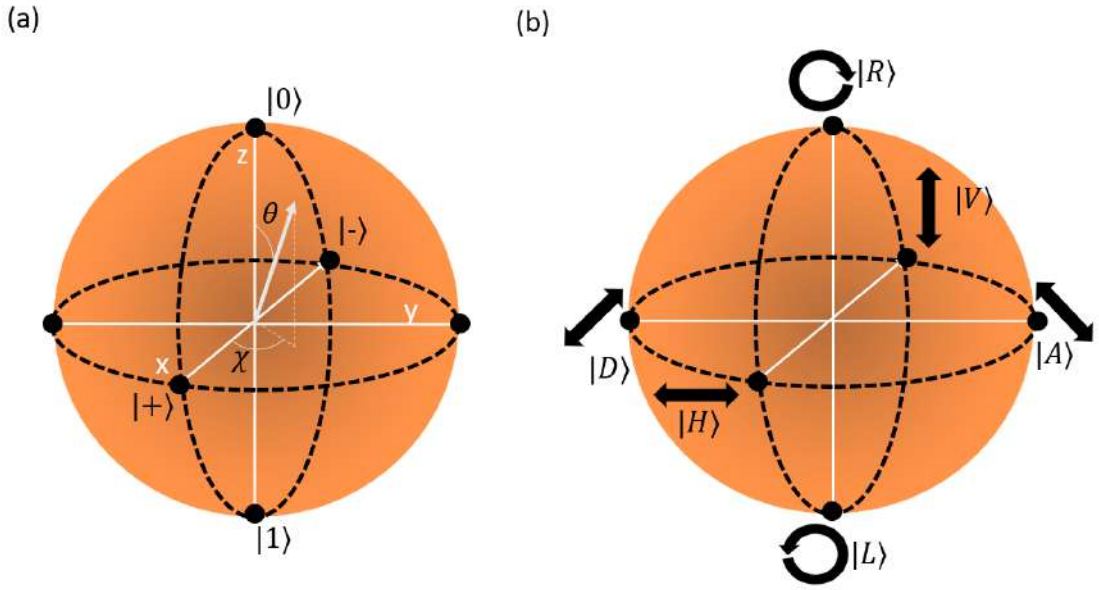


Figure 1-1: (a) Bloch sphere, for qubit states. The poles contain the computational basis states while the equator contains their equally weighted superpositions. (b) Poincareśphere for polarisation modes.

state in Eq. (1.3) is pure. We can represent it using outer-products of the pure vector state, $|\Psi\rangle$, mapping it to a density matrix

$$\begin{aligned} \rho_\Psi &= |\Psi\rangle\langle\Psi|, \\ &= \begin{pmatrix} a \\ b \end{pmatrix} \otimes \begin{pmatrix} a^* & b^* \end{pmatrix} \\ &= \begin{pmatrix} |a|^2 & ab^* \\ ba^* & |b|^2 \end{pmatrix}. \end{aligned} \tag{1.4}$$

The matrix version is still normalised under the trace norm, so that $\mathrm{Tr}(\rho_\Psi) = 1$, where Tr denotes the trace operator. This can represent a process that produces photons that are identical. In the case where the photons are not identical, or in other words occupy states that are not necessarily the same, the system can be an

ensemble (statistical mixture) of several pure states,

$$\begin{aligned}\rho &= \sum_i p_i \rho_m, \\ &= \sum_i p_i \left|\Psi_m\right\rangle \left\langle\Psi_m\right|, \end{aligned} \tag{1.5}$$

where the states ρ_m occur with a probability $p_m = \mathrm{Tr}(\rho_m^\dagger \rho)$, and the states ρ_m are not necessarily orthogonal. If the density matrices are indeed othogonal and complete, i.e., $\mathrm{Tr}(\left|\Psi_i\right\rangle \left\langle\Psi_i|\Psi_j\right\rangle \left\langle\Psi_j\right|) = \delta_{ij}$ and $\sum_i \left|\Psi_i\right\rangle \left\langle\Psi_i\right| = \mathbb{1}$ then the state is said to be maximally mixed and not pure. The purity of a density matrix can be computed from $\mathrm{Tr}(\rho^2)$ ranging from zero for mixed states to one for pure states. Just as there is a decomposition of pure states, there is also a compact decomposition with a basis for two dimensional matrices given by,

$$\{\ \mathbb{1}_2 = \begin{pmatrix} 1 & 0 \\ 0 & 1 \end{pmatrix},\ \sigma_x = \begin{pmatrix} 0 & 1 \\ 1 & 0 \end{pmatrix},\ \sigma_y = \begin{pmatrix} 0 & -i \\ i & 0 \end{pmatrix},\ \sigma_z = \begin{pmatrix} 1 & 0 \\ 0 & -1 \end{pmatrix}\ \},$$

which are the identity matrix, $\mathbb{1}_2$ and the three Pauli matrices satisfying $\mathrm{Tr}(\sigma_i) = 0$. Accordingly, any qubit density matrix can be decomposed as

$$\rho = \frac{\mathbb{1}_2}{2} + \sum_i b_i \sigma_i. \tag{1.6}$$

Here $\mathbb{1}_2$ is the identity matrix, $\overline{\mathbf{b}} = (b_1, b_2, b_3)$ is called the Bloch vector while σ_i are the Pauli matrices. Since the density matrix must be semi-positive definite, $|\overline{\mathbf{b}}| \leq 1$. The eigenvalues and eigenvectors corresponding to each Pauli matrix are shown in Table 1.1. Crucially, the eigenvectors of σ_z, corresponding to the computational basis, are on the poles of the Bloch sphere and are aligned with the z-axis. The σ_x eigenvectors map the states on the x-axis and correspond to the Hadamard basis states $|\pm\rangle$ and the σ_y eigenstates are on the poles of the y-axis. Therefore the Pauli matrices form an over complete basis for the qubit states. Next, we explore an internal DOF of photons that can be used to encode qubit states.

Table 1.1: Eigenvalues and eigenvectors of the Pauli matrices.

	Eigenvalues	Eigenvector
σ_z	± 1	$\{\|0\rangle \equiv \begin{pmatrix}1\\0\end{pmatrix}, \|1\rangle \equiv \begin{pmatrix}0\\1\end{pmatrix}\}$
σ_y	± 1	$\{\frac{1}{\sqrt{2}}\begin{pmatrix}1\\-i\end{pmatrix}, \frac{1}{\sqrt{2}}\begin{pmatrix}1\\i\end{pmatrix}\}$
σ_x	± 1	$\{\|+\rangle \equiv \frac{1}{\sqrt{2}}\begin{pmatrix}1\\1\end{pmatrix}, \|-\rangle \equiv \frac{1}{\sqrt{2}}\begin{pmatrix}1\\-1\end{pmatrix}\}$

1.1.1 Polarisation modes

The polarisation of light is often associated with its spin angular momentum [28], a property that enables light to rotate objects about their origin. This phenomenon is observed when the light is circularly polarised. The direction of the rotating object indicates the handedness of the circular polarisation field.

At the single photon level each photon carries exactly $\pm 1\hbar$ per photon, where the sign is associated with the handedness of the circular polarisation photon field and hence can form a two level system using the circular polarisation basis. In optics, the Bloch sphere equivilent for polarisation states is called the Poincare´ sphere, shown in Fig. 1-1(b). Here the poles contain the right $|R\rangle \equiv |0\rangle$ and left $|L\rangle \equiv |1\rangle$ circular polarisation modes.

Assuming the decomposition of qubits states in Eq. (1.3), we see that $\theta = \pi/2$ can be associated with states on the equator, corresponding to electric field oscillations about the xy plane. Here well known linear polarisation states can be found to include

$$|H\rangle = 1/\sqrt{2}\left(|R\rangle + |L\rangle\right), \tag{1.7}$$

$$|V\rangle = 1/\sqrt{2}\left(|R\rangle - |L\rangle\right), \tag{1.8}$$

$$|D\rangle = 1/\sqrt{2}\left(|R\rangle + i\,|L\rangle\right), \tag{1.9}$$

$$|A\rangle = 1/\sqrt{2}\left(|R\rangle - i\,|L\rangle\right), \tag{1.10}$$

listed as the linear the horizontal (H) and vertical (V) polarisation states followed by the rectilinear diagonal (D) and anti-diagonal (A) polarisation states, corresponding

to phases $\chi = 0$, π, $\pi/2$ and $3\pi/2$, respectively.

It should be trivial to see that the right and left circular polarisations are determined by $\theta = 0$ and $\theta = \pi$, respectively. For $\theta = (0, \pi)$, one obtains various elliptical polarisation states. Therefore using the parameters (θ, χ) it is possible to express any polarisation qubit.

1.2 Qudits

Upon recognising that polarisation qubits imposed fundamental limits on quantum communication protocols, i.e., admitting only one bit of information per photon, numerous protocols were extended to multi-level encoding schemes [29], ushering in high dimensional ($d > 2$) quantum information [17]. The migration from traditional qubit to high dimensional qudits is motivated by the fact that higher dimensional states offer increased information capacity and security [29–31], protection against optimal quantum cloning machines [22, 32, 33] and resilience to noise [34].

1.2.1 High dimensional states

In higher dimensions, $d > 2$, we can express states on the Hilbert space by simply increasing the size of our encoding basis. We achieve this by increasing the number of elements in the computational basis. That is by constructing a basis with $d > 2$ elements; $\mathcal{B}_d = \{|j\rangle, i = 0, 1, ..d-1\}$ satisfying, $|\langle i|j\rangle| = \delta_{ij})$, for all $|i\rangle, |j\rangle \in \mathcal{B}_d$. For example, in three dimensions we have the basis

$$\mathcal{B}_3 = \{|0\rangle = \begin{pmatrix} 1 \\ 0 \\ 0 \end{pmatrix}, |1\rangle = \begin{pmatrix} 0 \\ 1 \\ 0 \end{pmatrix}, |2\rangle = \begin{pmatrix} 0 \\ 0 \\ 1 \end{pmatrix}\}, \tag{1.11}$$

spanning the state-space for qutrits ($d = 3$). Accordingly, a qutrit pure state can be written as

$$|\Psi\rangle = a_1 |0\rangle + a_2 |1\rangle + a_3 |2\rangle, \tag{1.12}$$

having a corresponding density matrix,

$$\begin{aligned}\rho_{\psi} &= \begin{pmatrix} a_0 \\ a_1 \\ a_2 \end{pmatrix} \otimes \begin{pmatrix} a_0^* & a_2^* & a_2^* \end{pmatrix}, \\ &= \begin{pmatrix} |a_0|^2 & a_0 a_1^* & a_0 a_2^* \\ a_1 a_0^* & |a_2|^2 & a_1 a_2^* \\ a_2 a_0^* & a_2 a_1^* & |a_3|^2 \end{pmatrix}. \end{aligned} \tag{1.13}$$

In general, any high dimensional purestate can be written as the superpositon state

$$|\Psi\rangle = \sum_{j=0}^{d-1} a_j \, |j\rangle \, , \tag{1.14}$$

where a_i are complex coefficients that determine the state $|\Psi\rangle$ up to a global phase. Similarly to the qubit states, the normalisation condition requires that the coefficients satisfy $\sum_j |a_j|^2 = 1$.

The density matrices can also be expressed using the computational basis as

$$\rho = \sum_{m,n=0}^{(} d-1) c_{mn} \, |m\rangle \, \langle n| \, . \tag{1.15}$$

The components of the density matrix are given by c_{mn} and there are exactly d^2 of them. In addition to the decomposition in Eq. (1.15), there exists another decomposition with $d^2 - 1$ Gell-Mann matrices, τ_k, following

$$\rho = \frac{\mathbb{1}_d}{d} + \sum_{k=0}^{d^2-1} t_k \tau_k, \tag{1.16}$$

where $\bar{\mathbf{t}} = (t_0, t_1, ..t_{d^2-1})$ are coefficients of the Gell-Mann matrices. The Gell-mann matrices are also trace-less, othorgonal and have d eigenvectors. In order to determine the coefficients t_k, a set of tomographically complete measurements are required and these can be the eigenvectors of each matrix. This means that $(d^2 - 1)$ observables

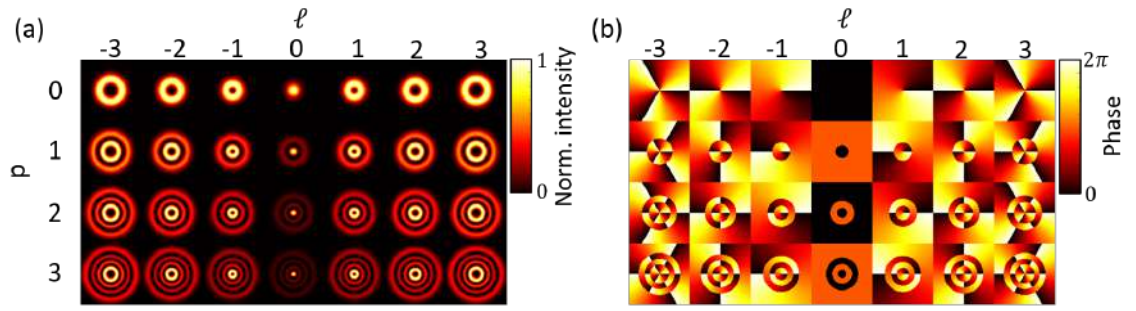


Figure 1-2: High dimensional spatial modes of light. (a) Normalised intensity and (b) phase profiles of LG modes for various discrete radial (p) and OAM indices (ℓ).

are required to completely describe the state. Alternatively mutually unbiased bases can be used [35], requiring $d+1$ observables, though there are restrictions on d [36].

Now that we have established what qudits (or high dimensional states) are, the goal is to use photonic DOFs that have the properties listed above.

1.2.2 High dimensional spatial modes with orbital angular momentum

Photons have internal DOFs that span higher dimensional Hilbert spaces, e.g., time [37–39], path [40, 41] and transverse spatial modes [15, 16, 42]. In particular, high dimensional transverse spatial modes that carry quantised amounts of orbital angular momentum (OAM) are slowly showing feasibility in freespace [20, 22, 43–46], optical fiber [47] and underwater [48, 49] quantum communication channels. Here, we focus on the transverse spatial mode DOF. Firstly, let us revisit the wave description light where the transverse oscillations of the electric field are characterised by field functions, $U(\overline{\mathbf{r}}, z, t)$, satisfying the wave equation [50]. The parameters $\overline{\mathbf{r}} = (x, y)$, z and t are the transverse, longitudinal and temporal coordinates, respectively.

Under the paraxial approximation (the limit of small beam divergence in the traverse plane) it can be assumed that transverse components of spatial modes are a slowly varying function of z, i.e. satisfying the paraxial inequality [28]

$$|\frac{\partial^2}{\partial^2 z}U(\overline{\mathbf{r}}, z)| << k|\frac{\partial}{\partial z}U(\overline{\mathbf{r}}, z)|. \tag{1.17}$$

It follows that the differential equation that governs the propagation of these fields can be written as [28]

$$(\nabla_{\perp}^2 + ik^2\frac{\partial}{\partial z})U(\overline{\mathbf{r}}, z) = 0, \tag{1.18}$$

where $\nabla_{\perp}^2$ is the transverse component of the Laplacian differential operator. Equation (1.18) is called the paraxial approximation of the Helmholtz equation. In the cylindrical coordinates, general solutions to Eq. (1.18) have the form

$$U(r, \phi, z) = u(r, z)e^{i\ell\phi}. \tag{1.19}$$

Here ϕ and r are the azimuthal and radial coordinates, respectively, while $\ell \in \mathbb{Z}$ is an integer, and $u(r, z)$ is the radial profile of the beam. These solutions have a characteristic complex profile, $e^{i\ell\phi}$, indicative of light beams that carry orbital angular momentum OAM. The integer, ℓ, has a physical significance: ℓ is the helicity or topological charge of the vortex present in the field and each photon has an OAM of $\ell\hbar$. Moreover, the phase profiles have $|\ell|$ characteristic dislocations that correspond to complete cycles of 2π. It was Allen et. al. [51] who first generated OAM light beams and since then they are used throughout the photonics community. Current methods for generating and detecting photons carrying OAM include the use of phase elements that utalise dynamic phase control on spatial light modulators (SLM) [52], geometric phase control using birefringent liquid crystals [53–55] and recently emerging metasurface technology [56, 57].

An example of a photon field that carries OAM is a Gaussian mode that is imprinted with the characteristic azumthal phase profile of OAM modes, i.e. $\exp\left(-\frac{r^2}{w_0^2}\right)\times \exp(i\ell\phi)$. However, such a field is instead a Hypergoemetric-Gaussian mode [58]and has a radial profile that changes with propagation though maintaining its azimuthal profile. On the contrary, a well known mode family that maintains the radially dependent amplitude and phase profiles in the paraxial regime is the of Laguerre-Gaussian

(LG) mode family, expressed here as

$$U_{\ell p}^{LG}(r,\phi,z) = C_{\ell p}\ \left[\sqrt{2}\frac{r}{w(z)}\right]^{\ell} {L_p}^{\ell}\left(\frac{2r^2}{w(z)^2}\right)\frac{w_0}{w(z)}\exp\left(-i\psi_{p\ell}(z)\right)\times \exp\left(-i\frac{k}{2q(z)}r^2\right)\exp\left(-\frac{r^2}{w(z)^2}\right)\exp(i\ell\phi), \tag{1.20}$$

where the function $L_p^{\ell}(\cdot)$ is the associated Laguerre polynomial, $w(z) = w_0\sqrt{1+(z/z_R)}$ is the beam size of the Gaussian envelope as the field propagates in the z direction while w_0 is its corresponding radius at the $z=0$ plane, with $z_R = \pi {w_0}^2/\lambda$ representing the Gaussian mode Rayleigh range. The term depending on $q(z) = z - iz_R$ is the complex beam parameter and $\psi_{p\ell}(z) = (2p+|\ell|+1)\tan^{-1}(z/z_R)$ is the Gouy phase. The constant factor $C_{\ell p}$ is a normalisation constant so that $\int |U_{\ell p}^{LG}(r,\phi,z)|^2 d^2r = 1$. The second moment radius of LG beams increases in size with $|\ell|$ and p according to $w_{\ell,p} = \sqrt{2p+|\ell|+1}\times w_0$.

In Fig. 1-2(a) and Fig. 1-2(b) various LG intensity, ($|U_{\ell p}^{LG}(r,\phi,z)_{\ell p}|^2$), and phase profile, mod $\left[\arg\left(U_{\ell p}^{LG}(r,\phi,z=0)\right),2\pi\right]$, are shown. The intensity profile has a region of null intensity, centered at the origin and a radius that increases with $|\ell|$. Furthermore, the field has $p+1$ or p concentric rings for $|\ell|>0$ or $|\ell|=0$, respectively.

Interestingly, OAM basis modes that have LG profiles have been measured at the single photon level using interferometers [59] and refractive optical elements [60]. Moreover, they have been used in high dimensional encoding schemes for single photons [21], entangled two [61] and three photon GHZ states [62]. In such applications, the field profiles in Eq. (1.20) are used to describe basis states of the transverse DOF of photons following the expansion

$$|\ell,p\rangle = \iint U_{\ell p}^{LG}(x,y)\,|x\rangle\,|y\rangle\,dxdy, \tag{1.21}$$

where $|x\rangle\,|y\rangle$ are continuous position state vectors in Cartesian coordinates, such that $\langle x'|x\rangle = \delta(x-x')$ and $\langle y'|y\rangle = \delta(y-y')$, are inner products in the position basis resulting in Dirac delta functions [63]. It follows that $\langle y'|\,\langle x'|x\rangle\,|y\rangle = \langle x'|x\rangle\,\langle y'|y\rangle = \delta(x-x')\delta(y-y')$. Accordingly, the overlap between any two states $|\ell_1,p_1\rangle$ and $|\ell_2,p_2\rangle$

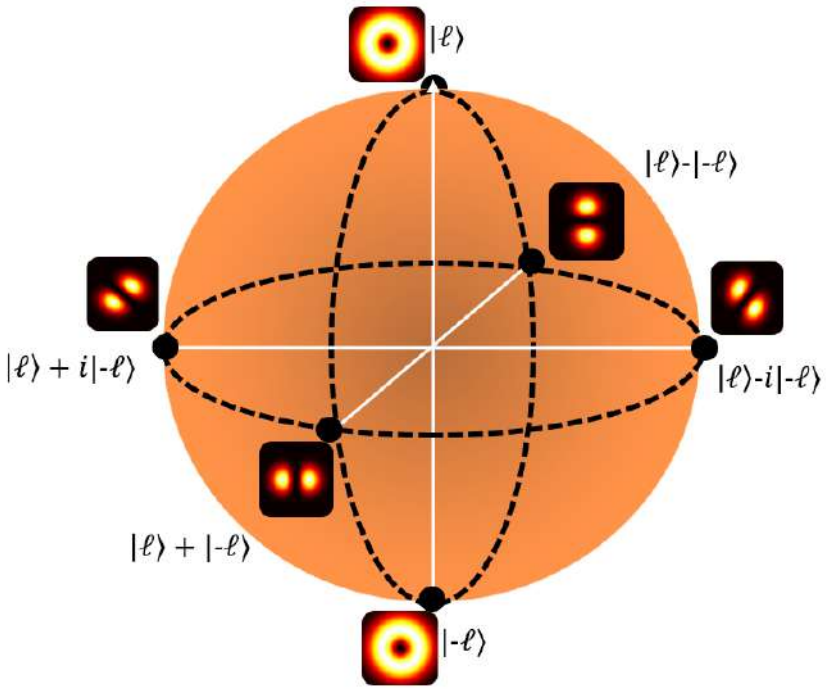


Figure 1-3: Any two LG basis modes can be used to construct a Bloch (or equivalently Poincaré) sphere for spatial qubits. We show an example for OAM modes in the $\ell = \pm 1$ subspace where $p = 0$.

is

$$\begin{aligned}
\langle p_1, \ell_1 | \ell_2, p_2 \rangle &= \iint U^{LG*}_{\ell_1,p_1}(x_1, y_1) dx_1 dy_1 \iint U^{LG}_{\ell_2,p_2}(x_2, y_2) \langle x_1 | x_2 \rangle \langle y_1 | y_2 \rangle dx_2 dy_2, \\
&= \iint U^{LG*}_{\ell_1,p_1}(x_1, y_1) dx_1 dy_1 \iint U^{LG}_{\ell_2,p_2}(x_2, y_2) \delta(x_2 - x_1) \delta(y_2 - y_1) dx_2 dy_2, \\
&= \iint U^{LG*}_{\ell_1,p_1}(x, y) U^{LG}_{\ell_2,p_2}(x, y) dx dy, \\
&= \delta_{\ell_1,\ell_2} \delta_{p_1,p_2}, \qquad (1.22)
\end{aligned}$$

owing to the orthonormality of the LG basis modes. This means that any two distinct LG modes are orthogonal. Therefore a qubit state-space analogous to the polarisation Poincaré sphere, can be constructed for any two independent OAM modes [64]. In Fig. 1-3, we show an example of a qubit space for $p = 0$ and $\ell = \pm 1$. Here, the north and south poles are the basis states $|\ell\rangle \equiv |\ell, p = 0\rangle$ and $|-\ell\rangle \equiv |-\ell, p = 0\rangle$. The superposition states are located on the equator. Any qubit state on this subspace can

be written as

$$|\psi_{\ell\theta\chi}\rangle = \cos(\theta/2)\, e^{i\chi}\,|\ell\rangle + \sin(\theta/2)\, e^{-i\chi}\,|-\ell\rangle\,, \tag{1.23}$$

parameterised by θ and χ, similar to qubits on the Bloch sphere. Since $\ell \in \mathbb{Z}$ and $p \in \mathbb{Z}^+$, there are infinitely many such qubit subspaces. In general, the basis states $|\ell, p\rangle$ span the high dimensional Hilbert space and is overcomplete over the azimuthal and radial coordinate. Accordingly, the collection of d modes, i.e. $\{|\ell_j, p_j\rangle\,, j = 0, 1..d-1\}$ spans a d dimensional Hilbert space, $\mathcal{H}_d$. This means that we can map the spatial mode ket states to state vectors with d entries. Using the vector notation we can proceed in discussing photons states with coupled DOF and two photon states in higher dimensions.

1.2.3 High dimensional hybrid polarisation modes

Another avenue for increasing the dimensions of photon is through the coupling of independent DOFs to create hybrid states. In particular, the polarisation ($\mathcal{H}_2^{SPIN}$) and OAM ($\mathcal{H}_d^{OAM}$) (see Fig. 1-4(a)) Hilbert spaces can be combined to construct a higher dimensional subspace [65], called the higher order Poincaré sphere (see Fig. 1-4(b) and (c)). If the spatial DOF also spans the two dimensional Hilbert space, then the subspace is a tensor product of the polarisation qubit and spatial qubit state spaces, respectively. The resulting Hilbert space is $\mathcal{H}_2^{SPIN} \otimes \mathcal{H}_2^{OAM}$. Each qubit, subspace is a span of the scalar mode basis $\{|R\rangle\,|\ell\rangle\,, |L\rangle\,|-\ell\rangle\}$ (Fig. 1-4(a)) and $\{|R\rangle\,|-\ell\rangle\,, |L\rangle\,|\ell\rangle\}$ (Fig. 1-4(c)). Poles contain the scalar basis modes where the polarisation and OAM are just scalar separable products. The equator contains nonseparable superpositions states that cannot be written as independent as scalar separable products. We can construct a complete basis from modes on the equator

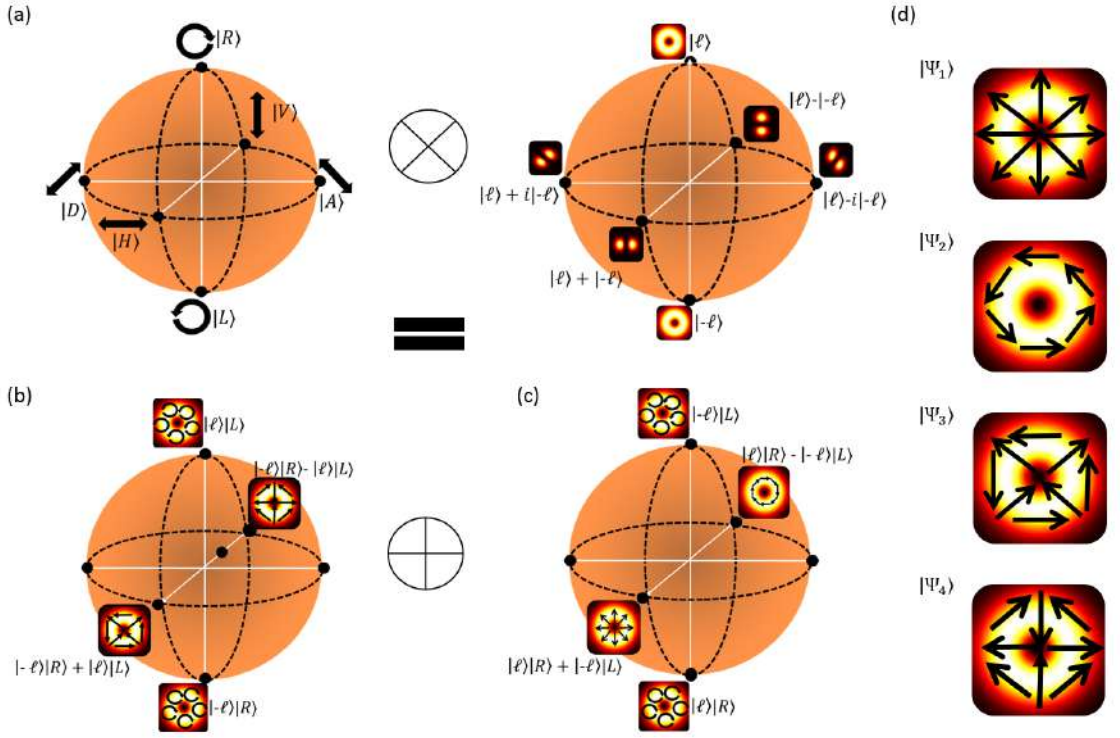


Figure 1-4: The Higher order Poincaré (HOP) sphere is a 4 dimensional state space formed from the (a) tensor product between the polarisation and two dimensional ($\pm\ell$) state-space. (b)-(c) The resulting subspaces contain spatial modes ranging from scalar fields to vectorial fields. Orthogonal vector modes namely the radially ($|\Psi_1\rangle$), azimuthally ($|\Psi_2\rangle$) polarised and hybrid electric $|\Psi_{3,4}\rangle$ modes (from left to right).

of the spheres:

$$\left|\Psi_1^{\ell}\right\rangle = \frac{1}{\sqrt{2}}(|R\rangle\,|\ell\rangle + |L\rangle\,|-\ell\rangle), \tag{1.24}$$

$$\left|\Psi_2^{\ell}\right\rangle = \frac{1}{\sqrt{2}}(|R\rangle\,|\ell\rangle - |L\rangle\,|-\ell\rangle), \tag{1.25}$$

$$\left|\Psi_3^{\ell}\right\rangle = \frac{1}{\sqrt{2}}(|R\rangle\,|-\ell\rangle + |L\rangle\,|\ell\rangle), \tag{1.26}$$

$$\left|\Psi_4^{\ell}\right\rangle = \frac{1}{\sqrt{2}}(|R\rangle\,|-\ell\rangle - |L\rangle\,|\ell\rangle), \tag{1.27}$$

resulting in a high dimensional ($d = 4$) encoding basis that can be used for quantum key distribution [66]. We show the polarisation profiles for each mode in Fig. 1-4(d). The polarisation of the fields is nonuniform across the transverse plane of the fields. These light fields have been a topic of great interest in the classical and

quantum optics community [67–69], especially for possessing correlations that are ubiquitous to nonlocal quantum entangled states. Before introducing this topic, we first establish the description of the two photon Hilbert space and then subsequently introduce entanglement.

1.3 Two photon states in high dimensions

Two independent photons, A and B, defined on Hilbert spaces $\mathcal{H}_A$ and $\mathcal{H}_B$, respectively, have a joint state that is an element of the tensor product space $\mathcal{H}_{AB} = \mathcal{H}_A \otimes \mathcal{H}_B$. For example, if each photon is a qutrit state $|0\rangle_A = \begin{pmatrix} 1 \\ 0 \\ 0 \end{pmatrix}$ and $|2\rangle_B = \begin{pmatrix} 0 \\ 0 \\ 1 \end{pmatrix}$ then the combined state is given by

$$|0\rangle_A \otimes |2\rangle_B = \begin{pmatrix} 1 \\ 0 \\ 0 \end{pmatrix} \otimes \begin{pmatrix} 0 \\ 0 \\ 1 \end{pmatrix} = \begin{pmatrix} 1\begin{pmatrix} 0 \\ 0 \\ 1 \end{pmatrix} \\ 0\begin{pmatrix} 0 \\ 0 \\ 1 \end{pmatrix} \\ 0\begin{pmatrix} 0 \\ 0 \\ 1 \end{pmatrix} \end{pmatrix} = \begin{pmatrix} n_1 = 0 \\ n_2 = 0 \\ n_3 = 1 \\ . \\ . \\ . \\ n_8 = 0 \\ n_9 = 0 \end{pmatrix}, \tag{1.28}$$

resulting in an a state vector with nine, n_i ($i = 1..9$), entries. This is because the two photon subspace has dimensions d^2, resulting from the product of the dimensions of the individual subspaces. We can further compute the two photon qutrit basis set

from the tensor product between the bases of each photon resulting in

$$\begin{aligned}\mathcal{B}_{AB} &= \mathcal{B}_A \otimes \mathcal{B}_B, \\ &= \{|0\rangle_A, |1\rangle_A, |2\rangle_A\} \otimes \{|0\rangle_B, |1\rangle_B, |2\rangle_B\}, \\ &= \{|0\rangle_A \otimes |0\rangle_B, |0\rangle_A \otimes |1\rangle_B, .., |2\rangle_A \otimes |1\rangle_B, |2\rangle_A \otimes |2\rangle_B\},\end{aligned} \tag{1.29}$$

having nine basis vectors. In general, for any dimensions d_A and d_B, for each photon, the basis can be expressed as

$$\mathcal{B}_{AB} = \{|m\rangle_A \otimes |n\rangle_B, \ \forall m = 0, 1, ..d_A - 1 \text{ and } n = 0, 1, ..d_B - 1\}, \tag{1.30}$$

where each photon is spanned by the bases $\{|m\rangle_A\}$ and $\{|n\rangle_B\}$, respectively. As such, an arbitrary two photon pure state can be written as a superstition

$$|\Psi\rangle_{AB} = \sum_{m=0}^{d_A-1} \sum_{n=0}^{d_B-1} a_{mn} |m\rangle_A \otimes |n\rangle_B, \tag{1.31}$$

We drop the tensor product symbol ($\otimes$) and use the short hand notation $|\cdot\rangle_A |\cdot\rangle_B$. Furthermore, the density matrix for an arbitrary quantum states has the form

$$\rho_{AB} = \sum_{m,n,k,l} c_{mnkl} |m\rangle_A |n\rangle_B \langle l|_B \langle k|_A. \tag{1.32}$$

with components $|m\rangle_A |n\rangle_B \langle l|_B \langle k|_A$ having coefficients c_{mnkl}.

1.3.1 Entangled states

There is a special class of quantum states that have correlations that have no classical equivalent. Einstein, Padolsky and Rosen (EPR) introduced these states in their seminal paper [1] with the intention of using them as examples of states that expose the incompleteness of quantum mechanics. Paradoxically, the correlations produced by these states violate local relativistic causality and realism in classical mechanics,

allowing for measurements on one subsystem to effect the outcomes of measurements of their other counterparts even when spatially separated. This phenomenon was later called 'Verschränkung' in German, by Schrödinger, and translates as entanglement in English.

To clearly define entanglement, it is instructive to first introduce separable states. Firstly, let us consider the decomposition in Eq. (1.31), which describes a system of two spatially separated photons, A and B. If the photons are not entangled then the final state can be written as the separable product state

$$|\Psi\rangle = |\psi\rangle_A \otimes |\varphi\rangle_B \,, \tag{1.33}$$

where $|\psi\rangle_A = \sum_{i=0} b_i \, |i\rangle_A$ and $|\varphi\rangle_B = \sum_{j=0} c_j \, |j\rangle_B$. Conversely, the state is entangled if it cannot be written as a separable product of the individual subsystems, i.e., $|\Psi\rangle_{AB} \neq |\psi\rangle_A \otimes |\varphi\rangle_B$, implying that the state is nonseparable. John Bell, devised a statistical test [70], with an inequality that can be violated by states that are nonseparable, and in particular the states

$$\begin{aligned}
|\Phi\rangle^{\pm}_{AB} &= \frac{1}{\sqrt{2}}(|0\rangle_A \, |0\rangle_B + |1\rangle_A \, |1\rangle_B), \\
|\Phi\rangle^{\pm}_{AB} &= \frac{1}{\sqrt{2}}(|0\rangle_A \, |0\rangle_B - |1\rangle_A \, |1\rangle_B), \\
|\Psi\rangle^{\pm}_{AB} &= \frac{1}{\sqrt{2}}(|0\rangle_A \, |1\rangle_B + |1\rangle_A \, |0\rangle_B), \\
|\Psi\rangle^{\pm}_{AB} &= \frac{1}{\sqrt{2}}(|0\rangle_A \, |1\rangle_B - |1\rangle_A \, |0\rangle_B),
\end{aligned} \tag{1.34}$$

are known as maximally entangled Bell-states. From these equations it is clear that a projection onto of the eigenstates of subsystem A determines the outcome of subsystem B. For example, in Eq. (1.34), a measurement of the state $|0\rangle_A$ in photon A, results in $|1\rangle_B$ for photon B.

The Bell states shown in Eq. (1.34) are only two dimensional. In high dimensions,

an entangled state can be written as

$$|\Psi\rangle = \sum_{j=0}^{d-1} \lambda_j \, |j\rangle_B \, |j\rangle_B \, , \tag{1.35}$$

where $|\lambda_j|^2$ is the probability of detecting the biphoton state $|j\rangle_A \, |j\rangle_B$ spanning a d dimensional basis. Here, $|j\rangle_A \, |j\rangle_B$ is called a Schmidt basis. For $\lambda_j = 1\sqrt{d}$, the state is maximally entangled and the number d is called the Schmidt number [71]. For states where $0 < \lambda_j \leq 1$ the Schmidt number can be estimated as [72],

$$K = \frac{\left(\sum_j |\lambda_j|^2\right)^2}{\sum_j |\lambda_j|^4}, \tag{1.36}$$

which evaluates as $K = 1$ for completely separable states and is $K \geq 2$ for states that are nonseperable. It is possible to generate entanglement with the spatial DOF. Recent demonstrations have included different mode families such as the LG [73], Ince-Gaussian [74] and Bessel Gaussian [75] basis states.

Spontaneous parametric down-conversion (SPDC) is one way of generating entangled photons. In this process, a high frequency pump photon is absorbed by the crystal and converted into two lower frequency (down-converted) photons which are highly correlated in polarisation [76–79], momenta [41] and temporal DOF [38,80,81]. The conservation in momentum also results in the conservation of OAM and therefore the entanglement thereof [75, 82–84]. In the LG basis for OAM modes, the Schmidt decomposition for SPDC is given by [85, 86]

$$|\Psi\rangle = \sum_{\ell_1,\ell_2,p} \lambda_{\ell_1\ell_2 p} \, |\ell_1, p\rangle_A \, |\ell_2, p\rangle_B \, , \tag{1.37}$$

where $|\lambda_{\ell_1\ell_2 p}|^2$ is the probability of finding photon A and B in the state $|\pm\ell, p\rangle$. The dimensionality of the state is limited by the distribution of $|\lambda_{\ell_1\ell_2 p}|^2$. Due to OAM conservation in the SPDC process, the OAM of the pump photon sets the restriction that, $\ell_{pump} = \ell_1 + \ell_2$, ensuring that OAM is always conserved. There are several methods for increasing the number of accessible modes which include tuning phase-matching

conditions (momentum conservation conditions) at the crystal [61], adjusting the detection mode sizes or by shaping the modes [86] and even selecting different mode families [87] thus maximising the maximum number of accessible modes. To this end, valid tests of quantum entanglement using the Bell inequality violations in two [84] and up to twelve dimensions [88], quantum state tomography [35, 89], entanglement witnesses [42] have all been demonstrated with SPDC photons using the transverse spatial DOF of photons.

1.3.2 Nonlocal hybrid entanglement and classical hybrid entanglement

While the states in Eq. (1.37) are entangled in single DOFs, there exists a class of quantum entangled states where the internal DOFs of each photon are completely independent. Such states are said to be hybrid entangled and have previously been prepared between polarisation and path [14, 90], polarisation and OAM [91] and polarisation and time-bin [92]. The states can be prepared as maximally entangled qubits, for example, in the polarisation and OAM basis they can be expressed as

$$\left|\Psi^{\ell}\right\rangle_{AB} = \frac{1}{\sqrt{2}}\left(\left|R\right\rangle_{A}\left|\ell\right\rangle_{B} + \left|L\right\rangle_{A}\left|-\ell\right\rangle_{B}\right), \tag{1.38}$$

where photon A and B are defined in the circular polarisation (spin) and OAM bases, respectively. When photon A is projected onto the state $|R\rangle$, photon B will collapse onto the state $|\ell\rangle$, similarly, a projection of photon A onto the state $|L\rangle$, will result in the collapse of photon B into the state $|-\ell\rangle$. This means that the measurements are strongly correlated even though the individual photons are defined in independent DOFs. Interestingly these exotic states have been used for fundamental tests of quantum mechanics such as the complementary principle [93] through quantum eraser experiments [14, 94, 95].

Interestingly, vector modes also demonstrate entanglement like correlations [96]. First notice the resemblance between a vector mode, e.g., in Eq. (1.24), and the hybrid entangled state in Eq. (1.38). Both these states represent systems that have

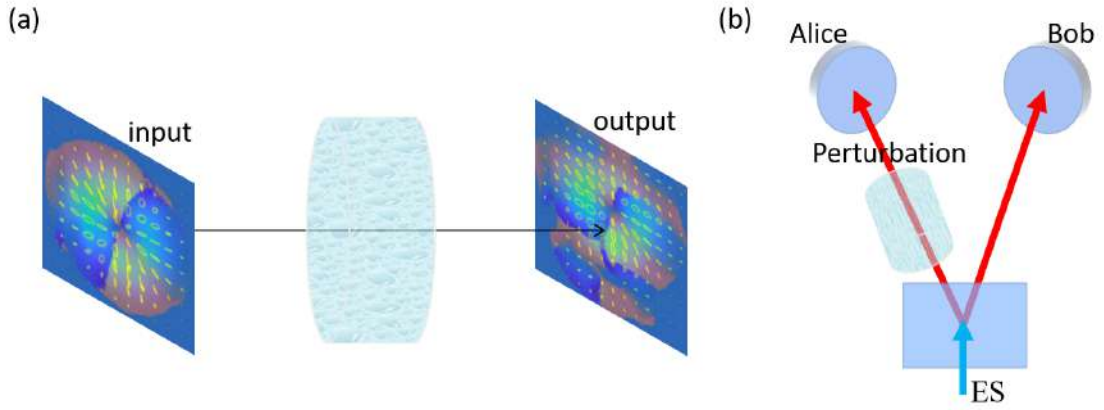


Figure 1-5: (a) A vectorial field propagates through a channel that distorts the spatial amplitude, phase and polarisation field. The input field is mapped to the output field having evolved as a result of the channel perturbation. (b) An entanglement source (ES) creates two strongly correlated photons where one goes through free-space while the other is perturbed. At the end of the channel, Alice and Bob perform correlation measurements on the two bi-photon state.

nonseparable correlations with the discrepancy being in the nature of the correlations: for hybrid entanglement, spatial separation is involved and therefore nonlocality plays a crucial role in the nonseparable correlations, while for vector modes the nonseparable correlations are between the internal DOFs, locally, within the photon field. Therefore, for vector modes, the labels A and B mark the internal DOFs of the same photons and are therefore classically entangled [97, 98]. Today classical entanglement though controversial, is finding applications to quantum walks [99,100], process tomography of entangled channels [101] and metrology [102].

1.4 Quantum channels

In Fig. 1-5(a), we show a vector mode before and after it propagates through a noisy channel. After the channel, the entire field is completely distorted. A current challenge has been to mitigate such deleterious effects so that the quality of photons signals is preserved after a quantum channel. Turbid [103–106] and turbulent media [107–114] can distort the transverse spatial amplitude and phase profiles of photons due to rapid variations in the refractive index profile. Similarly, birefringence

(polarisation dependent refractive index) and imperfections in optical fibers [115,116] are main pertubations that can rotate polarsation fields or cause inter-modal coupling. Moreover, partially obstructed photons can also result in information loss due to diffraction [26]. On the other hand, high dark count rates in detectors, stray light and inefficient photon sources can reduce the purity of higher dimensional quantum states [27] since these mechanism can introduce some degree of mixture to the state [117].

To see the impact of quantum channels on quantum states, we adopt the operational definition for channel operators, $\mathcal{E}(\cdot)$, acting on an initial state ρ [118]

$$\mathcal{E}(\rho) = \sum_i A_i \rho A_i^\dagger, \tag{1.39}$$

that we assume is completely positive and trace preserving (CPTP), meaning that the operators A_i satisfy, $\sum_i A_i A_i^\dagger = \mathbb{1}$. Here operators A_i are called Krauss operators, and can be further decomposed using a matrix basis $\{\tilde{E}_k,\ \mathrm{Tr}\left(\tilde{E}_k \tilde{E}_l\right) = d\delta_{kl}\}$ as $A_i = \sum_k a_{ik}\tilde{E}_k$. Subsequently, the channel mapping can be rewritten as [119]

$$\mathcal{E}(\rho) = \sum_{kl}^{d^2-1} \tilde{E}_k \rho \tilde{E}_l^\dagger \chi_{kl}. \tag{1.40}$$

The matrix components, $\chi_{kl} = \sum_{pq} a_{kp} a_{lq}^*$, are entries of the positive Hermitian matrix, χ, that determines the channel in the $\{\tilde{E}_k\}$ basis.

There is a one-to-one correspondence between CPTP maps and specific density matrices that the channels can map onto, i.e., $\mathcal{E} \to \rho_{\mathcal{E}}$, owing to the Choi–Jamiołkowski isomorphism [120,121] or commonly referred to as channel-state duality [122]. To elucidate this concept, let us consider a two photon state that is maximally entangled, $|\Phi^+\rangle = 1/\sqrt{d}\sum_{j=0}^{d-1} |j\rangle |j\rangle$ and subsequently interacts with a quantum channel that transforms it as

$$\rho_{\mathcal{E}} = \mathbb{1} \otimes \mathcal{E} \left|\Phi^+\right\rangle \left\langle\Phi^+\right|. \tag{1.41}$$

The operator $\mathbb{1} \otimes \mathcal{E}$ represents a single sided channel acting on a maximally entangled state, where nothing happens to one photon (hence the identity, $\mathbb{1}$) while its twin

interacts with the channel $\mathcal{E}$. The situation is illustrated in Fig. 1-5(b). Suppose the channel can be represented by a unitary operator that is trace preserving, therefore mapping the initial state onto another pure state, i.e. $|j\rangle \rightarrow \sum_i t_{ij} |i\rangle$. For transverse spatial modes, channels of this nature can be, for example, represented by atmospheric turbulence [24], optical aberrations in underwater channels [123] or refractive index imperfections in short optical fibers [124]. Accordingly, if we represented the channel transmission matrix as $T = \sum_{ij} t_{ij} |i\rangle \langle j|$, the transformed two photon state is [125]

$$(\mathbb{1} \otimes \mathcal{E}) |\Phi\rangle = \frac{1}{\sqrt{d}} \sum_{i,j=0}^{d-1} t_{ij} |j\rangle |i\rangle , \tag{1.42}$$

where the coefficients, relating to the channel are imprinted onto the final state, and can be used to undo the effects of the channel [125]. Konrad et al. [126] also revealed an intriguing aspect of entangled states that are subjected to single sided channels. The authors, showed that the input and output degree of entanglement of photons, concurrence [127], after a single sided channel only depends on the evolution of maximally entangled states as depicted in the relation

$$C(\mathbb{1} \otimes \mathcal{E} |\psi_{in}\rangle) = C(\rho_{\mathcal{E}}) \times C(|\psi_{in}\rangle) , \tag{1.43}$$

where $C(|\psi_{in}\rangle)$, is the concurrence of the input state $|\psi_{in}\rangle$ before traversing the channel while $C(\rho_{\mathcal{E}})$ is the concurrence of the maximally entangled state after the channel $\mathcal{E}$. This means that the degree of entanglement of any input state $|\psi_{in}\rangle$ decays proportional to a maximally entangled state. This finding has been confirmed through numerical [128] and experimental [101] studies focusing on spatial mode entanglement decay and characterisation through turbulence.

Another class of quantum channels that are encountered in practical settings, are a type of depolarisation channel, that models the influence of external noise entering the system and reducing the coherence of quantum states [27]. The growing interest in these classes of states is due to the the potential resilience of high dimensional quantum states to noise [34]. The state decomposition after such channels is given

by

$$\rho_p = p\left|\Psi_d\right\rangle\left\langle\Psi_d\right| + \frac{1-p}{d^2}\mathbb{1}_{d^2}, \tag{1.44}$$

where $\left|\Psi_d\right\rangle$ is the transmitted high dimensional entangled state, and $\mathbb{1}_{d^2}$ is the identity operator containing the noise contribution to the state. Here p can be associated with the purity of the state, ranging from a maximally mixed ($p = 0$) to a pure state ($p = 1$). Interestingly, the isotropic state is separable for $p \leq 1/(d+1)$ and entangled otherwise. It is important to have knowledge of p and d since the quality of the generated state depends on them. For example, in generalised high dimensional Bell inequality tests, non-local correlations can only be confirmed when $p > 2/S_d$ where S_d is the Bell parameter [129].

Standard procedures for overcoming some of these perturbations includes quantum error correction methods [125, 130, 131], that require full knowledge of how the states evolve through the channel, often requiring a process tomography (reconstruction of the channel operator) to determine all d^4 components of the channel operator [132], e.g. in Eq. 1.40.

1.5 Outline

This thesis will explore several approaches for engineering robust photon states that span higher dimensional Hilbert spaces by either manipulating their intrinsic properties to make them immune to malignant effects of perturbative channels, or by tailoring efficient characterisation methods that yield important parameters about the state after the perturbation. We draw attention to the spatial (and sometimes combined polarisation) DOF both locally and nonlocaly with entangled states. Our overarching goals are executed in five subsequent chapters as follows:

In Chapter 2, we introduce our first perturbation, solid obstructions, that are diffractive, mimicking dust particles in the air, and show that we can tailor the radial profile so that the generated photons can be used for quantum key distribution (QKD) in the presence of obstructions. The photon states that we tailor are self-reconstructing vector modes that are modulated with a non-diffracting Bessel-Gaussian (BG) envelope. Using a prepare-measure (BB84) protocol, we demonstrate that these mode fields offer higher information capacity after solid diffractive objects in comparison to Laguerre-Gaussian modes.

In Chapter 3, we introduce our second perturbation, optical turbulence. Here, we will show that a single maximally nonseparable vector mode is sufficient to predict the behaviour of arbitrary vector OAM states through a unitary channel, showing interesting features about the performance of various modes through the channel such as the decay dynamics for different mode orders. We will invoke channel state duality in our demonstration, a quantum tool, to devise our approach. This method illustrates the benefit of applying quantum tools to the study of coherent laser light and single photon states with nonseparable (equivalently entangled) internal DOFs.

In Chapter 4, we build onto the work from chapter three by considering a hidden feature of vector modes, namely their invariance to unitary channels, thanks to their entanglement like properties. Here, we introduce a third family of pertubations, i.e. optical aberrations, that can emanate from, element misalignment, or dynamic processes during propagation in transparent media with a spatially varying refractive

index profile and are unitary in the spatial DOF. We will show that the unitary nature of the channel makes vector fields immune to the perturbations and that the channel operation can easily be undone. Moreover, the work will address prior contradictions in the community on the robustness of vectorial photon fields in both quantum and classical channels.

In Chapter 5, we demonstrate a novel approach for transmitting multiple entangled states through a heterogeneous free-space and fiber quantum channel. We engineer hybrid entanglement non-locally, between two photons that are spatially separated. Each photon will be described in an independent DOF; the polarisation (spin) state of one photon will be entangled to the OAM state of its twin photon. Enabling for the polarised photon to be transmitted through a long distance fiber channel while the high dimensional OAM photon will be transmitted through free-space. Since the photon that carries the spatial mode can take on any OAM state, we will demonstrate that the channel can transmit multiple hybrid entangled states subspaces through the same conventional single mode fibre.

Lastly, in Chapter 6, we will encounter our last channel, a noisy quantum entangled two photon channel that is encroached in white noise, known to affect the purity and dimensionlity of quantum entangled states. The focus will be on devising a technique that can characterise the effective dimensions and purity of entangled states defined on large Hilbert spaces. A set of conditional measurements that return a visibility that scales monotonically with state dimensionality and purity will be constructed to demonstrate the versatility of the approach, we will showcase it with two bases, the OAM and pixel bases, showing that it works over a wide range of noise levels.

Chapter 2

Self healing quantum communication through obstructions

The work in this chapter was published in:

- **Nape, I.**, Otte, E., Vallés, A., Rosales-Guzmán, C., Cardano, F., Denz, C. and Forbes, A., 2018. "Self-healing high-dimensional quantum key distribution using hybrid spin-orbit Bessel states.", Optics express, 26(21), pp.26946-26960.

Nape, I., lead the experiments with the second author, analysed the data and contributed to writing the manuscript under the guidance of the contributing coauthors.

2.1 Introduction

Quantum key distribution (QKD) enables two parties to securely exchange information detecting the presence of eavesdropping [133]. Unlike conventional cryptography, with unproven computational assumptions, the security of QKD relies on the fundamental laws of quantum mechanics [134], prohibiting the cloning of quantum information encoded in single photons [4]. Although current state of the art implementations have successfully transfered quantum states in free-space [135], optical fibers [136], and between satellites [137], efficient high capacity key generation and robust security are still highly sought-after.

Spatial modes of light hold significant promise in addressing these issues. The channel capacity can be exponentially increased by encoding information in the spatial degree of freedom (DoF) of photons and has been demonstrated with classical light in free-space and fibres [138]. Implementing QKD with high-dimensional (HD) states ($d > 2$) has also been demonstrated [20, 139], by exploiting the ability of each photon to carry up to $\log_2(d)$ bits per photon while simultaneously increasing the threshold of the quantum bit error rate (QBER). This makes HD QKD protocols more robust [29–31], even when considering extreme perturbing conditions, i.e., underwater submarine communication links [123]. While most studies to date have used spatial modes of light carrying orbital angular momentum (OAM) [140], reaching up to $d = 7$ [21], higher dimensions are achievable with coupled spatial and polarization structures, e.g. vector modes. These states have received recent attention in classical communication [141–144], in the quantum realm as a means of implementing QKD without a reference frame [145, 146], but only recently have both DoFs been used to increase dimensionality in QKD [147, 148].

To date, there has been only limited work on the impact of perturbations on HD entanglement and QKD with spatial modes [148–152]. In turbulence, for example, the key rates are known to decrease [153], with the latter to be compensated for large OAM states in the superposition. There has been no study on HD QKD through physical obstacles.

In this chapter, we take advantage of the self-healing properties in non-diffracting vector beams to show that the bit rate of a QKD channel, affected by partial obstructions, can be ameliorated by encoding information onto diffraction-free single photons. To this end, we generate a non-diffracting (self-reconstructing) set of mutually unbiased bases (MUB), formed by hybrid scalar and vector modes with a Bessel-Gaussian (BG) transverse profile. We herald a single photon with a BG radial profile by means of spontaneous parametric down-conversion (SPDC), generating paired photons and coupling OAM and polarization using a q-plate [53]. We characterize the quantum link by measuring the scattering probabilities, mutual information and secret key rates in a prepare-measure protocol for BG and Laguerre-Gaussian (LG) photons, comparing the two for various obstacle sizes. We find that the BG modes outperform LG modes for larger obstructions by more than 3×, highlighting the importance of radial mode control of single photons for quantum information processing and communication.

2.2 Self-healing Bessel modes

Since Bessel modes cannot be realized experimentally, a valid approximation, the Bessel-Gaussian (BG) mode, is commonly used [154]. This approximation inherits from the Bessel modes the ability to self-reconstruct in amplitude, phase [155, 156], and polarization [157–159], even when considering entangled photon pairs [152] or non-separable vector modes [160, 161]. Mathematically, they are described by

$$\begin{aligned}\mathcal{J}_{\ell,k_r}(r,\varphi,z) =& \sqrt{\frac{2}{\pi}} J_\ell\left(\frac{z_R k_r r}{z_R - \mathrm{i}z}\right) \exp\left(\mathrm{i}\ell\varphi - \mathrm{i}k_z z\right) \\ & \cdot \exp\left(\frac{\mathrm{i}k_r^2 z w_0 - 2kr^2}{4(z_R - \mathrm{i}z)}\right),\end{aligned} \tag{2.1}$$

where (r, φ, z) represents the position vector in the cylindrical coordinates, ℓ is the azimuthal index (topological charge). Furthermore, $J_\ell(\cdot)$ defines a Bessel function of the first kind , k_r and k_z are the radial and longitudinal components of the wave number $k = \sqrt{k_r^2 + k_z^2} = 2\pi/\lambda$. The last factor describes the Gaussian envelope with beam waist w_0 and Rayleigh range $z_R = \pi w_0^2/\lambda$ for a certain wavelength λ.

The propagation distance over which the BG modes approximate a non-diffracting mode is given by $z_{\max} = 2\pi w_0/\lambda k_r$. In the presence of an obstruction of radius R inserted within the non-diffracting distance, a shadow region of length $z_{\min} \approx 2\pi R/k_r\lambda$ is formed [162]. The distance $z_{\min}$ determines the minimum distance required for the beam to recover its original form, whereby full reconstruction is achieved at $2z_{\min}$ [155, 156].

We exploit this property with single photons that have non-separable polarization and OAM DoFs. By carefully selecting a k_r value, we show that the information of hybrid entangled single photon encoded with a Bessel radial profile can be recovered after the shadow region of an obstruction. Traditionally hybrid modes, while still new in the communication context, have not been controlled in radial profile. Indeed, the traditional generation approaches often result in very complex radial structures [163]. To control and exploit all spatial and the polarization DoFs for QKD we introduce a high-dimensional self-healing information basis constructed from non-orthogonal vector and scalar OAM BG spatial modes.

2.2.1 Non-diffracting information basis

In order to demonstrate the concept we will use the well-known BB84 protocol, but stress that this may be replaced with more modern and advantageous protocols with little change to the core idea as outlined here. In the standard BB84 protocol, Alice and Bob unanimously agree on two information basis. The first basis can be arbitrarily chosen in d dimensions as $\{|\Psi_i\rangle, i = 1..d\}$. However, the second basis must fulfill the condition

$$|\langle\Psi_i|\Phi_j\rangle|^2 = \frac{1}{d}, \tag{2.2}$$

making $|\Psi\rangle$ and $|\Phi\rangle$ mutually unbiased. Various QKD protocols were first implemented using polarization states, spanned by the canonical right $|R\rangle$ and left $|L\rangle$ circular polarization states constituting a two-dimensional Hilbert space, i.e., $\mathcal{H}_\sigma = \text{span}\{|L\rangle, |R\rangle\}$. More dimensions where later realized with the spatial DoF of pho-

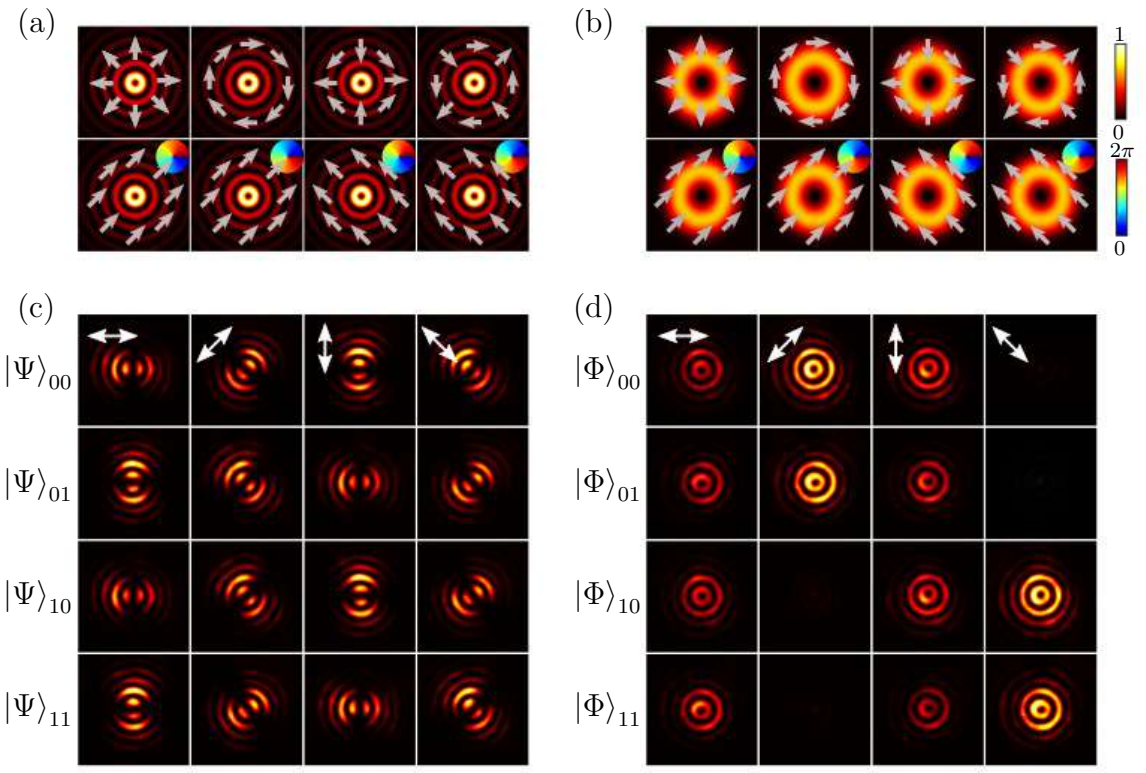


Figure 2-1: Intensity and polarization mappings of vector (first row) and scalar (second row) MUB modes with (a) BG and (b) LG radial profiles for $\ell = \pm 1$. The polarization projections on the (c) vector $|\Psi\rangle$ and (d) scalar $|\Phi\rangle$ basis BG modes. The vector modes have spatially varying polarizations which consequently render the polarization and spatial DoF as non-separable. This is easily seen in the variation of the transverse spatial profile when polarization projections are performed (orientation indicated by white arrow) on the $|\Psi\rangle$ modes. In contrast, the scalar modes have separable polarization and spatial DoF hence polarization projections only cause fluctuations in the intensity of the transverse profile for the $|\Phi\rangle$ modes.

tons [20, 21], using the OAM DoF spanning the infinite dimensional space, i.e. $\mathcal{H}_\infty = \bigoplus \mathcal{H}_\ell$, such that $\mathcal{H}_\ell = \{|\ell\rangle, |-\ell\rangle\}$ is qubit space characterized by a topological charge $\ell \in \mathbb{Z}$.

Here, we exploit an even larger encoding state space by combining polarization and OAM, $\mathcal{H}_\infty = \bigoplus \mathcal{H}_\sigma \otimes \mathcal{H}_\ell$ where $\mathcal{H}_4 = \mathcal{H}_\sigma \otimes \mathcal{H}_\ell$, is a qu-quart space spanned by the states $\{|L\rangle|\ell\rangle, |R\rangle|\ell\rangle, |L\rangle|-\ell\rangle, |R\rangle|-\ell\rangle\}$, described by the so-called higher-order Poincaré spheres (HOPSs) [164, 165]. These modes feature a coupling between the polarization and OAM DoFs, shown in Fig. 2-1. The HOPS concept neglects the radial structure of the modes, considering only the angular momentum content, spin

and orbital. Yet all modes have radial structure, shown in Fig. 2-1 (a) for BG and (b) for LG profiles. We wish to create a basis of orthogonal non-separable vector BG modes together with their MUBs for our single photon states.

Without loss of generality, we choose a mode basis on the $\mathcal{H}_4$ subspace with $\ell = \pm 1$ as our example. Our encoding basis is constructed as follows: we define the radial profile $\mathcal{J}_{\ell,k_r}(r)$ representing the radial component of the BG mode in Eq. (2.1). Our first mode set is comprised of a self-healing vector BG mode basis, mapped as

$$|\Psi\rangle_{00} = \frac{1}{\sqrt{2}}\mathcal{J}_{\ell,k_r}(r)\big(\,|R\rangle\,|\ell\rangle + |L\rangle\,|-\ell\rangle\,\big), \tag{2.3}$$

$$|\Psi\rangle_{01} = \frac{1}{\sqrt{2}}\mathcal{J}_{\ell,k_r}(r)\big(\,|R\rangle\,|\ell\rangle - |L\rangle\,|-\ell\rangle\,\big), \tag{2.4}$$

$$|\Psi\rangle_{10} = \frac{1}{\sqrt{2}}\mathcal{J}_{\ell,k_r}(r)\big(\,|L\rangle\,|\ell\rangle + |R\rangle\,|-\ell\rangle\,\big), \tag{2.5}$$

$$|\Psi\rangle_{11} = \frac{1}{\sqrt{2}}\mathcal{J}_{\ell,k_r}(r)\big(\,|L\rangle\,|\ell\rangle - |R\rangle\,|-\ell\rangle\,\big), \tag{2.6}$$

with some example polarization projections shown in Fig. 2-1 (c). The set of MUB modes is given by

$$|\Phi\rangle_{00} = \mathcal{J}_{\ell,k_r}(r)\,|D\rangle\,|-\ell\rangle\,, \tag{2.7}$$

$$|\Phi\rangle_{01} = \mathcal{J}_{\ell,k_r}(r)\,|D\rangle\,|\ell\rangle\,, \tag{2.8}$$

$$|\Phi\rangle_{10} = \mathcal{J}_{\ell,k_r}(r)\,|A\rangle\,|-\ell\rangle\,, \tag{2.9}$$

$$|\Phi\rangle_{11} = \mathcal{J}_{\ell,k_r}(r)\,|A\rangle\,|\ell\rangle\,, \tag{2.10}$$

where D and A are the diagonal and anti-diagonal polarization states (see Fig. 2-1 (d) for polarization projections). The set $|\Psi\rangle_{ij}$ and $|\Phi\rangle_{ij}$ are mutually unbiased and, therefore, form a reputable information basis for QKD in high dimensions.

As a point of comparison to the self-healing properties of the non-diffracting modes, we make use also of a similar alphabet but projecting the heralding photon onto a Gaussian mode, obtaining a helical mode in the other photon after traversing

a spin-to-orbital angular momentum converter [53]. We will refer to this as a LG mode in the remainder of the manuscript.

2.3 Methods

2.3.1 Single photon heralding

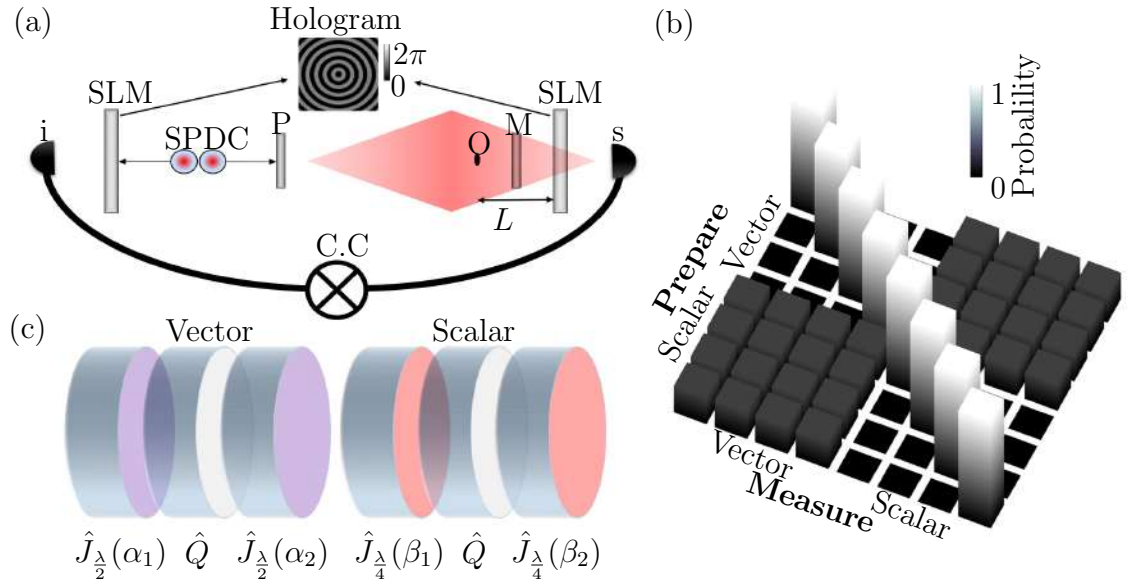


Figure 2-2: (a) Conceptual drawing of the QKD with self-healing BG modes. The SLMs post-select the self-healing BG radial profile from the SPDC source. The prepare (P) and measure (M) optics modulate and demodulate the OAM and polarization DoF of the heralded photon. The physical obstruction (O) is placed at a distance L from the right-most SLM, which decodes the radial information of Bob's photon. The optics are within $z_{\max} = 54$ cm distance of the BG modes depicted as the rhombus shape. The propagation of the post-selected BG mode can be determined via back-projection. (b) Numerical scattering probability matrix for the vector and scalar modes sets in free-space. The channels correspond to the probabilities $|C_{ij}|^2$ calculated from Eq. (2.22). (c) Optical elements required by Alice and Bob to prepare and measure the spin-coupled states of the heralded photons (cf. Table 2.1).

Heralded photon sources have been used as a means of producing single photons in QKD [166]. In this process, the heralded photon conditions the existence of its correlated twin. Moreover, the statistics of the heralded photon have low multi-photon probabilities which can be further remedied by using decoy states [167].

Here, we herald a single photon via SPDC where a high frequency photon ($\lambda =$

405 nm) was absorbed by a nonlinear crystal, generating a signal (s) and idler (i) correlated paired photons at $\lambda = 810$ nm. In the case of a collinear emission of s and i, the probability amplitude of detecting mode functions $|m\rangle_s$ and $|m\rangle_i$, respectively, is given by [168]

$$c_{s,i} = \int\int m_s^*(\mathbf{x}) m_i^*(\mathbf{x}) m_p(\mathbf{x}) d^2x, \tag{2.11}$$

where $m_p(\mathbf{x})$ is the field profile of the pump (p) beam which best approximates the phase-matching condition in the thin crystal limit; the Rayleigh range of the pump beam is much larger than the crystal length. The probabilities amplitudes $c_{s,i}$ can be calculated using the Bessel basis,

$$m_{s,i}(r,\varphi) = \mathcal{J}_{\ell_{s,i},k_r}(r)\exp(\mathrm{i}\ell_{s,i}\varphi), \tag{2.12}$$

where $\exp(\mathrm{i}\ell\varphi)$ corresponds to the characteristic azimuthal phase mapping onto the state vector $|\ell\rangle$. Taking into account a SPDC type-I process and a Gaussian pump beam, the quantum state used to encode and decode the shared key can be written in the Bessel basis as

$$|\Psi\rangle_{AB} = \sum c_{\ell,k_{r,1},k_{r,2}} |\ell, k_{r,1}\rangle_s |-\ell, k_{r,2}\rangle_i |H\rangle_s |H\rangle_i , \tag{2.13}$$

being $|\ell, k_r\rangle_s \sim J_{\ell,k_r}(r)|\ell\rangle$ and H the horizontal polarization state. The probability amplitudes $c_{\ell,k_{r,1},k_{r,2}}$ can be calculated using the overlap integral in Eq. (2.11). Experimentally $|c_{\ell,k_{r,1},k_{r,2}}|^2$ is proportional to the probability of detecting a coincidence when the state $|\ell, k_{r,1}\rangle_s |-\ell, k_{r,2}\rangle_i$ is selected. Coincidences are optimal when $|k_{r,1}|$ and $|k_{r,2}|$ are equivalent.

In this experiment, the idler photon (i) was projected into the state $|0, k_r\rangle_i$, heralding only the signal photons (s) with the same spatial state $|0, k_r\rangle_s$, as can be seen in the sketch of Fig. 2-2(a). Therefore, a prepare-measure protocol can be carried out by using the same s photon. In other-words, Alice remotely prepared her single photon with a desired radial profile from the SPDC before encoding the polarization

and OAM information.

2.3.2 Tailoring the desired spatial profile

Spatial light modulators (SLMs) are a ubiquitous tool for generating and detecting spatial modes [52, 169]. We exploit their on-demand dynamic modulation via computer generated holograms to post-select the spatial profiles of our desired modes (see hologram inset in Fig. 2-2(a)). For the detection of BG modes, we choose a binary Bessel function as phase-only hologram, defined by the transmission function

$$T(r,\varphi) = \text{sign}\{J_\ell(k_r r)\}\exp(\text{i}\ell\varphi), \tag{2.14}$$

with the sign function sign$\{\cdot\}$ [170,171]. Classically, this approach has the advantage of generating a BG beam immediately after the SLM and, reciprocally, detects the mode efficiently [152]. Importantly, a blazed grating is used to encode the hologram, with the desired mode being detected in the first diffraction order [172] and spatial filtered with a single mode fiber (SMF).

Here, we set $k_r = 18\,\text{rad/mm}$ and $\ell = 0$ for the fundamental Bessel mode and, conversely, $k_r = 0$ to eliminate the multi-ringed Bessel structure.

2.3.3 Generation and detection

Liquid crystals q-plates represent a convenient and versatile way to engineer several types of vector beams [67]. In our setup, vector and scalar modes, described in Fig. 2-1, are either generated or detected, at Alice and Bob's prepare (P) and measure (M) stations in Fig. 2-2 (a), by letting signal photons pass through a combination of these devices and standard wave plates (see Fig. 2-2 (c)). A q-plate consists of a thin layer of liquid crystals (sandwiched between glass plates) whose optic axes are arranged so that they form a singular pattern with topological charge q. By adjusting the voltage applied to the plate it is possible to tune its retardation to the optimal value $\delta = \pi$ [173]. In such a configuration indeed the plate behaves like a standard half-wave plate (with an inhomogeneous orientation of its fast axis) and can be used

to change the OAM of circularly polarized light by $\pm 2q$, depending on the associated handedness being left or right, respectively. As such, the q-plate is used to achieve spin orbit coupling. In the Jones matrix formalism, the q-plate is represented by the operator

$$\hat{Q} = \begin{pmatrix} \cos(2q\varphi) & \sin(2q\varphi) \\ \sin(2q\varphi) & -\cos(2q\varphi) \end{pmatrix}, \tag{2.15}$$

where φ is the azimuthal coordinate. The matrix is then written in the following linear basis $\{|H\rangle = \begin{pmatrix} 1 \\ 0 \end{pmatrix}, |V\rangle = \begin{pmatrix} 0 \\ 1 \end{pmatrix}\}$. In our experiment we use q-plates with $q = 1/2$, and half-wave ($\frac{\lambda}{2}$) as well as quarter-wave ($\frac{\lambda}{4}$) plates for polarization control, represented by the Jones matrices

$$\hat{J}_{\frac{\lambda}{2}}(\theta) = \begin{pmatrix} \cos(2\theta) & \sin(2\theta) \\ \sin(2\theta) & -\cos(2\theta) \end{pmatrix}, \tag{2.16}$$

and

$$\hat{J}_{\frac{\lambda}{4}}(\theta) = \begin{pmatrix} \cos^2(\theta) + \mathrm{i}\sin^2(\theta) & (1-\mathrm{i})\sin(\theta)\cos(\theta) \\ (1-\mathrm{i})\sin(\theta)\cos(\theta) & \sin^2(\theta) + \mathrm{i}\cos^2(\theta) \end{pmatrix}. \tag{2.17}$$

Here, θ represents the rotation angle of the wave plates fast axis with respect to the horizontal polarization. The operator associated with the generation of the vector mode is

$$\hat{V}(\alpha_1, \alpha_2) = \hat{J}_{\frac{\lambda}{2}}(\alpha_2)\hat{Q}\hat{J}_{\frac{\lambda}{2}}(\alpha_1)\hat{P}_H, \tag{2.18}$$

where α_1 and α_2 are the rotation angles for the half-wave plates and $\hat{P}_H = \begin{pmatrix} 1 & 0 \\ 0 & 0 \end{pmatrix}$ represents the operator for a horizontal linear polarizer. Similarly, the operator for

the scalar modes is

$$\hat{S}(\beta_1,\beta_2) = \hat{J}_{\frac{\lambda}{4}}(\beta_2)\hat{Q}\hat{J}_{\frac{\lambda}{4}}(\beta_1)\hat{P}_H, \tag{2.19}$$

where β_1 and β_2 are the rotation angles for the quarter-wave plates.

Let the set $\mathcal{M}_1 = \{\hat{V}_i \,|\, \hat{V}_i \rightarrow |\Psi_i\rangle\,, i = 1..4\}$ be associated with the generation of vector modes from $\hat{V}(\alpha_1,\alpha_2)$, and $\mathcal{M}_2 = \{\hat{S}_j \,|\, \hat{S}_j \rightarrow |\Phi_j\rangle\ , j = 1..4\}$ for the scalar modes from $\hat{S}(\beta_1,\beta_2)$. The orientation of the angles required to obtain them is given in Table 2.1 for the vector and scalar modes (see also schematics of wave plates arrangement in Fig. 2-2 (c)).

Table 2.1: Generation of vector and scalar modes from a horizontally polarized BG mode ($\ell = 0$) at the input. The angles $\alpha_{1,2}$ and $\beta_{1,2}$ are defined with respect to the horizontal polarization. For each $\hat{V}_i$ and $\hat{S}_i$ we present the angles needed to perform the mapping of $\mathcal{M}_1 \rightarrow \{|\Psi_i\rangle\}$ and $\mathcal{M}_2 \rightarrow \{|\Phi_i\rangle\}$ with a one-to-one correspondence.

Vector, $\hat{V}(\alpha_1,\,\alpha_2)$			Scalar, $\hat{S}(\beta_1,\beta 2)$		
Operator	$\hat{J}_{\frac{\lambda}{2}}(\alpha_1)$	$\hat{J}_{\frac{\lambda}{2}}(\alpha_2)$	Operator	$\hat{J}_{\frac{\lambda}{4}}(\beta_1)$	$\hat{J}_{\frac{\lambda}{4}}(\beta_2)$
$\hat{V}_1$	0	–	$\hat{S}_1$	$-\pi/4$	0
$\hat{V}_2$	$\pi/4$	–	$\hat{S}_2$	$\pi/4$	$\pi/2$
$\hat{V}_3$	0	0	$\hat{S}_3$	$-\pi/4$	$\pi/2$
$\hat{V}_4$	$\pi/4$	0	$\hat{S}_4$	$\pi/4$	0

2.3.4 Scattering probability

Let $\hat{A}_i, \hat{B}_j \in \mathcal{M}_1 \cup \mathcal{M}_2$ represent operators selected by Alice and Bob, respectively. Alice first obtains a heralded pshoton from the SPDC with the input state $|\psi_{\text{in}}\rangle = \mathcal{J}_{0,k_r}|H\rangle$. Then, Alice prepares the photon in a desired state from the MUB with

$$|a_i\rangle = \hat{A}_i\mathcal{J}_{0,k_r}(r)\,|H\rangle\,, \tag{2.20}$$

and Bob similarly measures the state

$$|b_j\rangle = \hat{B}_j\mathcal{J}_{0,k_r}(r)\,|H\rangle\,. \tag{2.21}$$

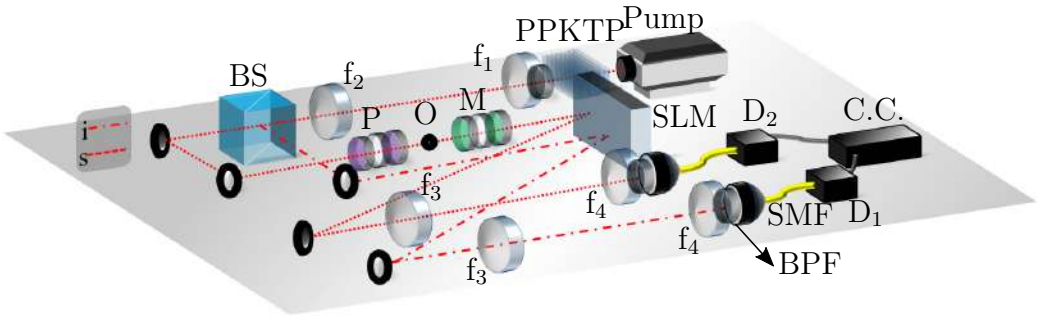


Figure 2-3: Experimental setup for the self-healing QKD. Pump: $\lambda = 405\,\text{nm}$ (Cobalt, MLD laser diode); f: Fourier lenses of focal length $f_{1,2,3\&4} = 100$ mm, 750 mm, 500 mm, 2 mm, respectively; PPKTP: periodically poled potassium titanyl phosphate (nonlinear crystal); BS: 50:50 beam splitter; s and i: signal and idler photon paths; P: preparation of the state (Alice); O: variable sized obstacle; M: measurement of the state (Bob); SLM: spatial light modulator (Pluto, Holoeye); BPF: band-pass filter; SMF: single mode fiber; $D_{1\&2}$: single photon detectors (Perkin Elmer); C.C.: coincidence electronics.

The probability amplitude of Bob's detection is

$$C_{ij} = \langle b_j | a_i \rangle = \int_0^{2\pi} \int_0^{\infty} \langle H | \, \mathcal{J}^*_{0,k_r}(r) \hat{B}^\dagger_j \hat{A}_i \mathcal{J}_{0,k_r}(r) \, | H \rangle \, r dr d\phi, \tag{2.22}$$

while the corresponding detection probabilities, $|C_{ij}|^2$, are presented in Fig. 2-2 (b).

2.4 Experimental set-up

Figure 2-3 is a schematic representation of our experimental setup. The continuous-wave pump laser (Cobalt MLD diode laser, $\lambda = 405\,\text{nm}$) was spatially filtered to deliver 40 mW of average power in a Gaussian beam of $w_0 \approx 170$ μm at the crystal (2-mm-long PPKTP nonlinear crystal), generating two lower-frequency photons by means of a type-I spontaneous parametric down-conversion (SPDC) process. By virtue of this, the signal and idler photons had the same wavelength ($\lambda = 810\,\text{nm}$) and polarization (horizontal).

The two correlated photons, signal and idler, were spatially separated by a 50:50 beam splitter (BS), with the idler photon projected into a Bessel state of 0 OAM, thus heralding a zero-order Bessel photon in the signal arm for the prepare-measure BB84 protocol. The signal photon traversed the preparation stage (P) where Alice

could prepare a vector or scalar state from the MUB alphabet using elements detailed in Fig. 2-2 (c). The signal photon was then propagated in free-space with an obstacle of variable size placed within the non-diffracting distance. This mimics a line-of-sight quantum channel. In our experiment we used the spatial light modulators (SLMs) to post-select a wave number of $k_r = 18\,\mathrm{rad/mm}$, thus realising a non-diffracting distance of $z_{\max} = 54$ cm. These values where verified by classical back-projection through the system [87]. The state measurement (M) was implemented after the obstacle by Bob. The SLM acted both as a horizontal polarization filter and as a post-selecting filter for the radial wave number. To conclude the heralding experiment, both photons were spectrally filtered by band-pass filters (10 nm bandwidth at full-width at half-maximum) and coupled with single mode fibers to single photon detectors ($D_{1\&2}$; Perkin-Elmer), with the output pulses synchronized with a coincidence counter (C.C.), discarding also the cases where the two photons exit the same output port from the BS.

2.4.1 Procedure and analysis

We measured the scattering matrix for the BG and, for comparison reasons, the LG profiles under three conditions: (FS) in free-space; (R_1) with a 600 μm radius obstruction placed strategically such that the complete decoding is performed after $L > z_{\min}$ (L: distance between obstruction and decoding SLM); and (R_2) with a 800 μm radius obstruction, placed at the same position. In the (R_2) the shadow region overlaps the detection system ($L < z_{\min}$) so that the mode is not able to self-reconstruct completely before being detected. We measure the quantum bit error rate (QBER) in each of these cases and computed the mutual information between Alice and Bob in $d = 4$ dimensions by [29]

$$I_{AB} = \log_2(d) + (1-e)\log_2(1-e) + (e)\log_2\left(\frac{e}{d-1}\right). \tag{2.23}$$

Here, e denotes the QBER. Lastly, we measured the practical secure key rate per signal state emitted by Alice, using the Gottesman-Lo-Lütkenhaus-Preskill (GLLP)

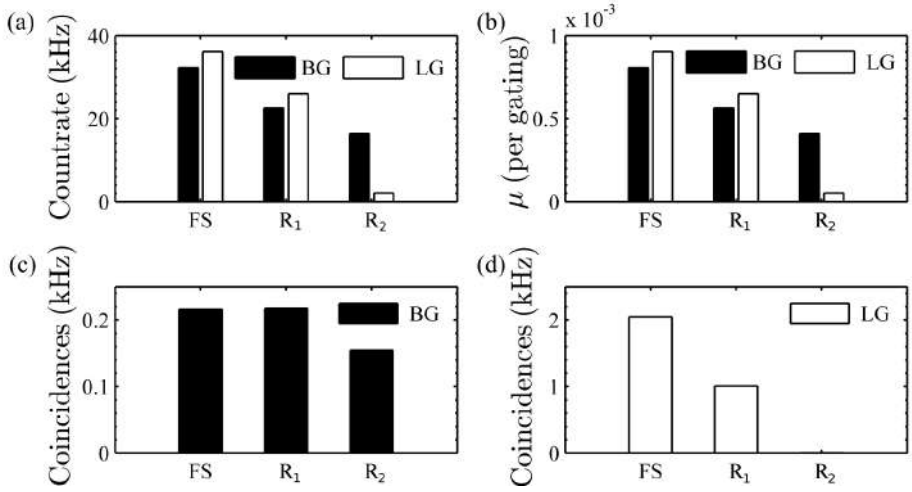


Figure 2-4: (a) Measured photon count rates and (b) average photon number (μ) per-gating window of 25 ns in free-space (FS) and the two obstructions ($R_1 = 600$ μm and $R_2 = 800$ μm) for the radially polarized mode $|\psi\rangle_{00}$. (c) and (d) show coincidence rates with the same obstructions for the BG and LG radial profiles, respectively. The BG count rate is lower for smaller obstructions due to the high k_r hologram on the SLM [87].

method [174, 175] for practical implementations with BB84 states, given by

$$R_\Delta = Q_\mu \left((1-\Delta) \left(1 - H_d \left(\frac{e}{1-\Delta} \right) \right) - f_{\text{EC}} H_d(e) \right), \tag{2.24}$$

where $H_d(\cdot)$ is the high-dimensional Shannon entropy and f_{EC} is a factor that accounts for error correction and is nominally $f_{\text{EC}} = 1.2$ for error correction systems that are currently in practice.

The photon gain is defined as $Q_\mu = \sum_n Y_n P_n(\mu)$ (in the orders of 10^{-4} for our experiment), where Y_n is the n-th photon yield while P_n is the probability distribution over n with respect to the average photon number μ, following sub-Poisson statistics for heralded photons produced from a SPDC source [175]. Y_n can be calculated from the background rate, $p_D = 2.5 \times 10^{-6}$ photons per gating window (25 ns), and n-signal detection efficiency η_n:

$$Y_n = \eta_n + p_D(1 - \eta_n), \tag{2.25}$$

where the n-signal detection efficiency η_n is given by

$$\eta_n = 1 - (1 - \eta)^n. \tag{2.26}$$

Here $\eta = \eta_d t_B$ is the transmission probability of each photon state with $\eta = 0.45 \times 0.8$ for Bob's detection (when accounting for the SLM grating). Furthermore, Δ is the multi-photon rate computed as $(1 - P_0 - P_1)/Q_\mu$ [175] where $P_{0,1}$ are the vacuum and single photon emission probabilities, respectively. The term $(1 - \Delta)$ accounts for photon splitting attacks [175]. In our experiment, we measured the photon intensities for every obstruction from the photon detection rates of the obstructed photon and deduced P_1 and P_0 assuming a thermal statistics of the heralded photon. We point out that it may be necessary to implement decoy states with a heralded source to ensure security against multi photon states owing to the thermal nature of the reduced photon state of SPDC correlated pairs [166, 175].

2.5 Results and Discussion

We performed the aforementioned experiment in four dimensions using heralded single photons with either a heralded LG mode or BG mode for the radial spatial profile, and compare their performance under the influence of varying sized obstructions.

2.5.1 Experimental results

The photon count-rates, mean-photon counts (per gating window) and coincidence-rates are presented in Fig. 2-4 (a) and (b), for the $|\Psi\rangle_{00}$ input state. As shown, the photon count rates decay for both the BG and LG radial profiles, however, more so for LG profile under the R_2 obstruction. The coincidences rates are recovered for the BG mode (Fig. 2-4 (c)) under the R_1 obstruction since L$> z_{\min}$ (detection is performed outside the shadow region of the obstruction). Further, the BG mode still demonstrates less decay for R_2 obstructed even when the mode has not reconstructed (since $L < z_{\min}$), as compared to LG (Fig. 2-4 (d)), where the coincidence rate is

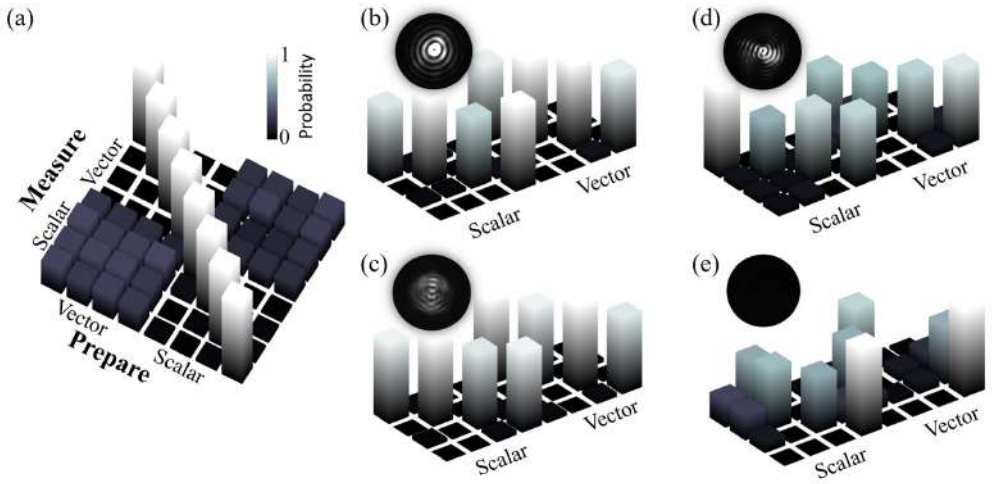


Figure 2-5: Crosstalk (scattering) matrix for vector and scalar modes in (a) (I) free-space having post-selected in a BG radial profile. The vector and scalar measured probabilities with the first obstruction (II) having a radius $R_1 = 600$ μm ($L > z_{\min}$) when taking into account (b) BG and (c) LG radial profiles. Measured probabilities with (III) an obstruction of $R_2 = 800$ μm ($L < z_{\min}$) when taking into account (d) BG and (e) LG radially profiled single photons.

seen to completely decay.

Next, we present the measured detection probability matrices for three tested cases in Fig. 2-5 using our high-dimensional information basis. In the free-space case, we measure QBERs of $e = 0.04 \pm 0.004$ for the BG and LG spatial profiles (see Fig. 2-5 (a) and Table 2.2). We compute a mutual information of $I_{AB} = 1.69$ bits/photon and a secure key rate of $R_\Delta/Q_\mu = 1.32$ bits/s per photon for both radial profiles.

Under the perturbation of the $R_1 = 600$ μm obstruction ($0.53\times$ the beam waist of the down converted photon), we measure a QBER of $e = 0.05$ for both spatial profiles, indicative of information retention, i.e. high fidelity. The intensity fields from the back-projected classical beam (see insets of Fig. 2-5 (b) and (c)), show self-healing of the BG mode at the SLM plane (see Fig. 2-5 (b)), although the LG is not completely reconstructed (see Fig. 2-5 (c)). The photons encoded with the LG profile may have a large component of the input mode which is undisturbed in polarization and phase. Furthermore, the coincidence counts decreases to 49% for the LG profile relative to the counts in free-space, as highlighted in Fig. 2-6 (a). In comparison, the BG modes show resilience thanks to the multiple concentric rings [176].

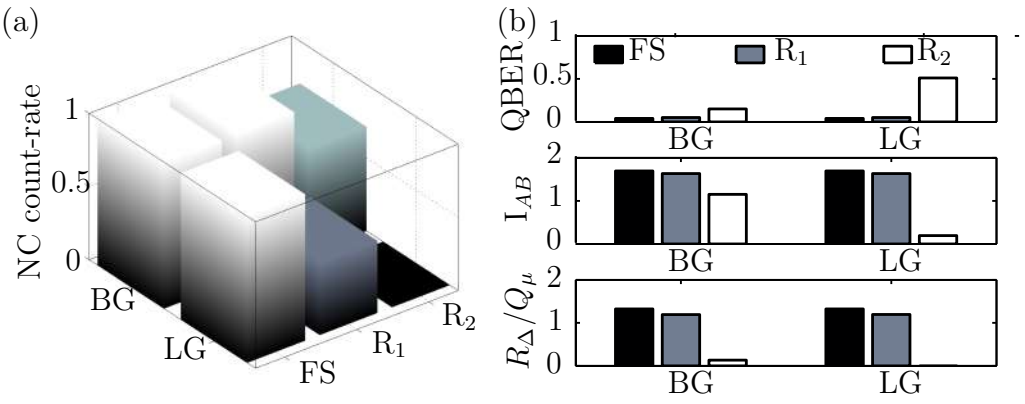


Figure 2-6: (a) Experimental normalized coincidence (NC) count-rate for the BG and LG MUB for free-space (FS) and the two obstructions ($R_1 = 600$ μm and $R_2 = 800$ μm) on the radially polarized mode $|\psi\rangle_{00}$. (b) The QBER, mutual information (I_{AB}) and key rate (R_Δ/Q_μ) for the BG and LG modes with no perturbation and under the two tested obstructions are shown.

Lastly, we investigate the security when the $R_2 = 800$ μm ($0.71\times$ the beam waist of the down converted photon) obstruction is used. Remarkably, as illustrated in Fig. 2-6 (a), the signal decreased by almost four orders of magnitude, remaining only the 0.07% of the signal for the LG set, but up to 71% for the BG self-healing mode set, owing to an earlier reconstruction of the BG radial profile in comparison to the LG radial profile. Based on the measurement results shown in Fig. 2-5 (d) and (e), we determine a QBER of $e = 0.15 \pm 0.01$ and $e = 0.51 \pm 0.00$ for the BG and LG modes, respectively. The mutual information (I_{AB}) and secure key rates are higher for the BG basis than the LG, even though the BG MUB has not fully reconstructed (see Fig. 2-6 (b)). Table 2.2 shows a summary of the measured security parameters for the BG and LG mode sets.

2.5.2 Discussion

We have presented a *proof-of-concept* experiment highlighting the importance of structuring photons in the complete spatial mode state. Here we have demonstrated the advantage when doing so with BG spatial modes for obstacle-tolerant QKD. Further, we have employed hybrid spin-orbital states to access high dimensions, with the spin-orbit states used to encode the information and the radial mode used to ame-

Table 2.2: Measured security parameters for the self-healing BG (LG) modes. NC represents the normalized coincidence counts. The normalization was performed with respect to the counts obtained from the free-space measurements.

BG (LG) modes			
	Free-space	$R_1 = 600\,\mu m$	$R_2 = 800\,\mu m$
QBER	0.04 ± 0.01 (0.04 ± 0.01)	0.05 ± 0.02 (0.05 ± 0.03)	0.15 ± 0.01 (0.51 ± 0.00)
I_{AB}	1.69 ± 0.06 (1.69 ± 0.03)	1.63 ± 0.1 (1.63 ± 0.02)	1.15 ± 04 $(0.19 \pm .004)$
Δ	$1.60\ 10^{-3}$ $(1.80\ 10^{-3})$	$1.10\ 10^{-3}$ $(1.30\ 10^{-3})$	$0.73\ 10^{-}3$ $(0.04\ 10^{-}3)$
$\frac{R_\Delta}{Q_\mu}$	1.32 ± 0.06 (1.32 ± 0.03)	1.19 ± 0.1 (1.19 ± 0.02)	0.13 ± 04 (0.01 ± 0.00)

liorate perturbations in the form of obstructions. Our scheme shows that with high-dimensional encoding and self-reconstruction, high information transmission rates are still achievable even in the presence of absorbing obstructions that perturb the traverse extent of the quantum channel. Our scheme exploits the radial DoF which has previously not been explored in HD QKD implementations with spatial modes. In our experiment the propagation length was tailored for laboratory implementation, but could be extended for practical long distance links as has been done at the classical level with scalar Bessel beams [177]. Doing so would likely increase the beam size as well as reduce the cone angle. In a realistic channel the obstruction could range in scale from the very small, e.g., dust particles in dry environments, to the very large, perhaps birds, and may even be in the transmitter or receiver itself, e.g., conventional mirror telescope designs that block part of the incoming light. To mimic this range in scale we have used obstructions that range in relative size to the mode from 0 (free-space) to 0.7× (very large). We have also used a very difficult high k_r value of 18 rad/mm, returning meter scale distances (54 cm in our case) for a beam radius in the order of 100s of μm. Thus links in the kilometer range could be produced with modest cm scale beams, or the heralding efficiency could be dramatically increased by lowering k_r [87] and instead increasing the beam size. These design trade-offs are afforded to the user by the use of BG modes over LG modes.

In free-space a common problem is phase distortions, such as turbulence. Here BG modes do not show complete reconstruction [178], nor does the hybrid combination add value [179], but classical studies have suggested that perhaps such modes may

be resilient to beam wander due to turbulence [180]. This is yet to be tested in the quantum regime. We predict that the ability to tailor both the size and k_r to achieve a desired distance may assist in keeping the beam size below the Fried scale.

In cases where the BG adds no advantage the radial mode should still be tailored correctly to a more appropriate choice. In this sense this study highlights the general case for complete control of the DoFs of the state for QKD, using BG modes as an example.

We also stress that although there are reported benefits with HD encoding, not all commonly used protocols have been generalized to high dimensions, for example, the SARG04 protocol [5] which is designed for robustness against the photon number splitting attacks or the B92 protocol which is a simpler version of the BB84 protocol [181], hence newer protocols such as the Round-Robin Differential-Phase-Shift are the subject of ongoing development in the context of spatial modes [182]. Importantly, there may be further improvements of our work by implementing our selection of modes with decoy states which has proven invaluable for HD QKD in both free-space and fiber [183, 184] and could be of higher value if implemented with heralded sources [175]. Although the scheme we present is filter based, i.e. filtering states one at a time, the experiment can be performed robustly and more efficiently using a deterministic detector for spin-orbit coupled states, sorting the modes in position [147]. This ensures high detection rates. Obtaining high switching between modes during generation would require fast modulators which is a serious experimental challenge when implementing HD QKD [185].

2.6 Conclusion

The self-healing property of the Bessel-Gaussian modes opens an important research field, being able to securely share the cryptographic key despite any possible obstruction partially blocking the quantum channel. We have shown in this manuscript the experimental results of the scattering probabilities, mutual information and secret key rates in a prepare-measure protocol, comparing two different modes forming the

QKD quantum state alphabet: Bessel-Gaussian (BG) and Laguerre-Gaussian (LG). Our results clearly show lower quantum bit error rate (QBER) by using BG modes when transmitting the shared key through a mostly blocked quantum channel. Concretely, we measured a QBER of 0.15 ± 0.01 and 0.51 ± 0.00 for the BG and LG modes, respectively. Furthermore, when almost completely blocking the channel, the mutual information for the BG modes only drops due to the increase of the noise with respect of the signal. The quantum state information can be reconstructed even when having barely any photons after the obstacle.

Chapter 3

A single vector beam can be used to charactersise turbulence channels

The work in this chapter was published in:

- **Nape, I.**, Mashaba, N., Mphuthi, N., Jayakumar, S., Bhattacharya, S. and Forbes, A., 2021. "Vector-mode decay in atmospheric turbulence: An analysis inspired by quantum mechanics.", Physical Review Applied, 15(3), p.034030.

Nape, I., performed the experiments, analysed the data and contributed to writing the manuscript under the guidance of the contributing coauthors.

3.0.1 Introduction

Structured light has become topical of late [186,187], with so called cylindrical vector vortex (CVV) beams [68] taking centre stage in numerous fundamental and applied studies [188,189]. For example, they form a family of natural solutions of free-space and optical waveguides, and have been used in optical trapping [190–192], metrology [193], as well as high capacity classical [194–196] and quantum [19,148,197,198] communication. To meet the demand of such growing applications, a plethora of generation methods have emerged, including directly from lasers [199–201], or externally with liquid crystal q-plate technology [202], metasurfaces [203,204], and spatial light modulators [205]. Detection has likewise matured to include deterministic detectors incorporating interferometers [206,207], mode sorters [208] or both [147], as well as fast digital Stokes measurements [209–211] and direct measures of the nonseparability or vector quality factor [96,212], giving a quantitative measure of how "vector" the vector beam is.

An open challenge in the context of classical and quantum communication is the propagation of such modes through media exhibiting spatially dependent perturbations. These might include thermal effects due to overheating of optical elements [213], rapid refractive index fluctuations in the atmosphere [109,214] and underwater [215], and in optical fibre [115,116]. In particular, atmospheric turbulence leaves the polarization of optical beams undisturbed while the spatial components degrade rapidly resulting in modal scattering and therefore information loss [128,179,216–221]. Consequently, information encoding with the spatial components of light is restricted to only several km [150,222]. In the case of vector beams having coupled polarization and spatial components, the polarization fields are indirectly impacted [223], resulting in the decay of nonseparability or "vectorness" [101].

Here we exploit parallels between nonseparability of vector beams and entanglement in quantum systems [98,101,102,224–228] to deploy a quantum toolkit for the study of vector beams in atmospheric turbulence. Importantly, we recognise that just as the degree of entanglement of any pure quantum state can be determined by that of

a maximally entangled state [126], courtesy of the Choi-–Jamiołkowski isomorphism (channel state duality) [120, 121], so it must be true that the dynamics of any vector beam in a one-sided noisy channel should be able to be inferred from the dynamics of just one beam, a purely inhomogeneously polarized field (a perfectly "vector" beam with orthogonal spatial modes), which from now on we will refer to as ideal vector vortex (VV) beams. In the context of OAM, any one of the CVV beams with oppoiste spin and OAM states would suffice, as well as VV beams in the linear polarization basis. Using such beams as a probe, we confirm the Choi-–Jamiołkowski isomorphism for classical vectorial light, and show that the"vectorness" decay of all initial beams can be predicted from the decay of an ideal VV beam. The approach is first outlined using CVV beams and then generalised to other VV beams for adaptability. We illustrate this for two OAM subspaces, $\ell = \pm 1$ and $\ell = \pm 10$, revealing from this measure a simple factor for the rate at which one subspace decays relative to the other. Our work not only offers a simple tool for probing classical communication channels, but also reveals insights into the decay dynamics of vectorial OAM light. While we have demonstrated the approach with OAM in the atmosphere, it can easily be adapted to other mode sets and media, and likewise to hybrid entangled quantum states.

3.1 Concepts

Here we elucidate the concept of channel state duality with nonseparable vector beams for Characterizing classical beams through perturbing media. We first introduce the key concepts of nonseparability in vector beams, vector beam decay through turbulence and then finally channel state duality. The core idea is that an ideal vector beam is sufficient to predict the behaviour of any vector beam, even partially "vector", through a channel.

3.1.1 Nonseparable vector modes

To construct an ideal VV beam we require a vectorial superposiiton of spatial mode and polarization where the nonseparability is maximum. We illustrate the concept of

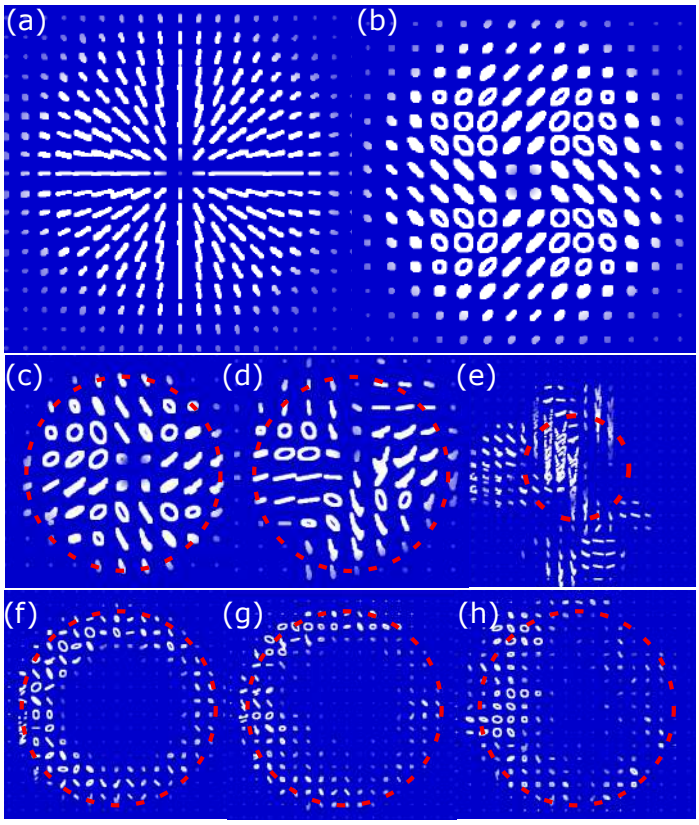


Figure 3-1: Example theoretical polarization field profiles of (a) a CVV beam and (b) a VV beam. The CVV beam has nonuniform linear polarization states while the VV beam varies between linear and elliptical polarization states. Both beams have a VQF of 1. Experimental polarization fields of vector modes transmitted through turbulence with varying strengths from left to right, initially encoded in OAM subspaces (c)-(e) $|\ell| = 1$ and (f)-(h) $|\ell| = 10$ in the second and third bottom panels, respectively. The turbulence strengths are $D/r_0 = 0$ (no turbulence), $D/r_0 = 2.5$ and $D/r_0 = 3.5$ in each column, respectively.

nonseparability using familiar CVV beams since they are ubiquitous in a myriad of applications [229]. Thereafter, we extend the concept to a family of VV beams by a simple change of basis in the polarization components.

CVV beams are natural solutions of the vectorial Helmholtz equation in cylindrical coordinates. An example of one such beam is shown in Fig. 3-1 (a), having a radially symmetric polarization field. Such beams are commonly represented as superpositions of scalar fields coupled to orthogonal circular polarization states, i.e.,

$$\Psi_\ell(\mathbf{r}) = a\exp(i\ell\phi)\hat{e}_R + b\ \exp(-i\alpha)\exp(-i\ell\phi)\hat{e}_L, \tag{3.1}$$

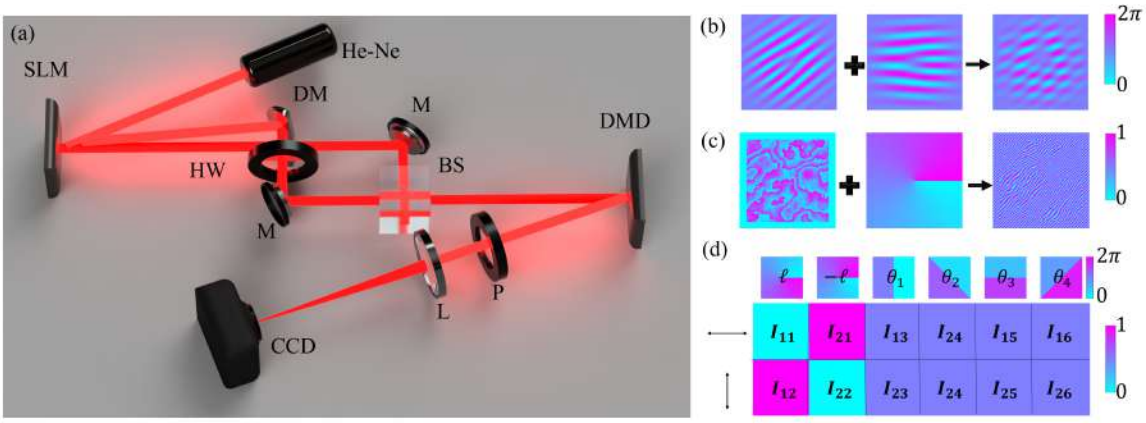


Figure 3-2: (a) Illustration of the experimental set up. A helium-neon (He-Ne) laser was expanded and collimated onto a spatial light modulater (SLM). On the SLM, two modes with oppositely charged OAM and distinct gratings frequencies were encoded on a single hologram as shown in (b). Upon propagation, the modes separated in path. Since they propagate closely, a D–shaped mirror (DM) as used to redirect one of them. A half-wave (HW) plate was used to rotate the polarization of the redirected beam. The modes were subsequently recombined at a beam-splitter (BS). The resulting mode was imaged to the digital micromirror device (DMD) where (c) turbulence was encoded in combination with the detection holograms. Polarisation projections were performed with a linear polarizer (P). Finally, the resulting mode was propagated to the far field with a 500 mm Fourier lens (L) where an on-axis intensity measurement was performed with a CCD camera. (d) Example of measurements needed to calculate the nonseparability, VQF, of vector modes.

where $\mathbf{r} = (r, \phi, z = 0)$ are the cylindrical coordinates, $\hat{e}_{R,L}$ are the canonical right and left circular polarization states, respectively. The polarization modes are coupled to spatial modes having characteristic azimuthal phase profiles $\exp(\pm i\ell\phi)$, associated with light fields carrying an OAM of $\pm\ell\hbar$ per photon, respectively. Here, the unbounded integer, $\pm\ell$, is the topological charge. The parameters, a, b and α are the relative amplitudes and phases between the the modes in the superposition. Next, we show that the coupling between the polarization and spatial components is reminiscent of quantum entanglement between two particles.

It is common to represent the polarization and spatial components of vector modes as state vectors using the Dirac notation from quantum mechanics, i.e., $\hat{e}_{R(L)} \rightarrow |R(L)\rangle$ and $\exp(\pm i\ell\phi) \rightarrow |\pm\ell\rangle$, enabling a more compact representation of Eq. (3.1)

following

$$|\Psi_\ell\rangle = a\,|\ell\rangle\,|R\rangle + b\exp(-i\alpha)\,|-\ell\rangle\,|L\rangle\,. \tag{3.2}$$

Here the bra-ket notation is used to mark the spatial and polarization components making it convenient to express each Degree of Freedom (DoF) as a unique subsystem analogous to two particle states in quantum mechanics. By clearly identifying each DoF, we wish to quantify the amount of nonseparability between them. This can be achieved by using the vector quality factor (VQF) [96, 212], which is an analogous measure of entanglement based on the concurrence [127], but between the internal DoF of the classical light fields. For the state in Eq. (3.2), the VQF, equivalently concurrence, is therefore given by VQF $= |ab|$ ranging from VQF $= 0$ for a separable scalar beam ($a = 0$ or $b = 0$) to VQF $= 1$ for a nonseparable vector beam ($a = b$); and otherwise partially "vector" for $0 <$ VQF < 1. This measure has been used in a myriad of experiments as a witness for nonseparability in classical beams [160, 209, 230].

Note that in the circular polarization basis, vector beams of varying nonseparability" are spanned on a four dimensional state-space and therefore have the general form

$$\begin{aligned}|\Phi_\ell\rangle = a\,|\ell\rangle\,|R\rangle + b\,|-\ell\rangle\,|R\rangle \\ + c\,|\ell\rangle\,|L\rangle + d\,|-\ell\rangle\,|L\rangle\,\big),\end{aligned} \tag{3.3}$$

with a corresponding degree of nonseparability

$$\text{VQF} = |ad - cb|, \tag{3.4}$$

assuming the coefficients satisfy, $(|a|^2 + |b|^2 + |c|^2 + |d|^2) = 1$. One can simply recover the previous vector beam for example by setting $(a = b)$ while $cb = 0$. This will become crucial when studying the decay of vector beams since we will always project onto the entire subspace $(\pm\ell)$ of spatial modes we started with.

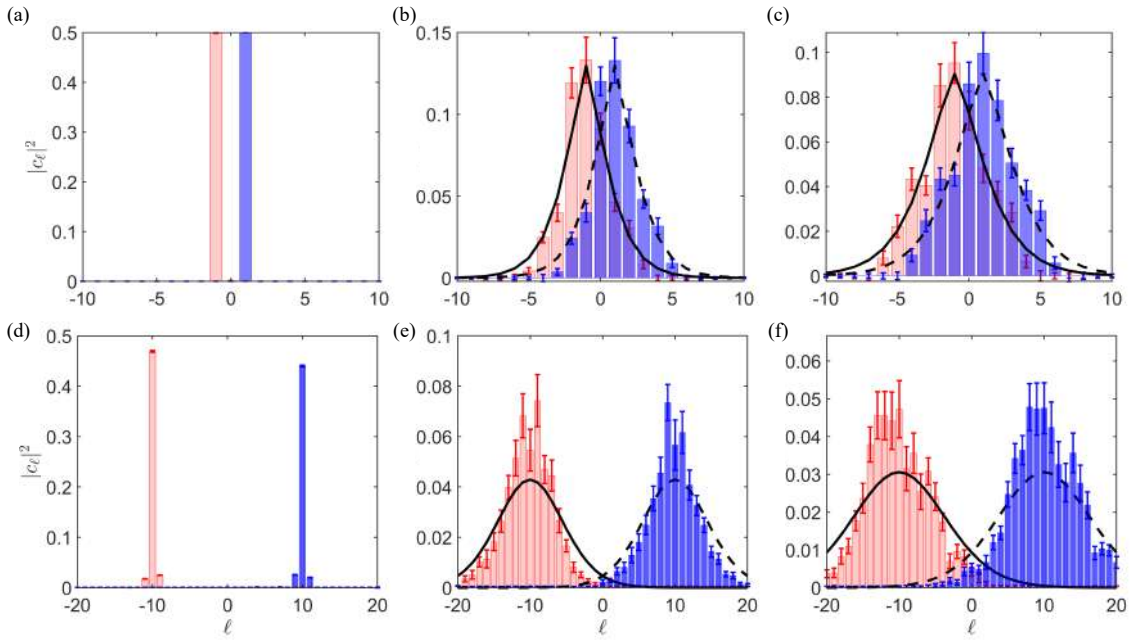


Figure 3-3: Measured modal spectrum for the vertical and horizontal polarized components of vector modes in OAM subspaces corresponding to $\ell = 1$ (top panel) and $\ell = 10$ (bottom panel), with (a,d) no turbulence $D/r_0 = 0$ and increased turbulence strengths of (b,e) $D/r_0 = 2.5$ and (c,f) $D/r_0 = 3.5$. The solid lines correspond to the theoretical spectrum. The asymmetry in the mode distributions can be attributed to the statistical fluctuations in the data due to imperfections induced by phase drifts from our interferometer as well as aberrations on the DMD.

Next, we show that the coupling between the DoFs of any spatial mode that is transmitted through a complex medium, using turbulence as an example, can be determined by that of a maximally nonseparable vector mode by exploiting channel state duality.

3.1.2 Vector mode propagation through turbulence from the perspective of quantum mechanics

Structured light is known to be perturbed in atmospheric turbulence [107]. In particular, a vector mode propagating through turbulence experiences phase dependent fluctuations that have an impact on its transverse spatial components. Assuming weak irradiance fluctuations approximated by Kolmogorov theory [214], the phase varia-

tions can be Characterized by the phase structure function, $D_\phi(\mathbf{r}_1, \mathbf{r}_2) = 6.88\Delta r/r_0$, where r_0 is the Fried parameter [231] describing the transverse scale of the atmospheric distortions and $\Delta r = |\mathbf{r}_1 - \mathbf{r}_2|$ are relative displacements in the transverse plane. For an optical system with a diameter (aperture) D, we can associate the turbulence strength with the normalised aperture size, D/r_0, relating turbulence strength to the relative transverse distance within which the refractive index is correlated. For example a large aperture size *seeing* a smaller Fried parameter ($D > r_0$) experiences more distortions than a smaller aperture *seeing* a larger Fried parameter ($D < r_0$). In this chapter, D approximates the size of the beam. We show examples of the the effect of turbulence on the polarization field of vector modes in Fig. 3-1 (c)-(h). The polarization field as well as the spatial distribution gets deformed with increasing turbulence strength (from left to right). We investigate how the distortions affect the nonsepability.

Now, since the atmosphere is non-birefringent, only the transverse spatial components of the mode expressed in Eq. (3.2) are perturbed and as a consequence there is modal scattering into adjacent OAM modes [223]. For example, an OAM mode corresponding to the state $|\ell\rangle$ traversing a medium with the channel matrix $\hat{T} = \sum_{m,n} c_{n,m} |m\rangle \langle n|$, transfers energy from the initial state into its neighbouring eigenmodes following the mapping

$$|\ell\rangle \xrightarrow{\hat{T}} \sum_m c_{\ell,m} |m\rangle , \tag{3.5}$$

where $P(\ell, m) = |c_{\ell,m}|^2$ is the conditional probability for the mode $|\ell\rangle$ to exchange energy with the mode $|m\rangle$. For Kolmogorov turbulence, the probabilities have been determined analytically [232] and are symmetric about $|\ell|$ for weak turbulence.

With this in mind, we can now describe the state of our CVV mode after it traverses the turbulent channel. Let us assume that vector mode is initially in the state

$$|\Psi_\ell\rangle = 1/\sqrt{2} \left(|\ell\rangle |R\rangle + |-\ell\rangle |L\rangle \right) . \tag{3.6}$$

Upon traversing the channel, the OAM modes scatter according to Eq. (3.5). By projecting back onto the initial OAM subspace, i.e., $\{|-\ell\rangle, |\ell\rangle\}$, we obtain the state

$$\begin{aligned}\left|\tilde{\Psi}_\ell\right\rangle = \mathcal{N}\big(&c_{\ell,\ell}\,|\ell\rangle\,|R\rangle + c_{\ell,-\ell}\,|-\ell\rangle\,|R\rangle \\ &+ c_{-\ell,\ell}\,|\ell\rangle\,|L\rangle + c_{-\ell,-\ell}\,|-\ell\rangle\,|L\rangle\big).\end{aligned} \tag{3.7}$$

Here $\mathcal{N}$ is a normalisation factor satisfying, $|\left\langle\tilde{\Psi}_\ell\middle|\tilde{\Psi}_\ell\right\rangle|^2 = 1$. We are assuming that the losses are identical for the spatial modes making up the vector beam, which is true for our case and indeed all the CVV beams. In this case the overall losses can be ignored as they play no part in the analysis. The VQF becomes

$$\mathrm{VQF}_{\mathrm{max}} = 2|\mathcal{N}|^2|c_{\ell,-\ell}c_{-\ell,\ell} - c_{\ell,\ell}c_{-\ell,-\ell}|. \tag{3.8}$$

By applying the notion of the Choi-–Jamiołkowski isomorphism (channel state duality), we hypothesis that any other vector mode with initial "vectorness" of $\mathrm{VQF}_{\mathrm{in}}$ will decay according to the factorisation law,

$$\mathrm{VQF}_{\mathrm{out}} = \mathrm{VQF}_{\mathrm{max}} \times \mathrm{VQF}_{\mathrm{in}}, \tag{3.9}$$

where $\mathrm{VQF}_{\mathrm{out}}$ is the nonseparability of the state after the channel. In other words, the decay of the any arbitrary vector beam can be inferred by simply propagating an ideal vector beam through the channel to find the scale factor, $\mathrm{VQF}_{\mathrm{max}}$. Rather than propagating many beams through the channel, only one beam has to be passed through to understand its impact. Remarkably, the channel's properties are determined by its interaction with a maximally nonseparable vector mode. This means that by knowing how a maximally nonseparable vector mode propagates through turbulence, it is possible to predict how the nonseparability of any other arbitrary superposition state evolves. Equation (3.9) also predicts that the trend is linear and an intercept at zero, with the decay of the CVV beam returning the slope ($\mathrm{VQF}_{\mathrm{max}}$).

This intriguing property, can be understood from the perspective of quantum

mechanics. Firstly, the channel weights, $|\langle\ell|\hat{T}|\ell\rangle|^2$, are imprinted on the input nonseparable state mapping the channel onto a pure state, as a consequence of the Choi–Jamiołkowski isomorphism [120, 121]. Equivalently, a vector mode traversing a noisy channel has similar properties owing to the nonseparability of the spatial and polarization components. This means that the final VQF of any partial nonseparable mode can be determined by that of a maximally nonseparable vector mode.

Finally, although we have used the CVV beam as a well-known example, in general the polarization and spatial components can be in any basis. For convenience going forward and in the experiment, we will convert to the horizontal ($|H\rangle$) and vertical ($|V\rangle$) polarization basis while the spatial profiles are defined in the Laguerre-Gaussian (LG) basis. As a result, we no longer have a CVV beam since there is no cylindrical symmetry in the polarization field. An example of our VV beam is shown in Fig. 3-1 (b), where the polarization states across the tranverse plane are mixtures of linear of elliptical states. Such a beam is represented by the state,

$$|\Psi_\ell\rangle = a\,|\ell\rangle\,|H\rangle + b\,|-\ell\rangle\,|V\rangle\,, \tag{3.10}$$

with the same VQF = 1 as that of Eq. (3.2). This serves to make it clear than any ideal VV is sufficient for the test.

3.2 Methods

3.2.1 Experimental set-up

We describe the generation and detection scheme illustrated in Fig. 3-2 (a). We used a helium-neon (He-Ne) laser with a central wavelength of 633 nm and collimated Gaussian field profile. As the approach is not influenced by the wavelength, we selected our laser for convenience only. We modulated the laser beam using a Phase only Holo-Eye Pluto spatial light modulate (SLM). To obtain the states $|\Psi\rangle_{\ell=1,10}$, we encoded the multiplexed holograms [229] with Laguerre Gaussian (LG) modes of charges $\ell = -1(-10)$ and $\ell = 1(10)$ and subsequently separated them in path using

a D shaped mirror. The amplitudes and phases of each mode were encoded using the Arrizon technique for complete amplitude and phase control [233]. An example of one of the holograms is shown in Fig. 3-2 (b).

Before interfering the two beams at the BS, we rotated the polarization of the reflected beam from the D–shape mirror by 45° using a half wave-plate. This converted the polarization from H to V. The two beams now had orthogonal polarizations. After combining the two beams, the resulting vector mode was transmitted to the digital micro-mirror device (DMD). On the DMD, we encoded Kolmogorov turbulence phase screens following [234] in combination with the detection holograms necessary for the VQF measurements. An example of one of the detection holograms is shown in Fig. 3-2 (c) as a combination of the detection mode and turbulence phase screen, resulting in a noisy detection hologram that has both the perturbation from turbulence and projection mode. The VQF projection holograms, with no turbulence, had phase profiles shown in the first row of Fig. 3-2 (d), shown for the $\ell = \pm 1$ subspace.

Lastly we used a polarizer to project onto the H and V polarization modes after the DMD. The resulting field was then propagated to the far field using a Fourier lens (L) and an on axis measurement of the intensity was recorded, providing the modal overlap of the input state, the simulated turbulence and the detection mode [235]. For each measurement we prepared up to 30 instances of each turbulence strength ranging from D/r_o=0 to 3.5 in steps of $D/r_o = 0.5$. An example of measurements for intensities I_{uv} is shown in Fig. 3-2 (d) for a perfect vector mode. The columns correspond to the spatial projections while the rows correspond to the polarization measurements. Next we show how the VQF (nonseparability) is measured.

3.2.2 Vector quality factor measurement

We follow the procedure outlined in ref. [96] to measure the nonseparability of vector modes. The VQF is given by

$$\text{VQF} = \sqrt{1 - \sum_{i}^{3} \langle \sigma_i \rangle^2}, \tag{3.11}$$

where the expectation values of the Pauli matrices $\langle\sigma_i\rangle$ can be obtained from

$$\langle\sigma_1\rangle = I_{13} + I_{23} - (I_{15} + I_{25}), \tag{3.12}$$

$$\langle\sigma_2\rangle = I_{14} + I_{24} - (I_{16} + I_{26}), \tag{3.13}$$

$$\langle\sigma_3\rangle = I_{11} + I_{21} - (I_{12} + I_{22}). \tag{3.14}$$

The detection probabilities I_{uv}, $u = \{1, 2\}$, $v = \{1, 2, ..., 6\}$ are determined from six identical projections of different polarization basis states, namely horizontal and vertical polarizations. The projections are performed by inserting a polarizer, set to 0° and 90° for the horizontal and vertical polarization projections, respectively. The six spatial measurements consist of projections onto OAM states $|\pm\ell\rangle$ and their four superpositions $|\theta\rangle = |-\ell\rangle + e^{i\frac{\theta}{|\ell|}}|\ell\rangle$ with $\theta = 0, \frac{\pi}{2}, \pi$ and $\frac{3\pi}{2}$. The spatial projections were encoded as binary holograms onto the digital micro-mirror device using the method in [236] tailored for amplitude only devices. Finally, the on-axis intensity, due to each projection is measured in the focal plane of a Fourier lens by a CCD camera, in the first diffraction order.

3.3 Results

3.3.1 Propagation of vector modes through turbulence

We first generated vector modes ($|\Psi_\ell\rangle$) and subsequently measured their resulting polarization ellipses/fields using Stokes polarometry. For brevity, the reader is directed to ref. [211] (sections 2 and 5) for calculations of the Stokes parameters and further details on extracting the polarization ellipses. The polarization profiles are shown in Fig. 3-1 (c)-(e) and (f)-(h) for $|\Psi_1\rangle$ and $|\Psi_{10}\rangle$, respectively. In each panel, the profiles are shown for increasing turbulence strengths $D = 0, 2.5$ and $D = 3.5$, from left to right. The intensity profile is shown to deteriorate in each instance confirming the presence of distortions in the transverse plane of the fields.

Next, we measured the modal spectrum of each polarization component averaged

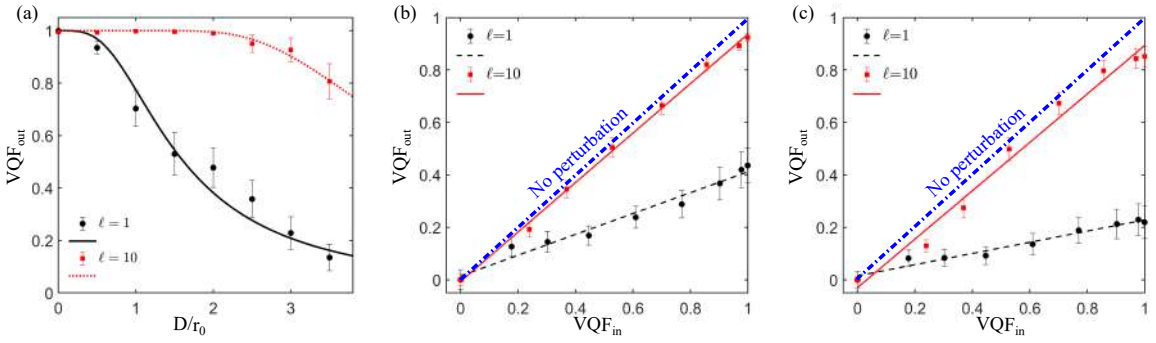


Figure 3-4: (a) Experimental results (points) and theoretical prediction (lines) for the degree of nonsepability of vector modes in the subspaces, $\ell = 1$ and 10, with increasing turbulence strength. Experimental output VQF with respect to the known input VQF under the effect of turbulence strengths of (b) $D/r_0 = 2.5$ and (c) $D/r_0 = 3.5$. In the absence of perturbations, the output VQF maps onto the diagonal ("No perturbation") line. The circles are for vector modes in the subspace of $\ell = 1$ and squares are for $\ell = 10$, while the lines are the theoretical prediction based on the isomorphism. The horizontal error-bars are smaller than the points. Each data point was obtained from 30 realisations of the same turbulence strength.

over 30 instances of the same turbulence strength. The results are shown in Fig 3-3 (a)-(c) for $|\Psi_{\ell=1}\rangle$ and in Fig 3-3 (d)-(f) for $|\Psi_{\ell=10}\rangle$. For each ℓ dependent mode, the turbulence strength was $D/r_0 = 0$ (a , d) D/r_0=2.5 (b , e) and D/r_0=3.5 (c, f). In each plot, the distribution on the right corresponds the horizontally polarized mode (blue) while the distribution on the left (red) corresponds to the vertically polarized mode. As expected, the mode distribution is symmetric about $|\ell|$, consistent with the theoretical distribution shown as lines [237]. We measured the width of each distribution as 2 times the standard deviation using the formula

$$\Delta\ell = 2\sqrt{\frac{\sum_m |m-\overline{\ell}|P(\ell,m)}{\sum_m P(\ell,m)}}, \tag{3.15}$$

where $\overline{\ell}$ is the mean OAM in the field. For $D/r_0 = 2.5$ we measured a width of $\Delta\ell = 3.18$ and $\Delta\ell = 6.64$ for $|\Psi_{\ell=1}\rangle$ and $|\Psi_{10}\rangle$, respectively, averaged over both polarization components of the beams. With an increased turbulence strength, $D/r_0 = 3.5$, we measured a width of $\Delta\ell = 4.44$ and $\Delta\ell = 8.79$. In both cases the OAM width of $\ell = 10$ vector modes is higher than that of $\ell = 1$ vector modes (2 times), showing that higher order OAM modes spread farther than lower order OAM modes, consistent

with theory [223].

While this reveals information about how the spatial components are perturbed, we now investigate how the polarization in tandem with the spatial components are affected, testing our isomorphism hypothesis.

To illustrate the effect of the mode scattering on the nonseparability, we show the theoretical (lines) and experimental (points) of VQF values measured for $|\ell| = 1, 10$ subspaces as a function of turbulence strength in Fig. 3-4 (a). The VQF of the $\ell = 10$ modes decay at lower rate than the VQF of the $\ell = 1$ modes, analogous to the decay of entangled photons through a single sided channel of turbulence [128]. This can be explained by the higher mode separation between the spatial components of the generated vector modes; the scattering onto the other modes happens in both cases, and it takes longer for larger OAM ($\ell = 10$) to diffuse onto opposite sides than for lower OAM ($\ell = 1$). While the above analysis was performed on input modes

Table 3.1: Analysis of the different OAM subspace through turbulence. The values in brackets correspond to the theoretical values. Here the gradients, m_ℓ, correspond to VQF_{max}.

D/r_0	$\Delta\ell$ ($\ell = 1$)	$\Delta\ell$ ($\ell = 10$)	m_1	R_1^2	m_{10}	R_{10}^2
0	0.05 (0)	0.84 (0)	-	-	-	-
2.5	3.18 (4.1)	6.64 (9)	0.40	0.97	0.94	0.99
3.5	4.44 (5.59)	8.79 (11.94)	0.21	0.97	0.92	0.98

with a high nonseparability ($VQF \approx 1$), next we evaluated how vector modes with a varying degree of nonseparability also decay under the same turbulence strength. We demonstrate this to confirm the channel state duality inherent in vector modes propagated through a perturbation channel acting on the spatial DoF. The results are shown in Fig. 3-4 (b) and (c) under turbulence conditions of $D/r_o = 2.5$ and 3.5, respectively. This was done for subspaces $\ell = \pm 1$ (circles) and $\ell = \pm 10$ (squares).

The error-bars for the x-axis are smaller than the points. To control the VQF of the input mode, we adjusted the grating depth of the hologram corresponding to the $\ell = -1(-10)$ mode. The plots show that the output VQF, i.e., VQF_{out}, has a linear relation to the input VQF where the line fitted through each data set has a gradient, m_ℓ or equivalently VQF_{max}, that is equivalent to the VQF of a maximally

nonseparable vector mode transmitted through the same turbulence. We show the gradient of each line in Table 3.1 as well as the goodness of fit, which are above $R^2 = 0.96$. A perfect fit would result in $R^2 = 1$. As shown, the gradients of the $\ell = 10$ modes is higher than that of $\ell = 1$, owing to the higher crosstalk in the $\ell = 1$ subspace as demonstrated earlier. For $D/r_o = 3.5$, we find that the $\ell = 10$ subspace, the gradient can be 4 times larger in comparison to the $\ell = 1$ subspace. Since the gradient indicates the maximum VQF that a vector mode with an input nonseparability of $\text{VQF}_{\text{in}} \approx 1$ can obtain, after propagating through the channel, all partially nonseparable vector modes within the same subspace are bounded on the interval $\text{VQF}_{\text{out}} \in [0, m_\ell]$ consistent with the factorisation law [126] for single sided channels indicating that vector modes posses the ability to probe channel state duality of noisy channels. Indeed, our results show that the decay in nonseparability of any vector mode decays through the medium according to the relation $\text{VQF}_{\text{out}} = \text{VQF}_{\text{in}} \times m_\ell = \text{VQF}_{\text{in}} \times \text{VQF}_{\text{max}}$ where $\text{VQF}_{\text{max}} = \text{VQF}(\hat{T}\,|\Psi\rangle_\ell)$ is the VQF of a vector mode, $|\Psi\rangle_\ell$, after traversing the channel, $\hat{T}$, and having an initial VQF of 1 while VQF_{in} is the VQF of the mode we wish to Characterize after the channel. The isomorphism implies that one maximally nonseparable vector beam is needed to probe a channel, from which the behaviour of all other vector beams can be inferred.

3.4 Discussion

Vector beams possess nonseparable coupling between their polarization and spatial components and exhibiting correlations similar to entangled pairs of photons. In this chapter, we used this fact to study the decay of vector beams in atmospheric turbulence both qualitatively and quantitatively by invoking properties such as channel state duality [120, 121] and the factorisation law [126]. These features are unique to quantum entangled states, and are commonly used for channel (medium) characterization [238]. Our results confirm that the nonseparability of any other partially (VQF < 1) nonseparable vector mode is purely determined by that of a maximally (VQF ≈ 1) nonseparable vector mode experiencing the same turbulence within the

same subspace of optical modes. Interestingly, this does not limit the method to characterization purposes but creates the possibility of using such vector modes as a means to overcoming quantum state perturbations, for example by selecting higher order modes (e.g., $\ell = 10$ as apposed to $\ell = 1$), or for unscrambling complex aberrations by using classical light or appropriate high dimensional quantum states [125]. The extension of the latter to classical beams could be used as an additional tool for adaptive optics since vector modes can carry information related to the channel/medium. While we demonstrated this method for turbulence, it can in principle be extended to various scenarios where optical aberrations are encountered, for example, arising from imperfections or overheating in optical elements in high power regimes or an optical medium that induces intermodal cross-talk through other mechanisms (e.g, a multimode fiber). In other words, the method is adaptable to any medium that is compatible with the modal scattering mechanism given in Eq. 3.5. Finally, we point out that the use of the DMD makes the approach very fast, up to kHz rates [239], which makes the approach "real-time" for most beam perturbation process such as turbulence, thermal loading, mechanical stress, and so on.

3.5 Conclusion

In summary, we exploited the concept of channel state duality analogously to Characterize the evolution of various vector/scalar modes through turbulence, demonstrating that the evolution of vector beams can be used to study how various spatial modes decay through turbulence. We showed this for two subspaces, $\ell = 1$ and $\ell = 10$, with our results demonstrating that higher order OAM vector modes decay rapidly while also maintaining a high nonseparability. We envisage that this technique also be used to study how the information capacity of the channel scales with the strength of perturbations since the VQF depends on the cross-talk in the channel. The work in this chapter is integral to the development of alternative methods for characterizing optical beams by borrowing principles from quantum mechanics, with possible applications in various scenarios where complex perturbations are encountered.

Chapter 4

Unraveling the invariance of vectorial photon fields in unitary channels

The work in this Chapter has been uploaded on a public repository:

- **Nape, I.**, Singh, K., Klug, A., Buono, W., Rosales-Guzmán, C., Franke-Arnold, S., Dudley, A. and Forbes, A., 2021. Revealing the invariance of vectorial structured light in perturbing media. arXiv preprint arXiv:2108.13890.

Nape, I., contributed to the theoretical framework, experiment, data analyses and manuscript preparation.

4.1 Introduction

Non-paraxial light is vectorial in 3D and has given rise to exotic states of structured light [187] such as optical skyrmions [240, 241], knotted strands of light [242, 243], flying donuts [244, 245] and Möbius strips [246]. Paraxial light too is vectorial, in 2D, characterised by an inhomogeneous polarisation structure across the transverse plane [247]. Vectorial structured light in 2D and 3D has been instrumental in a range of applications (see Refs. [15, 189, 248, 249] and references therein), for example, to drive currents with a direction dictated by the vectorial nature of the optical field [250, 251], imprinting the spatial structure into matter [252], enhanced metrological measurements [253, 254], probing single molecules [255], and to encode more information for larger bandwidths [143, 195, 256, 257]. They are easy to create in the laboratory using simple glass cones [258], stressed optics [259] and GRIN lenses [260], as well as from spatial light modulators and digital micro-mirror devices [205, 261], non-linear crystals [262, 263], geometric phase elements [53, 264], metasurfaces [203] and directly from lasers [265].

Given the importance of these structured light fields, much attention has focused on their propagation through optical systems that are paraxial [266], guided [267] and tight focussing [268,269], as well as in perturbing media such as turbid [103–106], turbulent [107–114] and underwater [215, 270, 271]. The conclusions are seemingly contradictory, with compelling evidence that the vectorial structure is stable, and equally compelling evidence that it is not, while the specific nature of each study prohibits making general conclusions on the robustness of vectorial light in arbitrary complex media.

Here we show that the inhomogeneity of a vectorial light field is impervious to all aberrations so long as they are unitary. We demonstrate this with two examples featuring strong aberrations: a tilted lens and atmospheric turbulence, treating each as a unitary channel. Our quantum-inspired framework explains the robustness of these light fields by virtue of unitary operations on the vectorial state, manifesting as an intact inhomogeneity even if the vectorial pattern appears spatially distorted due

to modal scattering in the component scalar spatial modes. We show that the channel action can be reversed by a reciprocal unitary process applied either pre-channel or post-channel, demonstrating full scalar and vector restoration, as well as cross-talk free detection of vectorial fields through complex media. Our study highlights the importance of measurement in the context of vectorial light fields, in doing so resolving a standing paradox on the robustness of vectorial light to perturbations, and provides a general framework for understanding the impact of arbitrary optical aberrations on vectorial structured light fields.

4.2 Concepts

4.2.1 Vectorial light and unitary channels

A vectorial structured light field can be written compactly in a quantum notation as the unnormalised state $|\Psi\rangle = |e_1\rangle_A |u_1\rangle_B + |e_2\rangle_A |u_2\rangle_B$, highlighting the non-separable nature of the two degrees of freedom (DoFs), A and B, denoting the polarization and the spatial degree of freedom, respectively. In this way, the vectorial field is treated as a quantum-like state (but not quantum and without non-local correlations), by virtue of its non-separable DoFs, akin to a locally entangled state [225, 226, 272, 273]. The polarisation DoF is expressed as any pair of orthonormal states, $\{|e_1\rangle$ and $|e_2\rangle\}$ while the spatial mode DoF is given by the orthonormal basis states $\{|u_1\rangle$ and $|u_2\rangle\}$. In a quantum sense, this vectorial structured field would be called a pure state. The vectorial nature can be quantified through a measure of its non-separability [96], a Vector Quality Factor (VQF) (equivalently concurrence) which for succinctness we will call its "vectorness", ranging from 0 (homogeneous polarisation structure of scalar light) to 1 (ideally inhomogeneous vectorial polarisation structure).

Now imagine that our vectorial light field, $|\Psi_{\text{in}}\rangle$, passes through an arbitrary aberrated optical channel, as illustrated in Figure 4-1, e.g., imperfect optics or a perturbing medium such as tissue, turbulence or underwater channels. If there is no birefringence (often there is not, but see discussion later) then this can be considered

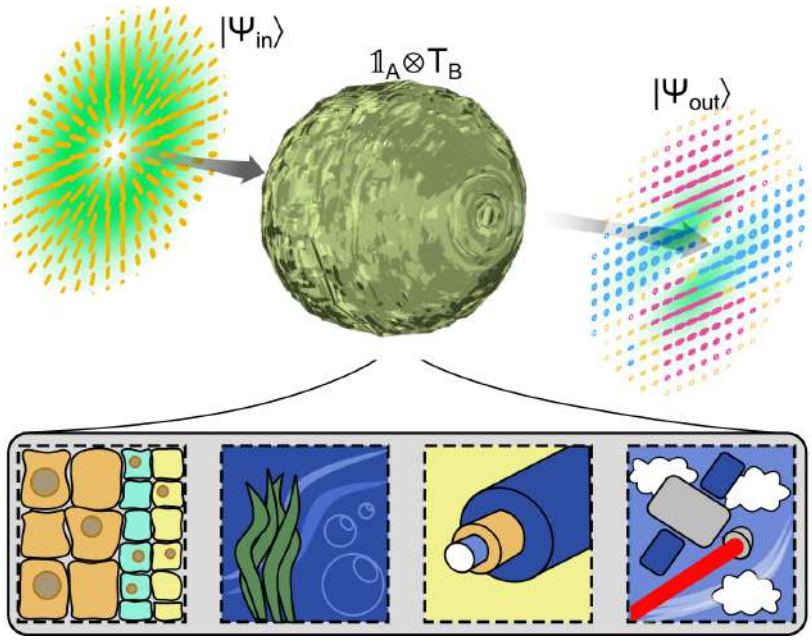


Figure 4-1: A vectorial light field, $|\Psi_{\text{in}}\rangle$, propagates through a perturbing medium and undergoes a unitary transformation, $\mathbb{1}_A \otimes T_B$, acting only on the spatial components. Such perturbing media can be organic tissue, underwater, optical fiber or the turbulent atmosphere (bottom panels). The resulting field, $|\Psi_{\text{out}}\rangle$, has a distorted intensity and polarisation structure.

a one-sided channel since the spatial mode (DoF B) is affected (distorted), while the polarisation (DoF A) is not. An open question is whether this implies that the entire polarisation structure of the state is likewise unaffected? To answer this, we note that such a one-sided channel is unitary to any input vectorial (pure) state since it may be written as a positive trace-preserving map, ensuring that the output must also be a vectorial (pure) state, with full details provided in the Supplementary Information (SI). The Choi-Jamiolkowski isomorphism [122] establishes a correspondence between the channel operator, T_B, and a quantum state, so that a measurement on one returns the other, invaluable for characterising quantum channels [125,126]. Applying this to our classical beam, justified because of its non-separability [274], the vectorial state after the channel is then $|\Psi_{\text{out}}\rangle = (\mathbb{1}_A \otimes T_B)\,|\Psi_{\text{in}}\rangle$, where $\mathbb{1}_A$ is the identity operator for DoF A with the subscript in $|\Psi\rangle$ indicating the input and output states. Importantly, the spatial components remain orthogonal even after a distorting medium: if the channel operator results in new ("distorted") modes in DoF B given by $|v_1\rangle$ and $|v_2\rangle$,

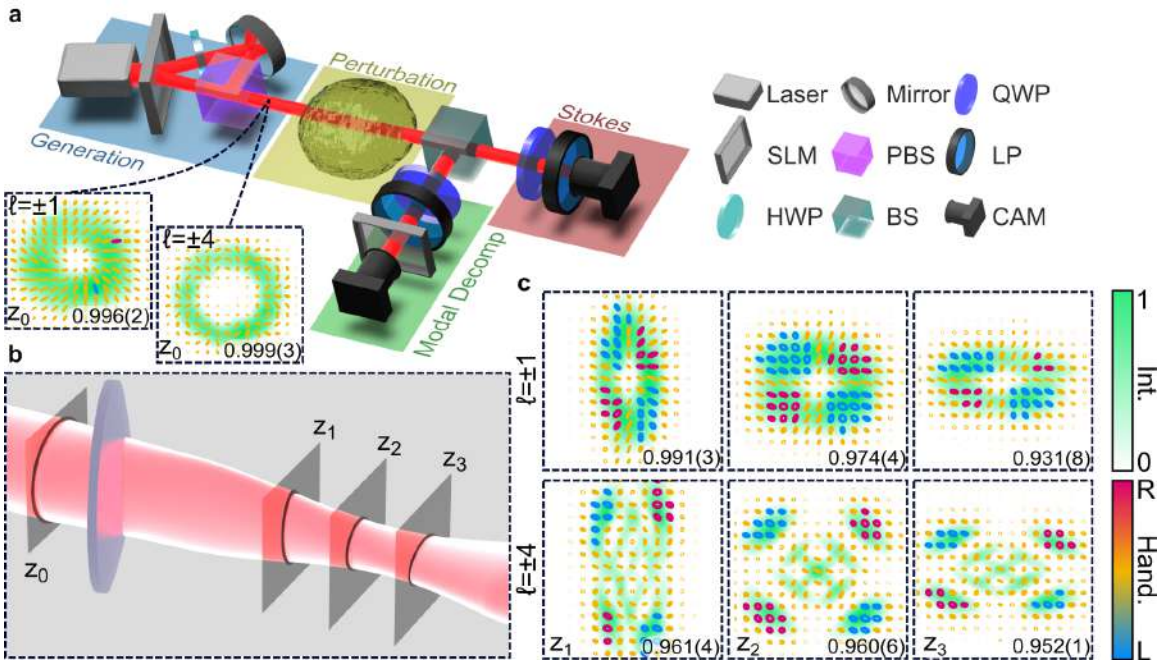


Figure 4-2: (a) The experiment has four stages: a generation stage to create the vectorial fields, a perturbation stage to pass it through a perturbing medium, and two detection stages to perform Stokes projections and modal decomposition. The insets show the initial $\ell = \pm 1$ (left panel) and $\ell = \pm 4$ (right panel) beams at plane Z_0. (b) Illustration of the propagation through a tilted lens, with exemplary measurement planes indicated as Z_1 through to Z_3. (c) The output $\ell = \pm 1$ and $\ell = \pm 4$ beams at these distances, confirm that the spatial structure alters with distance but that the vectorness (the inset number to each beam frame) does not, remaining above 93%. The optical elements comprise a HWP: half-wave plate, PBS: polarising beam splitter, Pol: polariser, BS: beam splitter, QWP: quarter-wave plate, and CAM: camera. All beam profiles are shown as false colour intensity and polarisation maps.

then one finds that $\langle v_1|v_2\rangle = \langle u_1| T_B^\dagger T_B |u_2\rangle = \langle u_1|u_2\rangle = 0$. For this reason, the output remains a non-separable vector beam with the same vectorness as the initial beam, although altered in its spatial structure, and now expressed in what we will call an adjusted basis, $\{|v_1\rangle$ and $|v_2\rangle\}$. Thus our description of the vectorial state has changed, it is now $|e_1\rangle_A |v_1\rangle_B + |e_2\rangle_A |v_2\rangle_B$, and (in general) its spatial structure too has altered in amplitude, phase and polarisation, but not its vectorial inhomogeneity (see appx. C.1).

Because the channel (with or without propagation) is unitary, the channel operator

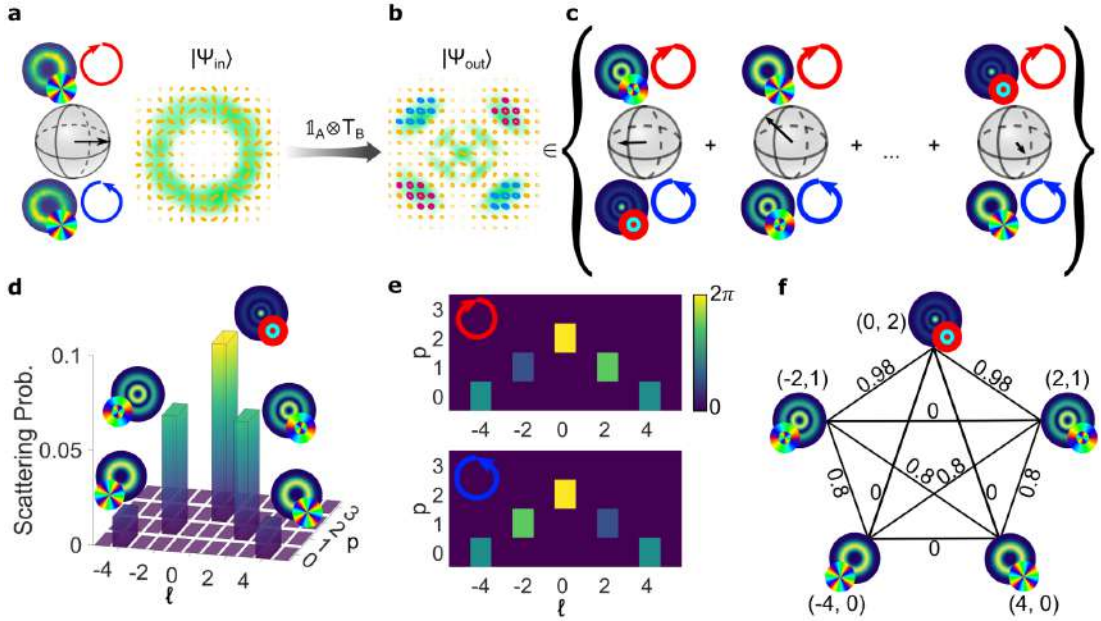


Figure 4-3: (a) The initial vector beam is geometrically represented by an equatorial state vector of unit length on a single $\ell = \pm 4$ HOP Sphere, indicative of a maximally non-separable pure state. The experimental basis states are shown on the poles (as intensities with their respective polarisation state on the right) and the vectorial sum (amplitude and polarisation structure) is shown on the equator. The tilted lens deforms the initial mode into (b), and this new state can be mapped to the sum of multiple HOP Spheres, each spanned by a different OAM and radial mode (c). Each of these potentially describes a mixed state of some degree of non-separability (non-unit and/or non-equatorial state vectors). The (d) scattering probabilities and (e) phases over the OAM (ℓ) and radial (p) modes for the right (left) ($R(L)$) circular polarisation components after the $\ell = \pm 4$ vectorial field traverses the tilted lens channel. The right and left components have equivalent scattering probabilities. There are $N = 5$ states, (ℓ, p), with non-zero probabilities and $N(N-1)/2 = 10$ pairs of xcmultiple subspaces that can be formed. (f) The pairs of states constituting the subspace and corresponding VQF for the vector field in that particular subspace can be represented with a graph having a set of vertices (as the contributing states) connected by weighted edges, respectively. The weights of the edges correspond to the VQF.

is unitary too, so that its Hermitian adjoint represents the inverse process

$$|\Psi_{\text{in}}\rangle = (\mathbb{1}_A \otimes T_B)^\dagger |\Psi_{\text{out}}\rangle \,, \tag{4.1}$$

pointing to a recipe that will unravel the vectorial light back to its original form without adaptive optics (see appx. C.3). We will demonstrate this correction both pre- and post-channel.

4.3 Methods

4.3.1 Vector beam generation

To generate vector beams, a horizontally polarized Gaussian beam from a HeNe laser (wavelength $\lambda = 633$ nm) was expanded and collimated using a $10\times$ objective and a 250 mm focal length lens. The expanded beam was then passed through a half-wave plate (HWP) before being separated into its horizontally (H) and vertically (V) polarized components using a Wollaston prism (WP). The plane at the WP was then imaged onto the screen of a digital micro-mirror device (DMD - DLP6500) using a 4f system. The separation angle of the polarization components from the WP of $\approx 1^\circ$ resulted in the diffracted 0^{th} order components overlapping. To create a desired scalar component mode of the form $U(\overline{\mathbf{r}}) = |U(\overline{\mathbf{r}})| \exp(i\Phi)$, where Φ is the phase of the field and U has maximum unit amplitude, the DMD was programmed with a hologram given by

$$H = \frac{1}{2} - \frac{1}{2}\text{sign}\left(\cos\left(\pi\phi + 2\pi G\right) - \cos(\pi A)\right), \tag{4.2}$$

with $G(\overline{\mathbf{r}}) = \mathbf{g} \cdot \overline{\mathbf{r}}$ a phase ramp function with grating frequencies $\mathbf{g} = (g_x, g_y)$, and $A(\overline{\mathbf{r}}) = \arcsin(|U(\overline{\mathbf{r}})|)/\pi$ and $\phi(\overline{\mathbf{r}}) = \Phi/\pi$ are the respective, appropriately enveloped, amplitude and phase of the desired complex fields at pixel positions $\overline{\mathbf{r}} = (x, y)$. Holograms for each polarization component (denoted as H_A and H_B) were multiplexed

on the DMD, where the grating frequencies (g_x, g_y) could be chosen to cause the H polarized 1^{st} diffraction order from H_A and the V polarized 1^{st} diffraction order from H_B to spatially overlap. This combined 1^{st} order contained our vector field which was subsequently spatially filtered at the focal plane of a 4f imaging system and imaged onto a second DMD. The second DMD was addressed with a single hologram of the same form as $H_{A/B}$ onto which the turbulence phase screens, along with any correlation filters were encoded (a quater-wave plate, QWP, was used to convert H and V polarization to right (R) and left (L) circular respectively). Polarization projections were made using a linear polarizer (LP) and a QWP before the second DMD. The intensities at the Fourier plane were captured using a CCD (FLIR Grasshopper 3) placed at the focal plane of a 2f imaging system.

4.4 Non-separability measurements

We measured the non-separability of the vector beams in a basis dependent and independent approach using Stokes parameters and modal decomposition, respectively (see sec. 4.4 and appx. C.6 for further details). Firstly, to measure the Stokes parameters, we used the reduced set of four Stokes intensities, I_H, I_D, I_R and I_L corresponding to the linearly polarized horizontal (H), diagonal (D) and the circular right (R) and left (L) polarizations. From these measurements we extracted the Stokes parameters,

$$S_0' = I_R + I_L, \tag{4.3}$$

$$S_1' = 2I_H - S_0, \tag{4.4}$$

$$S_2' = 2I_D - S_0, \tag{4.5}$$

$$S_3' = I_R - I_L. \tag{4.6}$$

The four intensity projections were acquired through the use of a linear polarizer (for I_H and I_D) rotated by 0 and $\pi/4$ radians together with a quarter-wave plate (for I_R and I_L), oriented at $\pm\pi/4$ radians relative to the fast axis. Subsequently,

the basis independent VQF (equivalently non-separability) was determined from $V = \sqrt{1-(S_1^2+S_2^2+S_3^2)/S_0^2}$, with $S_i = \int S_i'(\mathbf{r})d\mathbf{r}$ being the global Stokes parameters integrated over the transverse plane.

For the basis dependent approach, the overlap between orthogonally polarized projections of the field in question was used as a measure of non-separability, with unity overlap signalling that the field is completely scalar, while a zero overlap indicated a maximally non-separable vector field. This overlap can be characterized by the magnitude of the Bloch vector, s, lying on the surface of a sphere spanned by superpositions of a chosen pair of basis states $|\psi_{1,2}\rangle$. The magnitude can then be seen as a sum-in-quadrature of the Pauli matrix expectation values $\langle\sigma_i\rangle$, as their operation on the basis states gives the unit vectors of the sphere. We can determine these expectation values using projections $\langle P|$ into superpositions of the spatial basis components described by

$$\langle P_j| = \alpha_j\langle\psi_1| + \beta_j\langle\psi_2|\,. \tag{4.7}$$

With $(\alpha,\beta) = \{(1,0),(0,1),\frac{1}{\sqrt{2}}(1,1),\frac{1}{\sqrt{2}}(1,-1),$
$\frac{1}{\sqrt{2}}(1,i),\frac{1}{\sqrt{2}}(1,-i)\}$ for both $|R\rangle$ and $|L\rangle$. These 12 on axis intensity projections are used to calculate the length of the Bloch vector according to

$$\langle\sigma_1\rangle = (I_{13}+I_{23}) - (I_{14}+I_{24}) \tag{4.8}$$

$$\langle\sigma_2\rangle = (I_{15}+I_{25}) - (I_{16}+I_{26}) \tag{4.9}$$

$$\langle\sigma_3\rangle = (I_{11}+I_{21}) - (I_{11}+I_{22}), \tag{4.10}$$

where the i index of I_{ij} corresponds to the $\langle R,L|$ polarization projections and the j index represents the spatial mode projections defined above. The nonseparability is then given by $V = \sqrt{1-s^2}$. In this work the projections into the right- and left-circular polarization components was achieved using a linear polarizer and QWP. The subsequent spatial mode projections were performed using a correlation filter

encoded into a digital micro-mirror device (DMD), and a Fourier lens to produce on-axis intensities I_{ij}.

4.4.1 Adjusted basis measurement

To determine the adjusted basis, the complex amplitude of an aberrated probe field $|\Psi\rangle_{\text{probe}}$ needs to be measured (see appx. C.3). This field was approximated using a maximum likelihood estimation procedure, where far field intensities of the right- and left-polarized components of the ideal vector beam through turbulence were captured:

$$I^{R,L}_{\text{probe}} = \langle R, L|\psi(\mathbf{k}=0)\rangle_{\text{probe}}\,. \tag{4.11}$$

Where $|\psi\rangle_{\text{probe}}$ denotes the Fourier transform of $|\Psi\rangle_{\text{probe}}$ and $\mathbf{k} = (k_x, k_y)$. Simulated Fourier intensities, $|\psi\rangle_{\text{Zern}}$, of ideal beams modulated by a phase (modelled by possible weighted combinations of Zernike polynomials Z_j),

$$|\Psi_{\pm 1}\rangle_{\text{Zern}} = \text{LG}_0^{\pm 1} \exp\left(i \sum_j c_j Z_j\right), \tag{4.12}$$

were generated (spatial dependence has been omitted). The set of coefficients c_j which lead to the lowest square difference in intensity between the experimental and simulated cases,

$$\chi^2 = (I^R_{\text{probe}} - I^R_{\text{Zern}})^2 + (I^L_{\text{probe}} - I^L_{\text{Zern}})^2, \tag{4.13}$$

was used to determine the required basis for recovery of the initial beam.

4.5 Experiment and Results

4.5.1 Experimental demonstration: the tilted lens.

To validate this perspective, we built the set-up shown in Figure 4-2 (a), first creating our test vectorial fields before passing them through some perturbing medium. Without any loss of generality, we chose the left- and right-circular basis, $\{|e_1\rangle \equiv |R\rangle$ and $|e_2\rangle \equiv |L\rangle\}$, for the polarisation degree of freedom and spatial modes imbued with orbital angular momentum (OAM) following $\{|u_1\rangle \equiv |\ell\rangle$ and $|u_2\rangle \equiv |-\ell\rangle\}$, with ℓ the topological charge, forming the topical cylindrical vector vortex beams [68]. The resulting vectorial field was then analysed by both Stokes measurements and modal decomposition (outlined in appx. C.6 including the raw data). The superimposed intensity and polarisation (ellipse) profile of the initial beams (no perturbation) are shown in the inset of Figure 4-2 (a) for $\ell = \pm 1$ and $\ell = \pm 4$, both with a radial mode of $p = 0$, with corresponding mode numbers $N = 2p + |\ell| + 1$ of 2 and 5 respectively.

Next, we pass these beams through a highly aberrated system, a tilted lens, illustrated in Figure 4-2 (b). This is known to severely distort OAM modes and is routinely used as an OAM detector by breaking the beam into countable fringes [275]. The results at illustrative distances (Z_1 to Z_3) after the lens are shown in Figure 4-2 (c). The superimposed intensity and polarisation profiles reveal that while the vectorial structure distorts as one moves towards the far-field, the inhomogeneity as measured by the vectorness does not, corroborated by the vectorness of each beam (reported in the insets), all remaining above 93%, i.e., remaining fully vectorial as predicted by the unitary nature of the channel.

In contrast we see that the intensity profiles change morphology, and concomitantly polarisation structure. This change can be explained by the coupling of modes outside the original subspace by virtue of the channel operator: the channel scatters the original OAM modes into new mode sets that maintain the same mode number as the input modes. We can visualise this using the Higher Order Poincaré (HOP) Sphere, a geometric representation of vectorial structured light [65, 165]. The case

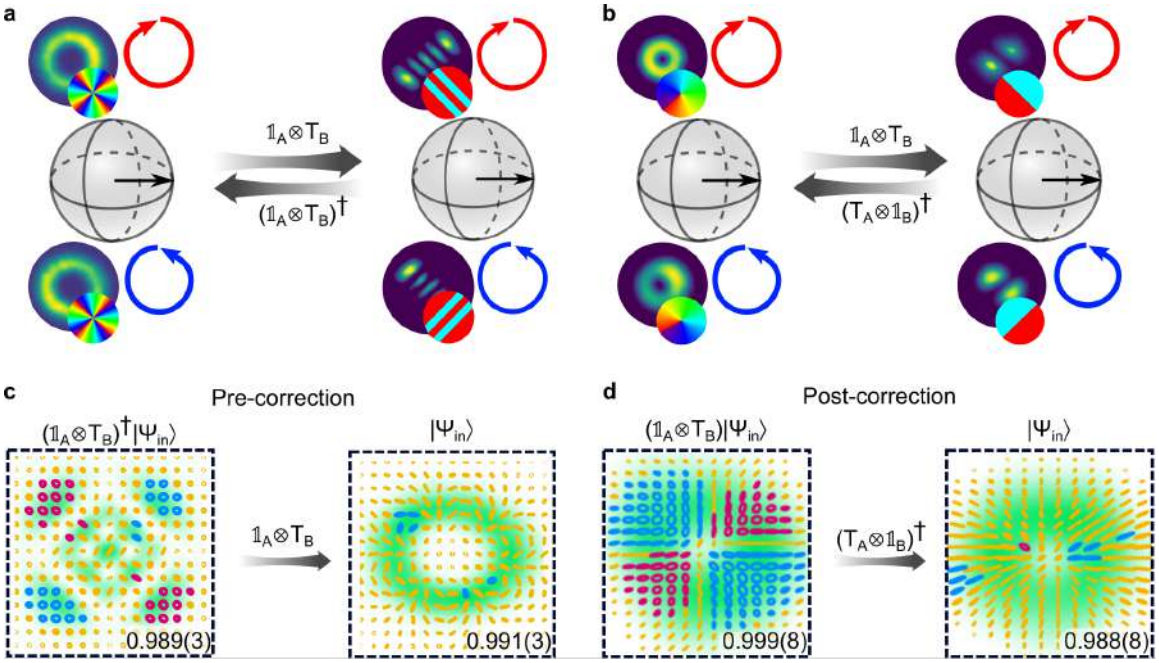


Figure 4-4: (a) The unitary channel (tilted lens) $\mathbb{1}_A \otimes T_B$ maps the initial $\ell \pm 4$ vector field from the equator of its s corresponding subspace onto a (b) new HOP Sphere spanned by an adjusted basis (shown as experimental images on the poles) where the vectorial structure is also a maximally non-separable pure state. Because the unitary channel is a change of basis, the inverse $(\mathbb{1}_A \otimes T_B)^\dagger$ can be applied to map the field back to the original sphere. The inversion can be done (c) pre-channel by inserting the state $(\mathbb{1}_A \otimes T_B)^\dagger |\Psi_{\text{in}}\rangle$, the conjugated field in the new basis, resulting in the desired corrected field $|\Psi_{\text{in}}\rangle$ after transmission. For (d) post-channel correction, the unitary nature of the channel is inverted after the channel. We show this for the $\ell = 1$ vector field, where the operation is simply a quarter waveplate, since $\mathbb{1}_A \otimes T_B = T_A \otimes \mathbb{1}_B$ for this subspace.

for $\ell = \pm 4$ is shown in Figure 4-3 as an illustrative example. The initial cylindrical vector vortex beam is visualised as an equatorial vector of unit length (a pure state), shown in Figure 4-3 (a). The channel (our tilted lens) maps this initial state to a new field, shown in Figure 4-3 (b), expressed across multiple HOP Spheres, illustrated in Figure 4-3 (c).

The new HOP Spheres are made up of all modal pairings that have non-zero modal powers (scattering probabilities). We quantify this by reporting the scattering probabilities and phases for every subspace, shown in Figures 4-3 (d) and (e), respectively. The initial modes ($\ell_{\text{in}} = \pm 4, p_{\text{in}} = 0$) now only contain $\approx$12% of the total modal power, with new modal subspaces emerging to carry the rest. The HOP Spheres are made of *pairings* of these modes, one on each pole, but not all contribute to the

vectorness. To determine the contributing pairs, we measure the vectorness for every possible pairing (there are $N(N-1)/2 = 10$ possibilities), with the results shown as a graph in Figure 4-4 (f). In the graph, each vertex corresponds to a non-zero state from (d) and the edges represent possible pairings to form a HOP Sphere. The weight of each edge corresponds to the vectorness of that pairing. The initial subspace $(\pm 4, 0)$ is no longer a non-separable state, with a vectorness of 0, while some of the new subspaces (new HOP Spheres) can be as high as 98%, i.e., pure vectorial states. The graph can be re-arranged with the zero weighted edges removed to reveal a $K_{3,2}$ bipartite graph structure with two independent vertex sets, $\mathcal{U} = \{(\pm 4, 0), (2, 0)\}$ and $\mathcal{V} = \{(\pm 2, 1)\}$, connected by 6 edges. Thus of the 10 unique subspaces created from the five scattered modes, only six are non-separable states, occurring for mapping combinations of states between $\mathcal{U}$ and $\mathcal{V}$. One can appreciate that this becomes ever more complicated as the complexity of the medium (and modal scattering) increases.

From this conventional perspective the situation is complicated, but only because the original (OAM) basis modes ($\{|u_1\rangle \equiv |\ell\rangle$ and $|u_2\rangle \equiv |-\ell\rangle\}$) are used to form the HOP Spheres. We offer a simplification by recognising the unitary nature of the transformation: one can visualise the action of the channel as a mapping (after the channel operation $(\mathbb{1}_A \otimes T_B)$ to a *single* HOP Sphere spanned by the new vectors forming an *adjusted basis*, $|v_1\rangle$ and $|v_2\rangle$, shown in Figure 4-4 (a). This mapping is a result of channel state duality, where the new spatial basis states that the non-separable vectorial field maps onto are isomorphic to the basis states of the unitary channel operation [122]. In this new "adjusted" HOP Sphere the state vector is again maximally non-separable and pure. The new adjusted basis states are complex structured light fields (one may say "distorted" modes due to the noisy channel), shown as experimental images on the poles. In some special cases the mode may be recognisable: for the $\ell = \pm 1$ state shown in Figure 4-4 (b) the mapping returns the Hermite-Gaussian modes as the adjusted basis. Pertinently, the initial state vector in the original HOP Sphere, and the new state vector in the adjusted HOP Sphere are both equatorial and of unit length, representing a maximally non-separable pure state. This explains why the polarisation structure appears to change (a change in

HOP Sphere) yet the inhomogeneity does not (the same state vector in each HOP Sphere).

Since the mapping is unitary it is possible to invert the action of the channel either as a pre-channel action or post-channel correction, both lossless; conveniently, the experimental steps to determine the channel unitary are straightforward: modal and Stokes projections. Using a pre-channel corrective step, we insert the adjusted basis vectorial mode into the tilted lens and allow the aberrations to unravel it back to the original initial state, shown in Figure 4-4 (c). For the $\ell = \pm 1$ example the required inversion operator is just a quarter wave plate, which can be derived analytically from Eq. 4.1 (see appx. C.4). The counter-intuitive notion that a polarisation element can be used to correct a channel that acts only on the spatial mode DoF is explained by the fact that the channel correction, $(\mathbb{1}_A \otimes T_B)^\dagger(\mathbb{1}_A \otimes T_B)$ can be rewritten as $T_A^\dagger T_A \otimes T_B^\dagger T_B = (T_A^\dagger \otimes \mathbb{1}_B)(T_A \otimes \mathbb{1}_B)$, so that the post-channel unitary, $T_B^\dagger = T_A^\dagger$, can be applied to the polarisation degree of freedom for $\ell = \pm 1$. The impact of this unitary is shown in Figure 4-4 (d) as a post-channel correction, restoring the full vectorial initial state.

4.5.2 The role of measurement

Given that the state vector after the channel lives on many HOP Spheres in the original basis, $\{|u_1\rangle$ and $|u_2\rangle\}$, but only one HOP Sphere in the adjusted basis, $\{|v_1\rangle$ and $|v_2\rangle\}$, it is pertinent to ask in which basis (or HOP Sphere) should one make the vectorial measurement? In the quoted vectorness values thus far, we have circumvented this problem by using a Stokes measurement approach to extract the degree of non-separability [209], with the benefit of sampling in a basis-independent fashion. In contrast, many measurements of structured light are basis dependent, e.g., in classical and quantum communication, where the basis elements form the communication alphabet. In Figure 4-5 (a) we show the outcome of a basis-dependent vectorness measurement in the original basis and in the adjusted basis, using the tilted lens as the channel. We see that for some symmetries the choice of basis has no impact on

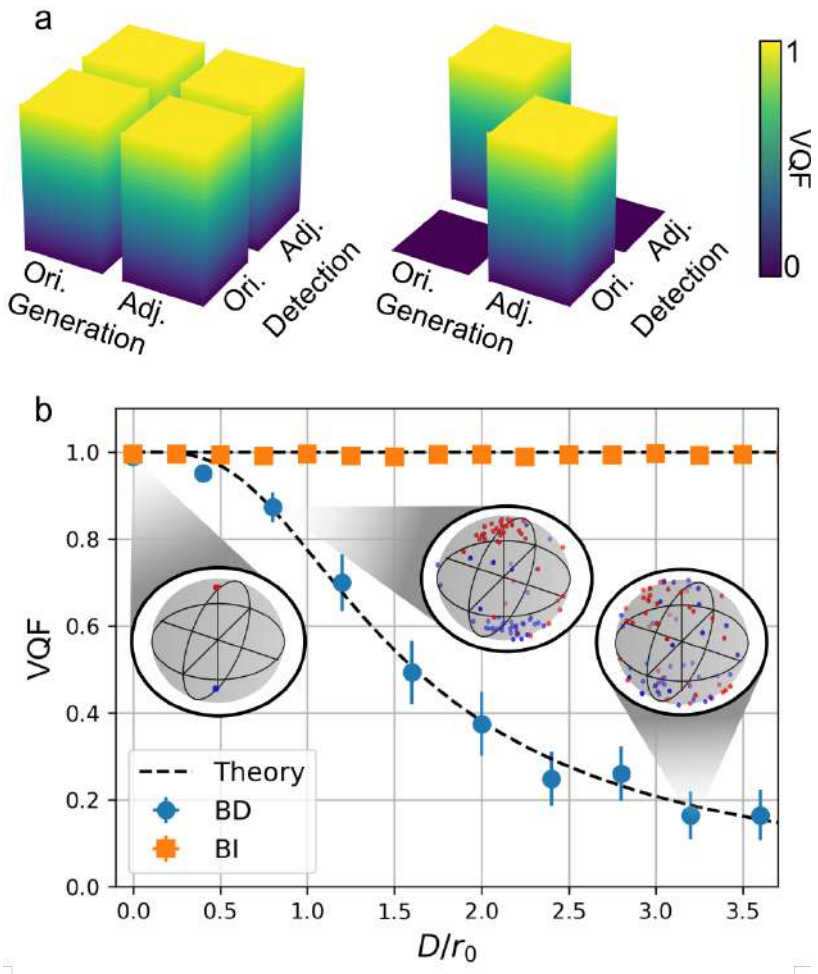


Figure 4-5: (a) Measurement of the vectorness in the original (Ori.) and adjusted (Adj.) basis $\ell = \pm 1$ (left) and $\ell = \pm 4$ (right) in the far-field of the tilted lens. (b) Measurement of the vectorness of an initial $\ell = \pm 1$ mode through experimentally simulated atmospheric turbulence as a function of the turbulence strength (D/r_0). A basis-dependent (BD) measurement in the original basis ($\ell = \pm 1$) shows a decay in vectorness, while the basis-independent (BI) approach reveals an invariance. Experimental data (points) show excellent agreement with theory (dashed curves). The insets show the left (red) and right (blue) polarisation projections on the $\ell = \pm 1$ modal sphere for three example turbulence strengths (low, medium and strong). Each point on the spheres represents one instance from the experimental turbulence ensemble. Error bars are plotted as standard deviations from 50 instances of simulated turbulence.

the outcome, as in the case of $\ell = \pm 1$, while for other vectorial fields the impact is significant ($\ell = \pm 4$). It should be noted that the $\ell = \pm 1$ beam through a tilted lens is a special case, because in modal space the state vector has simply been rotated. In general, it is the adjusted basis that always reveals the invariance of the vectorness. The failure of the measurement in the original basis is easily explained by the

concatenation of the measurement subspace to just one of the many HOP Spheres in which the state resides, and the consequent reduction of the state vector to a mixed and separable state because information is lost to other OAM subspaces.

To make clear that the tilted lens is not a special case, we alter the channel to atmospheric turbulence, and this time measure the vectorness as a function of the turbulence strength in the original basis and in a basis independent fashion, with the result shown in Figure 4-5 (b). We find that a measurement in the original basis shows a decay in the vectorial nature of the light as the turbulence strength increases, whereas the basis-independent approach reveals the unitary nature of turbulence: while the spatial structure is complex and altered, its vectorness remains intact and invariant to the turbulence strength. Here, all the measurements were performed in the far-field, so that the phase-only perturbations manifest as phase and amplitude effects. We clearly see the paradox: the vectorial structure can appear robust or not depending on how the measurement was done. This result highlights the important role of measurement in determining the salient properties of vectorial light fields.

The inset spheres in Figure 4-5 (b) show the left (red) and right (blue) state vector projections on the $\ell = \pm 1$ modal sphere [64] for low, medium and strong turbulence. Each instance of a turbulence strength is a red (blue) point, the scatter of which and deviation from the poles is indicative of modal cross-talk. This is a visual representation of why the vectorness decays when one considers only one sphere in the original basis: the original states are orthogonal (points on opposite poles with little scatter) but as turbulence increases they disperse across the sphere, resulting on superpositions of OAM, which become maximally mixed. For example, looking only at the $\ell = \pm 1$ subspace, the state may evolve following (ignoring normalisation): $|R\rangle|1\rangle \rightarrow |R\rangle|1\rangle + i|R\rangle|-1\rangle$ and likewise $|L\rangle|-1\rangle \rightarrow |L\rangle|-1\rangle - i|L\rangle|1\rangle$. The original vectorial state becomes $|R\rangle|1\rangle + |L\rangle|-1\rangle \rightarrow |L\rangle|-1\rangle + i|L\rangle|1\rangle + |R\rangle|1\rangle + |R\rangle|-1\rangle = (|R\rangle + i|L\rangle)(|1\rangle + |-1\rangle)$, which is a scalar, diagonally polarised, Hermite-Gaussian beam with a vectorness of 0. One can deduce from this simple example that if only some modal spaces are considered in the beam analysis, then vectorial modes can "decay" to become scalar, but scalar modes cannot "decay" to become vectorial.

4.5.3 Reversing turbulence distortions

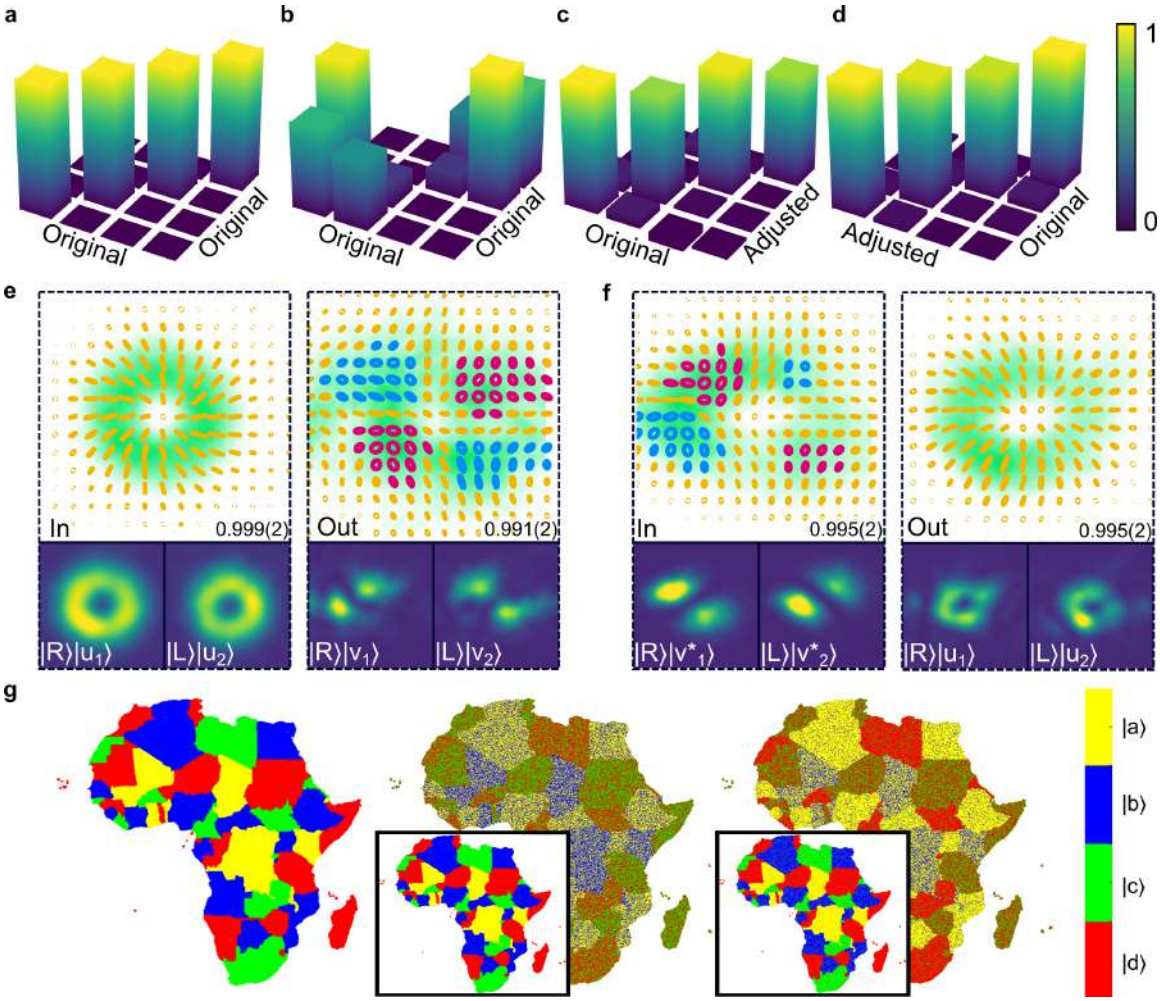


Figure 4-6: Cross-talk matrices for preparation and measurement in the original basis for (a) no turbulence and (b) medium turbulence ($D/r_0 = 1.6$). (c) Measuring or (d) preparing in the adjusted removes the cross-talk. (e) The unitary action of the channel distorts the polarization structure of the initial beam but not its vectorial homogeneity, with the vectorness given in the insets. Below the polarisation structure are the spatial modes composing the original basis ($u_{1,2}$) and perturbed basis ($v_{1,2}$) along with their polarization states $|R\rangle$ and $|L\rangle$. (f) The unravelling of the turbulence by a lossless unitary applied pre-channel, restoring the initial beam after the turbulence. The adjusted basis modes ($v^*_{1,2}$) and the corrected basis modes ($u_{1,2}$) are shown below the polarisation structures with their respective polarisation states. In (g), an image (left) encoded in the original basis is distorted after transmission through moderately weak (middle) and medium (right) turbulence. The same image is transmitted through the channel but decoded in the adjusted basis, for distortion-free communication, shown in the insets.

In our final example we keep atmospheric turbulence as our unitary channel because of its complex aberration profile. In Figure 4-6 (a) and (b) we show typical cross-

talk matrices with and without turbulence, respectively, where the input and output modes are both expressed in the original basis, $\{|R\rangle|u_1\rangle, |R\rangle|u_2\rangle, |L\rangle|u_1\rangle, |L\rangle|u_2\rangle\}$. The cross-talk in (b) is deleterious for both classical and quantum communication. However, the unitary nature of the channel means that there is an adjusted basis, $\{|R\rangle|v_1\rangle, |R\rangle|v_2\rangle, |L\rangle|v_1\rangle, |L\rangle|v_2\rangle\}$, where the state vector is pure. Consequently, a post- or pre-channel unitary can undo the action of the channel, removing the cross-talk, as shown in Figure 4-6 (c) and (d). The post-channel unitary is simply a measurement in the new adjusted basis, requiring nothing more than a change to the detection optics (holograms in our example) based on the channel under study. In Figure 4-6 (d), the preparation optics are programmed to prepare the state in the adjusted basis, but measure it in the original basis, once again returning a cross-talk free result. While the action of the channel is to distort the initial beam, as shown in Figure 4-6 (e), the channel action can be reversed as shown in Figure 4-6 (f), restoring the initial beam. This is a visualisation of the low cross-talk matrix in part (d): sending in the adjusted basis but measuring in the original basis. The scalar version of the basis modes are shown in Figures 4-6 (e) and (f) as insets below each polarisation profile, starting with the original modes, which become perturbed due to turbulence. The adjusted basis, with scalar versions shown in the insets of Figure 4-6 (f), maintains the orthogonality of the modes, and shows the key to the restoration of the initial field. When the adjusted basis is the input, the output is the corrected mode in the original basis. These results suggest that cross-talk free communication is possible with a judiciously selected basis set for the preparation or measurement, exploiting the fact that the vectorial state is intact in the adjusted basis. We use this fact in (g) to encode graphical information using our modal set, send it across the channel, and decode it on the other side. Turbulence causes cross-talk, distorting the image, but this can easily be overcome by simply decoding (measuring) in the adjusted basis, with results shown for medium and strong turbulence. A measurement in the adjusted basis reveals no modal decay, no cross-talk and high-fidelity information transfer across this noisy channel.

4.6 Discussion and Conclusion

Careful inspection of the studies that report vectorial robustness in noisy channels reveal that the distances propagated were short and the strength of perturbation low, mimicking a phase-only near-field effect where indeed little change is expected, and hence these are not true tests for robustness or invariance. Studies that claim enhanced resilience of vector modes over distances comparable to the Rayleigh length [108, 114] have used the variance in the field's intensity as a measure, a quantity that one would expect to be robust due to the fact that each polarisation component behaves independently and so will have a low covariance.

Our results show that vectorial structured light in complex media will evolve from the near-field to the far-field, generally appearing spatially distorted in amplitude, phase and polarisation structure, although unaltered in vectorial inhomogeneity. This is explained by the unitary nature of such channels, mapping the state from a HOP Sphere spanned by the original basis to a new HOP Sphere spanned by an adjusted basis, as if only our perspective has altered. Any measurement in the original basis will show an apparent "decay" of the vectorial structure in strongly perturbing media even though the degree of polarisation remains intact - a hidden invariance that can be observed through a judicious measurement. The role of measurement in quantum studies is well appreciated, and here too the vectorness of a classical beam can be found to be high *and* low, seemingly contradictory outcomes, yet both equally valid based on the choice of measurement. This is not only of fundamental importance but also of practical relevance: we have shown how to make a basis choice for preparation and/or measurement to negate modal cross-talk, with obvious benefits in classical and quantum communication across noisy channels, as well as in imaging through complex media.

The argument for robustness of vectorial light due to the fact that the polarisation is not affected in a non-birefringent channel is egregious: our quantum notation makes clear that the entire state is altered since its two DoFs are non-separable, in the same way that a true bi-photon quantum state is altered if just one of the two

photons is perturbed - both examples of one-sided channels. Ironically, the incorrect statement is true if the initial mode is *not* vectorial, since separable states (scalar homogenously polarised light) cannot become less scalar in a non-birefringent medium. Our statement is corroborated here by theoretical examples and experimental proof, particularly illustrated by the example of operating on the "unaffected" polarisation DoF to correct the entire vectorial state.

Our analysis has considered non-birefringent channels, but can be generalised by allowing the polarisation DoF to be perturbed while selecting the other DoF to be invariant, or by adjusting the theory to treat the medium as a two-sided channel to allow both DoFs to alter. We remark too that not all channels are unitary. In non-linear systems the vectorness can improve or degrade depending on the medium [230, 276, 277], and our results are not in contradiction to these findings. Finally, the notion of robustness implies that there must also be states that are not robust, and here we wish to clarify the role of a unitary operator versus a filter. It is always possible to convert noise into loss by a filtering process [278, 279], but this does not make the initial state robust to the medium, while the loss induced correction is non-unitary.

In conclusion, we have provided a general framework for understanding the impact of aberrations on vectorial light fields, in doing so revealing the unitary nature of many complex media, where the perturbation is understood as a simple unitary mapping. Because the mapping is unitary, it can be pre- or post-corrected in a lossless manner, armed only with simple Stokes and modal decomposition projections. Our work resolves a standing debate on the robustness of vectorial light in complex media, and will be invaluable to the exploding community working with vectorial structured light and its applications.

Chapter 5

Transporting multiple hybrid entangled states through optical fibers

- Liu, J., **Nape, I.**, Wang, Q., Vallés, A., Wang, J. and Forbes, A., 2020. "Multidimensional entanglement transport through single-mode fiber". Science advances, 6(4), p.eaay0837.

Nape, I., contributed to the theoretical framework, experiment, data analyses and manuscript preparation. Nape. I and Liu. J shared first author for this work.

5.1 Introduction

Entanglement is an intriguing aspect of quantum mechanics with well-known quantum paradoxes such as those of Einstein-Podolsky-Rosen (EPR) [280], Hardy [281], and Leggett [282]. Yet it is also a valuable resource to be harnessed: entangled particles shared with different distant observers can be used in quantum cryptography to set an unconditional secure key [283,284], in quantum teleportation to transfer quantum information [285–289], in super-dense coding [290, 291], in ghost imaging [292, 293], and are also an important part for quantum computation [294–296].

In the past few decades, quantum entanglement has been extensively explored for a variety of quantum information protocols. Standard quantum communication protocols exploit polarisation (or "spin" angular momentum) encoding with single photon and multipartite states. Up to now, entanglement transport has been verified over distances up to 1200 km via free space (satellite-based distribution) [297] and over 100 km through fibre using polarisation-entangled photons [298,299]. Exploiting high-dimensional entangled systems presents many opportunities, for example, a larger alphabet for higher photon information capacity and better robustness to background noise and hacking attacks [30, 300], increasing also the storage capacity in quantum memories [198, 301]. High-dimensional systems have been studied by correlations in various degrees of freedom, including position-time [302], energy-time [303,304], time-bin [38,305,306], time-frequency [307], and frequency [308]. More recently, the orbital angular momentum (OAM) of light, related to the photon's transverse mode spatial structure, has been recognized as a promising resource [309–311].

Despite these advances, quantum communication with spatial modes is still in its infancy, with reported entanglement transport in multi-mode fibre limited to less than 1 m [312,313] and to kilometre ranges using single photons states (no entanglement) in specially designed custom multi-mode fibre [314], still orders of magnitude less than that with polarisation, and lacking the ability to integrate into existing networks, a crucial element of any future quantum network [315–317]. Moreover, the mooted benefits of high-dimensional states against noise has yet to be realized

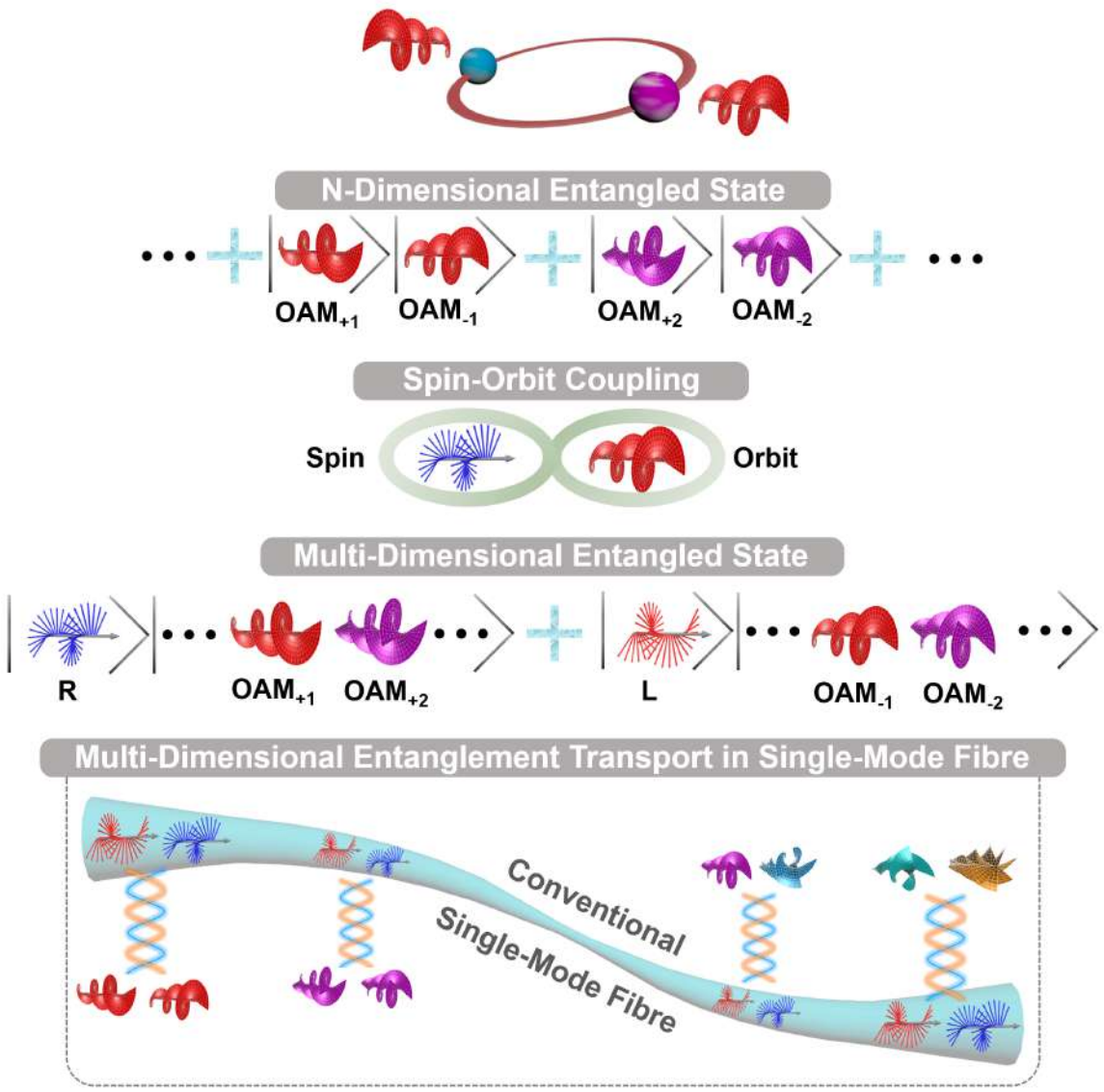


Figure 5-1: **Multi-dimensional entanglement transport through single-mode fibre.** An initially high-dimensional state is converted by spin-orbit coupling into multiple two dimensional hybrid entangled states. The polarisation (spin) photon has a fundamental spatial mode (Gaussian), facilitating transport down a SMF. By hybrid entanglement the infinite space of OAM is accessed by two-dimensional subspaces at a time.

in the laboratory, while a measured channel capacity has been found to be twice higher by multiplexing two-dimensional subspaces rather than transmitting the full four high-dimensional state [314]. This motivates us to seek alternative, immediately deployable solutions that are neither two-dimensional nor high-dimensional but rather "multi-dimensional".

Here we demonstrate the transport of multi-dimensional entangled states down conventional single-mode fibre (SMF) by exploiting hybrid entangled states. We combine polarisation qubits with high-dimensional spatial modes by entangling the spin-orbit (SO) degrees of freedom of a bi-photon pair, passing the polarisation (spin) photon down the SMF while accessing multi-dimensional OAM subspaces with the other photon in free space. We show high fidelity hybrid entanglement preservation down 250 m of SMF across two two-dimensional subspaces (2×2 dimensions) in what we refer to as multi-dimensional entanglement. We quantify our one-sided channel by means of quantum state tomography, Bell inequality and quantum eraser experiments. This work suggests an alternative approach to spatial mode entanglement transport in fibre, with the telling advantage of deployment over legacy optical networks with conventional SMF.

5.2 Concept and principle

The concept and principle of multi-dimensional spin-orbit entanglement transport through SMF is illustrated in Fig. 5-1. Light beams carrying OAM are characterized by a helical phase front of $\exp(i\ell\theta)$ [318], where θ is the azimuthal angle and $\ell \in [-\infty, \infty]$ is the topological charge. This implies that OAM modes, in principle, form a complete basis in an infinitely large Hilbert space. However, the control of such high-dimensional states is complex, and their transport requires custom channels, e.g. specially designed custom multi-mode fibre. On the contrary, polarisation is limited to just a two-level system but is easily transported down SMF. Here we compromise between the two-level spin entanglement and the high-dimensional OAM entanglement to transport multi-dimensional spin-orbit hyrbid entanglement. A consequence is that the entire high-dimensional OAM Hilbert space can be accessed, but two dimensions at a time. We will demonstrate that in doing so we are able to transport multi-dimensional entanglement down conventional fibre.

To see how this works, consider the generation of OAM-entangled pairs of photons by spontaneous parametric down-conversion (SPDC). The bi-photon state produced

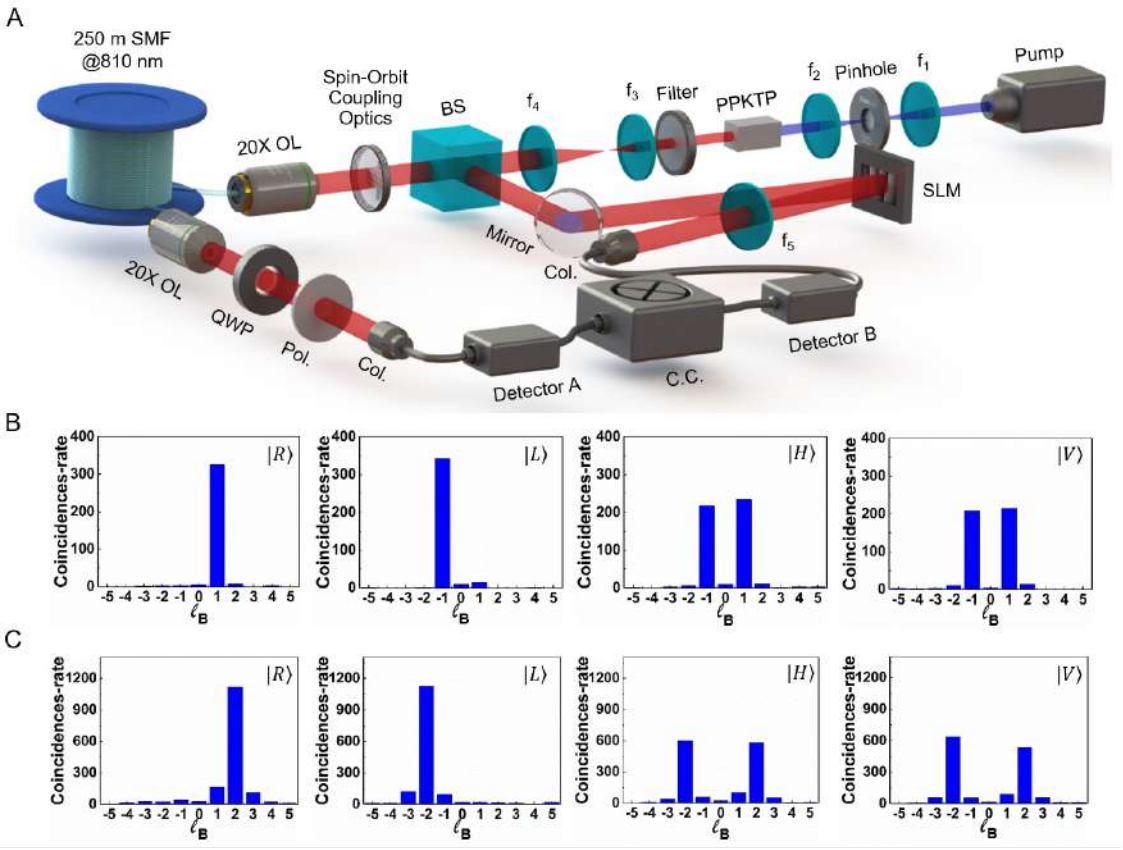


Figure 5-2: (a) Experimental setup. Pump: λ= 405 nm (Cobolt, MLD laser diode); f: Fourier lenses of focal length $f_{1;2;3;4;5}$ = 100 mm, 100 mm, 200 mm, 750 mm, 1000 mm, respectively; PPKTP: periodically poled potassium titanyl phosphate (nonlinear crystal); Filter: band-pass filter; BS: 50:50 beam splitter; QWP: quarter-wave plate; Pol.: polarizer; SLM: spatial light modulator; Col.: collimator, f=4.51 mm; C.C.: coincidence counter. (b) Measured coincidence count rate for the mode spectrum of the $\ell = \pm 1$ subspace and (c) the $\ell = \pm 2$ subspace after transmitting through 250 m of SMF. All coincidence-rates given as coincidences per second.

from the type-I SPDC process can be expressed in the OAM basis as

$$|\psi\rangle_{AB} = \sum_{\ell} c_{\ell} \, |H\rangle_A \, |H\rangle_B \, |\ell\rangle_A \, |-\ell\rangle_B \, , \tag{5.1}$$

where $|c_\ell|^2$ is the probability of finding photon A and B in the eigenstates $|\pm\ell\rangle$, respectively, and $|H\rangle$ is the horizontal polarisation. Subsequently one of the photons (e.g. photon A), from the N-dimensional OAM-entangled photon pair, is passed through a spin-orbit coupling (SOC) optics for OAM to spin conversion, resulting in

a hybrid multi-dimensional polarisation (spin) and OAM entangled state

$$\left|\Psi^{\ell}\right\rangle_{AB} = \frac{1}{\sqrt{2}}\big(\left|R\right\rangle_{A}\left|\ell_1\right\rangle_{B} + \left|L\right\rangle_{A}\left|\ell_2\right\rangle_{B}\big). \tag{5.2}$$

Here $|R\rangle$ and $|L\rangle$ are the right and left circular polarisation (spin) eigenstates on the qubit space $\mathcal{H}_{A,\text{spin}}$ of photon A and $|\ell_1\rangle$ and $|\ell_2\rangle$ denotes the OAM eigenstates on the OAM subspace $\mathcal{H}_{B,\text{orbit}}$ of photon B. The state in Eq. (5.2) represents a maximally entangled Bell state where the polarisation degree of freedom of photon A is entangled with the OAM of photon B. Each prepared photon pair can be mapped onto a density operator $\rho_{\ell} = \left|\Psi^{\ell}\right\rangle\left\langle\Psi^{\ell}\right|$ with $\left|\Psi^{\ell}\right\rangle \in \mathcal{H}_{A,\text{spin}} \otimes \mathcal{H}_{B,\text{orbit}}$ by actively switching between OAM modes sequentially in time: the larger Hilbert space is spanned by multiple two dimensional sub-spaces, multi-dimensional states in the quantum channel. For simplicity we will consider subspaces of $|\pm\ell\rangle$ but stress that any OAM subspace is possible, only limited by the SOC device characteristics. We can represent the density matrix of this system as

$$\rho_{AB} = \sum_{l=1}^{\infty} \gamma_{\ell}\rho_{\ell}, \tag{5.3}$$

where γ_{ℓ} represents the probability of post-selecting the hybrid state ρ_{ℓ}. The density matrix pertaining to system related to photon B is

$$\rho_B = \text{Tr}_A(\rho_{AB}) = \sum_{\ell=0}^{\infty} \frac{\gamma_{\ell}}{2}\big(\left|\ell\right\rangle_{B}\left\langle\ell\right|_{B} + \left|-\ell\right\rangle_{B}\left\langle-\ell\right|_{B}\big), \tag{5.4}$$

where $\text{Tr}_A(\cdot)$ is the partial trace over photon A. While photon B is in a superposition of spatial modes (but a single spin state), photon A is in a superposition of spin states but only a single fundamental spatial mode (Gaussian), i.e., $\left|\psi\right\rangle_{A} \propto (|L\rangle + |R\rangle)\,|0\rangle$ and $\left|\psi\right\rangle_{B} \propto |H\rangle\,(|\ell\rangle + |-\ell\rangle)$. As a consequence, photon A can readily be transported down SMF while still maintaining the spatial mode entanglement with photon B. Importantly, we stress that we use the term "multi-dimensional" as a proxy for multi-OAM states due to the variability of OAM modes in the reduced state of photon B: any one of these infinite possibilities can be accessed by suitable SOC optics, offering distinct advantages over only one two-dimensional subspace as is the case

with polarisation.

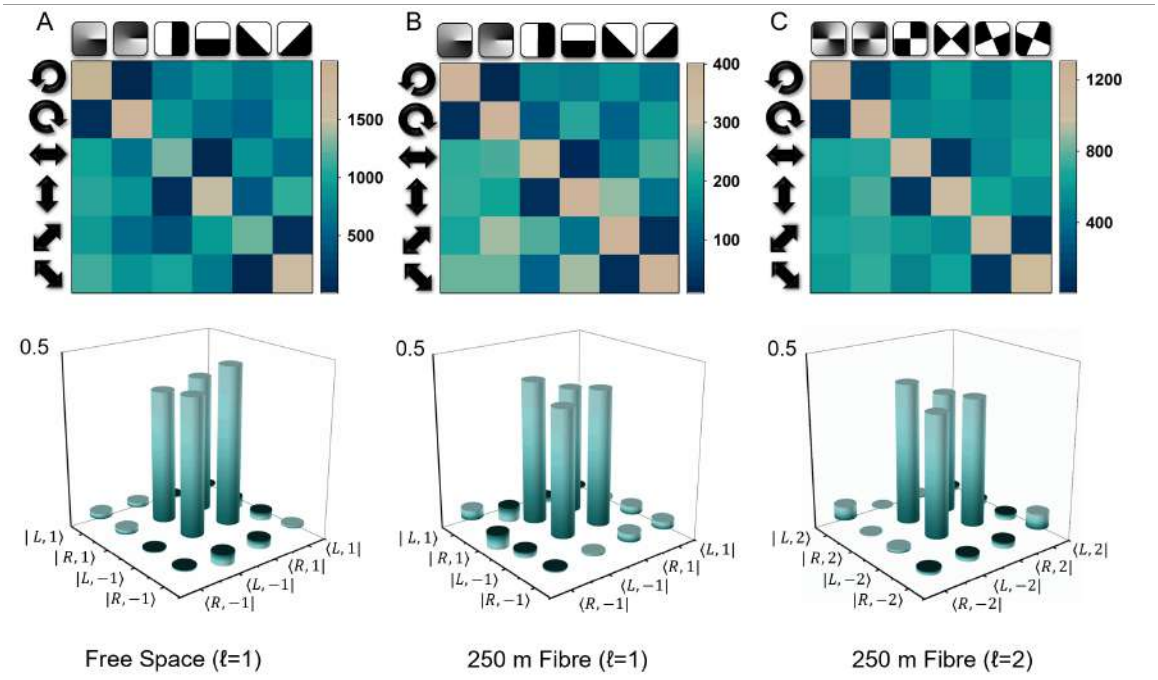


Figure 5-3: (a) $\ell = \pm 1$ in free space for system verification with (b) $\ell = \pm 1$ and (c) $\ell = \pm 2$ subspaces after transmitting the hybrid state through a one-sided 250 m SMF channel. The top panels show the raw tomography data for the 6×6 projections, the rows representing polarisation measurements on photon A and the columns representing holographic measurements on photon B. The bottom panels show the outcome of the tomography, a density matrix for each subspace.

5.3 Methods

5.3.1 The experiment

We prepare the state in Eq. (5.2) via post-selection from the high-dimensional SPDC state. In this section the SOC optics is based on q-plates [53]. The q-plate couples the spin and OAM degrees of freedom following

$$\begin{aligned} |R\rangle\,|\ell\rangle &\xrightarrow{q\text{-plate}} |L\rangle\,|\ell - 2q\rangle\,, \\ |L\rangle\,|\ell\rangle &\xrightarrow{q\text{-plate}} |R\rangle\,|\ell + 2q\rangle\,, \end{aligned} \tag{5.5}$$

where q is the topological charge of the q-plate. Accordingly, the circular polarisation eigenstates are inverted and an OAM variation of $\pm 2q$ is imparted on the photon depending on the handedness of the input circular polarisation (spin) state. Transmission of photon A through the SMF together with a detection acts as a post-selection, resulting in the desired hybrid state. Hence, considering N different OAM states $\pm\ell_n$ and N different q-plates with different topological charge q_n (such as $\ell_n \pm 2q_n = 0$), would allow us to access $2 \times N$ dimensions using a single SMF.

The experimental setup for multi-dimensional spin-orbit entanglement transport through SMF is shown in Fig. 5-2(a). A continuous-wave pump laser (Cobolt MLD diode laser, λ= 405 nm) was spatially filtered by a pinhole with a diameter of 100 μm to deliver 118 mW of average power in a Gaussian beam at the nonlinear crystal (a temperature controlled 10-mm-long PPKTP crystal), generating two lower-frequency photons by means of a degenerate type-I SPDC process. By virtue of this, the signal and idler photons had the same wavelength (λ= 810 nm) and polarisation (horizontal). The residual pump beam was filtered out by a band-pass filter with the centre wavelength of 810 nm and bandwidth of 10 nm. The two correlated photons, signal and idler, were spatially separated by a 50:50 beam-splitter (BS), with the signal photon A interacting with the spin-orbit coupling optics, e.g. q-plate, for orbit to spin conversion. Subsequently, photon A was coupled into the 250 m SMF by a 20× objective lens to transmit through the fibre and coupled out by another 20× objective lens. The idler photon B was imaged to the spatial light modulator (SLM) with lenses f_3 and f_4. After that, photon B was imaged again by f_5 and collimator, being coupled into a SMF, hence spatial filtered also, for detection.

The projective measurements were done by the quarter-wave plate (QWP) along with a polarizer for photon A, and SLM along with a SMF for photon B. Photon A, encoded with polarisation eigenstates was transmitted through the SMF while photon B, encoded with multi-dimensional OAM eigenstates, was transported through free space. Finally, both photons were detected by the single photon detectors, with the output pulses synchronized with a coincidence counter (C.C.).

5.3.2 Characterisation

5.3.2.1 Fidelity

We calculate the fidelity of our states from [319]

$$F = \mathrm{Tr}\Big(\sqrt{\sqrt{\rho_T}\rho_P\sqrt{\rho_T}}\Big)^2, \tag{5.6}$$

where ρ_T is the density matrix representing a target state and ρ_P is the predicted (or reconstructed) density matrix taking values ranging from 0 to 1 for $\rho_T \neq \rho_P$ and $\rho_T = \rho_P$, respectively. For a target state that is pure, such as the given in Eq. (5.2), i.e., $\rho_T = \left|\Psi^\ell\right\rangle\left\langle\Psi^\ell\right|$, the fidelity can be also expressed as

$$F = \mathrm{Tr}\Big[\rho_T\rho_P\Big] = \left\langle\Psi^\ell\right|\rho_P\left|\Psi^\ell\right\rangle. \tag{5.7}$$

5.3.2.2 Concurrence

. We use the concurrence as our measure of entanglement, calculated from

$$C_\Theta(\rho) = max\{0, \lambda_1 - \sum_{i=2}\lambda_i\}, \tag{5.8}$$

where ρ is the density matrix of the system being studied (mixed or pure), λ are the eigenvalues of the operator R= $\sqrt{\rho}\sqrt{\tilde{\rho}}$ in descending order with $\tilde{\rho} = \Theta\rho^*\Theta$ and * denotes a complex conjugation. The operator Θ represents any arbitrary anti-unitary operator satisfying $\langle\psi|\,\Theta\,|\phi\rangle$=$\langle\phi|\,\Theta^{-1}\,|\psi\rangle$ for any state $|\phi\rangle$ and $|\psi\rangle$, if $\Theta^{-1} = \Theta^\dagger$.

5.3.2.3 State tomography

The density matrix of a single photon in a two-dimensional state space ($\mathcal{H}_2$), can be represented as a linear combination of the Pauli matrices [320]

$$\rho = \frac{1}{2}\big(\mathbb{I}_0 + \sum_{3}^{k=1} b_k \sigma_k\big), \tag{5.9}$$

where $\mathbb{I}_0$ is the two-dimensional identity operator, σ_k are the trace-less Pauli operators with complex coefficients b_k. In this work we consider the density matrix of a hybrid entangled state similar to Eq. (5.2). It can be expressed as

$$\rho = \frac{1}{2}\big(\mathbb{I}_A \otimes \mathbb{I}_B + \sum_{3}^{m,n=1} b_{mn} \sigma_{Am} \otimes \sigma_{Bn}\big), \tag{5.10}$$

here $\mathbb{I}_{AB}$ is the two photon identity matrix and σ_{Am} and σ_{Bn} are the Pauli matrices that span the two-dimensional hybrid space for polarisation and OAM respectively.

We reconstruct each hybrid state, ρ_ℓ, via a quantum state tomography. This entails performing a series of local projections $M_{ij} = P_A^i \otimes P_B^j$ where $P_{A,B}^{i,j}$ are projections on photon A and photon B, respectively, and using the resulting measurement outcomes to reconstruct the state [89]. The detection probabilities on a system with a corresponding density matrix (ρ) are

$$p_{ij} = Tr[M_{ij} \rho M_{ij}^\dagger]. \tag{5.11}$$

The overall projections constitute an over-complete set of measurements on the two photon subspace.

In the experiment, photon A is projected onto the spin basis states $|R\rangle$ and $|L\rangle$, along with their equally weighted superpositions of linear anti-diagonal, diagonal, horizontal, vertical polarisation states, i.e $|A\rangle, |D\rangle, |H\rangle$ and $|V\rangle$, respectively. Similarly, photon B is locally projected onto the eigenstates $|\pm\ell\rangle$ along with superpositions

$$|\theta\rangle = \frac{1}{\sqrt{2}}\big(|\ell\rangle + e^{i\theta}|-\ell\rangle\big), \tag{5.12}$$

for relative phase $\theta = \frac{3\pi}{2}, \pi, \frac{\pi}{2}, 0$.

5.3.2.4 CHSH Bell violation

To further characterise the non-local correlations in each hybrid subspace, a violation of the Clauser-Horne-Shimony-Holt (CHSH) Bell inequality [321] with the two photon system is used. First, we project photon B onto the states, $\theta_A = \{\frac{3\pi}{2}, \pi, \frac{\pi}{2}, 0\}$, corresponding to A, V, D, H polarisation states while we measure the photon coincidence rate as a function of θ_B (relative phase between $|\ell\rangle$ and $|-\ell\rangle$ in arm B). The variation of the number of coincidences with the angle θ_B is in agreement with expected non-classical correlations. We define the CHSH-Bell parameter S as [84]

$$S = |E(\theta_A, \theta_B) - E(\theta_A, \theta'_B) + E(\theta'_A, \theta_B) + E(\theta'_A, \theta'_B)|\,, \tag{5.13}$$

with $E(\theta_A, \theta_B)$ calculated from coincidence events

$$\begin{aligned} E(\theta_A, \theta_B) &= \frac{\xi(\theta_A, \theta_B) - \xi'(\theta_A, \theta_B)}{\xi(\theta_A, \theta_B) + \xi'(\theta_A, \theta_B)}, \\ \xi(\theta_A, \theta_B) &= C(\theta_A, \theta_B) + C\left(\theta_A + \frac{\pi}{2}, \theta_B + \frac{\pi}{2}\right), \\ \xi'(\theta_A, \theta_B) &= C\left(\theta_A + \frac{\pi}{2}, \theta_B\right) + C\left(\theta_A, \theta_B + \frac{\pi}{2}\right). \end{aligned} \tag{5.14}$$

Here $C(\theta_A, \theta_B)$ represents measured coincidence counts. The Bell parameter can be characterized as $S \leq 2$ for separable states and $2 < S \leq 2\sqrt{2}$ for maximally entangled states.

5.4 Results

We first evaluate the SMF quantum channel by measuring the OAM mode spectrum after transmitting through 250 m SMF. Figures 5-2(b) and 5-2(c) show the mode spectrum of the $\ell = \pm 1$ and $\ell = \pm 2$ subspaces, respectively. We project photon A onto right circular polarisation (R), left circular polarisation (L), horizontal polarisation

(H) and vertical polarisation (V) by adjusting the QWP and polarizer at the output of the fibre, while measuring the OAM of photon B holographically with a SLM and SMF. The results are in very good agreement with a channel that is impervious to OAM. When the orthogonal polarisation states are selected on photon A ($|L\rangle$ and $|R\rangle$), an OAM state of high purity is measured for photon B, approximately 93% for $\ell = \pm 1$ and approximately 87% for $\ell = \pm 2$. The slightly lower value for the $\ell = \pm 2$ subspace is due to concatenation of two SOC optics for the hybrid entanglement step.

To confirm the state and the entanglement conservation, we perform a full quantum state tomography on the hybrid state to reconstruct the density matrix. Figure 5-3 shows the state tomography measurements and resulting density matrices for both the $\ell = \pm 1$ and $\ell = \pm 2$ subspaces after 250 m SMF, with the free space $\ell = \pm 1$ shown as a point of comparison (see appx. D.0.1 for more results in free space and in 2 m SMF). The fidelity against a maximally entangled state is calculated to be 95% for the $\ell = \pm 1$ and 92% for the $\ell = \pm 2$ subspaces. This confirms that the fibre largely maintains the fidelity of each state. Using concurrence (C) as our measure of entanglement we find $C = 0.91$ for free space, down slightly to $C = 0.9$ for $\ell = \pm 1$ and $C = 0.88$ for $\ell = \pm 2$.

The state tomography results depicted for each of the subspaces have different average coincidence count rates due to several small imperfections during the experimental realization: different collection efficiency depending on the detected spatial mode, temperature fluctuations in the nonlinear crystal oven causing a slight reduction in the SPDC efficiency, and some error in the rotation of the wave plates may have caused differences in the state tomography outcome depending on the projections. Nonetheless, the fidelity of the free-space density matrix is still higher due to the minimal cross-talk between the orthogonal modes (across the diagonal).

To carry out a non-locality test in the hybrid regime we define the two sets of dichotomic observables for A and B: the bases a and $\tilde{a}$ of Alice correspond to the linear polarisation states $\{|H\rangle, |V\rangle\}$ and $\{|A\rangle, |D\rangle\}$, respectively, while the bases b and $\tilde{b}$ of Bob correspond to the OAM states $\{\cos\left(\frac{\pi}{8}\right)|\ell\rangle - \sin\left(\frac{\pi}{8}\right)|-\ell\rangle, -\sin\left(\frac{\pi}{8}\right)|\ell\rangle + \cos\left(\frac{\pi}{8}\right)|-\ell\rangle\}$ and $\{\cos\left(\frac{\pi}{8}\right)|\ell\rangle + \sin\left(\frac{\pi}{8}\right)|-\ell\rangle, \sin\left(\frac{\pi}{8}\right)|\ell\rangle - \cos\left(\frac{\pi}{8}\right)|-\ell\rangle\}$. From the data

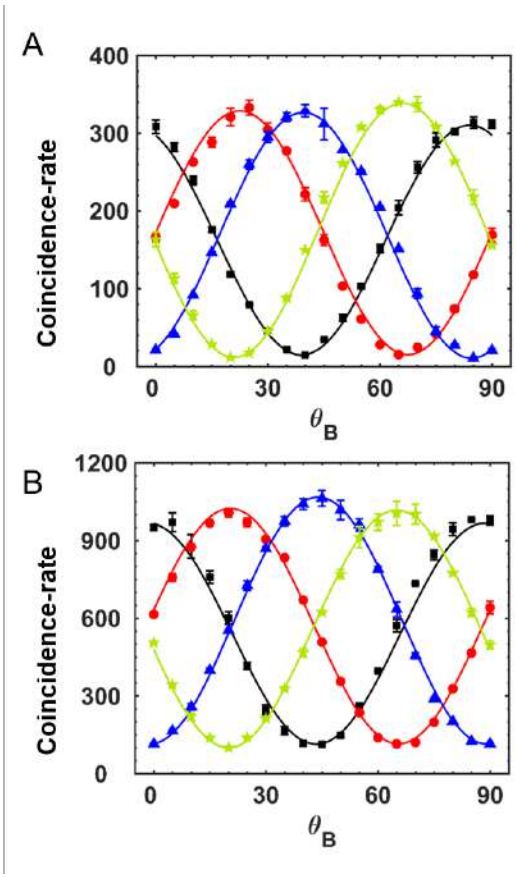


Figure 5-4: Measured correlations between photon A (polarisation) and photon B (OAM) in (a) the $\ell = \pm 1$ subspace after 250 m SMF and (b) the $\ell = \pm 2$ subspace after 250 m SMF. Photon A is projected onto the states $\theta_A = \{\frac{3\pi}{2}, \pi, \frac{\pi}{2}, 0\}$, corresponding to A, V, D, H polarisation states and known to maximally violate the Bell inequality, while the superposition hologram is rotated in arm B through an angle θ_B. All coincidence-rates given as coincidences per second.

shown in Fig. 4 we calculate the CHSH Bell parameters in free space and through SMF . We find CHSH Bell parameters of $S = 2.77 \pm 0.06$ and $S = 2.47 \pm 0.09$ for the $\ell = \pm 1$ subspace in free space and in 250 m of SMF, respectively, reducing to $S = 2.51 \pm 0.04$ and $S = 2.25 \pm 0.19$ for the $\ell = \pm 2$ subspace. In all cases we violate the Bell-like inequality.

5.4.1 A hybrid quantum eraser

Next we use the same experimental setup to demonstrate a hybrid quantum eraser across 250 m SMF. We treat OAM as our "path" and the polarisation as the "which

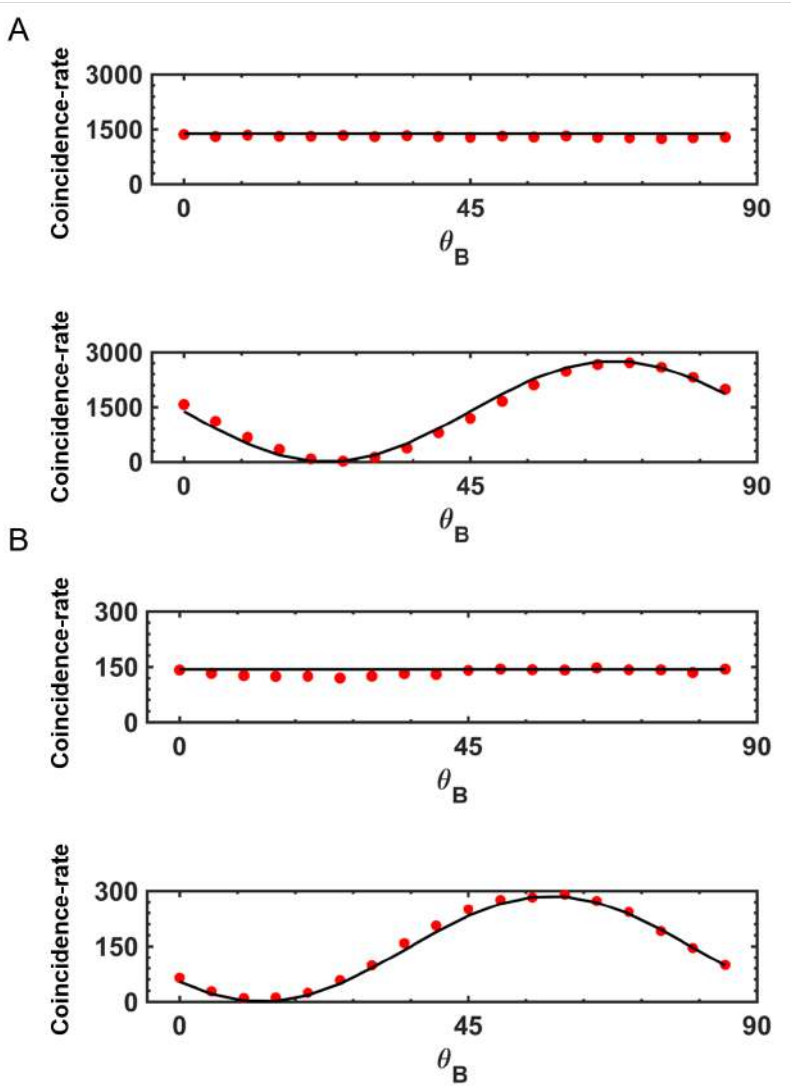


Figure 5-5: Experimental coincidence count-rates for distinguishing and erasing the OAM, in the the $\ell = \pm 1$ subspace, of photon B upon transmitting photon A through (a) free space and through (b) 250 m SMF. OAM (path) information is introduced into the system with a QWP, and a polariser selecting one of the markers. Here we select the state $|H\rangle$ and as seen, the spatial distribution of photon B is uniform with minimal visibility. In the complimentary case, the path markers are collapsed onto a superposition $|+\rangle$ or equivalently $|D\rangle$, with the polariser and all the path information removed, manifesting as prominent visible azimuthal fringes. All coincidence-rates given as coincidences per second.

path" marker to realize a quantum eraser with our hybrid entangled photons. We first distinguish the OAM (path) information in the system by marking the OAM eigenstates of photon B with linear polarisations of photon A. In this experiment, we

achieve this by placing a QWP before a polarizer, transforming Eq. (5.2) to

$$\left|\tilde{\Psi}^{\ell}\right\rangle_{AB} = \frac{1}{\sqrt{2}}\big(\,|H\rangle_A\,|\ell_1\rangle_B + |V\rangle_A\,|\ell_2\rangle_B\,\big). \tag{5.15}$$

By selecting either polarisation states, $|H\rangle$ or $|V\rangle$, the distribution of photon B collapses on one of the OAM eigenstates, $\ell_{1,2}$, having a uniform azimuthal distribution and fringe visibility of $\mathrm{V} \equiv \frac{(\mathrm{max}-\mathrm{min})}{(\mathrm{max}+\mathrm{min})} = 0$, reminiscent of the smeared pattern that is observed from distinguishable (non-interfering) paths in the traditional quantum eraser [322]. The OAM information can be erased by projecting photon A onto the complimentary basis of the OAM markers, i.e., $|\pm\rangle = \frac{1}{\sqrt{2}}(|H\rangle \pm |V\rangle)$, causing the previously distinguished OAM (paths) to interfere, thus creating azimuthal fringes that can be detected with an azimuthal pattern sensitive scanner. The fringes appear with a visibility of $\mathrm{V} = 1$ indicative of OAM information reduction [94]. The appearance in azimuthal fringes of photon B is indicative of OAM information being erased from photon B. Importantly, it is noteworthy to point out that here the QWP acts as the path marker while the polariser acts as the eraser. Notably, complementarity between path information and fringe visibility (V) is essential to the quantum eraser. By defining the two distinct paths using the OAM degree of freedom, we find that it is possible to distinguish ($V = 0.05 \pm 0.01$) and erase ($V = 0.98 \pm 0.002$) the OAM path information of a photon through the polarisation control of its entangled twin in free space. With only marginal loss of visibility after transmitting through 250 m SMF, conserving the entanglement with the ability to distinguish ($V = 0.11 \pm 0.01$) and erase ($V = 0.93 \pm 0.01$) the OAM path information.

Though the eraser procedure was performed on the $\ell = \pm 1$ subspace, it can be extended to higher subspaces: depending on the SOC device that is used for photon A, the SLM holograms implemented for scanning the azimuthal fringes of photon B can be adapted to the relevant subspace.

5.5 Discussion and Conclusion

In our work, any two-dimensional subspace of the high-dimensional space is accessible by simply changing the SOC optic. In our experiment we used two sets of the SOC optics, each for selecting $\ell = \pm 1$, in order to reach $\ell = \pm 2$; this introduced additional distortions which reflected in the lower performance as compared to $\ell = \pm 1$. Nevertheless, even with this arrangement the entanglement was still preserved over an extended distance of 250 m, which we have demonstrated through quantum state tomography, Bell inequality violations and a novel quantum eraser experiment. Moreover, the demonstration of two two-dimensional subspaces is double what would be possible with only polarisation entanglement. While we used OAM states of $\{|\ell\rangle, |-\ell\rangle\}$ it is possible to select any two orthogonal OAM states from the N-dimensional space to establish the OAM basis, i.e. $\{|\ell_1\rangle, |\ell_2\rangle\}\ \forall\ \ell_1 \neq \ell_2$. In addition, one can also choose any orthogonal polarisation states, for example, $\{|R\rangle, |L\rangle\}$, $\{|H\rangle, |V\rangle\}$ or $\{|A\rangle, |D\rangle\}$. This can be done by specially designed spin-orbit coupling optics and has already been demonstrated classically [203]. In this way, our work may be extended by judiciously selecting states for reducing coupling with the environment and therefore preserve the entanglement of the system over even longer distances.

Excitingly, our work opens a new path towards multiplexed QKD down conventional SMF. Multiplexed QKD has been demonstrated with OAM modes down *custom* optical fibre and shown to double the key rate of transmitting a four-dimensional state [314]. In our approach each spatial mode, e.g., the OAM modes, would correspond to an independent channel, as a long as all counterparts are post-selected with different ℓ, forming an interesting rerouting quantum optical hub. In addition to deployment over conventional fibre, this multiplexing advance requires only the use of already existing technology in the form of OAM mode sorters [323].

Importantly, our scheme offers an alternative to high-dimensional entanglement transport over long distance, the latter limited by both fundamental and practical issues. These include the need for multiple photons to teleport high-dimensions [324],

the excessively long measurement times to reconstruct such states [35], and the difficulty in experimental execution of high-dimensional spatial mode teleportation [325]. The mooted benefits of high-dimensional states are likewise yet to be realised experimentally: robustness to noise has not been shown for spatial mode entanglement, while existing models consider only white noise and not the more troublesome modal coupling noise terms. Further, the benefit is derived in part from the existence of K dimensional entanglement in the initial D dimensional state, but without any recipe for finding or specifying what K might be. Because of these issues, laboratory QKD (in speciality fibre) has revealed that it is far better to use the higher-dimensions for multiplexing than it is to encode information directly in them. Our approach is a compromise that reaps the benefits of multiple states while the allowing immediate deployment across legacy networks. No other spatial mode solution allows this.

In conclusion, we have outlined a new approach to transporting entanglement through fibre in a manner that allows deployment over a conventional network of SMF. The result is based on hybrid entangled states, allowing access to multiple dimensions: an infinite number of two-dimensional subspaces. Together these subspaces span the entire high-dimensional Hilbert space that would be available by spatial mode entanglement. Our experimental demonstration over 250 m SMF and at double the dimensions available to polarisation shows that this scheme is a viable approach to circumvent the technological hurdles of deploying spatial mode entanglement.

Chapter 6

Quantifiying Dimensionality and Purity in High Dimensional Entanglement

The work in this chapter was published in:

- **Nape, I.**, Rodríguez-Fajardo, V., Zhu, F., Huang, H.C., Leach, J. and Forbes, A., 2021. "Measuring dimensionality and purity of high-dimensional entangled states". **Nature Communications**, 12(5159), pp.1-8.

Nape, I., performed the theory calculations, the experiments, analysed the data and contributed to writing the manuscript under the guidance of the contributing coauthors.

6.1 Introduction

High-dimensional quantum states are widely used to increase secure information bandwidth and improve security bounds for quantum communication [17]. Through the precise control of high dimensional photonic states [326], i.e., time-energy, transverse momentum, spatial degrees of freedom or all of them simultaneously [327], the potential benefits of high dimensional state encoding are taking center stage. Recent developments in this direction have displayed the feasibility of quantum information processing that is robustness against optimal quantum cloning machines [32,33], environmental noise [34] and improved information rates [328], demonstrating a significant advantage in comparison to traditional qubit encoding.

Despite the advantages of high-dimensional quantum states, certifying and quantifying the dimensionality of such systems still remains challenging, particularly in the presence of noise. The intuitive approach of simply measuring the width of the modal spectrum is a necessary but not sufficient condition to determine dimensionality as it fails to account for non-local correlations. Consequently, many techniques have been developed to witness, bound and attempt to quantify high-dimensional quantum states. These include approximating the density matrix via quantum state tomography (QST) with multiple qubit state projections [329], using mutually unbiased bases [35, 330] to probe the states or incorporating self-guided approaches [131, 331], and testing non-local bi-photon correlations by generalised Bell tests in higher dimensions [83, 139, 332]. However, the spectrum measurements do not confirm entanglement, the QST approach scales unfavourably with dimension, only bounds or witnesses are possible with the mutually unbiased bases method and the dimension to be probed must be known a priori (e.g., valid for prime or prime power dimensions), and finally, the high-dimensional Bell tests can fail the fair sampling condition [73,88]. A further limitation in the present state-of-the-art is that certain dimensionality measurements consider only pure states [35,333], yet noise mechanisms always introduce some degree of mixture to the system [117], which has a detrimental effect on the accuracy of measured dimensions due to the reduced purity [27]. Yet, knowing the

purity and dimension of the state is crucial for fundamental tests of quantum mechanics as well as for quantum information processing protocols, setting the required violation of inequalities in the former, and the information capacity of the state, the allowed error bounds in secure communication systems, and the requirement for entanglement distillation in the latter.

In this work we present a scheme to simultaneously quantify the dimensionality and purity of a bi-photon high-dimensional entangled state, even in the presence of noise, using the isotropic state as our test example. By measuring coincidence fringes from carefully crafted projective measurements, we are able to accurately measure the dimensionality and purity of our entangled state from the visibility, which is only reproducible by entangled photons. We first outline the concept and theory and then demonstrate it experimentally on states with arbitrary purity and a wide range of dimensions. To show the versatility of our approach, we use it to measure entanglement in the topical photonic orbital angular momentum (OAM) basis, and the pixel (position) basis, commonly used in quantum imaging. With knowledge of the visibilities, purity and dimensionality, we have sufficient information to infer other salient measures. Our quantitative technique is simple, robust, and scales favourably (linearly) with dimension, making it ideal for practical implementations of quantum protocols with general high-dimensional photonic quantum entangled states, even under undesired noise conditions.

6.2 Implementation

6.2.1 Concept

The task here is to quantify the effective dimensions and purity of an entangled photonic state. If the state is assumed pure and without noise, then the problem is trivial. Here we wish to make as few assumptions as possible, and consider the more general case of arbitrary mixed states in the presence of noise. Incorporating noise into the description of high-dimensional states is highly topical of late and

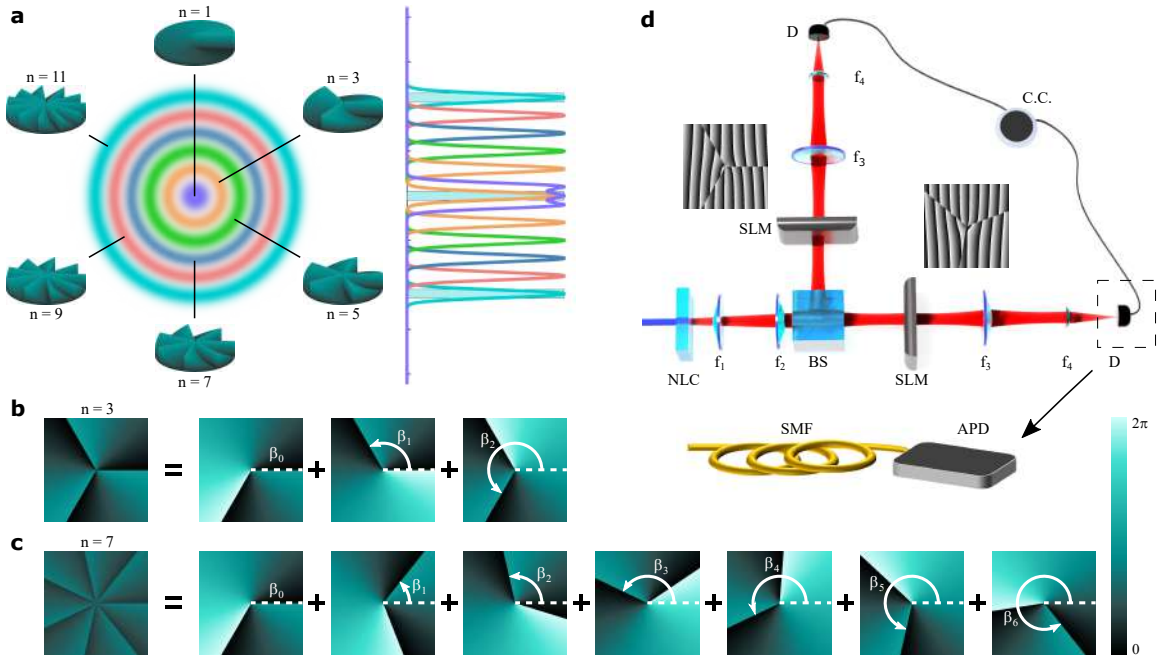


Figure 6-1: (a) Conceptual visualisation of different analysers sampling various portions of a high dimensional discrete Hilbert space. Mode analysers construction for (b) $n = 3$ and (c) $n = 7$ superpositions of fractional OAM states where β_i is an orientation angle. (d) Schematic of the experimental setup used to measure the dimensionality and purity of a quantum system. (NLC: Nonlinear crystal, $f_{1,2,3,4}$: lens, BS: 50:50 Beam-splitter, SLM: Spatial light modulator, D: detector, APD: avalanche photo diode coupled to a single mode fiber (SMF), C.C.: coincidence counter)

very much in its infancy, with a full understanding of its deleterious impact only slowly emerging [34]. In general, the purity of the quantum system, and therefore the entanglement between photon pairs, is reduced due to noise introduced by the source, the environment and/or the detection system, very often in the form of white noise produced by background photons, high dark counts in single photon detectors and unwanted multiphoton events [27]. We follow convention [34] and model such noisy quantum systems by an isotropic state following

$$\rho = p\left|\Psi\right\rangle\left\langle\Psi\right| + \left(\tfrac{1-p}{d^2}\right)\mathbb{1}_{d^2}, \tag{6.1}$$

which considers contributions of both the pure, $|\Psi\rangle$, and a mixed part, $\mathbb{1}_d^2$ (d^2-dimensional identity operator), parts. Although this will be our target state for extracting the purity and dimensionality, it does not appear in the construction of

the analysers nor the measurement procedure itself. As such, the state and the parameters to be extracted may be modified to incorporate other factors, for example, mode dependent noise due to the resolution limits of detection devices [334]. The pure part, $|\Psi\rangle = \sum_{i=0}^{d-1} \lambda_j |j\rangle |j\rangle$, can be decomposed using the Schmidt basis states, $|j\rangle |j\rangle \in \mathcal{H}_d^2$ with corresponding Schmidt coefficients, λ_j. A variety of entangled, quantum states (time, energy, position, hybrid and hyper-entangled) can be decomposed in this way, therefore covering a vast number of cases. Here p is a parameter that determines the purity of the state, and varies from a maximally mixed (separable) state for $p = 0$ to a completely pure (entangled) state for $p = 1$. The purity of a non-separable d dimensional state is given by $\mathrm{Tr}(\rho^2)$ where $1/d < \mathrm{Tr}(\rho^2) \leq 1$, while the bounds on p are, $1/(d+1) < p \leq 1$. Hence, since $1/(d+1) \sim 1/d$ for high-dimensional states, it suffices to use the notion of purity and p, interchangeably. We use $K = 1/\sum_j |\lambda_j|^4$ as a measure of the local dimensions of the pure part of the state [72].

Our procedure allows us to quickly establish K and p, i.e. the dimensionality of the pure component and its probability. Another common measure of dimensionality is the Schmidt Rank [71], which we will denote as d_{ent}. The d_{ent} refers to the dimensionality of the entire state, not just the pure component, and it is possible to deduce d_{ent} from our approach through knowledge of K and p (See appx. E.1 and E.10).

As we characterise the pure component of the state and establish the overall purity, the number of required measurements scales linearly with the dimension d of the probed Hilbert space. This provides a significant gain in speed for high-dimensional states.

Thus, our proposed method is a fast, accurate, and simple procedure to characterise the properties of two-photon high-dimensional entangled states.

The working principle of our technique is visualised in Fig. 6-1 (a), where a set of custom analysers probe distinct parts of a discrete Hilbert space. We can think of each analyser as a probe that scans a sparse set of modes, reminiscent of a conditional measurement that indicates whether there is entanglement within the subspace or not. By combining the information gathered from a number of such analysers, we infer how many dimensions the state occupies. We will demonstrate this procedure both

theoretically and experimentally.

It is instructive to illustrate the concept by example. Consider a pair of photons entangled in their polarisation, energy-time, momentum or in the spatial basis [15], so-called structured light [187], the former useful to access high-dimensions, with up to 100×100 dimensions already demonstrated [335]. In this work we will consider two examples: the OAM basis [16, 140] and the pixel (position) basis [42]. Due to the great potential of the former, particularly for quantum information processing and communications [20, 47, 62, 197, 222, 325, 336–344], we first illustrate and demonstrate our method for OAM entangled states. In this case, the basis states, $|\ell_1\rangle\,|\ell_2\rangle$, are associated with an azimuthal phase profile $\exp(i\ell_{1,2}\phi)$, with $\ell_{1,2} \in \mathbb{Z}$ being the topological charge and $\ell_{1,2}\hbar$ OAM per photon. An OAM entangled pure state can be expressed as

$$|\Psi\rangle = \sum_{\ell_{1,2}=-\infty}^{\infty} \lambda_{\ell_{1,2}} \,|\ell_1\rangle_A \,|\ell_2\rangle_B \,, \tag{6.2}$$

where $|\lambda_{\ell_{1,2}}|^2$ is the probability of generating photons in the states $|\pm\ell_{1,2}\rangle$ for photons A and B, respectively. For our experimental tests with a Gaussian pumped SPDC source, the state only has non-zero probabilities when $\ell \equiv \ell_1 = -\ell_2$. While in general the state $|\Psi\rangle$ can be represented using an unbounded number of eigenmodes as shown, i.e., $d \to \infty$, we truncate $|\Psi\rangle$ to d eigen-states. This is simply applying common sense: one should select a Hilbert space with a dimension large enough to test in based on what you are looking for (analogous to selecting a camera area that is large enough to fit the image you hope to measure). Importantly, since our approach scales linearly with test dimension, there is no significant penalty for selecting a test dimension that is "too big", in stark contrast to QST-based approaches (See appx. E.12 and Table E.2) . In this sense, d may be chosen at will.

To gain access to various parts of the Hilbert space, we make use of high dimensional mode projectors that map onto the states

$$|M,\alpha\rangle_n = \mathcal{N} \sum_{j=0}^{d-1} c^n_{w_j,M}(\alpha)\,|j\rangle \,, \tag{6.3}$$

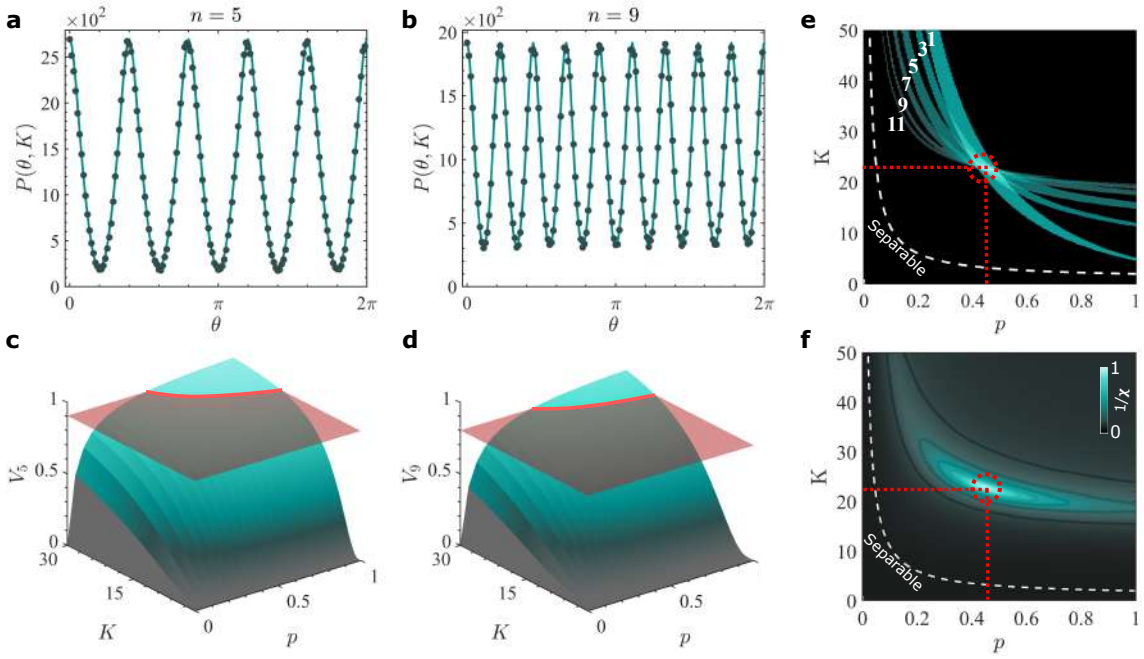


Figure 6-2: Experimental (points) and theoretical (solid lines) coincidence count rates resulting from projections of photons A and B onto the states $|M,\theta\rangle_n$ and $|-M,0\rangle_n$, respectively, as a function of the relative orientation angle θ for (a) $n = 5$ and (b) $n = 9$. Theoretical visibility as a function of the dimensionality (K) and purity (p) for (c) $n = 5$ and (d) $n = 9$, exemplifying it increases monotonically with both parameters. The (red) planes intersecting the curves are the experimental visibilities, with the possible solution space for each shown as a red trajectory. The resulting trajectories for $n = 1, 3, ...11$ are shown in (e), where the thickness of each is due to the uncertainty in the visibility outcome. The dimension and purity of the system are found where they coincide, shown as a dashed red circle. (f) The later corresponds to the optimal (p, K) that minimise the function $\chi^2(p, K)$, or, equivalently, maximizes $\sqrt{1/\chi^2}$, where the minimum of χ^2 is now shown as a peak corresponding to $(p, K) = (0.45 \pm 0.03, 22.84 \pm 0.62)$. The critical bound, $p \leq 1/(K + 1)$, separating entangled and separable states is marked by the white dashed line.

where $\mathcal{N}$ is a normalisation factor, $|j\rangle$ are the basis states on the d dimensional space. The coefficients, $c^n_{w_j,M}(\alpha)$, control the amplitudes and phases of the modes in the superposition. For OAM basis states, the coefficients can be represented accordingly by replacing the index w_j with the topological charge $\ell = j - (d-1)/2$. Examples of the phase profiles for two such analysers are shown in Fig. 6-1 (b) and (c) for $n = 3$ and $n = 7$, respectively, with full details on their construction in the Methods section and appx. E.2 - E.4. While n and M can be chosen arbitrarily, we find it optimal to set n as an odd positive integer and $M = n/2$ (See appx. E.5).

Next, we project each entangled photon onto the superposition states $|M,0\rangle_n$

and $|M,\theta\rangle_n$, respectively, where $\theta = [0, \pi/n]$ controls the relative phases between the modes in the superposition. In the context of OAM this translates into a relative rotation by an angle θ. A typical experimental setup for implementing this is sketched in Fig. 6-1 (d). Entangled photon pairs are generated in a non-linear crystal (NLC) and subsequently projected onto the states $|M,\theta\rangle$ and $|-M,0\rangle$ by means of holograms programmed onto spatial light modulators (SLMs) having the transmission functions $U_n(\phi;\theta)$ and $U_n^*(\phi;0)$, respectively. In the OAM degree of freedom, the holograms correspond to fractional OAM modes [345], known to have a non-integer azimuthal phase gradient. The modulated photons are then coupled into single mode fibers and measured in coincidences. The outcome probability of such a measurement, i.e., $|\langle 0,-M|_n \langle\theta,M|_n \rho |M,\theta\rangle_n |-M,0\rangle_n|$, is

$$P_n(\theta;p,K) = pP_n(\theta,K) + \frac{1-p}{K^2} I_n(0,K), \tag{6.4}$$

where $I_n(0,K)/K^2$ is the probability resulting from the overlap of the analysers with the maximally mixed state and $P_n(\theta,K) = \left|\sum_{\ell=-(K-1)/2}^{(K-1)/2} \lambda_\ell c^n_{\ell,M}(0) c^n_{-\ell,M}(\theta)\right|^2$ is the overlap probability with the pure state, with $M = n/2$ the fractional charge and λ_ℓ the initial bi-photon OAM spectrum. For a pure state, the probability curves have a parabolic shape following $P_n(\theta) = (\pi(2t-1) - n\theta)^2/\pi^2$, where $t = 1, 2, \ldots\ n$. In Fig. 6-2 (a) and (b), we show as solid lines the theoretical probabilities (calculated using Equation (6.4)) of such a measurement as function of θ.

We choose odd values of n and $M = n/2$ to ensure a high visibility, which increases monotonically with K and p for each analyser (See appx. E.6 and Fig. E-5). In general, both the shape and visibility of the fringes yield information about the state. To make the approach accurate and precise, we measure several visibilities, V_n, for $n = 1, 3, 5 \ldots 2N-1$, and infer the state properties by the intersection of their solution spaces (Fig. 6-2 (e)).

6.3 Methods

6.3.1 High dimensional state projections

Our analysers project onto the high dimensional Hilbert space, $\mathcal{H}_d$, mapping onto the states in Equation (6.9), i.e $|M,\alpha\rangle_n$, repeated here as

$$|M,\alpha\rangle_n = \mathcal{N}\sum_{j=0}^{d-1} c^n_{w_j,M}(\alpha)\,|j\rangle\,, \tag{6.5}$$

composed of coherent superpositions of basis states $|j\rangle \in \{|j\rangle\,, j = 0, 1..d-1\}$ with tune-able phases and amplitudes

$$c^n_{w_j,M}(\alpha) = e^{-i\pi w_j(n-1)/n} A^n_{w_j} c_{w_j,M}(\alpha), \tag{6.6}$$

and where $w_j = j - (d-1)/2$ and the factors

$$c_{w_j,M}(\alpha) = -\frac{ie^{-iw_j\alpha}}{\pi(M-w_j)}. \tag{6.7}$$

and

$$A^n_{w_j} = \begin{cases} 1, & \mod\{w_j, n\} = 0 \\ 0, & \text{otherwise} \end{cases}. \tag{6.8}$$

Here, $c_{w_k,M}(\alpha)$ controls the relative phases and amplitudes of the eigenmodes and $A^n_{w_j}$ modulates the coefficients' amplitudes while $\alpha \in [0, 2\pi/n]$. The spectrum given by Equation (E.40) can be tuned by carefully selecting n, therefore enabling precise control of the subspaces that will be probed.

In the OAM basis, i.e $|\ell\rangle \in \mathcal{H}_d$, the index w_j can be replaced with the index $\ell \in \mathcal{Z}$. The mode projectors can be constructed from spiral phase profiles having the

transmission function

$$U_n(\phi,\alpha) = \mathcal{M}\sum_{k=0}^{n-1}\exp\left(i\Phi_M\left(\phi;\beta_k\oplus\alpha\right)\right), \tag{6.9}$$

that is constructed from superpositions of fractional OAM modes [345,346],

$$\exp\left(i\Phi_M(\phi;\alpha)\right) = \begin{cases} e^{iM(2\pi+\phi-\alpha)} & 0\leq\phi<\alpha \\ e^{iM(\phi-\alpha)} & \alpha\leq\phi<2\pi \end{cases}, \tag{6.10}$$

having the same charge, M, but rotated by an angle $\beta_k\oplus\alpha = \mathrm{mod}\left\{\beta_k+\alpha, 2\pi\right\}$ for $\beta_k = \frac{2\pi}{n}k$, as illustrated in Figs. 6-1 (b) and (c) for $n=3$ and $n=7$, respectively. Here, ϕ is the azimuthal coordinate and $\mathcal{M}$ a normalization constant.

For the pixel basis, we constructed the holograms on a $d = D\times D$ grid with each square corresponding to a "pixel" state. The coefficients corresponding to a projection onto the state, $|M,\alpha\rangle_n$, can be mapped as

$$C_{r,c} = c^n_{w_{o-1},M}(\alpha), \tag{6.11}$$

where $o = (r-1)D - c$, for each index pair, $r, c = 1,\ 2,\ 3...d$, locating the row and column index of each pixel state on the grid. This mapping converts the list of coefficients, c_{w_j} (for $j = 0,\ 1...\ d$-1), into a square matrix $C_{r,c}$. To construct the hologram we then extract the amplitude and phase of the matrix components of C and obtain,

$$U_{r,c} = B_{r,c}\mathrm{mod}\{\arg\left(C_{r,c}\right), 2\pi\}, \tag{6.12}$$

where $B_{r,c} = |C_{r,c}|/\max\left(C\right)$. The final hologram can then be obtained by re-sampling U onto a high resolution grid that can be loaded onto the SLM. In this work, we re-sampled each projection hologram onto a 200×200 grid. Example holograms for 9×9 states that were resampled onto a 200×200 grid are shown in Fig. 6-4 (b).

6.3.2 Experimental setup.

The experimental setup for the generation and measurement of entangled photons is illustrated schematically in Fig. 6-1 (d). A potassium-titanium-phosphate (PPKTP) type I nonlinear crystal (NLC) was pumped with a 405 nm wavelength diode laser. The crystal temperature was set to obtain co-linear signal and idler entangled SPDC photons centred at a wavelength 810 nm. The photon pairs were then separated in path using a 50:50 beam splitter (BS). Each entangled photon was imaged onto a spatial light modulator (SLM) using a $4f$ telescope (f_1 and f_2 having focal lengths of 100 mm and 500 mm, respectively), then subsequently coupled into single mode fibers with a second $4f$ telescope (lenses f_3 and f_4 having focal lengths of 750 mm and 2 mm, respectively) and finally detected with avalanche photo-detectors (APDs). Signals from each arm were measured in coincidences within a 25 ns coincidence window. The entangled photons were filtered with 10 nm bandpass filters centered at a wavelength of 810 nm. For our experimental demonstration, we restrict our measurements to a specific optical setup and we varied the purity of the entangled state by introducing background noise in the form of white light. To obtain a high purity state (p=0.45 in K=22 dimensions), we had to reduce the laser power using an ND filter such as to reduce multi-photon emission events, known to have an impact on the purity of the SPDC photons [27]. To increase the noise in the system for the OAM basis measurements, we introduced background noise in the form of white light emitted by an incandescent light bulb until the quantum contrast (equivalently signal-to-noise ratio) dropped to 3. The measuremnt procedure of the quantum contrast is discussed in the appx. E.9.

6.3.3 Optimal purity and dimensionality calculation

Using the fact that the visibility obtained for each analyser is affected by the dimensionality and purity of the input state, we describe the procedure for determining their values for a given entangled quantum system, assuming it can be modelled by the isotropic state in Equation (E.29). We measure the probability curves for N

analysers each with $n = 1, 3, ..., 2N - 1$, and compute their corresponding visibilities $V_n := V_n(p, K)$. This results in a set of N nonlinear equations that depend on the parameters p and K. We then determine the optimal (p, K) pair that best fit the function $V_n(p, K)$ to all N measured visibilities by employing the method of least squares (LSF), which aims to minimise the objective function

$$\chi^2(p, K) = \sum_{i=1}^{N} |V_{2i-1}^{\text{The.}}(p, K) - V_{2i-1}^{\text{Exp.}}|^2, \tag{6.13}$$

where the terms in the summation are the residuals (absolute errors) for each $n = 2i - 1$ visibility measurement (Exp.) with respect to the theory (The.).

6.4 Results

6.4.1 Orbital angular momentum basis measurements

The set-up used to demonstrate our scheme is shown conceptually in Fig. 6-1 (d) with the corresponding detailed description in the Methods section. We measure the coincidences between the signal and idler photons for analyser projections on both arms as a function of the relative rotation angle of the holograms. To achieve this, we encoded the fractional OAM mode analyser on the SLM in the signal arm fixed at an angle $\theta = 0$, while the conjugate mode was encoded in the idler arm and rotated at angles $\theta \in [0, 2\pi]$.

To illustrate the operation of our technique we measured the coincidence-rates for six ($N = 6$) analysers with $n = 1, 3, 5, 7, 9$ and 11, and $M = n/2$, with example outcomes for $n = 5$ and 9 shown as filled circles in Fig. 6-2(a) and (b), respectively. No background subtraction was performed on the measurements to leave noise in the system, which was deliberately increased to enact a range in purities for test purposes. Importantly, the periodicity in the detected probabilities confirms the azimuthal n-fold symmetry predicted by our theory (solid curve). Because the visibility is a monotonically increasing function of dimension and purity, a measured visibility

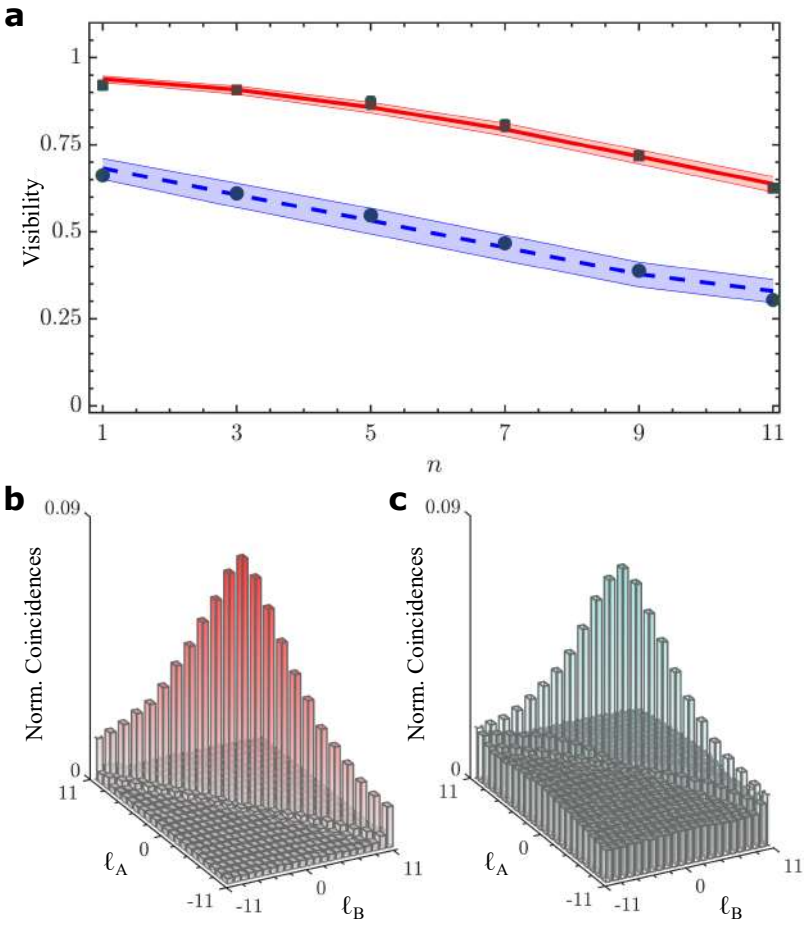


Figure 6-3: (a) Visibility measurements for low (top solid line) and high noise (bottom dashed line) levels. The points are the experimental visibilities while the lines correspond to the fitted values of dimension and purity. Measured spiral spectrum for the (b) low and (c) high noise levels. The shaded area corresponds to the uncertainty in the fit (standard deviation).

returns a range of possible (p, K) values, a "trajectory" or curve in the (p, K) space. This is illustrated in Fig. 6-2 (c) and (d), where the measured visibility (red horizontal plane) intercepts the visibility function along a curve (red curve) that restricts the possible solutions, K and p, to those consistent with the measurement outcome. The set of such curves from measuring many visibilities (each with its own analyser/projection) then restricts the final solution to a narrow region in (p, K), whose uncertainty (width) is determined primarily from the uncertainly in the visibility measurement. An example is shown in Fig. 6-2 (e), where each solution trajectory is projected onto the (p, K) plane. Final values and uncertainty of (p, K) can be determined by an appropriate routine to find the interception of all such trajectories by a minimisation procedure, as shown in Fig. 6-2 (f).

Using this approach we infer the purity and dimensionality of the system to be $(p, K) = (0.45 \pm 0.03, 22.84 \pm 0.62)$.

In Fig. 6-3 (a) we show the six measured visibilities as square data points together with the calculated visibility (solid red line) based on the inferred (p, K), which clearly match very well. This is confirmation of the minimisation procedure for finding the intercept. In order to assess the procedure under high noise levels, we introduced background noise using a white light source and repeated the measurements, shown as the circle data points and the associated blue dashed line in Fig. 6-3. The average quantum contrast (See appx. E.8), measured from the spiral spectrum in Fig. 6-3 (c) and (d), dropped from $Q = 19.19$ to $Q = 3.76$, resulting in a reduced purity and dimensionality of $(p, K) = (0.13 \pm 0.01, 17.73 \pm 0.71)$. Note that the minimisation was performed over the parameters (p, K), but additional parameters could also be added, for example, to take account of the modal cross-talk in the observed data. In our case, we choose the minimisation over a small set of parameters in order to keep the method and model simple.

As a form of validation of these results, we estimate values from other techniques, with the comparison given in Table E.1. If the dimension and noise are known or assumed, then it is possible to calculate the purity following $\hat{p} = (Q-1)/(Q-1+K)$ where Q is the quantum contrast and K the dimension [27]. Likewise, if the state is

Noise level	p	K	Q	$\hat{p}$	$\hat{K}$
low	0.45 ± 0.03	22.84 ± 0.62	19.19 ± 0.22	0.44 ± 0.01	22 ± 1
high	0.13 ± 0.01	17.73 ± 0.71	3.76 ± 0.57	0.13 ± 0.02	18 ± 1

Table 6.1: Measured purity (p) and dimensionality (K), under low and high noise levels, compared to estimates from other methods. Here Q is the average quantum contrast. Our experiment used a gating time of 25 ns for the coincidences with averaging over 10 s. Reduced the gating time, increasing the averaging time and taking care with the experimental conditions would significantly enhance the purities [42], even for the low noise conditions.

assumed to be pure and not mixed, and background subtraction is done to remove noise, then the spiral spectrum can be used to get an upper bound on the dimension. For the two noise cases in Table E.1, low and high, we find purity estimates of $\hat{p} \approx 0.44 \pm 0.01$ and $\hat{p} \approx 0.13 \pm 0.02$ from estimates of the dimensionality of $\hat{K} \approx 22 \pm 1$ and $\hat{K} \approx 18 \pm 1$, respectively. These values are in excellent agreement with our results, which did not require any such assumptions, nor any noise adjustments.

6.4.2 Pixel basis measurements.

To illustrate that OAM is only as an example and that the approach is general, we perform the same procedure using the pixel basis, shown in Fig. 6-4 (a). Here the spatial basis is position as "pixels" in the transverse plane, with the number of pixels setting the test dimension. The size and number would be judiciously chosen based on the source of biphotons and the imaging resolution of the optical system. We use grids from 3×3 up to 11×11, thus testing to over 100 dimensions. Holograms for three analyser cases are shown in Fig. 6-4 (b) for the 81 dimensional example, where the phases within the 9×9 pixel grid are shown to change. Although there is no resemblance to the prior OAM holograms, the measurement procedure is identical. From the resulting visibilities we again infer the key parameters from the intersection of the trajectories in (p, K) space, shown visually in Fig. 6-4 (c) and (d).

Our approach has the benefit of a wealth of information in the analyser visibilities, as well as knowledge of both K and p. This is sufficient to infer other key information (See Fig. E-7), such as an estimate of the state fidelity (F_p) and the Schmidt Rank, $d_{\text{ent}} = K \times F_p$ (See appx. E.10 and ref. [71]). We show the outcome for this

measurement in Fig. 6-4 (e), where the "effective dimensions" as measured by the Schmidt Rank decreases as the purity decreases, becoming separable below a critical value that corresponds to the separability boundaries shown in Fig. 6-2 (e) and (f). Our data is shown with deliberately introduced noise to reduce the purity, and juxtaposed with the case of background subtraction to eliminate the noise. Here we see that the Schmidt Rank gives a lower bound for the system. Our technique can detect correlations below the separability criterion for isotropic states, meaning that it is sensitive to correlations even in extreme noise situations, which may prove valuable in situations such as high resolution quantum imaging in real-world scenarios [347].

6.5 Discussion

A quantitative measure of dimensionality and purity, particularly in the presence of (inevitable) deleterious noise that degrades the purity, is crucial for many quantum protocols and studies. For example, there is a minimum purity needed to witness entanglement in a given dimension [2, 348, 349], setting the transition from separable to entangled states. Likewise, knowing the purity is important in entanglement distillation processes since it informs whether the noise can be removed for a given dimension [350, 351], while in entanglement based quantum communication there is a minimum purity [129] associated with security [352]. In turn, the dimensionality sets the information capacity of the state for quantum information processing and the error tolerance in quantum communication protocols, while high-dimensional states are important for fundamental tests of quantum mechanics where qubits will not suffice [353, 354]. Now we have demonstrated a simple approach to return these crucial numbers. Although this chapter is not a report on noise in high-dimensional quantum systems, we have deliberately introduce noise in order to demonstrate the robustness of the approach, and to attain a range in purities for test purposes. The impact of noise in realising pure high-dimensional quantum states is only beginning to emerge [34], revealing that the there are limits to the dimensionality that can

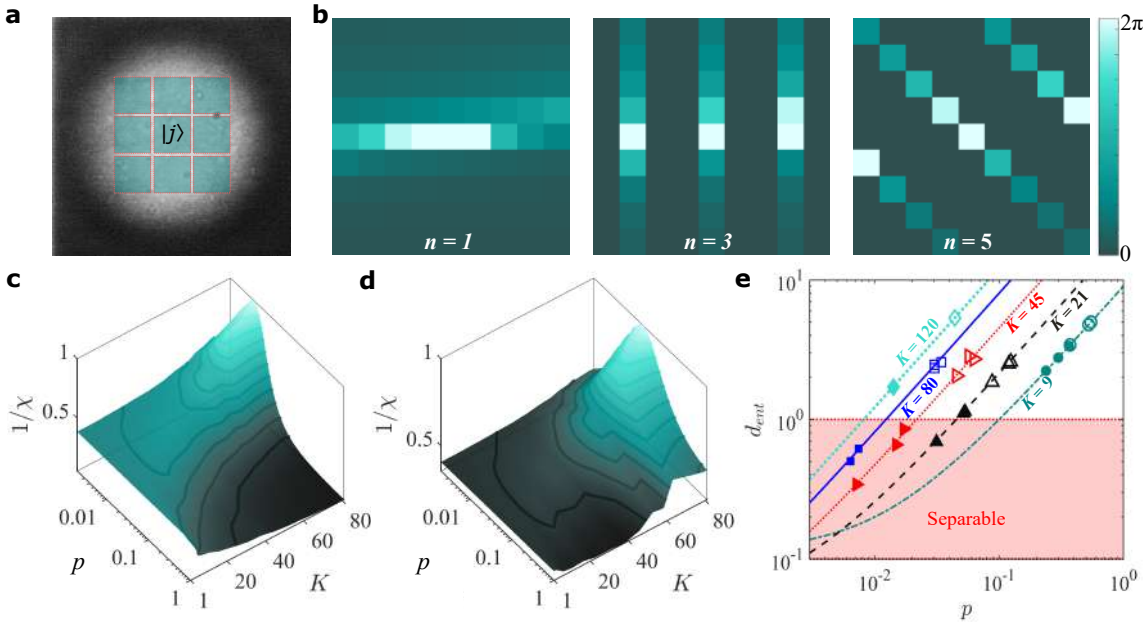


Figure 6-4: (a) The basis of our entanglement is expressed as pixels, illustrated here across the SPDC source (measured at the crystal), where each pixel is our state, $|j\rangle$. (b) Example holograms in this basis for the visibility measurements, shown here for $n = 1$, 3 and 5. (c) and (d) show the measurement outcomes for two example cases of dimension and purity, with and without background subtraction, respectively. All the measurements outcomes are plotted as data points in (e) showing the Schmidt Rank, d_{ent} as a function of purity, p, in excellent agreement with theory (lines). The dimensionality, K, is quoted for each case. Error bars are too small to be visualised.

be reached based on the quantum contrast and noise in the system. Our findings are entirely consistent with these reports. Although in the final test we have added noise (accidentals) subtraction to illustrated the juxtaposed position, this is strictly speaking not advisable [355].

Unlike a conventional Schmidt decomposition, we do not assume the state is pure, and the dimension extracted from our technique is conditioned on the presence of entanglement: a maximally mixed and maximally entangled system cannot yield the same result. While our approach would benefit from knowledge of the modal spectrum, which can be measured very quickly [356, 357], the outcome on purity and dimensionality are only modestly affected by typical spectrum shapes (See Fig. E-5), e.g., in our examples the uncertainty in dimensionality is $\approx 5\%$ with knowledge of the spectrum, increasing to $\approx 10\%$ without.

In addition to well-established quantum tomography tools, there are several new

methods for characterising, measuring, and extracting information about different quantum states [131,330,331]. Each method has its own set of pros and cons, regarding measurement time, the total number of required measurement settings, and the ease of implementation. The method that we present here complements the existing techniques, providing one of the fastest mechanisms to extract and estimate valuable information about high-dimensional entangled quantum states.

The advantage of our method is the linear scaling to the number of measurements and the flexibility of the minimisation procedure. Our approach is thus a excellent candidate for a fast and easy test of purity and dimensionality prior to a more lengthy tomography, if necessary. One of the limitations of our technique is that prior knowledge of the form of the underlying state is required for accurate fitting. Thus, we cannot provide definite proof of entanglement in an assumption-free manner.

However, the easy construction of our analysers and the resulting measurement of only visibilities reduces the complexity of characterising quantum states significantly when contrasted with QST based approaches. Finally, our measurement approach has been tested against the topical isotropic state, but we point out that the construction of the analyzers is not dependent on this state. This is analogous to other methods where extracting a measure always requires a target state, e.g., the fidelity from a QST measured against a maximally entangled state. We envisage that it may be possible to generalise the theory to extract key parameters from states other than just the isotropic state.

In summary, we have developed a simple yet powerful technique to measure the dimensionality and purity of high dimensional entangled photonic quantum systems. Our approach is robust, fast, and provides quantitative values rather than bounds or witnesses, and works on both pure and mixed states. Our scheme exploits visibility in fringes after joint projections, making it fast and easy to implement, returning the key parameters of the system in a fraction of the time that a QST would take. Thus we believe that our approach will be useful as a quick test with minimal experimental effort prior to more comprehensive state testing, valuable to the active research in high-dimensional spatial mode entanglement and foster its wide-spread deployment

in quantum based protocols.

Chapter 7

Conclusions

7.1 Concluding remarks

This thesis outlines techniques that may be crucial for future deployment of quantum channels that use high dimensional transverse spatial modes as a means to increasing the encoding capacity of quantum communication protocols. The focus was on developing techniques for overcoming channel perturbations that can distort the transverse spatial amplitude, phase and polarisation profiles of photons. The channel perturbations that were considered are solid obstructions, atmospheric turbulence, optical aberrations, mode mixing in optical fibres, and environmental noise. For this reason, the methods reported in this Thesis add on to the existing toolbox for transmitting, controlling and characterising photon fields in various media. Our approaches ranged from judiciously selecting mode families that are resilient to particular obstructions and perturbations or studying the evolution of spatially structured photons through typical optical aberrations and noise mechanisms and subsequently designing measurement procedures that revealed crucial information that can be used to remedy the deleterious effects of the medium under investigation.

To begin, in Chapter 1, we introduced high dimensional states of single and two photon states and highlighted the significance of higher dimensional encoding in contrast to traditional two qubits, showing that the encoding basis of photons can be expanded in two ways: i) by encoding the information in the transverse spatial pro-

file of photons and ii) by combining the spatial and polarisation degrees of freedom (DOF). In the final section, we discussed the deleterious effects of channel perturbations, highlighting the various techniques that are commonly used for mitigating them. Moreover, we presented some of the challenges that come with implementing them. This chapter sets the scene for the chapters that followed.

In Chapter 2, we introduced the first perturbation in the form of solid obstructions, acting on photons encoded using transverse spatial modes that carry orbital angular momentum (OAM). The obstructions were small micron-sized particles that partially blocked the path of a photon field, resulting in optical diffraction. We showed that a quantum channel having such pertubations, can result in photon loss and crosstalk [26] but by using photons with Bessel-Gaussian radial profiles we were able to harness their previously discovered resilience even at the single photon level [152]. The novelty on our approach came in using polarisation and the spatial DOF in nonseparable vector modes and their scalar counterparts to construct a secure communication channel. Another advancement made in this chapter was in utalising higher dimensional encoding with four dimensional basis states. We focused our analysis of the channel to the application of quantum key distribution showing that it is possible to exchange quantum information even when photons are partially obstructed. To show the benefit of our encoding technique we performed a similar analysis on modes with Laguerre-Gaussian spatial profiles, with our results clearly indicating that the BG vector modes perform far better in the presence of obstructions.

While our choice of the radial profile for our nonseparable vector fields made them immune to diffraction, there is another class pertubations that can completely distort the transverse spatial amplitude, phase and polarisation profiles of photons, namely channels with spatially varying refractive index profiles, e.g., turbulence and optical aberrations. In Chapter 3 and 4, we dealt with distortion of this kind. Initially, in 3, we showed that the nonseprability, equivilently entanglement, between the polarisation and spatial components of vector beams can be used as a tool for characterising photon fields that are perturbed by optical turbulence. To achieve this, we invoked the principle of channel state duality, a purely quantum mechanical feature that grants

maximally nonseparable vector fields the ability to map onto a state that contains all the channel dynamics. From this demonstration, we showed that a single vector mode is sufficient for predicting the decay of any other field in the same subspace by showing that the nonseparability of any field is determined by that of a maximally nonseparable vector beam. Although this work can reveal the decay dynamics of vectorial (and scalar) fields under any aberration that is unitary in nature, we also asked ourselves whether these fields even decay at all? This was motivated by the fact that entangled states are invariant under unitary transformations.

Indeed, in Chapter 4, we illustrated that this is true for vector modes since the phase dependent aberrations only perturbed the spatial components of the fields while the polarisation components were unaffected. But this is only true in the nearfield since a spatially dependent phase only pertubation transfers a global phase onto the field components. However, we showed that the phase distortions appeared to change the amplitude, phase and polarisation of the fields upon propagation although a basis independent measurement revealed that the spatial and polarisation components remained nonseparable. By using the fact that nonseparability and entanglement are equivalent, and that the unitary nature of the channel only causes a change of basis, we where able to show that the measurement and preparation procedure can be adjusted to undo the effects of the channel by invoking the channel state duality to find the basis that the channel maps the spatial components onto. Through this procedure we were able to recover all the information scattered by the channel and demonstrated its usefulness for encoding classical/quantum information over a scattering channel. This work brought classical or local entanglement, i.e. entanglement between the internal DOF of light, showcasing its practical significance to applications in both classical and quantum communication.

In the last two chapters we introduce truly non-local entangled systems and also devised technique for overcoming technical challenges in high dimensional encoding in the presence of deleterious effects that can inhibit their performance.

Accordingly, in Chapter 5 we demonstrated a new approach for transmitting multi-modal entanglement, for the first time, through a fiber that only supports one spatial

mode via a heterogeneous free-space and fiber network. Here, hybrid entanglement with nonlocal polarisation-spatial mode correlations was the main workhorse of our implementation. This work overcomes the challenge of transmitting spatial modes through optical fibers. The hybrid entangled states span infinite number of two-dimensional subspaces due to the high dimensional nature of the spatial DOF. The channel spanned over 250 m of fiber length which transmitted the polarisation qubits that were entangled to multiple spatial modes, showing that this scheme is a viable approach to circumvent the technological hurdles of deploying spatial mode entanglement through fiber channels, ushering in a new way of utalising multidimensional entangled photons in heterogeneous quantum channels that exploit a multi-level encoding basis.

While the method in Chapter 5 makes intelligent use of photons with independent properties to realise information encoding in a quantum channel, next we considered devising a robust technique that accurately characterises quantum entangled correlations so that the quality of the generated correlations are known. In Chapter 6, we developed a powerful technique for measuring the dimensionality and purity of high dimensional entangled photonic quantum systems that are encroached by white noise. In the procedure, a conditional measurement in the form of a visibility obtained from projective measurements with tailored superposition states, were used to extract information about the purity and dimensionality of two dimensional entangled photons. The visibilities scaled monotonically with increasing dimensions and purity showing that the visibility strongly depended on the number of linearly independent modes that constitute the state as well as the quality of the correlations. Our approach is robust, fast, and provides quantitative values. A key facet of our procedure is that it returned key parameters of the underlying state in a fraction of the time than what a QST would take, adding value to active research in high-dimensional spatial mode entanglement. This can be crucial in practical applications where noise can have a negative impact on the state and an initial estimations of the state is required.

7.2 Future work

The work presented in this Thesis presents several techniques for overcoming perturbations in quantum channels comprised of spatial and (or) polarisation states for single and two photon states, crucial for the transmission of photons through noisy freespace, underwater and optical fiber channels. The findings reported here add on to the toolbox for using structured quantum light [187] for quantum communication applications. Here, we highlight some of the aspects of the work that can be improved and expanded on in future work.

In future, we hope to explore the possibility of extracting complete information about a quantum channel using a single vectorial field and not just limit their use to performing an analysis for a small subset of modes. This kind of research is strongly linked with finding the eigenmodes of a quantum channel, i.e. the orthogonal eigenvectors that are invariant of the unitary operator representing the channel. While this in general is also related to quantum process tomography [132], it is interesting to ask whether a single vector mode can be used to retrieve the whole channel matrix instead of performing a complete tomography to retrieve it?

Another aspect of our work to consider expanding on is, again, related to tomography. In most state tomography procedures, the measurement are overcomplete and make no assumption about the underlying state although the models commonly used in maximum likelihood algorithms [89] assume a more general decomposition of the state. Our dimensionality and purity measurement (Chapter 6) technique is limited in this sense because the fitting procedure used assumes a specific model that does not cover a wide class of quantum states while the projective measurements also do not obeying fair sampling though they are very sensitive to the state dimensions as desired. Therefore, in future, we hope to generalise the method to various classes of quantum states while the projective measurements can also be improved by considering the use of positive operator-valued measurements (POVM) [118] that sample a larger portion of the Hilbert space. As is, the method only requires knowledge of the Schmidt basis expansion of the entangled state should work if the channel is unitary

and the change of basis mapping is known. It may also be interesting to use a hybrid approach that combines the use of vector modes to study the evolution of the channel while the dimensionality measurement procedure is employed for quantifying the dimensionality and purity of the entangled Schmidt basis modes.

Lastly, the multidimensional nature of the optical fiber based hybrid channel that was presented in Chapter 5 enables for the transmission of independent hybrid states across a single mode fiber channel, it however does not produce high dimensional superposition states beyond qubits. We may consider replacing the spin-orbit coupling effect with another optic that can couple the OAM to an alternative DOF that is also high dimensional in nature. For example, such a transformation can be achieved using a mode sorter [60] which can convert the OAM states to path states. Once each OAM state is converted to path, it can be coupled to a multicore single mode fibre and recombined afterwards. As such, the channel will be able to transmit true higher dimensional states while benefiting from utalising coupled DOF and conventional single mode optical fibers that can span long distances.

Appendix A

Scattering probability of OAM in turbulence

The detection probability of an OAM beam propagated through turbulence can computed from

$$P(l,m) = \iint C_\psi(r,\Delta\theta,z) r dr \times \frac{\exp(-im\Delta\theta)}{2\pi} d\Delta\theta, \tag{A.1}$$

where ℓ is the input OAM index of the beam, and m is the index for the scattered mode, while $C_\psi\left(r,\Delta\theta,z\right)$ is the rotational coherence function defined in the cylindrical coordinates, (r,θ,z) defined as [24]

$$C_\psi(r,\Delta\theta,z) = \langle \psi^*(r,0,z)\psi(r,\Delta\theta,z) | \psi^*(r,0,z)\psi(r,\Delta\theta,z) \rangle \,. \tag{A.2}$$

Here $\psi(r,\theta,z) = u(r,\theta,z)\exp(i\phi(r,\theta))$ is the beam profile after propagating a distance z with an initial profile of $u(r,\theta,0)$ at the waist plane and $\exp(i\phi(r,\theta))$ is the accumulated phase according to the Rytov approximation.

For LG beams, the integral in Eq. (A.1) has been solved analytically, yielding the

in the expression [237]

$$P(l,m) = (\frac{1}{t})^{|\ell|+1}\left(\frac{t-1}{t+1}\right)^{n}\sum_{k=0}^{|\ell|}\binom{|\ell|+n}{k} \times \binom{2|\ell|-k}{\ell}\binom{4t}{(t-1)^2}^{k-|\ell|} \tag{A.3}$$

where $n = |\ell - m|$, $t = \sqrt{1+\zeta}$ while $\zeta = 3.44 \times 2^{2/3}(w_0/r_0)^2$ where w_0 is the is the waist size of the Gaussian argument in the LG mode and r_0 is the Fried parameter. We re-scaled the Gaussian argument, i.e. $w_\ell = w_0/\sqrt{|\ell|+1}$, so that each OAM mode has the same diameter, $D := \sqrt{8}w_\ell$ [214] and turbulence strength, D/r_0.

Appendix B

Synthesis of turbulence

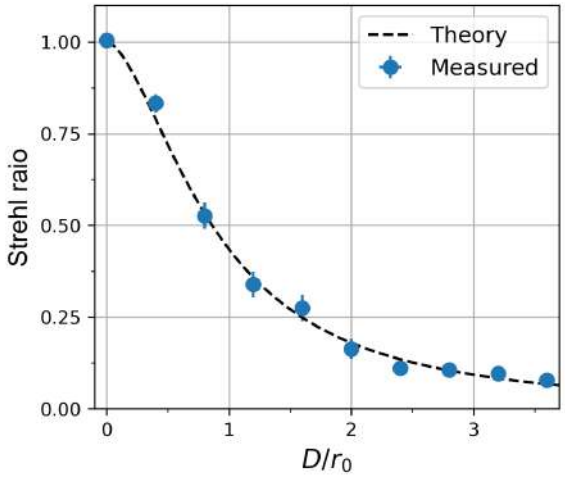


Figure B-1: The Strehl ratio (SR) for increasing turbulence strength D/r_0. Theoretical (programmed) values are plotted as a solid line and experimentally measured points are represented as blue markers.

We model turbulence as a random phase screen Θ that captures the refractive index variations in the atmosphere. The statistics of such a screen are well known. Two useful characterisations of Θ are the phase structure function, defined as

$$D(\bar{\mathbf{r}}) = \left\langle |\Theta(\bar{\mathbf{r}}' + \bar{\mathbf{r}}) - \Theta(\bar{\mathbf{r}}')|^2 \right\rangle, \tag{B.1}$$

and the Weiner spectrum Φ which is related to $D(\overline{\mathbf{r}})$ by

$$D(\overline{\mathbf{r}}) = 2\int \mathrm{d}^2\mathbf{k}\ \Phi(\mathbf{k})[1-\cos(2\pi\mathbf{k}\cdot\overline{\mathbf{r}})], \tag{B.2}$$

where $\langle\cdot\rangle$ denotes the ensemble average. In the Kolmogorov model, these expressions are

$$D(\overline{\mathbf{r}}) = 6.88\left(\frac{\|\overline{\mathbf{r}}\|}{r_0}\right)^{5/3}, \tag{B.3}$$

and

$$\Phi(\mathbf{k}) = \frac{0.023}{r_0^{5/3}}\|\mathbf{k}\|^{-11/3}, \tag{B.4}$$

where r_0 is the Fried parameter [358]. These quantities, which are taken over many iterations of Θ, are not the same as Θ itself, which is a random variable, or its equally random power spectrum

$$P(\mathbf{k}) = \mathcal{F}\{\Theta\} = \int \mathrm{d}^2\overline{\mathbf{r}}\ \Theta \exp\left(-i2\pi\mathbf{k}\cdot\overline{\mathbf{r}}\right), \tag{B.5}$$

where $\mathcal{F}$ denotes the Fourier transform. In fact, $\Phi(\mathbf{k})$ is the covariance function of $P(\mathbf{k})$. To simulate a turbulent screen Θ, a matrix of random values must be generated whose statistics match Eq. B.3 and Eq. B.4. If we could find $P(\mathbf{k})$, we could extract Θ using the inverse Fourier transform. We sample $P(\mathbf{k})$ from a random distribution with zero mean and variance equal to $\Phi(\mathbf{k})$. Such a method [359] samples the Kolmogorov Weiner spectrum over a square grid of $N \times N$ points with indices (i, j) as

$$\Phi(i,j) = 0.023\left(\frac{2D}{r_0}\right)^{5/3}(i^2+j^2)^{-11/3}, \tag{B.6}$$

where D is the length of the aperture over which we are considering Θ. We would then multiply $\sqrt{\Phi}$ by a matrix $\mathbf{M}$ of random, complex values with zero mean and variance 1, giving us an instance of $P(\mathbf{k})$, and inverse Fourier transform the resultant matrix to produce the phase screen Θ. However, this does not properly describe the $\|\mathbf{k}\|^{-11/3}$ behaviour since the smallest sampled frequency is $1/D$. Frequencies with periods greater than D (corresponding to indices smaller than 1) are thus not included. To

counteract this, subharmonic terms must be included by evaluating Φ at frequencies whose periods are greater than D and multiplying by a weighting factor which takes into account the fractional sampling contribution. Taking the real component only gives

$$\Theta = \Re\{\mathcal{F}^{-1}\{\mathbf{M}\sqrt{\Phi}\}\} \tag{B.7}$$

where Φ includes the subharmonic contributions.

The phase screens must be calibrated to ensure that their turbulence strength is consistent with the programmed value of D/r_0. The Strehl ratio (SR) provides a convenient link between measured intensities and turbulence strength D/r_0. It is defined as the ratio of the average on axis intensity with, $\langle I(\mathbf{0})\rangle$, and without, $I_0(\mathbf{0})$, turbulence. For a plane wave in Kolmogorov theory it is

$$\mathrm{SR} = \frac{\langle I(\mathbf{0})\rangle}{I_0(\mathbf{0})} \approx \frac{1}{\left(1 + (D/r_0)^{5/3}\right)^{6/5}}. \tag{B.8}$$

Experimentally, one would calculate the SR for a range of turbulence strengths D/r_0 while adjusting the parameter D of the phase screens so that the measured $(\langle I(\mathbf{0})\rangle / I_0(\mathbf{0}))$ and programmed values agree. Fig. B-1 shows such a calibration curve, where the solid line represents the theoretical (programmed) strength and the markers denote experimentally measured values.

Appendix C

Supplementary material: invariant vectorial photon fields

C.1 Transmitting vector beams through unitary single sided channels

Suppose we have a vector beam that we would like to transmit through a single sided channel, $\mathbb{1}_A \otimes T_B$, where $\mathbb{1}_B$ is the identity matrix while T_B is a unitary operator, i.e., $T_B^\dagger = T_B^{-1}$. The subscripts A, B refer to the polarization and spatial degrees of freedom respectively. Such channels are known to be completely postive mappings and are trace preserving [121]. We can define our vector mode in a compact manner using Dirac notation

$$|\Psi\rangle = |e_1\rangle_A |u_1\rangle_B + |e_2\rangle_A |u_2\rangle_B \,, \tag{C.1}$$

where the spatial components $\{|u_1\rangle$ and $|u_2\rangle\}$ are orthogonal. In the basis, $\{|j\rangle \,, j = 1, 2, ..d\}$, we can express the spatial components of $|\Psi\rangle$ as

$$|u_1\rangle = \sum_j \alpha_j |j\rangle \,, \tag{C.2}$$

and

$$|u_2\rangle = \sum_j \beta_j |j\rangle . \tag{C.3}$$

Here α_j and β_j are the expansion coefficients of u_{12}, respectively. We can also express T_B in our chosen basis $\{|j\rangle\}$:

$$T_B = \sum_{jn} \tau_{jn} |n\rangle \langle j| , \tag{C.4}$$

where the channel maps any state $|j\rangle_B$ onto to the state $\sum_n \tau_{jn} |n\rangle$ with coefficients τ_{jn}, having the property that $\sum_n (\tau_{in})^* \tau_{nj} = \delta_{ij}$, due to the unitary nature of T_B.

Upon transferring $|\Psi\rangle$ through the channel, the spatial components become

$$\begin{aligned} |v_1\rangle &= \sum_j \alpha_j \sum_n \tau_{jn} |n\rangle , \\ &= \sum_n \sum_j (\alpha_j \tau_{jn}) |n\rangle , \\ &= \sum_n \alpha'_n |n\rangle , \end{aligned} \tag{C.5}$$

and

$$\begin{aligned} |v_2\rangle &= \sum_j \beta_j \sum_m \tau_{jm} |m\rangle , \\ &= \sum_m \sum_j (\beta_j \tau_{jm}) |m\rangle , \\ &= \sum_m \beta'_m |m\rangle . \end{aligned} \tag{C.6}$$

Consequently, after the channel, $|\Psi\rangle$ is mapped onto to the state

$$|\Psi\rangle_{\text{out}} = |e_1\rangle_A |v_1\rangle_B + |e_2\rangle_A |v_2\rangle_B . \tag{C.7}$$

The expansion coefficients of the spatial components can be extracted via modal decomposition on each independent polarisation state.

Importantly, the spatial components remain orthogonal: $\langle v_1|v_2\rangle = \langle v_1| T_B^\dagger T_B |u_2\rangle = \langle u_1|u_2\rangle = 0$.

C.2 Nonseparability of the transformed vector mode

The nonseparability or vector quality factor [360] of a vector beam can range from 0 to 1, for scalar fields (separable) and for completely nonseparable vector beams, respectively. For the vector beam in Eq. (C.7), the nonseparability will remain 1 provided the final projections are performed in the new basis $\left|u'_{1,2}\right\rangle$. However when projected back into the initial basis, the vector modes in Eq. (C.1) can be mapped onto

$$\begin{aligned} |\Phi_\ell\rangle = a\,|e_1\rangle_A\,|u_1\rangle_B + b\,|e_1\rangle_A\,|u_2\rangle_B \\ + c\,|e_2\rangle_A\,|u_1\rangle_B + d\,|e_2\rangle_A\,|u_2\rangle_B\,, \end{aligned} \tag{C.8}$$

with a corresponding degree of nonseparability

$$\mathrm{V} = |ad - cb|, \tag{C.9}$$

assuming the coefficients satisfy, $(|a|^2 + |b|^2 + |c|^2 + |d|^2) = 1$. When the modes are completely scattered, then $a = b = c = d = 1/2$ and hence $V = 0$. This means that the nonseparability will decay if the state is measured in the initial subspace. Otherwise, if there is no modal scattering then $a = b$ while $cb = 0$, therefore the VQF is 1.

We can show this with the tilted lens channel, where performing the measurements for $\ell = \pm 1$ and $\ell = \pm 4$ (now in basis $|v_{1,2}\rangle$) using the old basis ($|u_{1,2}\rangle$), is a form of post-selection onto the state $|\Psi_{out}\rangle = c_1\,|R\rangle\,|u_1\rangle + c_2\,|R\rangle\,|u_2\rangle + c_3\,|L\rangle\,|u_1\rangle + c_4\,|L\rangle\,|u_2\rangle$ with a resulting V that can be estimated from $2|c_1c_4 - c_2b_3|$. The scattering coefficients can be computed as $c_1 = \langle u_1|v_1\rangle$, $c_2 = \langle u_2|v_1\rangle$, $c_3 = \langle u_1|v_2\rangle$ and $c_4 = \langle u_2|v_2\rangle$. For the

Subspace	c_1	c_2	c_3	c_4	V
$\ell = \pm 1$ $(u_{1,2})$	1/2	i/2	1/2	-i/2	1
$\ell = \pm 1$ $(v_{1,2})$	1/2	0	0	1/1	1
$\ell = \pm 4$ $(u_{1,2})$	1/2	1/2	1/2	1/2	0
$\ell = \pm 4$ $(v_{1,2})$	1/2	0	0	1/2	1

Table C.1: **Impact of selecting the measurement subspace**. The theoretical scattering complex coefficients for tilted lens and resulting vectorness (V) from measurements in the incorrect ($u_{1,2}$) and correct ($v_{1,2}$) subspace for $\ell = \pm 1(4)$. In each case, the VQF is computed from $2|c_1c_4 - c_2c_3|$.

titled lens, the coefficients are shown in Table C.1 where the overlap was performed. Expressions of $|u_{1,2}\rangle$ and $|u_{1,2}\rangle$ for the tilted lens can be found in the Supplementary material in terms of the HG basis. As expected, the $\ell = \pm 1$ V does no change since the mapping is within the same subspace, consistent with the experimental plots in Fig. 1(a). In contrast, $\ell = \pm 4$ has vectorness values of 0 and 1 for the incorrect and correct measurement subspace, respectively, reaffirming our experimental results.

C.3 Undoing the effects of the channel

We have now seen that a vector beam $|\Psi\rangle$, interacting with the unitary channel, $\mathbb{1}_A \otimes T_B$, maps onto a new vector beam $|\Psi\rangle_{\text{out}}$. Here we show that we can recover the vector beam $|\Psi\rangle$ by probing the channel a with a probe state $|\Psi\rangle_{\text{probe}}$ and later using it's modal content to prepare a new vector beam $|\Phi\rangle$ which will then be converted to $|\Psi\rangle$, our target mode, upon traversing the channel.

To achieve this we first send in a probe state

$$|\Psi\rangle_{\text{probe}} = |e_1\rangle_A \sum_j \alpha_j^* |j\rangle_B + |e_2\rangle_A \sum_j \beta_j^* |j\rangle_B \,, \tag{C.10}$$

that is encoded with the complex conjugated coefficients of $|\Psi\rangle$, through the channel. After undergoing the channel the probe state is mapped to

$$|\Psi\rangle_{\text{probe}} \xrightarrow{\mathbb{1}_A \otimes T_B} |e_1\rangle_A \sum_{jn} \alpha_j^* \tau_{jn} |n\rangle_B + |e_2\rangle_A \sum_{jm} \beta_j^* \tau_{jm} |m\rangle_B . \tag{C.11}$$

The coefficients of the modal expansion in each field can be measured via modal decomposition. Using the extracted coefficients, we can then send the new mode

$$|\Phi\rangle = |e_1\rangle_A \left|u_1^{'}\right\rangle_B + |e_2\rangle_A \left|u_2^{'}\right\rangle_B , \tag{C.12}$$

$$= |e_1\rangle_A \sum_{jn} \alpha_j \tau_{nj}^* |n\rangle_B + |e_2\rangle_A \sum_{jm} \beta_j \tau_{mj}^* |m\rangle_B , \tag{C.13}$$

through the channel. Here $|\Phi\rangle$ has the conjugated coefficients of probe state after interacting with channel which are in-fact the coefficients of our desire target state $|\Psi\rangle$ coupled with the scattering coefficients from the channel. To see that $|\Phi\rangle$ maps to the target state $|\Psi\rangle$ after traversing the channel, we can observe the evolution of, $|v_{12}\rangle$:

$$\begin{aligned} T_B \left|u_1^{'}\right\rangle &= \sum_{jn} \alpha_j \tau_{jn}^* T_B |n\rangle , \\ &= \sum_{jnk} \alpha_j \tau_{jn}^* \tau_{nk} |k\rangle , \\ &= \sum_{jk} \alpha_j \sum_{n} \tau_{jn}^* \tau_{nk} |k\rangle , \\ &= \sum_{jk} \alpha_j \delta_{jk} |k\rangle , \qquad \text{(C.14)} \\ &= \sum_{j} \alpha_j |j\rangle \qquad \text{(C.15)} \\ &= |u_1\rangle . \qquad \text{(C.16)} \end{aligned}$$

Similarly, $\left|u_2^{'}\right\rangle$, maps onto

$$T_B \left|u_2^{'}\right\rangle = \sum_j \beta_j \left|j\right\rangle , \\ = \left|u_2\right\rangle . \tag{C.17}$$

This gives us the spatial components of $|\Psi\rangle$, as desired.

C.4 Examples with a titled lens

Vector beams can be used to imprint information about a spatially dependent perturbation. If the channel is unitary and single sided, then the spatial information can be imprinted on the polarisation field. The following steps show how one can obtain the transformation corresponding to a unitary channel via the polarisation pattern of vector beam and maybe also undo the evolution.

Suppose we have a vector beam given by

$$\left|\psi\right\rangle_{\text{in}} = \left|R\right\rangle_A \left|\ell\right\rangle_B + \left|L\right\rangle_A \left|-\ell\right\rangle_B , \tag{C.18}$$

that is prepared in the right (R) and left (L) circular polarisation basis and the OAM spatial basis characterised by eigenstates with indices $\pm\ell$. This vector beam can be found on the Higher order Poincaré Sphere (HoPS) spanned by the basis modes $\{ \left|R\right\rangle_A \left|\ell\right\rangle_B , \left|L\right\rangle_A \left|-\ell\right\rangle_B \}$

When transmitted through a unitary and single sided channel, the OAM modes can scatter the spatial components into arbitrary ℓ's, but what remains is that the mode still remains a vector beam due to the invariance of nonseparability to unitary transformations. Since the vector beam can map the channel, we will show that this information can be used to make corrections on the beam with a simple unitary transformation. Lets see an example with a transformation that only induces transitions on a qubit space.

Consider the case where $\ell = \pm 1$ for our vector beam. The unitary mapping follows

$$|\ell\rangle \xrightarrow{T_B} \frac{|\ell\rangle + i\,|-\ell\rangle}{\sqrt{2}} \tag{C.19}$$

$$|-\ell\rangle \xrightarrow{T_B} \frac{|\ell\rangle - i\,|-\ell\rangle}{\sqrt{2}} \tag{C.20}$$

mapping the spatial components onto another set of orthogonal modes. This can be performed using a titled lens. Once the vector beam interacts with the lens and is subsequently propagated to the far-field, it evolves into the state

$$|\psi\rangle_{\text{out}} = |R\rangle_A \left(\frac{|\ell\rangle_B + i\,|-\ell\rangle_B}{\sqrt{2}}\right) + |L\rangle_A \left(\frac{|\ell\rangle_B - i\,|-\ell\rangle_B}{\sqrt{2}}\right), \tag{C.21}$$

which is still nonseparable since the spatial components are orthogonal. All that the unitary transformation did was to perform a change of basis in the spatial components. With further manipulation, we arrive at

$$|\psi\rangle_{\text{out}} = \left(\frac{|R\rangle_A + |L\rangle_A}{\sqrt{2}}\right)|\ell\rangle_B + i\left(\frac{|R\rangle_A - |L\rangle_A}{\sqrt{2}}\right)|-\ell\rangle_B, \tag{C.22}$$

$$= |H\rangle_A\,|\ell\rangle_B + |V\rangle_A\,|-\ell\rangle_B\,. \tag{C.23}$$

which resembles the original mode except that the OAM components are now marked by the horizontal ($|H\rangle_A$) and vertical ($|V\rangle_A$) states. We see that the channel performed a simple change of basis in the spatial components which affects the polarisation field therefore mapping us onto a new HoPs sphere that is spanned by $\{\,|H\rangle_A\,|\ell\rangle_B$, $|V\rangle_A\,|-\ell\rangle_B\,\}$. Moreover, for this specific case, the relative phases between the spatial coordinates were transferred to the polarisation components.

To obtain the original state, $|\psi\rangle_{\text{in}}$, we simply need to apply a unitary transformation, $\hat{U} = T_B^{\dagger}$, so that

$$|\psi\rangle_{\text{in}} = \hat{U}\,|\psi\rangle_{\text{out}}\,. \tag{C.24}$$

Therefore cancelling out the effect of the channel.

For our example, a quarter-wave plate at an angle of $\theta = 45^\circ$ maps the polarisation field back to its original state. This is possible because the relative phase between the spatial modes was uniform. In general the polarisation mapping can be spatially dependent.

Alternatively, since the unitary maps the initial spatial modes basis to a new one, we can use the new modes in the detection system. For example, if we start with the mode

$$|\psi\rangle_{\text{in}} = |R\rangle_A |\ell\rangle_B + |L\rangle_A |-\ell\rangle_B \,, \tag{C.25}$$

, and send it through the channel T_B, we arrive at the new mode

$$|\psi\rangle_{\text{out}} = |R\rangle_A |\chi_1\rangle_B + |L\rangle_A |\chi_2\rangle_B \,. \tag{C.26}$$

where $T_B |\pm\ell\rangle_B = |\chi_{1,2}\rangle_B$ are the transformed basis modes. In the next sections we describe how the LG modes can generally be mapped onto new modes with the titled lens.

C.5 Titled lens mapping

Following [361], the decomposition of LG modes into HG modes can be written as

$$\text{LG}_{n,m}(x,y,z) = \sum_{N}^{k=0} i^k b(n,m,k) \text{HG}_{N-k,k}(x,y,z) \tag{C.27}$$

where $l = n - m$, $p = \min(n,m)$ and $b(n,m,k)$ is given by

$$b(n,m,k) = \left(\frac{(N-k)!k!}{2^N n!m!}\right)^{1/2} \frac{1}{k!} \frac{\mathrm{d}^k}{\mathrm{d}t^k} \left[(1-t)^n (1+t)^m\right]_{t=0} \quad . \tag{C.28}$$

The same b coefficients are also present when an HG mode is decomposed into

LG_p^l	HG modes decomposition
0,0	$HG_{0,0}$
0,1	$\frac{1}{\sqrt{2}}HG_{1,0} + \frac{i}{\sqrt{2}}HG_{0,1}$
0,-1	$\frac{1}{\sqrt{2}}HG_{1,0} - \frac{i}{\sqrt{2}}HG_{0,1}$
0,2	$-\frac{1}{2}HG_{0,2} + \frac{i}{\sqrt{2}}HG_{1,1} + \frac{1}{2}HG_{2,0}$
0,-2	$-\frac{1}{2}HG_{0,2} - \frac{i}{\sqrt{2}}HG_{1,1} + \frac{1}{2}HG_{2,0}$
0,4	$\frac{1}{4}HG_{0,4} - \frac{1}{2}iHG_{1,3} - \frac{1}{2}\sqrt{\frac{3}{2}}HG_{2,2} + \frac{1}{2}iHG_{3,1} + \frac{1}{4}HG_{4,0}$
0,-4	$\frac{1}{4}HG_{0,4} + \frac{1}{2}iHG_{1,3} - \frac{1}{2}\sqrt{\frac{3}{2}}HG_{2,2} - \frac{1}{2}iHG_{3,1} + \frac{1}{4}HG_{4,0}$

Table C.2: Decomposition of LG modes into HG modes.

HG modes at 45^o as in

$$HG_{n,m}(\frac{x+y}{\sqrt{2}}, \frac{x-y}{\sqrt{2}}, z) = \sum_{N}^{k=0} b(n,m,k)HG_{N-k,k}(x,y,z). \tag{C.29}$$

Intuitively, converting an LG into an HG mode is a question of rephasing modes. This is possible by exploiting the Gouy phase through a cylindrical lens. By using a lens with different focal lengths for two axis, i.e. astigmatic, it is possible to change the Rayleigh length of two coordinates independently, thus adding a relative phase to modes of a given geometry. It means that it is not possible to convert any mode in any direction, the nodal lines have to be parallel to the axes of the astigmatism. The HG modes are a suitable basis because they are completely separable in the direction of the astigmatism.

At the conversion plane, the cylindrical lens gives a $\pi/2$ phase between each HG mode that composes the input LG mode. In this sense, the action of the tilted lens in a given LG mode can be seen as:

$$LG_p^l(x,y,z) \rightarrow \sum_{k=0}^{N} b(l+p,p,k)HG_{N-k,k}(x,y,z) \tag{C.30}$$

for $l > 0$ and

$$LG_p^l(x,y,z) \rightarrow \sum_{k=0}^{N} b(p,p-l,k)HG_{N-k,k}(x,y,z) \tag{C.31}$$

otherwise.

LG_p^l	HG modes after conversion
0,0	$HG_{0,0}$
0,1	$\frac{1}{\sqrt{2}}HG_{1,0} + \frac{1}{\sqrt{2}}HG_{0,1}$
0,-1	$\frac{1}{\sqrt{2}}HG_{1,0} - \frac{1}{\sqrt{2}}HG_{0,1}$
0,2	$\frac{1}{2}HG_{0,2} + \frac{1}{\sqrt{2}}HG_{1,1} + \frac{1}{2}HG_{2,0}$
0,-2	$\frac{1}{2}HG_{0,2} - \frac{1}{\sqrt{2}}HG_{1,1} + \frac{1}{2}HG_{2,0}$
0,4	$\frac{1}{4}HG_{0,4} + \frac{1}{2}HG_{1,3} + \frac{1}{2}\sqrt{\frac{3}{2}}HG_{2,2} + \frac{1}{2}HG_{3,1} + \frac{1}{4}HG_{4,0}$
0,-4	$\frac{1}{4}HG_{0,4} - \frac{1}{2}HG_{1,3} + \frac{1}{2}\sqrt{\frac{3}{2}}HG_{2,2} - \frac{1}{2}HG_{3,1} + \frac{1}{4}HG_{4,0}$

Table C.3: Modal decomposition of LG after a tilted lens transformation.

Alternatively, as described in [362], this astigmatic mode converter can be seen as a unitary transformation in each mode order subspace. The definition in terms of HG modes, which are the eigenstates of this transformation, is given by:

$$L_D = \sum_{m=0}^{D-1} e^{i(m-n)\frac{\pi}{4}} \left|HG_{m,n}\right\rangle \left\langle HG_{m,n}\right| \tag{C.32}$$

where $D = N+1$ is the dimension of the subspace of the input mode and $n = D-m-1$.

C.5.1 Wave optics description

Following ref [275], the ray transfer matrix for the tilted lens $\mathbf{M}_{TL}$ is given by:

$$\mathbf{M}_{TL} = \mathbf{M}_z \mathbf{M}_{lens} \mathbf{M}_{z_0} = \begin{pmatrix} \mathbf{A} & \mathbf{B} \\ -\mathbf{C}/f & \mathbf{D} \end{pmatrix} \tag{C.33}$$

where $\mathbf{A}$, $\mathbf{B}$, $\mathbf{C}$, $\mathbf{D}$ are 2×2 diagonal matrices whose elements are $c_1 = \sec\theta$, $c_2 = \cos\theta$, $a_j = 1 - zc_j/f$, $d_j = 1 - z_0 c/f$ and $b_j = z_0 + zd$ for $j = 1, 2$. The matrices M_{z_0} and M_z describe free space propagation before and after the lens by distances z_0 and z respectively. M_{lens} describes a lens rotated around the y axis (vertical) by an angle θ. How a ray matrix is interpreted as a transfer function can be found in [363].

From the generalized Huygens-Fresnel integral, an electric field that propagates

through this optical element is given by

$$\begin{aligned} E_2(x_2, y_2) =& \frac{i/\lambda}{|B|^{1/2}} \iint \mathrm{d}x\mathrm{d}y E_1(x_1, y_1) \\ & \times \exp\left[\frac{-(i\pi)}{\lambda}\phi(x_1, x_2, y_1, y_2)\right] \end{aligned} \tag{C.34}$$

where $|B|$ is the determinant of $\mathbf{B}$ and

$$\begin{aligned} \phi(x_1, x_2, y_1, y_2) =& x_1^2 a_1/b_1 + y^2 a_2/b_2 + x_2^2 d_1/b_1 + y_2^2 d_2/b_2 \\ & - 2(x_1 x_2/b_1 + y_1 y_2/b_2) \end{aligned} \tag{C.35}$$

is the applied phase.

C.6 Basis dependent and basis independent non-separability measurements

A classical vector light field represents a hybrid-entanglement system, where the polarization and spatial mode degrees of freedom (DoFs) are non-separable. Since our one sided channel only affects the spatial mode DoF it is expected that a spatial mode basis dependent non-separability measurement should be affected by the channel while a basis independent measurement should remain invariant. We have show that the mode dependent non-separability is recoverable if the spatial mode basis is appropriately chosen. This is an important development as it allows for the recovery of mode dependent quantum correlations across such channels [274]. In this section we will outline the basis independent non-separability measurement based on Stokes intensity projections as well as the basis dependent non-separability measurement based on spatial mode projections of orthogonally polarized components - both of which are based on the quantum mechanical concept of concurrence.

C.6.1 Basis independent non-separability

Consider a vector field of the form

$$|\Psi\rangle = |H\rangle_A |\psi_H\rangle_B + |V\rangle_A |\psi_V\rangle_B \tag{C.36}$$

where $|\psi_{H,V}\rangle_B$ are arbitrary unnormalized spatial modes. We can then expand the spatial modes into some orthonormal two dimensional basis set $|\psi_\pm\rangle_B$, giving the general form

$$\begin{aligned} |\Psi\rangle = a|H\rangle_A|\psi_+\rangle_B + b|H\rangle_A|\psi_-\rangle|_B \\ + c|V\rangle_A|\psi_+\rangle_B + d|V\rangle_A|\psi_-\rangle|_B. \end{aligned} \tag{C.37}$$

This state has a concurrence given by $C(|\Psi\rangle) = 2|ad-bc|$. By selecting a negligible global phase, we can express the orthonormal states as [209]

$$|\psi_\pm\rangle = \frac{1}{\sqrt{2(1 \pm \langle\tilde{\psi}_H|\tilde{\psi}_V\rangle)}}(|\tilde{\psi}_H\rangle \pm |\tilde{\psi}_V\rangle), \tag{C.38}$$

where $|\tilde{\psi}_{H,V}\rangle = |\psi_{H,V}\rangle/\langle\psi_{H,V}|\psi_{H,V}\rangle$. This gives a concurrence $C(|\Psi\rangle) = 2\sqrt{\langle\psi_H|\psi_H\rangle\langle\psi_V|\psi_V\rangle - |\langle\psi_H|\psi_V}$ Since we now have the concurrence expressed in terms of the initial arbitrary unnormalized spatial components we can use the spatially varying Stokes parameters $S_i'(\mathbf{r})$ ($\mathbf{r}$ being the rtansverse spatial coordinates), to retrieve the degree of non-separability using the global Stokes parameters, $S_i = \int \mathrm{d}^2\mathbf{r}\, S_i'$, by exploiting the following relationships:

$$S_0 = \langle\psi_H|\psi_H\rangle + \langle\psi_V|\psi_V\rangle, \tag{C.39}$$

$$S_1 = \langle\psi_H|\psi_H\rangle - \langle\psi_V|\psi_V\rangle, \tag{C.40}$$

$$S_2 = \langle\psi_H|\psi_V\rangle + \langle\psi_V|\psi_H\rangle, \tag{C.41}$$

$$S_3 = i(\langle\psi_H|\psi_V\rangle - \langle\psi_V|\psi_H\rangle), \tag{C.42}$$

This convenient result allows us to determine the non-separability in a basis independent manner according to $C(|\Psi\rangle) = \sqrt{1 - (S_1^2 + S_2^2 + S_3^2)/S_0^2}$. In this work the

Stokes parameters were determined (for convenience) by the measurement of the reduced set of four Stokes intensities (I_H, I_D, I_R and I_L), where $I_i = \langle\psi_i|\psi_i\rangle$) - according to

$$S_0 = I_R + I_L, \tag{C.43}$$

$$S_1 = 2I_H - S_0, \tag{C.44}$$

$$S_2 = 2I_D - S_0, \tag{C.45}$$

$$S_3 = I_R - I_L. \tag{C.46}$$

The four intensity projections were acquired through the use of a linear polarizer (for I_H and I_D) together with a quater-wave plate (for I_R and I_L) [211].

C.6.2 Basis dependent non-separability

Consider a vector field of the form

$$|\Psi\rangle = |H\rangle_A |\psi_H\rangle_B + |V\rangle_A |\psi_V\rangle_B . \tag{C.47}$$

The concurrence can be determined from $C(\Psi) = \sqrt{1 - s^2}$ where s is the length of the vector when maps the state to a Bloch sphere defined by a chosen orthogonal set of orthonormal basis spatial modes $|\psi_{1,2}\rangle$ (resulting in the measurements dependence on this choice of basis) - given by

$$s = \left(\sum_i \langle\sigma_i\rangle^2 \right)^{1/2}, \tag{C.48}$$

where $\langle\sigma_i\rangle$ are the expectation values of the Pauli matrices [360]. We can determine these expectation values using projections $\langle P|$ into superpositions of the spatial basis components described by

$$\langle P_j| = \alpha_j\langle\psi_1| + \beta_j\langle\psi_2| . \tag{C.49}$$

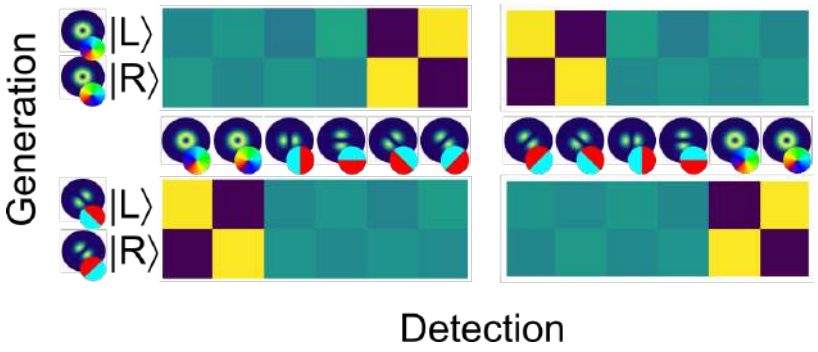


Figure C-1: Basis dependent measurement for tilted lens with input mode of $\ell = 1$.

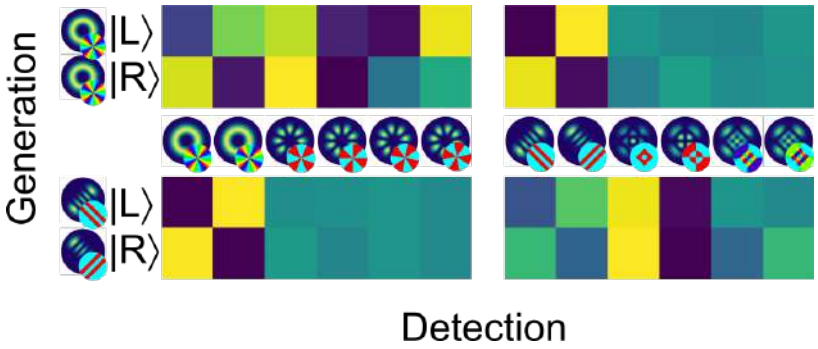


Figure C-2: Basis dependent measurement for tilted lens with input mode of $\ell = 4$.

With $(\alpha, \beta) = \{(1,0), (0,1), \frac{1}{\sqrt{2}}(1,1), \frac{1}{\sqrt{2}}(1,-1),$
$\frac{1}{\sqrt{2}}(1,i), \frac{1}{\sqrt{2}}(1,-i)\}$ for both $|H\rangle$ and $|V\rangle$. These 12 on axis intensity projections are used to calculate the length of the Bloch vector according to

$$\langle \sigma_1 \rangle = (I_{13} + I_{23}) - (I_{14} + I_{24}) \tag{C.50}$$

$$\langle \sigma_2 \rangle = (I_{15} + I_{25}) - (I_{16} + I_{26}) \tag{C.51}$$

$$\langle \sigma_3 \rangle = (I_{11} + I_{21}) - (I_{11} + I_{22}) \tag{C.52}$$

where the i index of I_{ij} corresponds to the $\langle H, V|$ polarization projections and the j index represents the spatial mode projections defined above. In this work the projections into the horizontal and vertical polarization components was achieved using a linear polarizer. The subsequent spatial mode projections were performed using a correlation filter encoded into a digital micro-mirror device (DMD), and a Fourier lens to produce on-axis intensities I_{ij}.

In Fig. C-1 and C-2 we can see basis dependent measurements for the vector mode depicted in section C.4 when passed through a tilted lens. While in Fig. C-1 the OAM state is $\ell = 1$ and we can see a simple shift in basis, in Fig. C-2 the OAM state is $\ell = 4$ there is considerable crosstalk. These measurements were used to calculate the VQF values in Fig. 4-5(a).

C.7 Basis independent VQF propagation of uncertainty

To record our intensity images, we used a FLIR Grasshopper3 CCD camera operating at 16-bit depth. Therefore the measurement uncertainty in a single pixel of a given normalized intensity image is $\Delta_{meas} \approx 7.63 \times 10^{-6}$. The propagation of this uncertainty into a pixel in a calculated Stokes parameter is then $\Delta_{S_i'} = \sqrt{2\Delta^2_{meas}}$, while the uncertainty in the global parameters gains dependence in the number of pixels (N) integrated over $\Delta_{S_i} = \sqrt{2\Delta^2_{meas}N^2}$. Finally the uncertainty in the VQF is a function of the measured VQF, N and ΔI according to

$$\Delta_{VQF} = \frac{\sqrt{8\Delta^2_{meas}N^2}}{VQF}\,. \tag{C.53}$$

In this work $N \in [100, 480]$ to accommodate changes in beam size (e.g. due to propagation from the tilted lens). Therefor our $\Delta_{VQF} \in [2.16 \times 10^{-3}, 1.04 \times 10^{-2}]$.

C.8 Stokes Parameters

In order to represent spatially non uniform polarisation, the following Stokes parameters were calculated using the intensity data from polarisation projections, as described in the Methods section. In Fig. C-3 are the Stokes parameters for Fig. 4-2. The insets show the input modes and the respective parameters are in C-3(a). When propagating through a tilted lens, the transformation of the polarisation structure can be seen in Fig. 4-2(c) and their respective parameters can be seen in C-3(b).

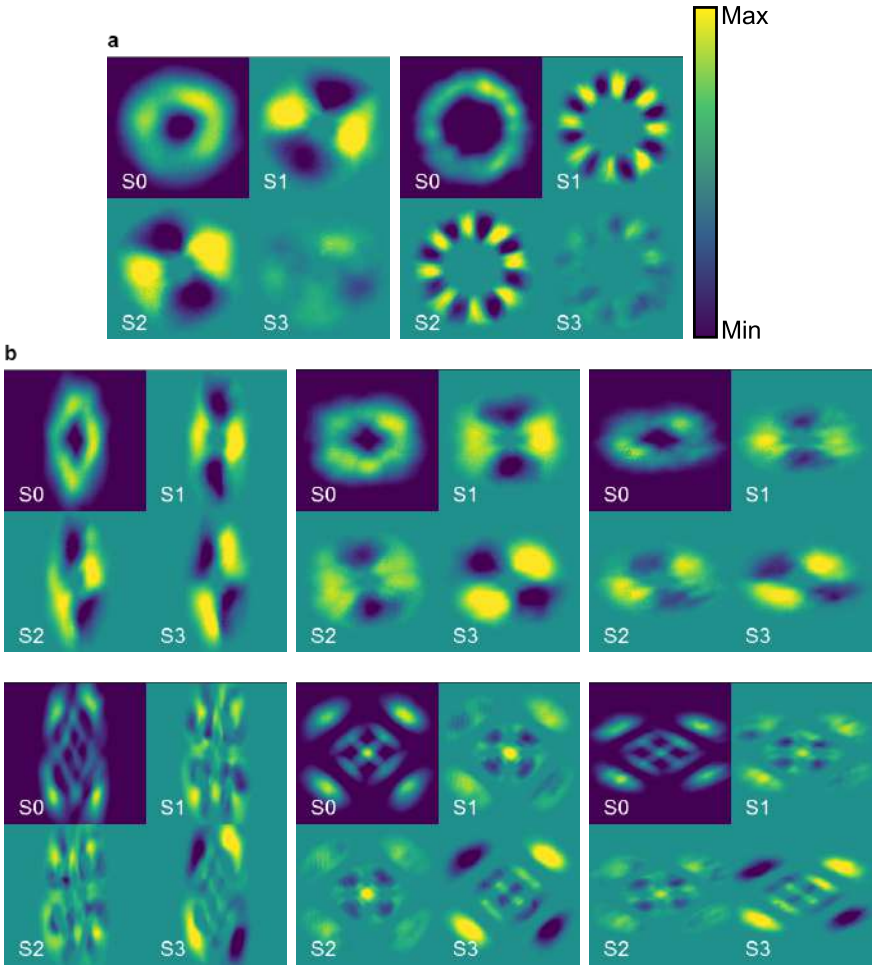


Figure C-3: **Stokes Parameters for transverse modes going through a tilted lens in Fig. 4-2.** Column (a) Shows the parameters for the modes on the inset of Fig. 4-2(a). The set of Fig. 4-2 (b) show the parameters for the modes depicted in Fig. 4-2(c) in sequence.The minimum and maximum values are $\{0, 1\}$ for S_0 and $\{-1, 1\}$ for $S_{1,2,3}$.

Mode	VQF value	VQF error
Figure 1(a)		
$\ell = 1$	0.996952	$\pm$0.002164
$\ell = 4$	0.999133	$\pm$0.003239
Figure 1(c)		
z_1,$\ell = 1$	0.991797	$\pm$0.003263
z_1,$\ell = 4$	0.961124	$\pm$0.004715
z_2,$\ell = 1$	0.974518	$\pm$0.004871
z_2,$\ell = 4$	0.960012	$\pm$0.006294
z_3,$\ell = 1$	0.931651	$\pm$0.008339
z_3,$\ell = 4$	0.952852	$\pm$0.010871
Figure 2(f)		
In (Row 1)	0.999133	$\pm$0.003239
Out (Row 1)	0.960012	$\pm$0.006294
In (Row 2)	0.989600	$\pm$0.003271
Out (Row 2)	0.991154	$\pm$0.003266
Figure 2(g)		
Input	0.999707	$\pm$0.008634
Tilted Lens	0.998234	$\pm$0.008647
QWP	0.988016	$\pm$0.008737
Figure 4(e)		
In	0.999418	$\pm$0.002807
Out	0.991506	$\pm$0.002829
Figure 4(f)		
In	0.995465	$\pm$0.002818
Out	0.995430	$\pm$0.002818

Table C.4: VQF Values and errors.

Figure C-4 shows the stokes parameters for modes in Fig. 4-4. In Fig. 4-4(c) we show pre-channel correction, with the respective parameters in C-4(a). In Fig. 4-4(d) we show post-channel correction and the respective parameters are in C-4(b).

In Fig. C-5 are the parameters used to show the polarisation structure in Fig. 4-6 (e) and (f). In (a) are the parameters for Fig. 4-6(e) where left corresponds to "In" mode and right to "Out" mode. In (b) are the parameters for Fig. 4-6(f) where left is "In" and right is "Out".

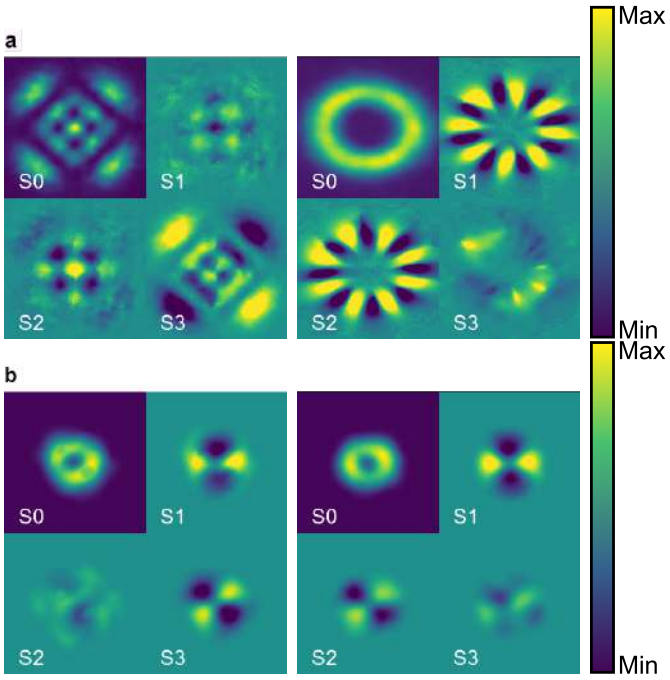


Figure C-4: **Stokes Parameters for the correction of modes depicted in Fig. 4-4.** Row (a) Shows the parameters for Fig. 4-4(c). On the second row (b) are the parameters for Fig. 4-4(d). The minimum and maximum values are $\{0, 1\}$ for S_0 and $\{-1, 1\}$ for $S_{1,2,3}$.

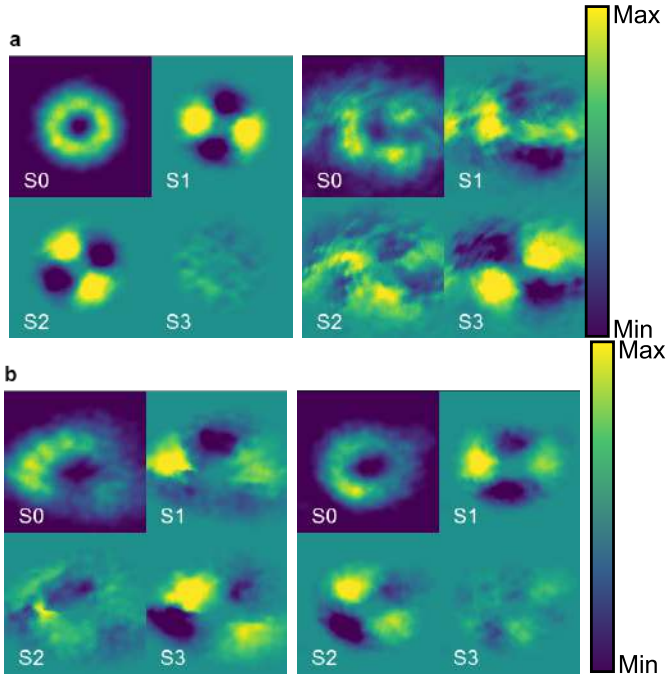


Figure C-5: **Stokes Parameters for modes affected by turbulence depicted in Fig. 4-6.** (a) Shows the parameters for Fig. 4-6(e) In (left) and Out (right). (b) Shows the parameters for Fig. 4-6(f) In (left) and Out (right). The minimum and maximum values are $\{0, 1\}$ for S_0 and $\{-1, 1\}$ for $S_{1,2,3}$.

Appendix D

Supporting data for multi-mode SMF fiber channel

D.0.1 Modal spectrum data after the two meter fiber

We also evaluate the mode spectrum after transmitting through 2 m SMF ($\ell = \pm 1$ subspace) and in free space ($\ell = \pm 2$ subspace). Figure D-1(a) demonstrates the mode spectrum of $\ell = 1$ subspace after transmitting through 2 m fibre. The measured mode spectrum of $\ell = \pm 2$ subspace in free space is illustrated in Fig. D-1(b). We get $\ell = \pm 2$ subspace by using two q-plates with one half-wave plate (HWP) inserted in between.

D.0.2 Supporting density matrix reconstruction data

We also perform the quantum state tomographies for $\ell = \pm 1$ subspace through 2 m fibre transmission and $\ell = \pm 2$ subspace in free space as shown in Figs. D-2(a) and D-2(b), respectively. The reconstructed density matrices are demonstrated with fidelity 94% for $\ell = \pm 1$ subspace through 2 m fibre transmission and 93% for $\ell = \pm 2$ subspace in free space.

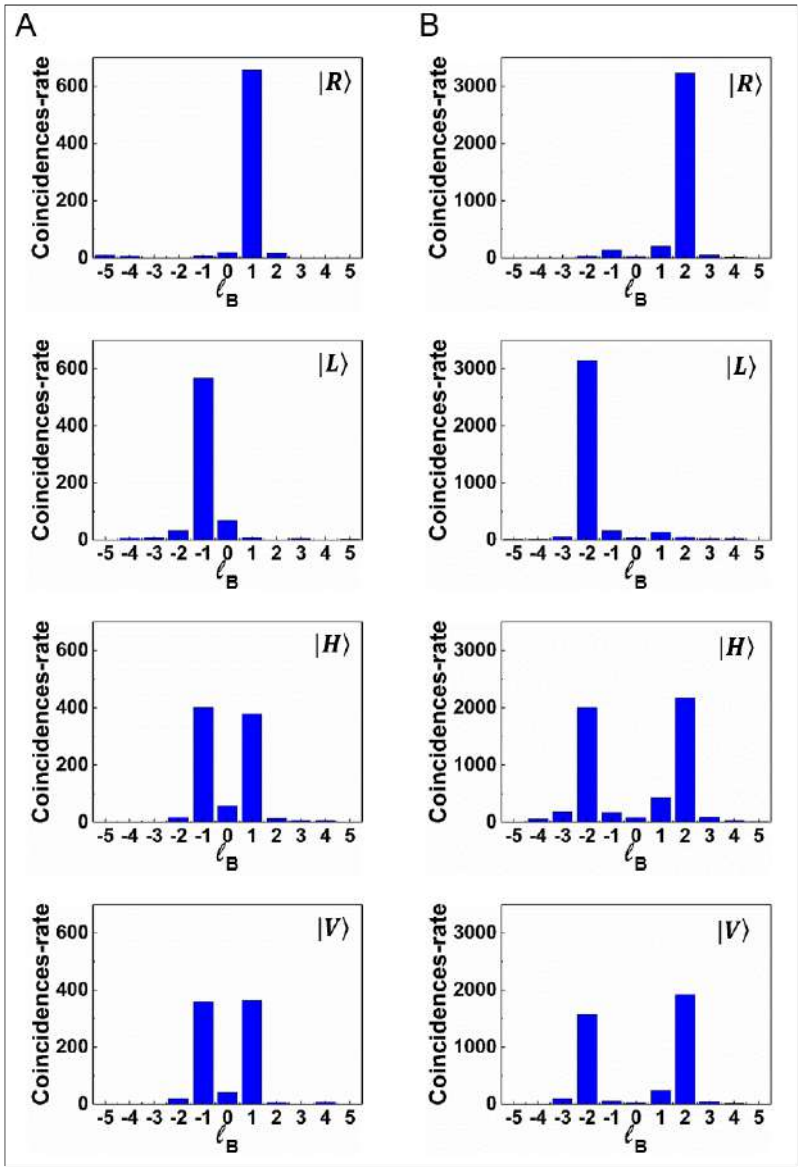


Figure D-1: The measured mode spectrum of (a) $\ell = \pm 1$ subspace after transmitting through 2 m SMF and (b) $\ell = \pm 2$ subspace in free space by projecting photon A onto a polarisation state and decomposing the OAM of photon B while measuring the coincidence count rate.

D.0.3 Supporting quantum eraser data

We also carry out a non-locality test in the 2 m SMF. As shown in Figs. D-3(a) and D-3(b) we get the $S = (2.71 \pm 0.04)$ and $S = (2.51 \pm 0.04)$ for subspace $\ell = \pm 1$ in 2 m SMF and $\ell = \pm 2$ subspace in free space, respectively. Furthermore, we realize quantum eraser with polarisation-OAM hybrid entangled photon in the 2 m SMF.

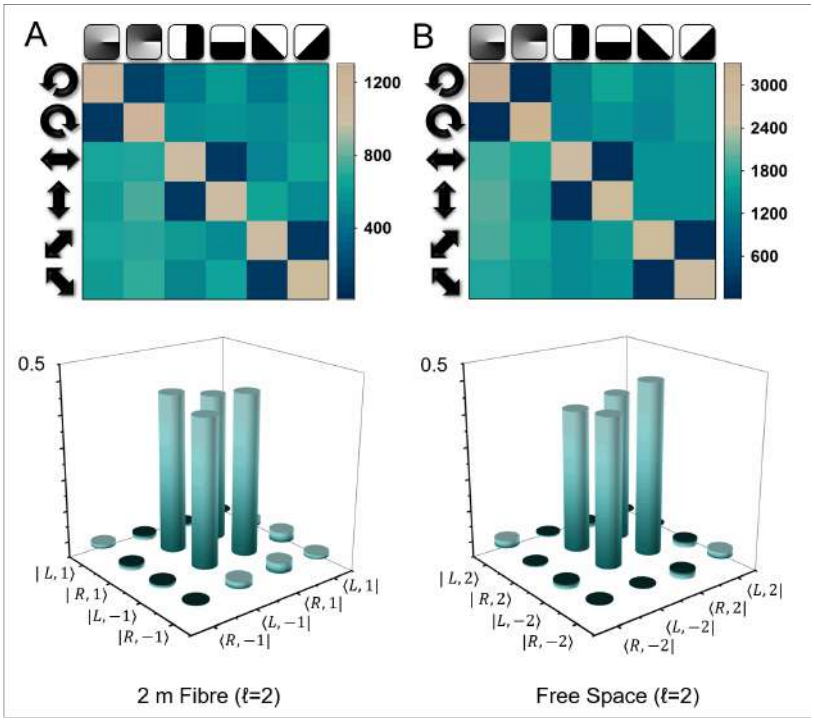


Figure D-2: Experimental tomography measurements upon transmitting photon A through (a) 2 m SMF for $\ell = \pm 1$ subspace and in (b) free space for $\ell = \pm 2$ subspace. The bottom panels show the reconstructed density matrices through 2 m SMF for $\ell = \pm 1$ subspace and in free space for $\ell = \pm 2$ subspace, respectively.

By defining the two distinct paths using the OAM degree of freedom, we have shown that through polarisation-OAM hybrid entanglement, it is possible to distinguish (V $= 0.09 \pm 0.01$) and erase (V $= 0.97 \pm 0.002$) the OAM path information of a photon through the polarisation control of its entangled twin in 2 m SMF.

D.0.4 Tabulated concurrence and fidelity data

	$\ell = \pm 1$				$\ell = \pm 2$			
	F	F_n	C	C_n	F	F_n	C	C_n
Free-space	95%	100%	0.91	1.00	93%	100%	0.88	1.00
2m	94%	99%	0.89	0.98	\	\	\	\
250m	90%	95%	0.82	0.90	86%	92%	0.77	0.88

Table D.1: Fidelity and concurrence values in free space, through 2 m SMF and 250 m SMF for $\ell = \pm 1$ and $\ell = \pm 2$ subspaces.

Here we represent all the fidelity and concurrence values in Table D.1. F and C

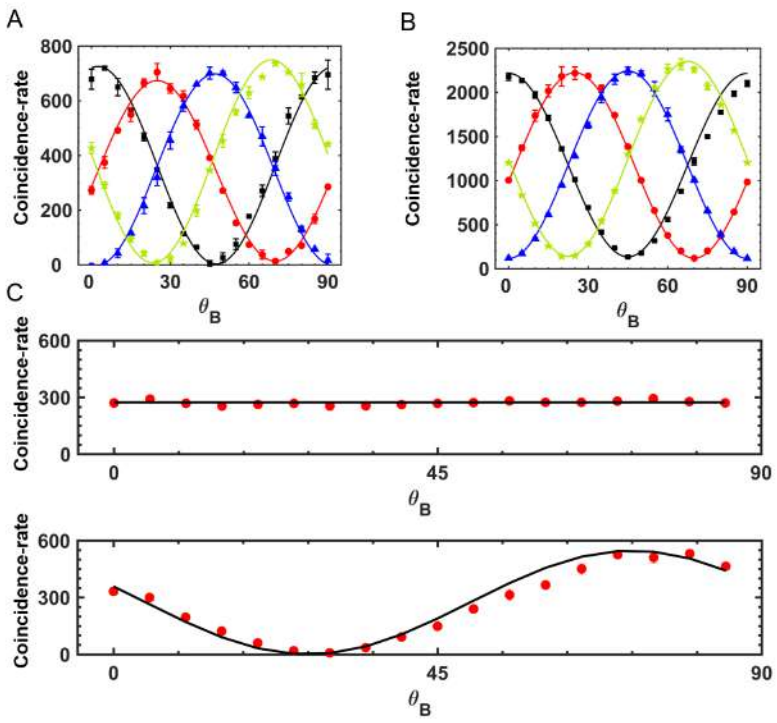


Figure D-3: Measured correlations between photon A (polarisation) and photon B (OAM) in (a) the $\ell = \pm 1$ subspace after 2 m SMF and in (b) the $\ell = \pm 2$ subspace for free space propagation. (c) Experimental coincidence count-rates for distinguishing and erasing the OAM ($\ell = \pm 1$ subspace) of photon B upon transmitting photon A through 2 m SMF.

stand for fidelity and concurrence, while F_n and C_n stand for Fidelity and concurrence normalized to the values in free space for corresponding ℓ subspaces. Since we focus on the difference between free space and SMF transmission, comparing fidelity and concurrence values normalized to free space let the actual performance in SMF stand out. If the free space fidelity is F_1 and the fidelity through 250 m SMF is F_2 then the actual performance can be described as $F_n = \frac{F_2}{F_1}$. This works for all fidelity and concurrence as well.

Appendix E

E.1 Dimensionality of Pure States

To quantify dimensionality, we adopt the definition of Schmidt number from Ref. [72] for pure states and later show how it can be used to determine the Schmidt rank [71, 330]. The former, which we shall use in this thesis, determines the number of modes needed to describe the state irrespective of the spectrum shape. Consider the Schmidt basis states, $|j\rangle\,|j\rangle$, spanning a high dimensional Hilbert space for two photons, i.e. $\mathcal{H}\otimes\mathcal{H}$. Using this basis, we can describe a nonseparable entangled state as

$$|\Psi\rangle = \sum_{j=0}^{\infty} \lambda_j\,|j\rangle\,|j\rangle\,, \tag{E.1}$$

where $|\lambda_j|^2$ is the probability of detecting the biphoton state $|j\rangle\,|j\rangle$. The dimensionality of such a state can be obtained from

$$K = \frac{\left(\sum_j |\lambda_j|^2\right)^2}{\sum_j |\lambda_j|^4}. \tag{E.2}$$

Examples of various types of distributions for $|\lambda_j|^2$ are shown in Fig. E-1 for $K = 21$ for the OAM basis where the Schmidt basis modes have the form $|\ell\rangle\,|-\ell\rangle \in \mathcal{H}\otimes\mathcal{H}$. The distributions are: a square distribution, corresponding to a maximally entangled state within a given ℓ-range,

$$\lambda_\ell = 1/\sqrt{2L+1},\ |\ell| \le L; \tag{E.3}$$

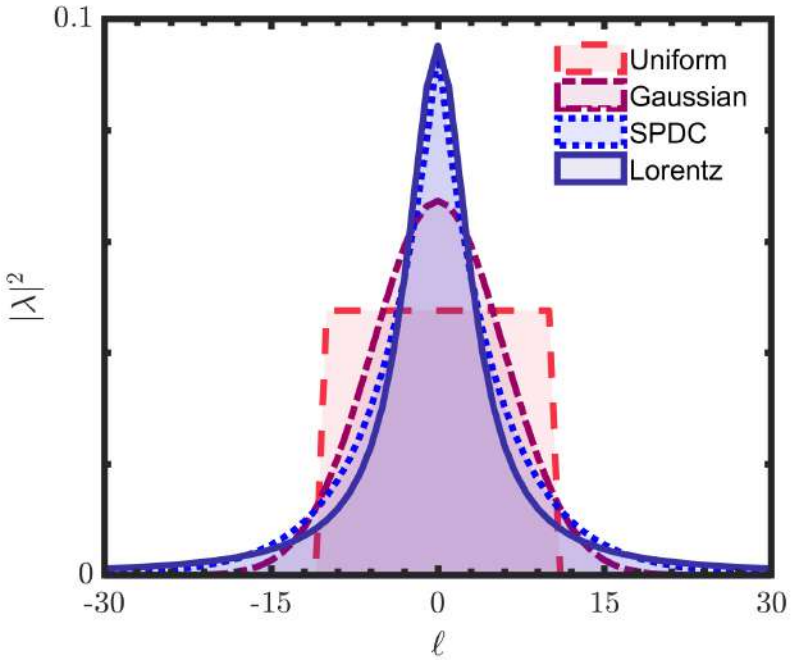


Figure E-1: **Modal spectrum shapes.** Examples of various OAM (ℓ) distributions for a quantum source possessing OAM entanglement.

a Gaussian (normal) distribution

$$|\lambda_{\ell_g}|^2 \propto \exp\left[-\frac{|\ell|^2}{\gamma_G^2}\right], \tag{E.4}$$

where γ_G scales with the width of the distribution; a SPDC source [85, 86]

$$|\lambda_{\ell_S}|^2 \propto \left(\frac{2\gamma_S^2}{1+\gamma_S^2}\right)^{|\ell|}, \tag{E.5}$$

where γ_S is determined by the experimental conditions; and a Lorentz distribution

$$|\lambda_{\ell_L}|^2 \propto \frac{1}{\pi\gamma_L\left(1+\frac{\ell^2}{\gamma_L^2}\right)}, \tag{E.6}$$

where γ_L is a scaling parameter.

For convenience, we relate the Schmidt number to the scaling parameters as, $\gamma_S \approx \sqrt{(K-1)/4}$ and $\gamma_G \approx 2.5066K$ for the SPDC and normal distributions, respectively. Later, we show how one can use the dimensional (K) together with purity to deduce

the Schmidt rank (entanglement dimensionality) [71] for mixed states. Moreover these definitions are not restricted to the SPDC modes or OAM modes. We will in subsequent sections show how the technique can be extended to other degrees of freedom.

E.2 High dimensional state projections

To introduce the projections required for our technique, we will describe them in the OAM basis and later generalise them to other degrees of freedom, i.e. the pixel basis. We take this approach since the projections were initially discovered in the OAM basis [345]. We can represent our analysers on the high dimensional Hilbert space using the OAM basis modes $|\ell\rangle \in \mathcal{H}_\infty$ as

$$|M,\alpha\rangle = \sum_{\ell=-\infty}^{\infty} c_{\ell,M}(\alpha)\,|\ell\rangle\,, \tag{E.7}$$

where the complex coefficients, $c_{\ell,M}(\alpha)$, are computed from the overlap integral, $\int e^{-i\ell\phi}e^{i\Phi_M(\phi;\alpha)}\,d\phi$. Here $e^{i\Phi_M(\phi;\alpha)}$ is the azimuthally dependent mode characterizing the analyser orientated at an angle α. These modes project onto fractional OAM states [345]. Note that a complete decomposition would require an expansion onto a complete basis that includes the radial component. For brevity, we restrict ourselves to the azimuthal degree of freedom, consistent with [345].

By computing the overlap integral, one arrives at complex amplitudes

$$c_{\ell,M}(\alpha) = -\frac{ie^{-i\ell\alpha}\sin(\mu\pi)}{\pi(M-\ell)}, \tag{E.8}$$

with μ representing the fractional part of the total charge M. The detection probability for each OAM mode with charge ℓ is therefore

$$P_\ell = |c_{\ell,M}(\alpha)|^2 = \frac{\sin^2(\mu\pi)}{\pi^2(M-\ell)^2}, \tag{E.9}$$

consistent with probability amplitudes computed in [345] for fractional OAM states.

We have shown that fractional OAM modes project onto the high dimensional state space of OAM modes with complex amplitudes given by Equation (E.8). Next, we tailor new amplitudes and phases by superimposing rotated fractional OAM modes

$$|M,\alpha\rangle_n = \mathcal{N}\sum_{k=0}^{n-1}|M,\beta_k\oplus\alpha\rangle\,, \tag{E.10}$$

where $\mathcal{N}$ is a normalization constant. Each fractional mode in this superposition has the same charge, M, but is rotated by an angle $\beta_k\oplus\alpha = \text{mod}\,\{\beta_k+\alpha,2\pi\}$, with $\beta_k=\frac{2\pi}{n}k$. In the OAM basis, Equation (E.10) becomes

$$\begin{aligned}|M,\alpha\rangle_n =&\mathcal{N}\sum_{k=0}^{n-1}\left\{\sum_{\ell}c_{\ell,M}(\beta_k\oplus\alpha)\,|\ell\rangle\right\},\\ =&\mathcal{N}\sum_{\ell}c^n_{\ell,M}(\alpha)\,|\ell\rangle\ ,\end{aligned} \tag{E.11}$$

where the coefficients $c^n_{\ell,M}(\alpha)$ are computed from

$$c^n_{\ell,M}(\alpha)=\sum_{k=0}^{n-1}c_{\ell,M}(\beta_k\oplus\alpha). \tag{E.12}$$

Using Equation (E.8) and the condition $\text{mod}\,\{\beta_k\oplus\alpha,2\pi\}=0$, we obtain

$$c^n_{\ell,M}(\alpha)=c_{\ell,M}(\alpha)\sum_{k=0}^{n-1}e^{i\beta_k\ell}. \tag{E.13}$$

Since the summation can be evaluated as a geometric series, after some simplification it results in

$$\sum_{k=0}^{n-1}e^{i\beta_k\ell}=e^{-i\pi\ell(n-1)/n}\csc\left(\frac{\pi\ell}{n}\right)\sin(\pi\ell).$$

Therefore the coefficients can be written as

$$c^n_{\ell,M}(\alpha)=e^{-i\pi\ell(n-1)/n}A^n_\ell\ c_{\ell,M}(\alpha)\,, \tag{E.14}$$

where

$$A_\ell^n = \csc\left(\frac{\pi\ell}{n}\right)\sin(\pi\ell)\,, \\ = \begin{cases} 0 & \mod\{\ell, n\} \neq 0 \\ 1 & \mod\{\ell, n\} = 0 \end{cases}. \tag{E.15}$$

Consequently, the overlap probabilities are $P_{\ell,n} = |\mathcal{N}\ A_\ell^n c_{\ell,M}(\alpha)|^2$. Importantly, the probabilities are independent of α. Accordingly, the new spectrum has the amplitudes $|c_{\ell,M}|$, but following the selection rule A_ℓ^n. Indeed, this new spectrum can be tuned by carefully selecting n, therefore enabling control of the OAM subspaces.

E.3 Decomposition of Entangled Photons

Our fractional OAM analysers can be decomposed into the OAM basis using entangled photons through digital spiral imaging. In this scheme, one photon from an entangled pair interacts with the analyser while its twin is decomposed in the OAM basis. The entangled photon pair has a biphoton state

$$|\Psi\rangle = \sum_{\ell=-L}^{L} \lambda_\ell\,|\ell\rangle\,|-\ell\rangle\,. \tag{E.16}$$

The probability amplitude for detecting the mth OAM mode, given a M charged fractional mode of n superpositions, is

$$\tilde{c}_m^n(\alpha) = \mathcal{M}\,\langle m|\,\langle M,\alpha|_n|\Psi|M,\alpha|_n|\Psi\rangle\,, \\ = \mathcal{M}\sum_{\ell=-L}^{L}\lambda_\ell\,\langle m|\ell|m|\ell\rangle\,\langle M,\alpha|_n| - \ell|M,\alpha|_n| - \ell\rangle\,. \tag{E.17}$$

where $\mathcal{M}$ is a normalisation constant such that $\sum_m |\tilde{c}_m^n(\alpha)|^2 = 1$. Due to the orthonormality of the OAM basis, the overlap $\langle m|\ell|m|\ell\rangle$ is simply the Kronecker delta function $\delta_{m,\ell}$, which evaluates as 0 if $\ell \neq m$ or 1 if $\ell = m$. Since from Equation (E.14) we know the expansion coefficients for the analyser in terms of the OAM

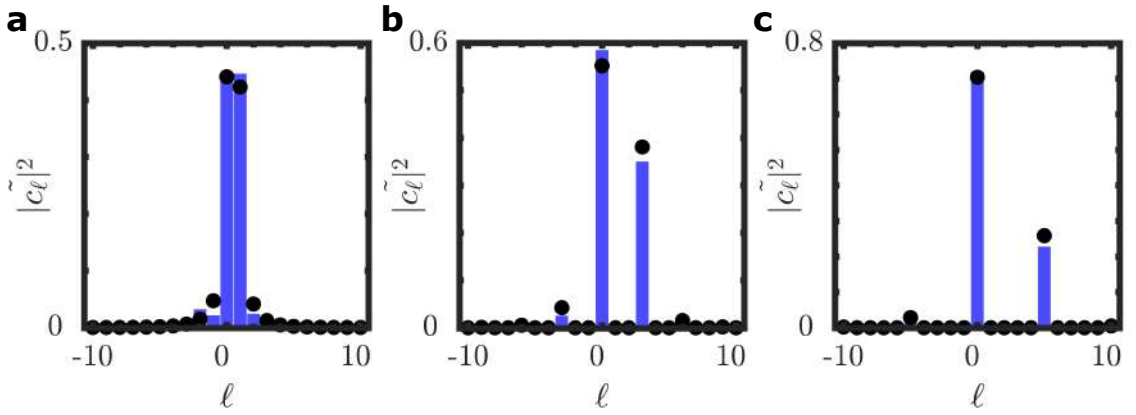


Figure E-2: **Modal decomposition of the state projectors.** Measured (bars) and theoretical spectrum (points) for fractional OAM analysers (a) $|M,\alpha\rangle_n = |0.5,0\rangle_1$, (b) $|M,\alpha\rangle_n = |1.5,0\rangle_3$, and (c) $|M,\alpha\rangle_n = |2.5,0\rangle_5$ resulting from digital spiral imaging with entangled photons. Here the weightings are modulated by the OAM spectrum of the entanglement source according to Equation (E.18).

basis, $\langle M,\alpha|_n|\ell|M,\alpha|_n|\ell\rangle$ evaluate as

$$\begin{aligned}\tilde{c}_m^n(\alpha) =& \mathcal{M}\sum_{\ell=-L}^{L}\delta_{m,\ell}\lambda_\ell\ \left[\mathcal{N}c_{-\ell}^n(\alpha)\right]^* \\ =& \mathcal{M}\mathcal{N}\ \lambda_m\ \left[c_{-m}^n(\alpha)\right]^*. \end{aligned} \tag{E.18}$$

These new weightings are simply the original coefficients of the analysers modulated by the spectrum of the entangled system. For a maximally entangled state, we obtain the expression $|\tilde{c}_m^n(\alpha)|^2 = |c_{-m}^n(\alpha)|^2$, being the original weightings of the analyser, as desired.

In Fig. E-2 we show the measured weightings for our SPDC system which has a normal distribution of OAM modes with $\Delta\ell = 11$ centered at $\ell = 0$. We show results for $|M,\alpha\rangle_n = |0.5,0\rangle_1, |1.5,0\rangle_3, |2.5,0\rangle_5$ for analysers $n = 1,3$ and 5 in Fig. E-2(a), (b) and (c), respectively. It can be seen that the theory (points) and experiment (bars) are in good agreement. To obtain these results, two photons where generated from an SPDC source and modulated with SLMs. One SLM was encoded with a fractional OAM mode projecting onto the state, $|M,0\rangle_n$, while the second SLM was encoded with OAM basis modes, $|\ell\rangle$.

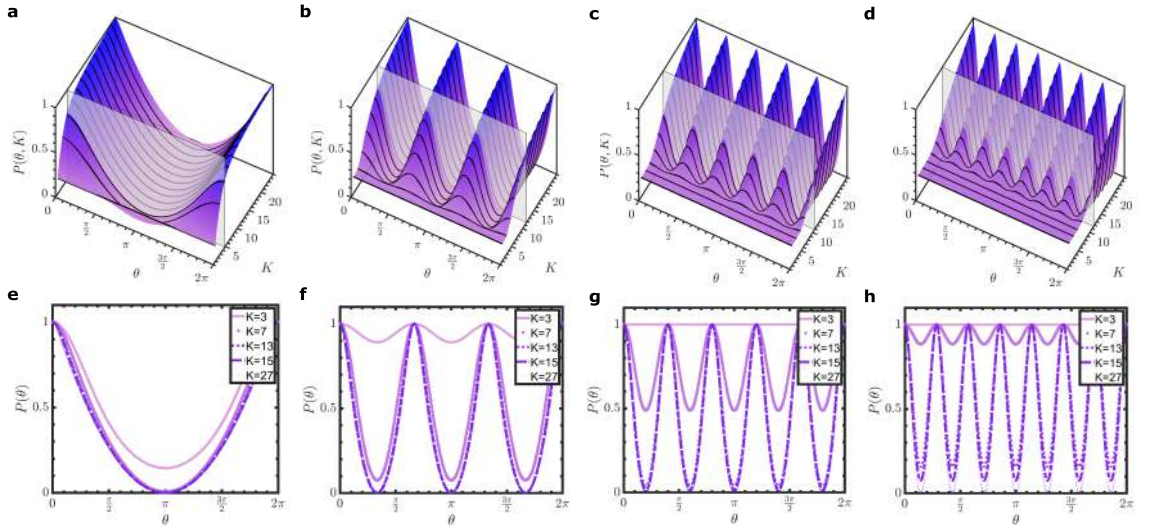


Figure E-3: **Detection probability vs relative orientation and dimensionality.** Simulated normalised probability curves for (a) $n = 1$, (b) $n = 3$, (c) $n = 5$ and (d) $n = 7$, with an analyser corresponding to $M = \frac{n}{2}$, as a function of the relative orientation θ between the two analysers and the dimensions, K, of the entanglement state. The bottom row of panels are probability curves for specific K values for each analyser. The normalisation to unity was performed to illustrate the impact of the dimensions on the visibility. Here, the OAM spectrum shape was assumed to follow a normal (Gaussian) distribution.

E.4 Detection Probability

Given a bipartite system of the form of Equation (E.16), we want to know what the detection probability is, due to the relative rotations of our fractional OAM analysers acting on the entangled photons. Suppose the first analyser projects onto the state $|M, \theta_1\rangle_n$, and the second analyser projects on the state $|-M, \theta_2\rangle_n$. A joint measurement on a two photon system using the two analysers is characterized by the product state $|M, \theta_1\rangle_n |-M, \theta_2\rangle_n$. The probability amplitude resulting from such a measurement is

$$\begin{aligned} C_n(\theta_1, \theta_2) &= {}_n\langle \theta_2, -M| \ {}_n\langle \theta_1, M|\Psi\rangle \\ &= \sum_{\ell=-\infty}^{\infty} \lambda_\ell \ {}_n\langle \theta_1, M|\ell\rangle \ {}_n\langle \theta_2, -M|-\ell\rangle \, . \end{aligned} \tag{E.19}$$

Therefore we only need to know how to decompose each of the analysers in the OAM basis to obtain the detection probability for the joint measurements. Using

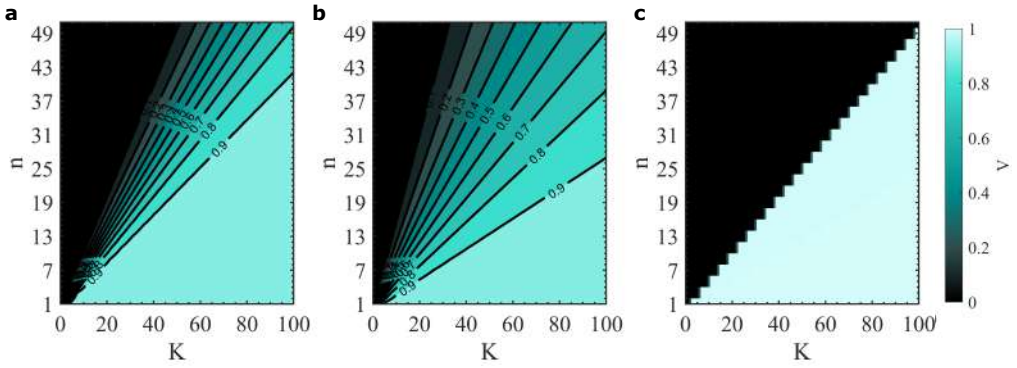


Figure E-4: **Visibility of entangled pure states with differing spectral shapes.** Contour plots of visibility vs dimensionality (K) and n (indexing the projection state $|M,\theta\rangle_n$) for the (a) Normal, (b) SPDC theory and (c) maximally uniform distribution (or maximally entangled pure state). Here we demonstrate the sensitivity of the analysers to the dimensions of a OAM entanglement. The visibilities from the maximally entangled state demonstrates the minimum number of modes required to have a visibility $V = 1$.

Equation (E.14), it follows that

$$C_n(\theta_1,\theta_2) \propto \sum_{\ell=-\infty}^{\infty} \underbrace{\lambda_\ell}_{\text{SPDC}} [\ \underbrace{c^n_{\ell,M}(\theta_1)}_{\text{analyser}}\ \underbrace{c^n_{-\ell,-M}(\theta_2)}_{\text{analyser}}\ ]^*. \tag{E.20}$$

We use this approach to numerically calculate the detection probabilities $|C_n(\theta_1,\theta_2)|^2$ by simply calculating the probability amplitudes for each analyser in the OAM basis with a desired rotation $\theta_{1,2}$ and multiplying them with the coefficients λ_ℓ that determine the quantum system being probed.

An alternative approach, can be to compute the overlap integral by considering the modal overlaps in the azimuthal degree of freedom, ϕ, following

$${}_n\langle\theta, M|\ell\rangle = \frac{1}{2\pi}\int \exp(-i\Phi_M(\phi;\theta)) \times \exp(i\ell\phi)\ d\phi, \tag{E.21}$$

with $\Phi_M(\phi;\theta)/\sqrt{2\pi}$ being the transmission function of the fractional OAM analyser projecting onto the state $|M,\theta\rangle_n$. We can rewrite the probability amplitude $C_n(\theta_1,\theta_2)$

as an overlap integral given by

$$C_n(\theta_1,\theta_2)=\frac{1}{4\pi}\sum_{\ell=-\infty}^{\infty}\big(\lambda_\ell\int e^{-i\Phi_M(\phi_1;\theta_1)}e^{i\ell\phi_1}\\ \times\int e^{-i\Phi_{-M}(\phi_2;\theta_2)}e^{-i\ell\phi_2}\ d\phi_1 d\phi_2\big), \tag{E.22}$$

where $\Phi_{\pm M}(\phi_{1,2},\theta_{1,2})$ are the phases of the fractional OAM analysers. Since $e^{-i\Phi_M(\phi_1;\theta_1)}$ has no ℓ dependence, we can introduce the summation into the second integral resulting in

$$C_n(\theta_1,\theta_2)=\frac{1}{2\pi}\int e^{-i\Phi_M(\phi_1;\theta_1)}\ \big(\int e^{-i\Phi_M(\phi_2;\theta_2)}\\ \times\frac{1}{2\pi}\sum_{\ell=-\infty}^{\infty}\lambda_\ell e^{i\ell(\phi_1-\phi_2)}d\phi_2\big)d\phi_1. \tag{E.23}$$

It is convenient to define the periodic function

$$\Lambda(\phi_1-\phi_2)=\frac{1}{2\pi}\sum_{\ell=-\infty}^{\infty}\lambda_\ell e^{i\ell(\phi_1-\phi_2)}, \tag{E.24}$$

with angular harmonics $e^{i\ell(\phi_1-\phi_2)}$ determined by the coefficients λ_ℓ, and use it to rewrite $C_n(\theta_1,\theta_2)$ as

$$C_n(\theta_1,\theta_2)=\frac{1}{2\pi}\int e^{-i\Phi_M(\phi_1;\theta_1)}\\ \left(\int e^{-i\Phi_M(\phi_2;\theta_2)}\Lambda(\phi_1-\phi_2)d\phi_2\right)d\phi_1. \tag{E.25}$$

Notice that the second integral is a convolution between $\Lambda(\phi_1-\phi_2)$ and the second analyser. As a example, we consider a maximally entangled state ($\lambda_\ell :=$ constant). In this case, $\Lambda(\phi_1-\phi_2)=\delta(\phi_1-\phi_2)$ and therefore

$$C_n(\theta_1,\theta_2)=\frac{1}{2\pi}\int e^{-i\Phi_M(\phi;\theta_1)}\ e^{-i\Phi_{-M}(\phi;\theta_2)}d\phi. \tag{E.26}$$

The integral now only depends in the transmission functions of the analysers with an

analytical solution found in [364].

We now calculate the probability $P_n(\theta_1, \theta_2) = |C_n(\theta_1, \theta_2)|^2$ as a function of relative orientation $\theta = (\theta_1 - \theta_2)$ between the two analysers and the dimensions, K, of an entangled system with some given OAM spectrum $|\lambda_\ell|^2$. The latter is embedded in the function $\Lambda(\phi_1 - \phi_2)$. Figures E-3(a)-(d) show examples of the probability surfaces assuming a normal (Gaussian) spectrum $|\lambda_\ell|^2$ for superposition states $n = 1, 3, 5$ and 7. In the second row of Fig. E-3, we show examples of the probability curves normalised to unity for several values of dimensionality K. Here, it can be seen that the frequency of the probabilities as a function of θ increases with n, owing to the n-fold symmetry in the phase profiles of the analysers.

Crucially, the exact shape and visibility of the curves depends on both the dimensions (K) of the state being probed and the number of superpositions (n). For all n's, the visibility for a specific K shows a decreasing trend as the number of superpositions n are increased. Therefore the analysers are sensitive to the dimensions of the system.

We also found that the shape of the spectrum affects the measured probabilities, as illustrated in Fig. E-4(a)-(c) for the normal (Gaussian), SPDC and square (maximally entangled) distributions, respectively.

Now that we have shown how the detected probabilities depended on the dimensions and superposition states measured, in the following section we study the relation between the visibility and dimensions quantitatively.

E.5 Visibility for Different Spectra

The visibilities are calculated from detection probabilities resulting from the projections of an entangled state with an initial OAM distribution $|\lambda_\ell|^2$ onto the states $|M, 0\rangle_n |-M, \theta\rangle_n$, where $\theta \in [0, 2\pi]$ is their relative rotation.

For example, for a square (uniform) ($K \to \infty$) distribution and n superpositions

of fractional modes the probability is given by [364]

$$\begin{aligned} P(\theta_1,\theta_2) =& |C(\theta_1,\theta_2)|^2 \\ =& a\sin^2\left(\frac{M\pi}{n}\right)+\cos^2\left(\frac{M\pi}{n}\right), \end{aligned} \tag{E.27}$$

with $a=(\pi(2t-1)-n\theta)^2/\pi^2$ for $\frac{2\pi}{n}(t-1)\leq\theta\leq\frac{2\pi}{n}(t), \quad t=1,...,n$, where t indexes each $2\pi/n$ period over the range of $0\leq\theta<2\pi$ and $\theta=\theta_1-\theta_2$. This oscillating function results in fringes with a visibility function given by

$$V_n(M)=\frac{1-\cos^2\left(\frac{M\pi}{n}\right)}{1+\cos^2\left(\frac{M\pi}{n}\right)}. \tag{E.28}$$

For $n=1$, parabolic fringes with perfect visibility occur when $M=\ell+0.5$ for all OAM integer charges ℓ. In contrast, when $n>1$ high visibility fringes occur for only specific choices of n and M. That is, parabolic fringes with high visibility ($V=1$) are expected when n is odd and $\mathrm{mod}\left\{M-\frac{n}{2},n\right\}=0$.

Contour plots of the visibilities with changing dimensions (K) and fractional OAM superpositions (n) for various OAM spectral shapes (Normal, SPDC, Uniform) are shown in Fig. E-4 (a)-(c) for pure states. As shown, the assumed spectrum can affect the visibility that is measured for various superpositions (n). The visibilities for each analyser (n) and spectrum shape are monotonic with increasing K. In particular, for the uniform spectrum (maximal entanglement in K dimensions) the visibility is 1 above some $K=d_n$ and zero below this. We further exploit this property to determine the dimensionality of an entanglement system.

E.6 Visibility of Mixed States

The visibilities that can be measured with our analysers are not only dependent on the effective dimensions of the system but also the purity. In particular, we consider the isotropic state,

$$\rho_p = p\left|\Psi_d\right\rangle\left\langle\Psi_d\right| + \frac{1-p}{d^2}\mathbb{I}_{d^2}, \tag{E.29}$$

which can decomposed into the high-dimensional entangled state, $|\Psi_d\rangle$, and the separable and mixed state, $1/d^2\mathbb{I}_{d^2} = 1/d^2\sum_{\ell,\ell'=-L}^{\ell,\ell'=L}|\ell\rangle|\ell'\rangle\langle\ell'|\langle\ell|$, where $\mathbb{I}_{d^2}$ is the identity operator. Such states model quantum systems that have noise contributions from the environment. Here p can be associated with the purity of the state ranging from a maximally mixed ($p = 0$) to a pure state ($p = 1$). Interestingly, the isotropic state is separable for $p \leq 1/(d+1)$ and entangled otherwise. Importantly, the generalised Bell inequality can also be violated when $p > 2/S_d$ where S_d is the Bell parameter [129]. We show that both p and d can be measured using our analysers. For convenience, we assume $d \approx K$, where K is the effective dimensionality of the pure state. We will demonstrate that we can measure both p and K using our analysers.

Firstly, we calculate the detection probabilities from the overlap, $P_n(\theta; K, p) = \text{Trace}(\hat{M}\rho_p)$ where $\hat{M}$ projects onto the states $|M, 0\rangle_n|-M, \theta\rangle_n$. As a result, the detection probability can be written as

$$P_n(\theta; p, K) = pP_n(\theta; K) + \frac{1-p}{K^2}I_n(0; K), \tag{E.30}$$

where $P_n(\theta, K) = \left|\sum_{\ell=-L}^{L}\lambda_\ell c_\ell^n(0)c_{-\ell}^n(\theta)\right|^2$ and $I_n(0; K) = \left|\sum_{\ell=-L}^{L}|c_\ell^n(0)|^2\right|^2$ is the overlap of the analysers with the maximally mixed state. Since the functions are periodic and obtain maximum and minimum values for $\theta = 0$ and π/n, respectively, we obtain the expression

$$\begin{aligned}\Delta P_n(p, K) &= P_n(0; p, K) - P_n(\pi/n; p, K)\\ &= p\Delta P_n(K),\end{aligned} \tag{E.31}$$

where $\Delta P_n(K) = P_n(0, p = 1, K) - P_n(\pi/n, p = 1, K)$. The visibilities can be

calculated from

$$V_n(p,K) = \frac{\Delta P_n(p,K)}{P_n(\pi/n;p,K) + P_n(0;p,K)}, \tag{E.32}$$

We show the dependence of the visibilities on the dimensions (K) and purity (p) in Fig. E-5 (a-c) for the Normal, SPDC and uniform distribution, respectively. Each panel shows the visibilties from various analysers depending on the number of superpositions (n). As shown the visibilities increase monotonically with increasing dimensions (K) as well as purity p for each analyser. However, as n increases the visibilities decrease for all p and K. Since the visibilities are monotonic in both p and K as well as n, we can exploit this property to map the dimensions of a quantum system. We favour this approach since the visibilities can be easily measured and require few measurements (peak and trough).

E.7 Visibility of Separable States

Consider a system that is completely separable,

$$\rho = 1/D \sum_{\ell_1 \ell_2} |\ell_1\rangle |\ell_2\rangle \langle\ell_2| \langle\ell_1|, \tag{E.33}$$

where the product states, $|\ell_1\rangle |\ell_2\rangle$, are orthogonal. We will show that such a state yields a visibility of zero. Firstly, the overlap probability of Equation (E.33) with our analyser projecting onto the state $|M,0\rangle_n |-M,\theta\rangle_n$, is

$$P(\theta) = \langle\theta,-M|_n \langle 0,M|_n \rho |M,0\rangle_n |-M,\theta\rangle_n \tag{E.34}$$

$$\propto \sum_{\ell_1,\ell_2} |c^n_{\ell_1,M}(0)|^2 |c^n_{\ell_2,M}(\theta)|^2, \tag{E.35}$$

which follows from Equation (E.11). Since, from Equation E.8, $|c^n_{\ell_2,M}(\theta)|^2 = |c^n_{\ell_2,M}(0)|^2$, Equation E.35 simplifies to

$$P(\theta) \propto (\sum_{\ell_1} |c^n_{\ell_1,M}(0)|^2)^2, \tag{E.36}$$

We see that $P(\theta) = P(0)$ for all θ, meaning that $|P(0) - P(\pi/n)| = 0$. This implies that the visibility of separable mixed states is always 0.

E.8 Verification of the Technique

Using our procedure we measured the dimensions and purity of SPDC photons with varying noise levels (low and high). The results are summarised in Table E.1. In the second and third column, we know what the input spectrum shape is (SPDC) and can therefore accurately optimise for the dimensions (K) and purity (p) of the state (see Results section). Further, if we guess the spectrum based on its shape (symmetry) we also obtain values that are similar to the expected results, with a relative error of up to $\approx 13\%$. This was done using the normal distribution as the function modelling the mode spectrum. Next, we verify our result using the values extracted from the spiral bandwidth.

To calculate the expected dimensions, $\hat{K}$, we used the coincidences from the spiral spectrum in the OAM basis, i.e C_{ℓ_A,m_B}, where ℓ_A denotes the mode index of photon A and m_B for photon B. Since we want the Schmidt number of the pure part of the state, we subtracted the accidentals and then used Equation (E.2), yielding results with a low relative error of 3%, validating our results. Subsequently, we estimated the purity $\hat{p}$ (see Results section). Note that no accidentals subtraction was performed in this case. Accordingly, to estimate the purity, we measured the quantum contrast using

$$Q = \bar{C}/\bar{C}', \tag{E.37}$$

taken from the ratio between the average coincidences in the anti-diagonal entries, $\bar{C} = \sum_\ell C_{\ell,-\ell}$ and the average noise contribution from coincidences excluding the

Noise level	p^{SPDC}	K^{SPDC}	p^{norm}	K^{norm}	Q	$\hat{K}$	$\hat{p}$
low	0.45 ± 0.03	22.84 ± 0.62	0.42 ± 0.02	20.00 ± 0.32	19.19 ± 0.22	22 ± 1	0.44 ±
high	0.13 ± 0.01	17.73 ± 0.71	0.13 ± 0.01	17.18 ± 0.34	3.76 ± 0.57	18 ± 1	0.13 ±

Table E.1: **Dimensionality and purity measurements in the OAM basis.** Measured purity (p) and dimensionality (K), under low and high noise levels, compared to estimates from other methods. Here Q is the average quantum contrast.

anti-diagonal entries, i.e $\bar{C}' = \frac{1}{d^2-d}\left(C_T - d\,\bar{C}\right)$. Here C_T corresponds to the total coincidences $C_T = \sum_{\ell,m} C_{\ell,m}$. Indeed, using the quantum contrast we obtained a purity that is comparable to that obtained from our method showing a relative error of only up to 2%.

E.9 Simulations in the Pixel Basis

We demonstrate our technique using the pixel basis. Firstly, we define an entangled state using the pixel position basis modes, $|j\rangle$ for $\{j = 1, 2...\}$. Since we are modelling the isotropic state in Equation (E.29), we define the pure part of the state as

$$|\Psi_d\rangle = \sum_{j=0}^{d-1} \lambda_j \, |j\rangle \, |j\rangle \tag{E.38}$$

on a d-dimensional space. Our analysers are now defined as

$$|M, \alpha\rangle_n = \mathcal{N} \sum_{j=0}^{d-1} c^n_{w_j,M}(\alpha) \, |j\rangle \, , \tag{E.39}$$

composed of coherent superpositions of basis states $|j\rangle \in \{|j\rangle \, , j = 0, 1..d-1\}$ with tune-able phases and amplitudes

$$c^n_{w_j,M}(\alpha) = e^{-i\pi w_j (n-1)/n} A^n_{w_j} c_{w_j,M}(\alpha), \tag{E.40}$$

and where $w_j = j - (d-1)/2$ and the factors

$$c_{w_j,M}(\alpha) = -\frac{i e^{-i w_j \alpha}}{\pi(M - w_j)}. \tag{E.41}$$

and

$$A^n_{w_j} = \begin{cases} 1, & \mod\{w_j, n\} = 0 \\ 0, & \text{otherwise} \end{cases} . \tag{E.42}$$

The projections follow the same procedure as in the OAM basis, i.e., projections onto the states $|M,0\rangle_n |-M,\theta\rangle_n$ at angles $\theta = 0$ and π/n. Subsequently, the visibilities can be measured from these two projections for each n^{th} analyser.

Examples of simulations for χ^2 over the parameter space (K,p) are shown in Fig. E-6 with the maximally entangled state.

E.10 Quantum State Fidelity and Schmidt Rank

Using our technique it is possible to determine how well the state, parametrised by K and p, generally approximates a maximally entangled state $|\Phi\rangle = \sum_i^d \gamma_i |i\rangle |i\rangle$ and how it generally performs with respect to well known entanglement witnesses.

Firstly, we note that our definition of the dimensionality (K), generally estimate the effective number of Schmidt modes required to describe a pure state and therefore reflects how large the Hilbert space is. From Fig. E-7 we see that K maintains a high value for very low values of p meaning that our measurement technique can sift out the dimensionality of the pure part of the state under extremely noisy conditions. As such, in the isotropic state, it gives us an indication of the number of modes that posses strong correlations, given a purity (probability) p.

To relate our measured dimensionality (K) with a common entanglement witness, we consider the operational definition of Schmidt rank, k [71], in comparison to our method. Firstly, the operational general definition of Schmidt rank [330], is the k for which

$$F(\rho,\Phi) \leq B_k(\Phi) \tag{E.43}$$

where $F(\rho,\Phi) = \mathtt{Tr}(\rho, |\Phi\rangle\langle\Phi|)$ is the fidelity while $B(\Phi) = \sum_i^k |\gamma_i|^2$. For a maximally entangled state, $B(\Phi) = k/d$. Therefore one finds the lower bound of the Schmidt

rank $k-1$ when $F(\rho,\Phi) > B_k(\Phi)$ [71,330]. For the isotropic state, the Schmidt rank is determined by $d_{ent} := dF(\rho,\Phi)$ [71]. Since the relation between the fidelity (F) and purity (p) is known, i.e.,

$$F_p = \frac{p(d^2-1)+1}{d^2} \tag{E.44}$$

we can estimate the fidelity of the state using our measured $d = K$ and as well as p. This means that for a state with an effective dimensionality of $d = K$, the Schmidt rank is given by $d_{ent} \approx KF_p$ [330]. We show both the entanglement dimensionality from [330] and our approximation $K * F_p$ in Fig. E-7, which are in good agreement.

E.11 Measurements in the Pixel Basis

In pixel basis we projected the photons onto the states $|M,0\rangle_n |-M,\theta\rangle_n$ for $\theta = 0, \pi/n$ and n = 1, 3, 5...$(d-1)/2+1$. From the measured probabilities we calculated the visibilities and applied the optimazation procedure to determine p and K. Here the model spectrum of the source was assumed to be normally distributed over the pixels.

We demonstrate the technique over square pixel states from 3×3, 5×5, 7×7, 9×9 and 11×11 grids constituting test dimensions of d = 9, 25, 49, 81 and 121, respectively. For the first three cases we varied the laser power in order to change the purity of the state for average photon numbers of μ = 0.002, 0.003 and 0.01 with an integration time of 10 seconds per measurement. For the 11×11 states, we had an average photon number of $\mu = 0.001$ while we used an integration time of 20 second per measurement. In this case the 11 projections produced $p = 0.01 \pm 0.004$ and $K = 119 \pm 1$ witout accidental subtraction. After accidental subtraction we obtained, $p = 0.04 \pm 0.002$ and $K = 121 \pm 2$. The purity in these cases was above the separability bound of $p = 0.0082$.

The results are shown in Fig. E-8 for the first three cases of grid states. Here, the dimensions (K) of the pure part of the state increases as the average photon

number in the system decreases due to the reduction in the number of multi-photon events from the SPDC source. The purity is also seen to improve showing that the measurement technique is sensitive to multi-photon events and noise in the system. The entanglement dimensions, do not seem to improve due the low purity in the system. This can be explained by the fact that as the dimensions of the system increase, a much higher purity is needed to ensure d-dimensional entanglement.

E.12 Comparison to State-of-the-art

We compare the number of measurement needed in our approach for determining the dimensionality and purity of a quantum state in the table E.2. As compared to QST and the recent two MuB approach, the number of measurements are far fewer; in our approach the number measurements scale linearly rather than quadratically for the other two approaches. This can significantly reduce the measurement time of quantum state characterisation.

	Our method	QST	2 MUB
No. of analysers	$\frac{d+1}{4} \sim \frac{d}{4}$	d^2 - 1	$2d$
Local proj.	$\sim \frac{d}{2}$	$(d^2-1)d^2$	$2d^2$

Table E.2: **Measurement scaling with dimensions.** Comparison of our technique to the traditional QST [329] and two MuB approach [330].

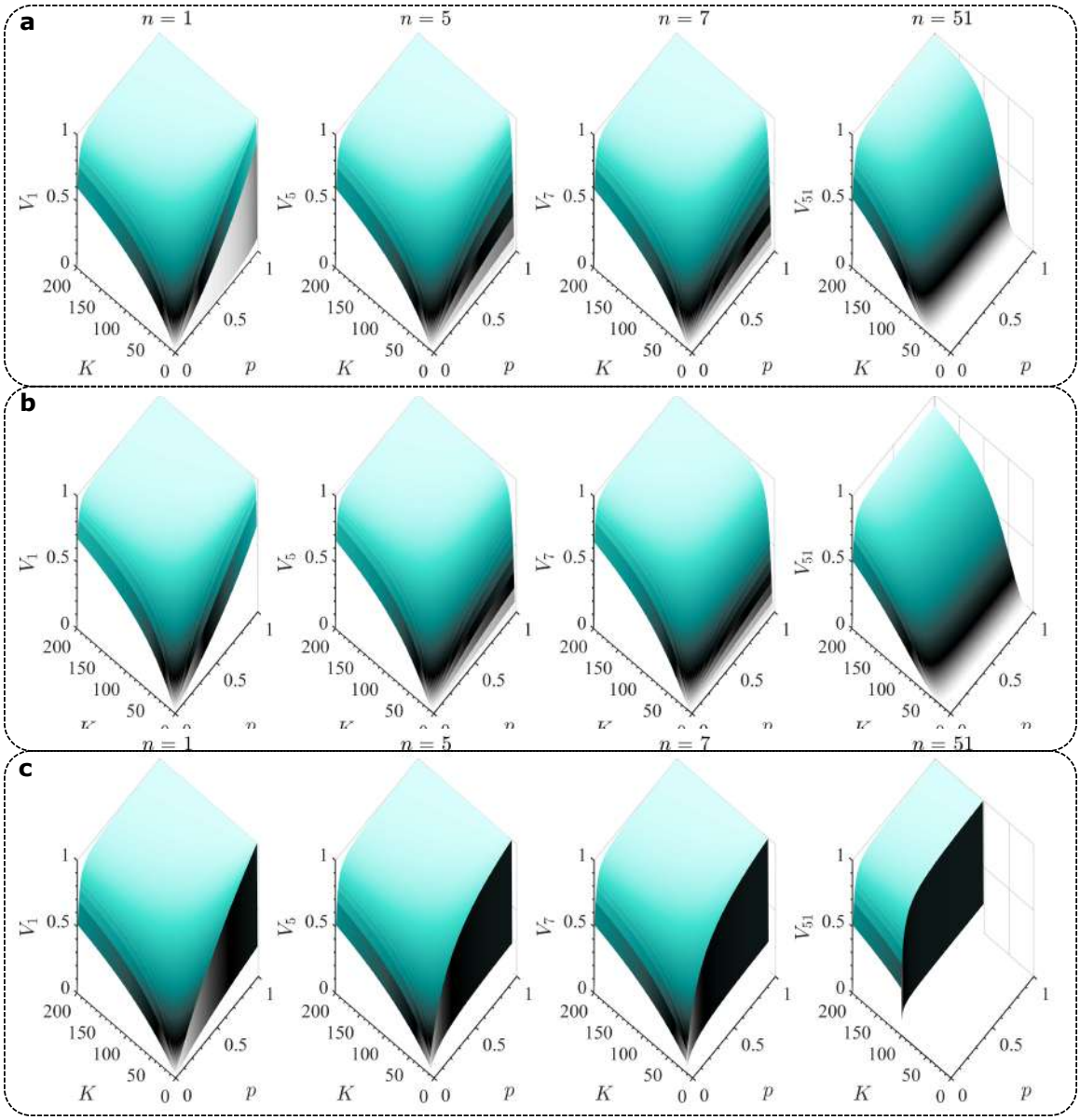


Figure E-5: **Impact of purity and dimensionality on visibility.** Visibility as a function of purity (p) and dimensions (K) for the (a) Normal, (b) SPDC theory and (c) the uniform (maximally entangled state) obtained for fractional OAM projections corresponding to $n = 1, 5, 7, 51$.

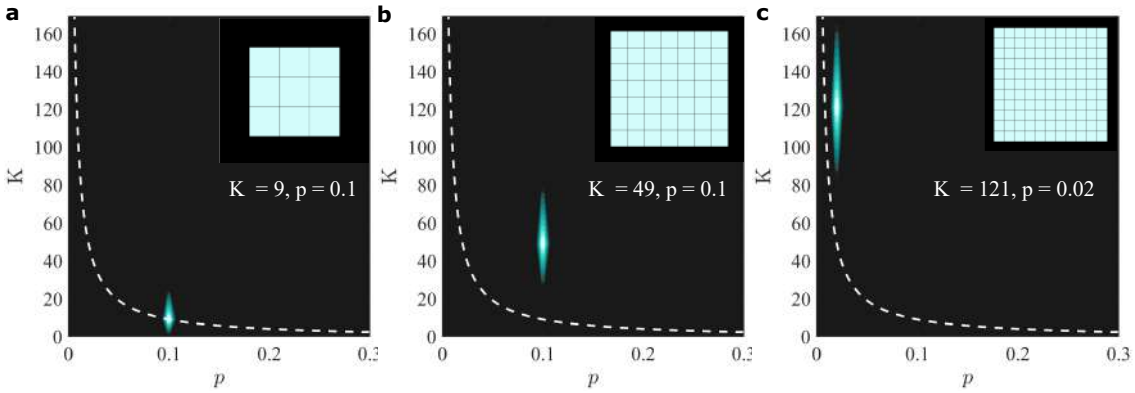


Figure E-6: **Simulations for the pixel basis.** Simulated χ vs K and p for input states with dimensions $d = 9, 49$ and 121. The white dashed line defines the boundary between the separable and entangled states.

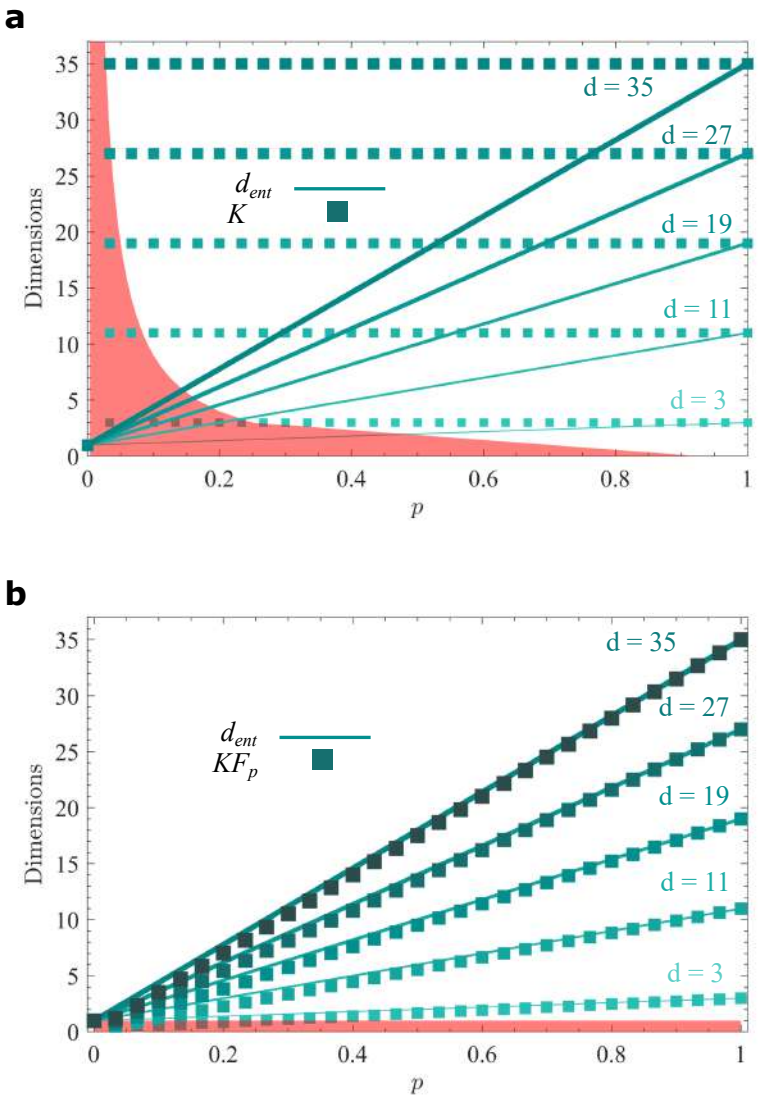


Figure E-7: **Dimensionality witness.** On the top panel we show simulations of calculated entanglement dimensions using the our approach, K, and the Schmidt rank, $d_{ent} = d \times F$, as a function of purity, p. In the bottom panel we show d_{ent} and our estimation as computed from $K \times F_p$, which are in good agreement.

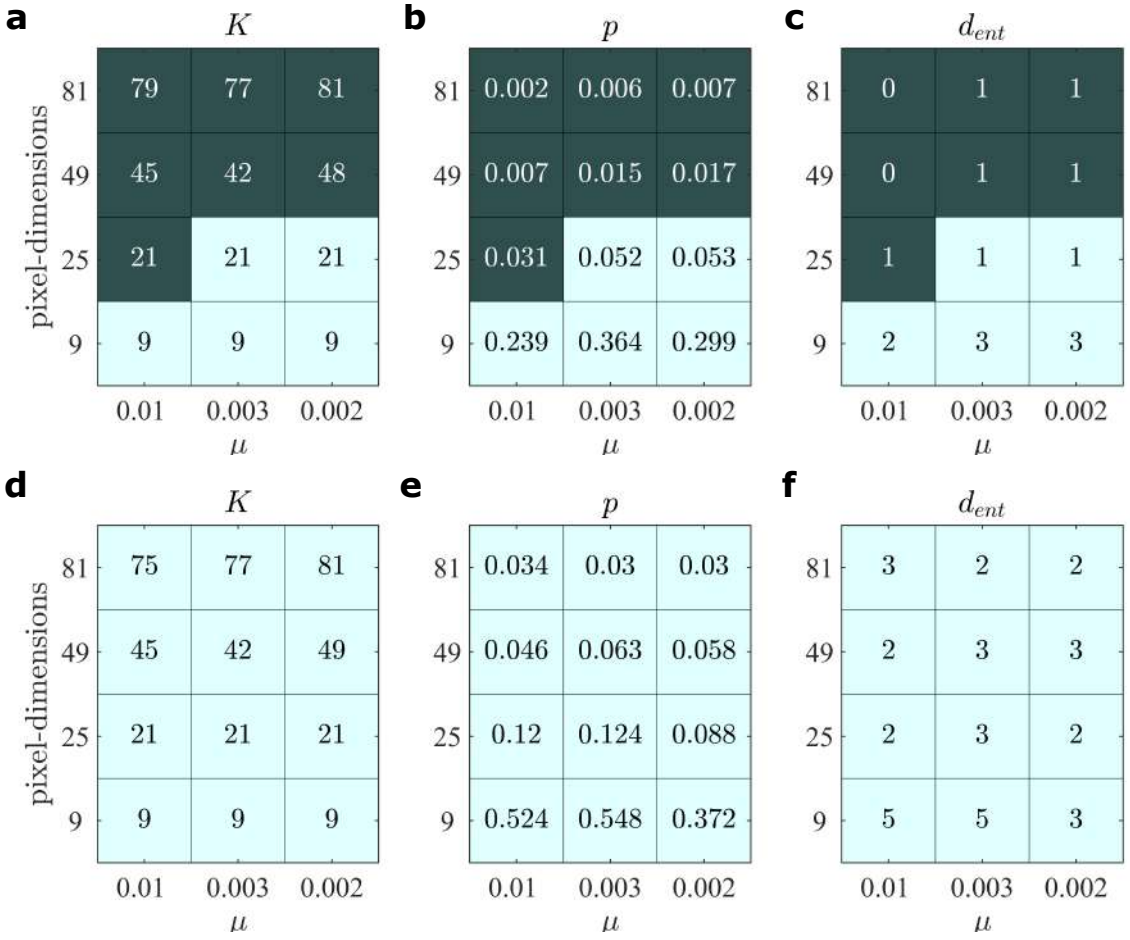


Figure E-8: **Dimensionality and purity measurements in the pixels basis.** Experimental data for measurements of dimensionality (K) and purity (p) in the pixel basis for various average photon numbers (μ). (a) - (c) are projections with different pixels dimensions (grids), without noise subtraction, while (d) - (f) have accidental noise subtraction. The light squares mark results for purities above the separability bound, $1/(K+1)$.

Bibliography

[1] A. Einstein, B. Podolsky, and N. Rosen, "Can quantum-mechanical description of physical reality be considered complete?," *Physical Review*, vol. 47, no. 10, p. 777, 1935.

[2] R. Horodecki, P. Horodecki, M. Horodecki, and K. Horodecki, "Quantum entanglement," *Reviews of Modern Physics*, vol. 81, no. 2, p. 865, 2009.

[3] A. Aspect, P. Grangier, and G. Roger, "Experimental tests of realistic local theories via Bell's theorem," *Physical Review Letters*, vol. 47, no. 7, p. 460, 1981.

[4] W. K. Wootters and W. H. Zurek, "A single quantum cannot be cloned," *Nature*, vol. 299, no. 5886, pp. 802–803, 1982.

[5] V. Scarani, A. Acin, G. Ribordy, and N. Gisin, "Quantum cryptography protocols robust against photon number splitting attacks for weak laser pulse implementations," *Physical review letters*, vol. 92, no. 5, p. 057901, 2004.

[6] N. Gisin, G. Ribordy, W. Tittel, and H. Zbinden, "Quantum cryptography," *Reviews of modern physics*, vol. 74, no. 1, p. 145, 2002.

[7] C. H. Bennett and G. Brassard, "Quantum cryptography: Public key distribution and coin tossing," *Proc. IEEE Int. Conf. on Comput. Syst. Signal Process. Bangalore, India*, pp. 175–179, 1984.

[8] C. H. Bennett, F. Bessette, G. Brassard, L. Salvail, and J. Smolin, "Experimental quantum cryptography," *Journal of cryptology*, vol. 5, no. 1, pp. 3–28, 1992.

[9] K. Mattle, H. Weinfurter, P. G. Kwiat, and A. Zeilinger, "Dense coding in experimental quantum communication," *Physical Review Letters*, vol. 76, no. 25, p. 4656, 1996.

[10] D. Bouwmeester, J.-W. Pan, K. Mattle, M. Eibl, H. Weinfurter, and A. Zeilinger, "Experimental quantum teleportation," *Nature*, vol. 390, no. 6660, pp. 575–579, 1997.

[11] J.-W. Pan, D. Bouwmeester, H. Weinfurter, and A. Zeilinger, "Experimental entanglement swapping: entangling photons that never interacted," *Physical review letters*, vol. 80, no. 18, p. 3891, 1998.

[12] W. Tittel, H. Zbinden, and N. Gisin, "Experimental demonstration of quantum secret sharing," *Physical Review A*, vol. 63, no. 4, p. 042301, 2001.

[13] A. Aspect, P. Grangier, and G. Roger, "Experimental realization of Einstein-Podolsky-Rosen-Bohm Gedankenexperiment: a new violation of Bell's inequalities," *Physical Review Letters*, vol. 49, no. 2, p. 91, 1982.

[14] S. Walborn, M. T. Cunha, S. Pádua, and C. Monken, "Double-slit quantum eraser," *Physical Review A*, vol. 65, no. 3, p. 033818, 2002.

[15] A. Forbes and I. Nape, "Quantum mechanics with patterns of light: progress in high dimensional and multidimensional entanglement with structured light," *AVS Quantum Science*, vol. 1, no. 1, p. 011701, 2019.

[16] M. Erhard, R. Fickler, M. Krenn, and A. Zeilinger, "Twisted photons: new quantum perspectives in high dimensions," *Light: Science & Applications*, vol. 7, no. 3, pp. 17146–17146, 2018.

[17] D. Cozzolino, B. Da Lio, D. Bacco, and L. K. Oxenløwe, "High-dimensional quantum communication: Benefits, progress, and future challenges," *Advanced Quantum Technologies*, vol. 2, no. 12, p. 1900038, 2019.

[18] A. Sit, F. Bouchard, R. Fickler, J. Gagnon-Bischoff, H. Larocque, K. Heshami, D. Elser, C. Peuntinger, K. Günthner, B. Heim, C. Marquardt, G. Leuchs, R. W. Boyd, and E. Karimi, "High-dimensional intracity quantum cryptography with structured photons," *Optica*, vol. 4, no. 9, p. 1006, 2017.

[19] M. De Oliveira, I. Nape, J. Pinnell, N. TabeBordbar, and A. Forbes, "Experimental high-dimensional quantum secret sharing with spin-orbit-structured photons," *Physical Review A*, vol. 101, no. 4, p. 042303, 2020.

[20] M. Mafu, A. Dudley, S. Goyal, D. Giovannini, M. McLaren, M. J. Padgett, T. Konrad, F. Petruccione, N. Lütkenhaus, and A. Forbes, "Higher-dimensional orbital-angular-momentum-based quantum key distribution with mutually unbiased bases," *Physical Review A*, vol. 88, no. 3, p. 032305, 2013.

[21] M. Mirhosseini, O. S. Magaña-Loaiza, M. N. O'Sullivan, B. Rodenburg, M. Malik, M. P. Lavery, M. J. Padgett, D. J. Gauthier, and R. W. Boyd, "High-dimensional quantum cryptography with twisted light," *New Journal of Physics*, vol. 17, no. 3, p. 033033, 2015.

[22] F. Bouchard, K. Heshami, D. England, R. Fickler, R. W. Boyd, B.-G. Englert, L. L. Sánchez-Soto, and E. Karimi, "Experimental investigation of high-dimensional quantum key distribution protocols with twisted photons," *Quantum*, vol. 2, p. 111, 2018.

[23] J. Pinnell, I. Nape, M. de Oliveira, N. TabeBordbar, and A. Forbes, "Experimental demonstration of 11-dimensional 10-party quantum secret sharing," *Laser & Photonics Reviews*, vol. 14, no. 9, p. 2000012, 2020.

[24] C. Paterson, "Atmospheric turbulence and orbital angular momentum of single photons for optical communication," *Physical review letters*, vol. 94, no. 15, p. 153901, 2005.

[25] V. N. Mahajan, "Optical imaging and aberrations(part ii, wave diffraction optics)," SPIE- The International Society for Optical Engineering, 1998.

[26] G. Sorelli, V. N. Shatokhin, F. S. Roux, and A. Buchleitner, "Diffraction-induced entanglement loss of orbital-angular-momentum states," *Physical Review A*, vol. 97, no. 1, p. 013849, 2018.

[27] F. Zhu, M. Tyler, N. H. Valencia, M. Malik, and J. Leach, "Is high-dimensional photonic entanglement robust to noise?," *AVS Quantum Science*, vol. 3, no. 1, p. 011401, 2021.

[28] D. L. Andrews and M. Babiker, *The angular momentum of light*. Cambridge University Press, 2012.

[29] N. J. Cerf, M. Bourennane, A. Karlsson, and N. Gisin, "Security of quantum key distribution using d-level systems," *Physical Review Letters*, vol. 88, no. 12, p. 127902, 2002.

[30] H. Bechmann-Pasquinucci and W. Tittel, "Quantum cryptography using larger alphabets," *Physical Review A*, vol. 61, no. 6, p. 062308, 2000.

[31] I. Ali-Khan, C. J. Broadbent, and J. C. Howell, "Large-alphabet quantum key distribution using energy-time entangled bipartite states," *Physical review letters*, vol. 98, no. 6, p. 060503, 2007.

[32] N. Gisin and S. Massar, "Optimal quantum cloning machines," *Physical Review Letters*, vol. 79, no. 11, p. 2153, 1997.

[33] F. Bouchard, R. Fickler, R. W. Boyd, and E. Karimi, "High-dimensional quantum cloning and applications to quantum hacking," *Sci Adv*, vol. 3, no. 2, p. e1601915, 2017.

[34] S. Ecker, F. Bouchard, L. Bulla, F. Brandt, O. Kohout, F. Steinlechner, R. Fickler, M. Malik, Y. Guryanova, R. Ursin, *et al.*, "Overcoming noise in entanglement distribution," *Phys Rev X*, vol. 9, no. 4, p. 041042, 2019.

[35] D. Giovannini, J. Romero, J. Leach, A. Dudley, A. Forbes, and M. J. Padgett, "Characterization of high-dimensional entangled systems via mutually unbiased measurements," *Physical Review Letters*, vol. 110, no. 14, p. 143601, 2013.

[36] T. Durt, B. G. Englert, I. Bengtsson, and K. Yczkowski, "On mutually unbiased bases," *International Journal of Quantum Information*, vol. 8, pp. 535–640, 2010.

[37] F. Bussières, J. A. Slater, J. Jin, N. Godbout, and W. Tittel, "Testing nonlocality over 12.4 km of underground fiber with universal time-bin qubit analyzers," *Physical Review A*, vol. 81, no. 5, p. 052106, 2010.

[38] D. Stucki, H. Zbinden, and N. Gisin, "A Fabry–Perot-like two-photon interferometer for high-dimensional time-bin entanglement," *Journal of Modern Optics*, vol. 52, no. 18, pp. 2637–2648, 2005.

[39] N. T. Islam, C. C. W. Lim, C. Cahall, J. Kim, and D. J. Gauthier, "Provably secure and high-rate quantum key distribution with time-bin qudits," *Science advances*, vol. 3, no. 11, p. e1701491, 2017.

[40] J. Kysela, M. Erhard, A. Hochrainer, M. Krenn, and A. Zeilinger, "Path identity as a source of high-dimensional entanglement," *Proceedings of the National Academy of Sciences*, vol. 117, no. 42, pp. 26118–26122, 2020.

[41] A. Rossi, G. Vallone, A. Chiuri, F. De Martini, and P. Mataloni, "Multipath entanglement of two photons," *Physical Review Letters*, vol. 102, no. 15, p. 153902, 2009.

[42] N. H. Valencia, V. Srivastav, M. Pivoluska, M. Huber, N. Friis, W. McCutcheon, and M. Malik, "High-dimensional pixel entanglement: efficient generation and certification," *Quantum*, vol. 4, p. 376, 2020.

[43] B. Ndagano and A. Forbes, "Characterization and mitigation of information loss in a six-state quantum-key-distribution protocol with spatial modes of light through turbulence," *Physical Review A*, vol. 98, p. 062330, 2018.

[44] M. Mirhosseini, O. S. Magaña-Loaiza, M. N. O'Sullivan, B. Rodenburg, M. Malik, M. P. J. Lavery, M. J. Padgett, D. J. Gauthier, and R. W. Boyd, "High-dimensional quantum cryptography with twisted light," *New Journal of Physics*, vol. 17, p. 033033, mar 2015.

[45] F. Hufnagel, A. Sit, F. Bouchard, Y. Zhang, D. England, K. Heshami, B. J. Sussman, and E. Karimi, "Underwater quantum communication over a 30-meter flume tank," *arXiv 2004.04821*, 2020.

[46] F.-X. Wang, W. Chen, Z.-Q. Yin, S. Wang, G.-C. Guo, and Z.-F. Han, "Characterizing High-Quality High-Dimensional Quantum Key Distribution by State Mapping Between Different Degrees of Freedom," *Physical Review Applied*, vol. 11, p. 024070, feb 2019.

[47] D. Cozzolino, E. Polino, M. Valeri, G. Carvacho, D. Bacco, N. Spagnolo, L. K. Oxenløwe, and F. Sciarrino, "Air-core fiber distribution of hybrid vector vortex-polarization entangled states," *Advanced Photonics*, vol. 1, no. 4, p. 046005, 2019.

[48] Y. Chen, W.-G. Shen, Z.-M. Li, C.-Q. Hu, Z.-Q. Yan, Z.-Q. Jiao, J. Gao, M.-M. Cao, K. Sun, and X.-M. Jin, "Underwater transmission of high-dimensional twisted photons over 55 meters," *PhotoniX*, vol. 1, p. 5, dec 2020.

[49] F. Hufnagel, A. Sit, F. Grenapin, F. Bouchard, K. Heshami, D. England, Y. Zhang, B. J. Sussman, R. W. Boyd, G. Leuchs, *et al.*, "Characterization of an underwater channel for quantum communications in the ottawa river," *arXiv preprint arXiv:1905.09437*, 2019.

[50] D. J. Griffiths, "Introduction to electrodynamics," 2005.

[51] L. Allen, M. W. Beijersbergen, R. Spreeuw, and J. Woerdman, "Orbital angular momentum of light and the transformation of laguerre-gaussian laser modes," *Physical Review A*, vol. 45, no. 11, p. 8185, 1992.

[52] C. Rosales-Guzmán and A. Forbes, *How to shape light with spatial light modulators*. SPIE Press, 2017.

[53] L. Marrucci, C. Manzo, and D. Paparo, "Optical spin-to-orbital angular momentum conversion in inhomogeneous anisotropic media," *Physical Review Letters*, vol. 96, p. 163905, Apr 2006.

[54] E. Brasselet, N. Murazawa, H. Misawa, and S. Juodkazis, "Optical vortices from liquid crystal droplets," *Physical review letters*, vol. 103, no. 10, p. 103903, 2009.

[55] J. Kim, Y. Li, M. N. Miskiewicz, C. Oh, M. W. Kudenov, and M. J. Escuti, "Fabrication of ideal geometric-phase holograms with arbitrary wavefronts," *Optica*, vol. 2, pp. 958–964, 2015.

[56] Z. Bomzon, G. Biener, V. Kleiner, and E. Hasman, "Space-variant Pancharatnam–Berry phase optical elements with computer-generated subwavelength gratings," *Optics Letters*, vol. 27, no. 13, pp. 1141–1143, 2002.

[57] R. C. Devlin, A. Ambrosio, D. Wintz, S. L. Oscurato, A. Y. Zhu, M. Khorasaninejad, J. Oh, P. Maddalena, and F. Capasso, "Spin-to-orbital angular momentum conversion in dielectric metasurfaces," *Optics express*, vol. 25, no. 1, pp. 377–393, 2017.

[58] E. Karimi, G. Zito, B. Piccirillo, L. Marrucci, and E. Santamato, "Hypergeometric-gaussian modes," *Optics letters*, vol. 32, no. 21, pp. 3053–3055, 2007.

[59] J. Leach, M. J. Padgett, S. M. Barnett, S. Franke-Arnold, and J. Courtial, "Measuring the orbital angular momentum of a single photon," *Physical review letters*, vol. 88, no. 25, p. 257901, 2002.

[60] M. P. Lavery, D. J. Robertson, G. C. Berkhout, G. D. Love, M. J. Padgett, and J. Courtial, "Refractive elements for the measurement of the orbital angular momentum of a single photon," *Optics express*, vol. 20, no. 3, pp. 2110–2115, 2012.

[61] J. Romero, D. Giovannini, S. Franke-Arnold, S. Barnett, and M. Padgett, "Increasing the dimension in high-dimensional two-photon orbital angular momentum entanglement," *Physical Review A*, vol. 86, no. 1, p. 012334, 2012.

[62] M. Malik, M. Erhard, M. Huber, M. Krenn, R. Fickler, and A. Zeilinger, "Multi-photon entanglement in high dimensions," *Nature Photonics*, vol. 10, pp. 248–252, 2016.

[63] D. J. Griffiths, *Introduction to quantum mechanics*. Cambridge University Press, 2016.

[64] M. J. Padgett and J. Courtial, "Poincaré-sphere equivalent for light beams containing orbital angular momentum," *Optics letters*, vol. 24, no. 7, pp. 430–432, 1999.

[65] G. Milione, H. Sztul, D. Nolan, and R. Alfano, "Higher-order poincaré sphere, stokes parameters, and the angular momentum of light," *Physical review letters*, vol. 107, no. 5, p. 053601, 2011.

[66] A. Sit, F. Bouchard, R. Fickler, J. Gagnon-Bischoff, H. Larocque, K. Heshami, D. Elser, C. Peuntinger, K. Günthner, B. Heim, C. Marquardt, G. Leuchs, R. W. Boyd, and E. Karimi, "High-Dimensional Intra-City Quantum Cryptography with Structured Photons," pp. 1–10, dec 2016.

[67] F. Cardano, E. Karimi, S. Slussarenko, L. Marrucci, C. de Lisio, and E. Santamato, "Polarization pattern of vector vortex beams generated by q-plates with different topological charges," *Applied Optics*, vol. 51, no. 10, pp. C1–C6, 2012.

[68] Q. Zhan, "Cylindrical vector beams: from mathematical concepts to applications," *Advances in Optics and Photonics*, vol. 1, no. 1, pp. 1–57, 2009.

[69] G. Volpe and D. Petrov, "Generation of cylindrical vector beams with few-mode fibers excited by Laguerre–Gaussian beams," *Optics Communications*, vol. 237, no. 1, pp. 89–95, 2004.

[70] J. S. Bell, "On the Einstein Podolsky Rosen paradox," *Physics*, vol. 1, no. 3, pp. 369–371, 1964.

[71] B. M. Terhal and P. Horodecki, "Schmidt number for density matrices," *Physical Review A*, vol. 61, no. 4, p. 040301, 2000.

[72] C. Law and J. Eberly, "Analysis and interpretation of high transverse entanglement in optical parametric down conversion," *Physical review letters*, vol. 92, no. 12, p. 127903, 2004.

[73] J. Romero, D. Giovannini, D. Tasca, S. Barnett, and M. Padgett, "Tailored two-photon correlation and fair-sampling: a cautionary tale," *New Journal of Physics*, vol. 15, no. 8, p. 083047, 2013.

[74] M. Krenn, R. Fickler, M. Huber, R. Lapkiewicz, W. Plick, S. Ramelow, and A. Zeilinger, "Entangled singularity patterns of photons in ince-gauss modes," *Physical Review A*, vol. 87, no. 1, p. 012326, 2013.

[75] M. McLaren, M. Agnew, J. Leach, F. S. Roux, M. J. Padgett, R. W. Boyd, and A. Forbes, "Entangled bessel-gaussian beams," *Optics Express*, vol. 20, no. 21, pp. 23589–23597, 2012.

[76] P. G. Kwiat, K. Mattle, H. Weinfurter, A. Zeilinger, A. V. Sergienko, and Y. Shih, "New high-intensity source of polarization-entangled photon pairs," *Physical Review Letters*, vol. 75, no. 24, p. 4337, 1995.

[77] P. G. Kwiat, E. Waks, A. G. White, I. Appelbaum, and P. H. Eberhard, "Ultrabright source of polarization-entangled photons," *Physical Review A*, vol. 60, no. 2, p. R773, 1999.

[78] A. Lamas-Linares, J. C. Howell, and D. Bouwmeester, "Stimulated emission of polarization-entangled photons," *Nature*, vol. 412, no. 6850, pp. 887–890, 2001.

[79] C. Cinelli, G. Di Nepi, F. De Martini, M. Barbieri, and P. Mataloni, "Parametric source of two-photon states with a tunable degree of entanglement and mixing: Experimental preparation of Werner states and maximally entangled mixed states," *Physical Review A*, vol. 70, no. 2, p. 022321, 2004.

[80] R. T. Thew, S. Tanzilli, W. Tittel, H. Zbinden, and N. Gisin, "Experimental investigation of the robustness of partially entangled qubits over 11 km," *Physical Review A*, vol. 66, no. 6, p. 062304, 2002.

[81] H. De Riedmatten, I. Marcikic, V. Scarani, W. Tittel, H. Zbinden, and N. Gisin, "Tailoring photonic entanglement in high-dimensional Hilbert spaces," *Physical Review A*, vol. 69, no. 5, p. 050304, 2004.

[82] A. Mair, A. Vaziri, G. Weihs, and A. Zeilinger, "Entanglement of the orbital angular momentum states of photons," *Nature*, vol. 412, no. 6844, pp. 313–316, 2001.

[83] A. C. Dada, J. Leach, G. S. Buller, M. J. Padgett, and E. Andersson, "Experimental high-dimensional two-photon entanglement and violations of generalized bell inequalities," *Nature Physics*, vol. 7, no. 9, pp. 677–680, 2011.

[84] J. Leach, B. Jack, J. Romero, M. Ritsch-Marte, R. Boyd, A. Jha, S. Barnett, S. Franke-Arnold, and M. Padgett, "Violation of a Bell inequality in two-dimensional orbital angular momentum state-spaces," *Optics Express*, vol. 17, no. 10, pp. 8287–8293, 2009.

[85] J. Torres, A. Alexandrescu, and L. Torner, "Quantum spiral bandwidth of entangled two-photon states," *Physical Review A*, vol. 68, no. 5, p. 050301, 2003.

[86] F. M. Miatto, A. M. Yao, and S. M. Barnett, "Full characterization of the quantum spiral bandwidth of entangled biphotons," *Physical Review A*, vol. 83, no. 3, p. 033816, 2011.

[87] M. McLaren, J. Romero, M. J. Padgett, F. S. Roux, and A. Forbes, "Two-photon optics of bessel-gaussian modes," *Physical Review A*, vol. 88, no. 3, p. 033818, 2013.

[88] A. C. Dada and E. Andersson, "On bell inequality violations with high-dimensional systems," *International Journal of Quantum Information*, vol. 9, no. 07n08, pp. 1807–1823, 2011.

[89] B. Jack, J. Leach, H. Ritsch, S. Barnett, M. Padgett, and S. Franke-Arnold, "Precise quantum tomography of photon pairs with entangled orbital angular momentum," *New Journal of Physics*, vol. 11, no. 10, p. 103024, 2009.

[90] L. Neves, G. Lima, A. Delgado, and C. Saavedra, "Hybrid photonic entanglement: Realization, characterization, and applications," *Physical Review A*, vol. 80, no. 4, p. 042322, 2009.

[91] E. Nagali and F. Sciarrino, "Generation of hybrid polarization-orbital angular momentum entangled states," *Optics Express*, vol. 18, no. 17, pp. 18243–18248, 2010.

[92] M. Fujiwara, M. Toyoshima, M. Sasaki, K. Yoshino, Y. Nambu, and A. Tomita, "Performance of hybrid entanglement photon pair source for quantum key distribution," *Applied Physics Letters*, vol. 95, no. 26, p. 261103, 2009.

[93] W. K. Wootters and W. H. Zurek, "Complementarity in the double-slit experiment: Quantum nonseparability and a quantitative statement of Bohr's principle," *Physical Review D*, vol. 19, no. 2, p. 473, 1979.

[94] I. Nape, B. Ndagano, and A. Forbes, "Erasing the orbital angular momentum information of a photon," *Physical Review A*, vol. 95, no. 5, p. 053859, 2017.

[95] L. Neves, G. Lima, J. Aguirre, F. Torres-Ruiz, C. Saavedra, and A. Delgado, "Control of quantum interference in the quantum eraser," *New Journal of Physics*, vol. 11, no. 7, p. 073035, 2009.

[96] M. McLaren, T. Konrad, and A. Forbes, "Measuring the nonseparability of vector vortex beams," *Physical Review A*, vol. 92, no. 2, p. 023833, 2015.

[97] R. J. Spreeuw, "A classical analogy of entanglement," *Foundations of physics*, vol. 28, no. 3, pp. 361–374, 1998.

[98] T. Konrad and A. Forbes, "Quantum mechanics and classical light," *Contemporary Physics*, vol. 60, no. 1, pp. 1–22, 2019.

[99] B. Sephton, A. Dudley, G. Ruffato, F. Romanato, L. Marrucci, M. Padgett, S. Goyal, F. Roux, T. Konrad, and A. Forbes, "A versatile quantum walk resonator with bright classical light," *PloS one*, vol. 14, no. 4, p. e0214891, 2019.

[100] F. Cardano, M. Maffei, F. Massa, B. Piccirillo, C. De Lisio, G. De Filippis, V. Cataudella, E. Santamato, and L. Marrucci, "Statistical moments of quantum-walk dynamics reveal topological quantum transitions," *Nature communications*, vol. 7, no. 1, pp. 1–8, 2016.

[101] B. Ndagano, B. Perez-Garcia, F. S. Roux, M. McLaren, C. Rosales-Guzman, Y. Zhang, O. Mouane, R. I. Hernandez-Aranda, T. Konrad, and A. Forbes, "Characterizing quantum channels with non-separable states of classical light," *Nature Physics*, vol. 13, no. 4, p. 397, 2017.

[102] F. Töppel, A. Aiello, C. Marquardt, E. Giacobino, and G. Leuchs, "Classical entanglement in polarization metrology," *New Journal of Physics*, vol. 16, no. 7, p. 073019, 2014.

[103] S. Mamani, L. Shi, T. Ahmed, R. Karnik, A. Rodríguez-Contreras, D. Nolan, and R. Alfano, "Transmission of classically entangled beams through mouse brain tissue," *Journal of biophotonics*, p. e201800096, 2018.

[104] I. Gianani, A. Suprano, T. Giordani, N. Spagnolo, F. Sciarrino, D. Gorpas, V. Ntziachristos, K. Pinker, N. Biton, J. Kupferman, *et al.*, "Transmission of

vector vortex beams in dispersive media," *Advanced Photonics*, vol. 2, no. 3, p. 036003, 2020.

[105] N. Biton, J. Kupferman, and S. Arnon, "Oam light propagation through tissue," *Scientific Reports*, vol. 11, no. 1, pp. 1–9, 2021.

[106] A. Suprano, T. Giordani, I. Gianani, N. Spagnolo, K. Pinker, J. Kupferman, S. Arnon, U. Klemm, D. Gorpas, V. Ntziachristos, *et al.*, "Propagation of structured light through tissue-mimicking phantoms," *Optics Express*, vol. 28, no. 24, pp. 35427–35437, 2020.

[107] M. A. Cox, N. Mphuthi, I. Nape, N. Mashaba, L. Cheng, and A. Forbes, "Structured light in turbulence," *IEEE Journal of Selected Topics in Quantum Electronics*, vol. 27, no. 2, pp. 1–21, 2020.

[108] Y. Gu, O. Korotkova, and G. Gbur, "Scintillation of nonuniformly polarized beams in atmospheric turbulence," *Optics letters*, vol. 34, no. 15, pp. 2261–2263, 2009.

[109] W. Cheng, J. W. Haus, and Q. Zhan, "Propagation of vector vortex beams through a turbulent atmosphere," *Optics express*, vol. 17, no. 20, pp. 17829–17836, 2009.

[110] Y. Cai, Q. Lin, H. T. Eyyuboğlu, and Y. Baykal, "Average irradiance and polarization properties of a radially or azimuthally polarized beam in a turbulent atmosphere," *Optics express*, vol. 16, no. 11, pp. 7665–7673, 2008.

[111] P. Ji-Xiong, W. Tao, L. Hui-Chuan, and L. Cheng-Liang, "Propagation of cylindrical vector beams in a turbulent atmosphere," *Chinese Physics B*, vol. 19, no. 8, p. 089201, 2010.

[112] T. Wang and J. Pu, "Propagation of non-uniformly polarized beams in a turbulent atmosphere," *Optics communications*, vol. 281, no. 14, pp. 3617–3622, 2008.

[113] M. A. Cox, C. Rosales-Guzmán, M. P. J. Lavery, D. J. Versfeld, and A. Forbes, "On the resilience of scalar and vector vortex modes in turbulence," *Optics Express*, vol. 24, pp. 18105–18113, 2016.

[114] P. Lochab, P. Senthilkumaran, and K. Khare, "Designer vector beams maintaining a robust intensity profile on propagation through turbulence," *Physical Review A*, vol. 98, no. 2, p. 023831, 2018.

[115] B. Ndagano, R. Brüning, M. McLaren, M. Duparré, and A. Forbes, "Fiber propagation of vector modes," *Optics express*, vol. 23, no. 13, pp. 17330–17336, 2015.

[116] S. Chen and J. Wang, "Theoretical analyses on orbital angular momentum modes in conventional graded-index multimode fibre," *Scientific reports*, vol. 7, no. 1, pp. 1–15, 2017.

[117] M. L. Almeida, S. Pironio, J. Barrett, G. Tóth, and A. Acín, "Noise robustness of the nonlocality of entangled quantum states," *Physical Review Letters*, vol. 99, no. 4, p. 040403, 2007.

[118] M. A. Nielsen and I. Chuang, *Quantum computation and quantum information*. 2002.

[119] I. L. Chuang and M. A. Nielsen, "Prescription for experimental determination of the dynamics of a quantum black box," *Journal of Modern Optics*, vol. 44, no. 11-12, pp. 2455–2467, 1997.

[120] A. Jamiołkowski, "Linear transformations which preserve trace and positive semidefiniteness of operators," *Reports on Mathematical Physics*, vol. 3, no. 4, pp. 275–278, 1972.

[121] M.-D. Choi, "Completely positive linear maps on complex matrices," *Linear algebra and its applications*, vol. 10, no. 3, pp. 285–290, 1975.

[122] M. Jiang, S. Luo, and S. Fu, "Channel-state duality," *Physical Review A*, vol. 87, no. 2, p. 022310, 2013.

[123] F. Bouchard, A. Sit, F. Hufnagel, A. Abbas, Y. Zhang, K. Heshami, R. Fickler, C. Marquardt, G. Leuchs, R. W. Boyd, *et al.*, "Underwater quantum key distribution in outdoor conditions with twisted photons," *arXiv preprint arXiv:1801.10299*, 2018.

[124] A. Sit, R. Fickler, F. Alsaiari, F. Bouchard, H. Larocque, P. Gregg, L. Yan, R. W. Boyd, S. Ramachandran, and E. Karimi, "Quantum cryptography with structured photons through a vortex fiber," *Optics letters*, vol. 43, no. 17, pp. 4108–4111, 2018.

[125] N. H. Valencia, S. Goel, W. McCutcheon, H. Defienne, and M. Malik, "Unscrambling entanglement through a complex medium," *Nature Physics*, vol. 16, no. 11, pp. 1112–1116, 2020.

[126] T. Konrad, F. De Melo, M. Tiersch, C. Kasztelan, A. Aragão, and A. Buchleitner, "Evolution equation for quantum entanglement," *Nature physics*, vol. 4, no. 2, pp. 99–102, 2008.

[127] W. K. Wootters, "Entanglement of formation and concurrence.," *Quantum Information & Computation*, vol. 1, no. 1, pp. 27–44, 2001.

[128] A. H. Ibrahim, F. S. Roux, M. McLaren, T. Konrad, and A. Forbes, "Orbital-angular-momentum entanglement in turbulence," *Physical Review A*, vol. 88, no. 1, p. 012312, 2013.

[129] D. Collins, N. Gisin, N. Linden, S. Massar, and S. Popescu, "Bell inequalities for arbitrarily high-dimensional systems," *Physical Review Letters*, vol. 88, p. 040404, Jan. 2002.

[130] K. Zhu, L. Yin, C. Wang, and G. Long, "Protecting the orbital angular momentum of photonic qubits using quantum error correction," *EPL (Europhysics Letters)*, vol. 132, no. 5, p. 50005, 2021.

[131] Z. Hou, J.-F. Tang, C. Ferrie, G.-Y. Xiang, C.-F. Li, and G.-C. Guo, "Experimental realization of self-guided quantum process tomography," *Physical Review A*, vol. 101, no. 2, p. 022317, 2020.

[132] M. Mohseni, A. T. Rezakhani, and D. A. Lidar, "Quantum-process tomography: Resource analysis of different strategies," *Physical Review A*, vol. 77, no. 3, p. 032322, 2008.

[133] C. H. Bennett, "Quantum cryptography: Public key distribution and coin tossing," in *International Conference on Computer System and Signal Processing, IEEE, 1984*, pp. 175–179, 1984.

[134] P. W. Shor and J. Preskill, "Simple proof of security of the bb84 quantum key distribution protocol," *Physical review letters*, vol. 85, no. 2, p. 441, 2000.

[135] T. Schmitt-Manderbach, H. Weier, M. Fürst, R. Ursin, F. Tiefenbacher, T. Scheidl, J. Perdigues, Z. Sodnik, C. Kurtsiefer, J. G. Rarity, *et al.*, "Experimental demonstration of free-space decoy-state quantum key distribution over 144 km," *Physical Review Letters*, vol. 98, no. 1, p. 010504, 2007.

[136] C. Gobby, Z. Yuan, and A. Shields, "Quantum key distribution over 122 km of standard telecom fiber," *Applied Physics Letters*, vol. 84, no. 19, pp. 3762–3764, 2004.

[137] S.-K. Liao, W.-Q. Cai, W.-Y. Liu, L. Zhang, Y. Li, J.-G. Ren, J. Yin, Q. Shen, Y. Cao, Z.-P. Li, *et al.*, "Satellite-to-ground quantum key distribution," *Nature*, vol. 549, no. 7670, pp. 43–47, 2017.

[138] N. Bozinovic, Y. Yue, Y. Ren, M. Tur, P. Kristensen, H. Huang, A. E. Willner, and S. Ramachandran, "Terabit-scale orbital angular momentum mode division multiplexing in fibers," *science*, vol. 340, no. 6140, pp. 1545–1548, 2013.

[139] S. Gröblacher, T. Jennewein, A. Vaziri, G. Weihs, and A. Zeilinger, "Experimental quantum cryptography with qutrits," *New Journal of Physics*, vol. 8, no. 5, p. 75, 2006.

[140] G. Molina-Terriza, J. P. Torres, and L. Torner, "Twisted photons," *Nature Physics*, vol. 3, no. 5, pp. 305–310, 2007.

[141] G. Milione, T. A. Nguyen, J. Leach, D. A. Nolan, and R. R. Alfano, "Using the nonseparability of vector beams to encode information for optical communication," *Optics Letters*, vol. 40, no. 21, p. 4887, 2015.

[142] P. Li, B. Wang, and X. Zhang, "High-dimensional encoding based on classical nonseparability," *Optics Express*, vol. 24, p. 15143, jun 2016.

[143] G. Milione, M. P. J. Lavery, H. Huang, Y. Ren, G. Xie, T. A. Nguyen, E. Karimi, L. Marrucci, D. A. Nolan, R. R. Alfano, and A. E. Willner, "4 × 20 Gbit/s mode division multiplexing over free space using vector modes and a q-plate mode (de)multiplexer.," *Optics letters*, vol. 40, no. 9, pp. 1980–3, 2015.

[144] J. Liu, S.-M. Li, L. Zhu, A.-D. Wang, S. Chen, C. Klitis, C. Du, Q. Mo, M. Sorel, S.-Y. Yu, X.-L. Cai, and J. Wang, "Direct fiber vector eigenmode multiplexing transmission seeded by integrated optical vortex emitters," *Light: Science & Applications*, vol. 7, no. 3, p. 17148, 2018.

[145] C. Souza, C. Borges, a. Khoury, J. Huguenin, L. Aolita, and S. Walborn, "Quantum key distribution without a shared reference frame," *Physical Review A*, vol. 77, pp. 1–4, 2008.

[146] G. Vallone, V. D'Ambrosio, A. Sponselli, S. Slussarenko, L. Marrucci, F. Sciarrino, and P. Villoresi, "Free-space quantum key distribution by rotation-invariant twisted photons," *Physical review letters*, vol. 113, no. 6, p. 060503, 2014.

[147] B. Ndagano, I. Nape, B. Perez-Garcia, S. Scholes, R. I. Hernandez-Aranda, T. Konrad, M. P. Lavery, and A. Forbes, "A deterministic detector for vector vortex states," *Sci Rep*, vol. 7, no. 1, p. 13882, 2017.

[148] A. Sit, F. Bouchard, R. Fickler, J. Gagnon-Bischoff, H. Larocque, K. Heshami, D. Elser, C. Peuntinger, K. Günthner, B. Heim, *et al.*, "High-dimensional in-

tracity quantum cryptography with structured photons," *Optica*, vol. 4, no. 9, pp. 1006–1010, 2017.

[149] M. Huber and M. Pawłowski, "Weak randomness in device-independent quantum key distribution and the advantage of using high-dimensional entanglement," *Physical Review A*, vol. 88, no. 3, p. 032309, 2013.

[150] M. Krenn, R. Fickler, M. Fink, J. Handsteiner, M. Malik, T. Scheidl, R. Ursin, and A. Zeilinger, "Communication with spatially modulated light through turbulent air across vienna," *New Journal of Physics*, vol. 16, no. 11, p. 113028, 2014.

[151] Y. Zhang, S. Prabhakar, A. H. Ibrahim, F. S. Roux, A. Forbes, and T. Konrad, "Experimentally observed decay of high-dimensional entanglement through turbulence," *Physical Review A*, vol. 94, no. 3, p. 032310, 2016.

[152] M. McLaren, T. Mhlanga, M. J. Padgett, F. S. Roux, and A. Forbes, "Self-healing of quantum entanglement after an obstruction," *Nature Communications*, vol. 5, pp. 3248 EP –, 02 2014.

[153] C. Erven, B. Heim, E. Meyer-Scott, J. Bourgoin, R. Laflamme, G. Weihs, and T. Jennewein, "Studying free-space transmission statistics and improving free-space quantum key distribution in the turbulent atmosphere," *New Journal of Physics*, vol. 14, no. 12, p. 123018, 2012.

[154] F. Gori, G. Guattari, and C. Padovani, "Bessel-gauss beams," *Optics Communications*, vol. 64, no. 6, pp. 491 – 495, 1987.

[155] D. McGloin, V. Garcés-Chávez, and K. Dholakia, "Interfering bessel beams for optical micromanipulation," *Optics Letters*, vol. 28, pp. 657–659, Apr 2003.

[156] I. A. Litvin, M. G. McLaren, and A. Forbes, "A conical wave approach to calculating bessel–gauss beam reconstruction after complex obstacles," *Optics Communications*, vol. 282, no. 6, pp. 1078 – 1082, 2009.

[157] G. Milione, A. Dudley, T. A. Nguyen, O. Chakraborty, E. Karimi, A. Forbes, and R. R. Alfano, "Measuring the self-healing of the spatially inhomogeneous states of polarization of vector bessel beams," *Journal of Optics*, vol. 17, no. 3, p. 035617, 2015.

[158] G. Wu, F. Wang, and Y. Cai, "Generation and self-healing of a radially polarized bessel-gauss beam," *Physical Review A*, vol. 89, p. 043807, Apr 2014.

[159] P. Li, Y. Zhang, S. Liu, H. Cheng, L. Han, D. Wu, and J. Zhao, "Generation and self-healing of vector bessel-gauss beams with variant state of polarizations upon propagation," *Optics Express*, vol. 25, pp. 5821–5831, Mar 2017.

[160] E. Otte, I. Nape, C. Rosales-Guzmán, A. Vallés, C. Denz, and A. Forbes, "Recovery of nonseparability in self-healing vector bessel beams," *Physical Review A*, vol. 98, no. 5, p. 053818, 2018.

[161] E. Otte, C. Rosales-Guzmán, B. Ndagano, C. Denz, and A. Forbes, "Entanglement beating in free space through spin-orbit coupling," *Light: Science & Applications*, vol. 7, p. e18009, 2018.

[162] Z. Bouchal, J. Wagner, and M. Chlup, "Self-reconstruction of a distorted nondiffracting beam," *Optics Communications*, vol. 151, no. 4, pp. 207 – 211, 1998.

[163] B. Sephton, A. Dudley, and A. Forbes, "Revealing the radial modes in vortex beams," *Applied Optics*, vol. 55, no. 28, pp. 7830–7835, 2016.

[164] G. Milione, H. I. Sztul, D. a. Nolan, and R. R. Alfano, "Higher-Order Poincaré Sphere, Stokes Parameters, and the Angular Momentum of Light," *Physical Review Letters*, vol. 107, p. 053601, jul 2011.

[165] A. Holleczek, A. Aiello, C. Gabriel, C. Marquardt, and G. Leuchs, "Classical and quantum properties of cylindrically polarized states of light," *Optics express*, vol. 19, no. 10, pp. 9714–9736, 2011.

[166] M. Eisaman, J. Fan, A. Migdall, and S. V. Polyakov, "Invited review article: Single-photon sources and detectors," *Review of scientific instruments*, vol. 82, no. 7, p. 071101, 2011.

[167] Q. Wang, W. Chen, G. Xavier, M. Swillo, T. Zhang, S. Sauge, M. Tengner, Z.-F. Han, G.-C. Guo, and A. Karlsson, "Experimental decoy-state quantum key distribution with a sub-poissionian heralded single-photon source," *Physical Review Letters*, vol. 100, no. 9, p. 090501, 2008.

[168] Y. Zhang, M. Mclaren, F. S. Roux, and A. Forbes, "Simulating spontaneous parametric down-conversion using classical light," in *SPIE Optical Engineering+ Applications*, pp. 919408–919408, International Society for Optics and Photonics, 2014.

[169] A. Forbes, A. Dudley, and M. McLaren, "Creation and detection of optical modes with spatial light modulators," *Advances in Optics and Photonics*, vol. 8, p. 200, jun 2016.

[170] J. Turunen, A. Vasara, and A. T. Friberg, "Holographic generation of diffraction-free beams," *Applied Optics*, vol. 27, pp. 3959–3962, Oct 1988.

[171] D. M. Cottrell, J. M. Craven, and J. A. Davis, "Nondiffracting random intensity patterns," *Optics Letters*, vol. 32, pp. 298–300, Feb 2007.

[172] J. A. Davis, D. M. Cottrell, J. Campos, M. J. Yzuel, and I. Moreno, "Encoding amplitude information onto phase-only filters," *Applied Optics*, vol. 38, pp. 5004–5013, Aug 1999.

[173] B. Piccirillo, V. D'Ambrosio, S. Slussarenko, L. Marrucci, and E. Santamato, "Photon spin-to-orbital angular momentum conversion via an electrically tunable q-plate," *Applied Physics Letters*, vol. 97, no. 24, p. 241104, 2010.

[174] D. Gottesman, H.-K. Lo, N. Lutkenhaus, and J. Preskill, "Security of quantum key distribution with imperfect devices," in *International Symposium onInformation Theory, 2004. ISIT 2004. Proceedings.*, p. 136, IEEE, 2004.

[175] M. Schiavon, G. Vallone, F. Ticozzi, and P. Villoresi, "Heralded single-photon sources for quantum-key-distribution applications," *Physical Review A*, vol. 93, no. 1, p. 012331, 2016.

[176] J. Mendoza-Hernández, M. L. Arroyo-Carrasco, M. D. Iturbe-Castillo, and S. Chávez-Cerda, "Laguerre–gauss beams versus bessel beams showdown: peer comparison," *Optics Letters*, vol. 40, no. 16, pp. 3739–3742, 2015.

[177] N. Ahmed, Z. Zhao, L. Li, H. Huang, M. P. Lavery, P. Liao, Y. Yan, Z. Wang, G. Xie, Y. Ren, *et al.*, "Mode-division-multiplexing of multiple bessel-gaussian beams carrying orbital-angular-momentum for obstruction-tolerant free-space optical and millimetre-wave communication links," *Scientific reports*, vol. 6, p. 22082, 2016.

[178] N. Mphuthi, R. Botha, and A. Forbes, "Are bessel beams resilient to aberrations and turbulence?," *JOSA A*, vol. 35, no. 6, pp. 1021–1027, 2018.

[179] M. A. Cox, C. Rosales-Guzmán, M. P. J. Lavery, D. J. Versfeld, and A. Forbes, "On the resilience of scalar and vector vortex modes in turbulence," *Optics Express*, vol. 24, no. 16, p. 18105, 2016.

[180] Y. Yuan, T. Lei, Z. Li, Y. Li, S. Gao, Z. Xie, and X. Yuan, "Beam wander relieved orbital angular momentum communication in turbulent atmosphere using bessel beams," *Scientific Reports*, vol. 7, p. 42276, 2017.

[181] H. Singh, D. Gupta, and A. Singh, "Quantum key distribution protocols: a review," *IOSR Journal of Computer Engineering (IOSR-JCE)*, vol. 16, 2014.

[182] F. Bouchard, A. Sit, K. Heshami, R. Fickler, and E. Karimi, "Round-robin differential-phase-shift quantum key distribution with twisted photons," *Physical Review A*, vol. 98, no. 1, p. 010301, 2018.

[183] S. Etcheverry, G. Cañas, E. Gómez, W. Nogueira, C. Saavedra, G. Xavier, and G. Lima, "Quantum key distribution session with 16-dimensional photonic states," *Scientific reports*, vol. 3, p. 2316, 2013.

[184] G. Cañas, N. Vera, J. Cariñe, P. González, J. Cardenas, P. Connolly, A. Przysiezna, E. Gómez, M. Figueroa, G. Vallone, *et al.*, "High-dimensional decoy-state quantum key distribution over multicore telecommunication fibers," *Physical Review A*, vol. 96, no. 2, p. 022317, 2017.

[185] E. Diamanti, H.-K. Lo, B. Qi, and Z. Yuan, "Practical challenges in quantum key distribution," *npj Quantum Information*, vol. 2, p. 16025, 2016.

[186] H. Rubinsztein-Dunlop, A. Forbes, M. V. Berry, M. R. Dennis, D. L. Andrews, M. Mansuripur, C. Denz, C. Alpmann, P. Banzer, T. Bauer, *et al.*, "Roadmap on structured light," *Journal of Optics*, vol. 19, no. 1, p. 013001, 2016.

[187] A. Forbes, M. de Oliveira, and M. R. Dennis, "Structured light," *Nature Photonics*, vol. 15, no. 4, pp. 253–262, 2021.

[188] B. Ndagano, I. Nape, M. A. Cox, C. Rosales-Guzman, and A. Forbes, "Creation and detection of vector vortex modes for classical and quantum communication," *Journal of Lightwave Technology*, vol. 36, pp. 292–301, Jan 2018.

[189] C. Rosales-Guzmán, B. Ndagano, and A. Forbes, "A review of complex vector light fields and their applications," *Journal of Optics*, vol. 20, no. 12, p. 123001, 2018.

[190] M. Li, S. Yan, Y. Zhang, Y. Liang, P. Zhang, and B. Yao, "Optical sorting of small chiral particles by tightly focused vector beams," *Physical Review A*, vol. 99, no. 3, p. 033825, 2019.

[191] Y. Zhang, B. Ding, and T. Suyama, "Trapping two types of particles using a double-ring-shaped radially polarized beam," *Physical Review A*, vol. 81, no. 2, p. 023831, 2010.

[192] N. Bhebhe, P. A. Williams, C. Rosales-Guzmán, V. Rodriguez-Fajardo, and A. Forbes, "A vector holographic optical trap," *Scientific reports*, vol. 8, no. 1, pp. 1–9, 2018.

[193] S. Berg-Johansen, F. Töppel, B. Stiller, P. Banzer, M. Ornigotti, E. Giacobino, G. Leuchs, A. Aiello, and C. Marquardt, "Classically entangled optical beams for high-speed kinematic sensing," *Optica*, vol. 2, no. 10, pp. 864–868, 2015.

[194] G. Milione, M. P. Lavery, H. Huang, Y. Ren, G. Xie, T. A. Nguyen, E. Karimi, L. Marrucci, D. A. Nolan, R. R. Alfano, *et al.*, "4× 20 gbit/s mode division multiplexing over free space using vector modes and a q-plate mode (de) multiplexer," *Optics letters*, vol. 40, no. 9, pp. 1980–1983, 2015.

[195] Y. Zhao and J. Wang, "High-base vector beam encoding/decoding for visible-light communications," *Optics Letters*, vol. 40, no. 21, pp. 4843–4846, 2015.

[196] A. E. Willner, "Vector-mode multiplexing brings an additional approach for capacity growth in optical fibers," *Light: Science & Applications*, vol. 7, no. 3, pp. 18002–18002, 2018.

[197] D. Cozzolino, D. Bacco, B. Da Lio, K. Ingerslev, Y. Ding, K. Dalgaard, P. Kristensen, M. Galili, K. Rottwitt, S. Ramachandran, *et al.*, "Orbital angular momentum states enabling fiber-based high-dimensional quantum communication," *Phys Rev Appl*, vol. 11, no. 6, p. 064058, 2019.

[198] V. Parigi, V. D'Ambrosio, C. Arnold, L. Marrucci, F. Sciarrino, and J. Laurat, "Storage and retrieval of vector beams of light in a multiple-degree-of-freedom quantum memory," *Nature communications*, vol. 6, no. 1, pp. 1–7, 2015.

[199] B. Sun, A. Wang, L. Xu, C. Gu, Z. Lin, H. Ming, and Q. Zhan, "Low-threshold single-wavelength all-fiber laser generating cylindrical vector beams using a few-mode fiber bragg grating," *Optics letters*, vol. 37, no. 4, pp. 464–466, 2012.

[200] D. Naidoo, F. S. Roux, A. Dudley, I. Litvin, B. Piccirillo, L. Marrucci, and A. Forbes, "Controlled generation of higher-order poincaré sphere beams from a laser," *Nature Photonics*, vol. 10, no. 5, pp. 327–332, 2016.

[201] H. Sroor, Y.-W. Huang, B. Sephton, D. Naidoo, A. Vallés, V. Ginis, C.-W. Qiu, A. Ambrosio, F. Capasso, and A. Forbes, "High-purity orbital angular

momentum states from a visible metasurface laser," *Nature Photonics*, vol. 14, pp. 498–503, 2020.

[202] L. Marrucci, "The q-plate and its future," *Journal of Nanophotonics*, vol. 7, no. 1, p. 078598, 2013.

[203] R. C. Devlin, A. Ambrosio, N. A. Rubin, J. B. Mueller, and F. Capasso, "Arbitrary spin-to–orbital angular momentum conversion of light," *Science*, vol. 358, no. 6365, pp. 896–901, 2017.

[204] J. B. Mueller, N. A. Rubin, R. C. Devlin, B. Groever, and F. Capasso, "Metasurface polarization optics: independent phase control of arbitrary orthogonal states of polarization," *Physical Review Letters*, vol. 118, no. 11, p. 113901, 2017.

[205] C. Rosales-Guzmán, X.-B. Hu, A. Selyem, P. Moreno-Acosta, S. Franke-Arnold, R. Ramos-Garcia, and A. Forbes, "Polarisation-insensitive generation of complex vector modes from a digital micromirror device," *Scientific Reports*, vol. 10, no. 1, pp. 1–9, 2020.

[206] E. Nagali, L. Sansoni, L. Marrucci, E. Santamato, and F. Sciarrino, "Experimental generation and characterization of single-photon hybrid ququarts based on polarization and orbital angular momentum encoding," *Physical Review A*, vol. 81, no. 5, p. 052317, 2010.

[207] S. Slussarenko, V. D'Ambrosio, B. Piccirillo, L. Marrucci, and E. Santamato, "The polarizing sagnac interferometer: a tool for light orbital angular momentum sorting and spin-orbit photon processing," *Optics Express*, vol. 18, no. 26, pp. 27205–27216, 2010.

[208] G. F. Walsh, "Pancharatnam-berry optical element sorter of full angular momentum eigenstate," *Optics Express*, vol. 24, no. 6, pp. 6689–6704, 2016.

[209] A. Selyem, C. Rosales-Guzmán, S. Croke, A. Forbes, and S. Franke-Arnold, "Basis independent tomography of complex vectorial light fields by stokes projections," *arXiv preprint arXiv:1902.07988*, 2019.

[210] A. Manthalkar, I. Nape, N. T. Bordbar, C. Rosales-Guzmán, S. Bhattacharya, A. Forbes, and A. Dudley, "All-digital stokes polarimetry with a digital micromirror device," *Optics letters*, vol. 45, no. 8, pp. 2319–2322, 2020.

[211] K. Singh, N. Tabebordbar, A. Forbes, and A. Dudley, "Digital stokes polarimetry and its application to structured light: tutorial," *JOSA A*, vol. 37, no. 11, pp. C33–C44, 2020.

[212] B. Ndagano, B. Perez-Garcia, F. S. Roux, M. McLaren, C. Rosales-Guzman, Y. Zhang, O. Mouane, R. I. Hernandez-Aranda, T. Konrad, and A. Forbes, "Process tomography of quantum channels using classical light," pp. 1–12, 2016.

[213] J. Whinnery, D. Miller, and F. Dabby, "Thermal convention and spherical aberration distortion of laser beams in low-loss liquids," *IEEE Journal of Quantum Electronics*, vol. 3, no. 9, pp. 382–383, 1967.

[214] L. C. Andrews and R. L. Phillips, "Laser beam propagation through random media," SPIE, 2005.

[215] F. Hufnagel, A. Sit, F. Bouchard, Y. Zhang, D. England, K. Heshami, B. J. Sussman, and E. Karimi, "Investigation of underwater quantum channels in a 30 meter flume tank using structured photons," *New Journal of Physics*, vol. 22, no. 9, p. 093074, 2020.

[216] F. S. Roux, "Infinitesimal-propagation equation for decoherence of an orbital-angular-momentum-entangled biphoton state in atmospheric turbulence," *Physical Review A*, vol. 83, no. 5, p. 053822, 2011.

[217] G. A. Tyler and R. W. Boyd, "Influence of atmospheric turbulence on the propagation of quantum states of light carrying orbital angular momentum," *Optics letters*, vol. 34, no. 2, pp. 142–144, 2009.

[218] B. J. Smith and M. Raymer, "Two-photon wave mechanics," *Physical Review A*, vol. 74, no. 6, p. 062104, 2006.

[219] N. Leonhard, G. Sorelli, V. N. Shatokhin, C. Reinlein, and A. Buchleitner, "Protecting the entanglement of twisted photons by adaptive optics," *Physical Review A*, vol. 97, no. 1, p. 012321, 2018.

[220] B.-J. Pors, C. Monken, E. R. Eliel, and J. Woerdman, "Transport of orbital-angular-momentum entanglement through a turbulent atmosphere," *Optics express*, vol. 19, no. 7, pp. 6671–6683, 2011.

[221] M. Malik, M. O'Sullivan, B. Rodenburg, M. Mirhosseini, J. Leach, M. P. Lavery, M. J. Padgett, and R. W. Boyd, "Influence of atmospheric turbulence on optical communications using orbital angular momentum for encoding," *Optics express*, vol. 20, no. 12, pp. 13195–13200, 2012.

[222] M. Krenn, J. Handsteiner, M. Fink, R. Fickler, and A. Zeilinger, "Twisted photon entanglement through turbulent air across vienna," *Proceedings of the National Academy of Sciences*, vol. 112, no. 46, pp. 14197–14201, 2015.

[223] C. Chen and H. Yang, "Characterizing the radial content of orbital-angular-momentum photonic states impaired by weak-to-strong atmospheric turbulence," *Optics Express*, vol. 24, no. 17, pp. 19713–19727, 2016.

[224] A. Aiello, F. Töppel, C. Marquardt, E. Giacobino, and G. Leuchs, "Quantum-like nonseparable structures in optical beams," *New Journal of Physics*, vol. 17, no. 4, p. 043024, 2015.

[225] A. Forbes, A. Aiello, and B. Ndagano, "Classically entangled light," *Progress in Optics*, vol. 64, p. 99, 2019.

[226] R. J. C. Spreeuw, "A classical analogy of entanglement," *Foundations of Physics*, vol. 28, pp. 361–374, 1998.

[227] J. H. Eberly, X.-F. Qian, A. A. Qasimi, H. Ali, M. A. Alonso, R. Gutiérrez-Cuevas, B. J. Little, J. C. Howell, T. Malhotra, and A. N. Vamivakas, "Quantum and classical optics–emerging links," *Physica Scripta*, vol. 91, no. 6, p. 063003, 2016.

[228] E. Toninelli, B. Ndagano, A. Vallés, B. Sephton, I. Nape, A. Ambrosio, F. Capasso, M. J. Padgett, and A. Forbes, "Concepts in quantum state tomography and classical implementation with intense light: a tutorial," *Advances in Optics and Photonics*, vol. 11, no. 1, pp. 67–134, 2019.

[229] C. Rosales-Guzmán, N. Bhebhe, and A. Forbes, "Simultaneous generation of multiple vector beams on a single slm," *Optics Express*, vol. 25, pp. 25697–25706, Oct 2017.

[230] H. Sroor, N. Lisa, D. Naidoo, I. Litvin, and A. Forbes, "Purity of vector vortex beams through a birefringent amplifier," *Physical Review Applied*, vol. 9, no. 4, p. 044010, 2018.

[231] D. L. Fried, "Statistics of a geometric representation of wavefront distortion," *JoSA*, vol. 55, no. 11, pp. 1427–1435, 1965.

[232] L. Zhang, F. Shen, B. Lan, and A. Tang, "Mode-dependent crosstalk and detection probability of orbital angular momentum of optical vortex beam through atmospheric turbulence," *Journal of Optics*, vol. 22, no. 7, p. 075607, 2020.

[233] V. Arrizón, U. Ruiz, R. Carrada, and L. A. González, "Pixelated phase computer holograms for the accurate encoding of scalar complex fields," *JOSA A*, vol. 24, no. 11, pp. 3500–3507, 2007.

[234] S. Zhao, J. Leach, L. Gong, J. Ding, and B. Zheng, "Aberration corrections for free-space optical communications in atmosphere turbulence using orbital angular momentum states," *Optics express*, vol. 20, no. 1, pp. 452–461, 2012.

[235] D. Flamm, D. Naidoo, C. Schulze, A. Forbes, and M. Duparré, "Mode analysis with a spatial light modulator as a correlation filter," *Optics letters*, vol. 37, no. 13, pp. 2478–2480, 2012.

[236] W.-H. Lee, "Binary computer-generated holograms," *Applied Optics*, vol. 18, no. 21, pp. 3661–3669, 1979.

[237] Y. Zhai, S. Fu, J. Zhang, X. Liu, H. Zhou, and C. Gao, "Turbulence aberration correction for vector vortex beams using deep neural networks on experimental data," *Optics Express*, vol. 28, no. 5, pp. 7515–7527, 2020.

[238] M. Malik, H. Shin, M. O'Sullivan, P. Zerom, and R. W. Boyd, "Quantum ghost image identification with correlated photon pairs," *Physical review letters*, vol. 104, no. 16, p. 163602, 2010.

[239] S. Scholes, R. Kara, J. Pinnell, V. Rodríguez-Fajardo, and A. Forbes, "Structured light with digital micromirror devices: a guide to best practice," *Optical Engineering*, vol. 59, no. 4, p. 041202, 2019.

[240] Y. Shen, Y. Hou, N. Papasimakis, and N. I. Zheludev, "Supertoroidal light pulses: Propagating electromagnetic skyrmions in free space," *arXiv preprint arXiv:2103.08431*, 2021.

[241] S. Gao, F. C. Speirits, F. Castellucci, S. Franke-Arnold, S. M. Barnett, and J. B. Götte, "Paraxial skyrmionic beams," *Physical Review A*, vol. 102, no. 5, p. 053513, 2020.

[242] H. Larocque, D. Sugic, D. Mortimer, A. J. Taylor, R. Fickler, R. W. Boyd, M. R. Dennis, and E. Karimi, "Reconstructing the topology of optical polarization knots," *Nature Physics*, vol. 14, no. 11, pp. 1079–1082, 2018.

[243] E. J. Galvez, B. L. Rojec, V. Kumar, and N. K. Viswanathan, "Generation of isolated asymmetric umbilics in light's polarization," *Physical Review A*, vol. 89, no. 3, p. 031801, 2014.

[244] A. Zdagkas, Y. Shen, C. McDonnell, J. Deng, G. Li, T. Ellenbogen, N. Papasimakis, and N. Zheludev, "Observation of toroidal pulses of light," *arXiv preprint arXiv:2102.03636*, 2021.

[245] S. Keren-Zur, M. Tal, S. Fleischer, D. M. Mittleman, and T. Ellenbogen, "Generation of spatiotemporally tailored terahertz wavepackets by nonlinear metasurfaces," *Nature communications*, vol. 10, no. 1, pp. 1–6, 2019.

[246] T. Bauer, P. Banzer, E. Karimi, S. Orlov, A. Rubano, L. Marrucci, E. Santamato, R. W. Boyd, and G. Leuchs, "Observation of optical polarization möbius strips," *Science*, vol. 347, no. 6225, pp. 964–966, 2015.

[247] T. G. Brown, "Unconventional polarization states: beam propagation, focusing, and imaging," *Progress in Optics*, vol. 56, pp. 81–129, 2011.

[248] J. Wang, F. Castellucci, and S. Franke-Arnold, "Vectorial light–matter interaction: Exploring spatially structured complex light fields," *AVS Quantum Science*, vol. 2, no. 3, p. 031702, 2020.

[249] E. Otte, C. Alpmann, and C. Denz, "Polarization singularity explosions in tailored light fields," *Laser & Photonics Reviews*, vol. 12, no. 6, p. 1700200, 2018.

[250] S. Sederberg, F. Kong, F. Hufnagel, C. Zhang, E. Karimi, and P. B. Corkum, "Vectorized optoelectronic control and metrology in a semiconductor," *Nature Photonics*, vol. 14, no. 11, pp. 680–685, 2020.

[251] Y. Fang, M. Han, P. Ge, Z. Guo, X. Yu, Y. Deng, C. Wu, Q. Gong, and Y. Liu, "Photoelectronic mapping of the spin–orbit interaction of intense light fields," *Nature Photonics*, vol. 15, no. 2, pp. 115–120, 2021.

[252] M. El Ketara, H. Kobayashi, and E. Brasselet, "Sensitive vectorial optomechanical footprint of light in soft condensed matter," *Nature Photonics*, vol. 15, no. 2, pp. 121–124, 2021.

[253] R. D. Hawley, J. Cork, N. Radwell, and S. Franke-Arnold, "Passive broadband full stokes polarimeter using a fresnel cone," *Scientific Reports*, vol. 9, Feb. 2019.

[254] L. Fang, Z. Wan, A. Forbes, and J. Wang, "Vectorial doppler metrology," *Nature Communications*, vol. 12, no. 1, pp. 1–10, 2021.

[255] V. Curcio, L. A. Alemán-Castañeda, T. G. Brown, S. Brasselet, and M. A. Alonso, "Birefringent fourier filtering for single molecule coordinate and height super-resolution imaging with dithering and orientation," *Nature communications*, vol. 11, no. 1, pp. 1–13, 2020.

[256] J. Zhang, X. Wu, J. Li, L. Lu, J. Tu, Z. Li, and C. Lu, "Fiber vector eigenmode multiplexing based high capacity transmission over 5-km fmf with kramers-kronig receiver," *Journal of Lightwave Technology*, 2021.

[257] Z. Zhu, M. Janasik, A. Fyffe, D. Hay, Y. Zhou, B. Kantor, T. Winder, R. W. Boyd, G. Leuchs, and Z. Shi, "Compensation-free high-dimensional free-space optical communication using turbulence-resilient vector beams," *Nature communications*, vol. 12, no. 1, pp. 1–8, 2021.

[258] N. Radwell, R. Hawley, J. Götte, and S. Franke-Arnold, "Achromatic vector vortex beams from a glass cone," *Nature communications*, vol. 7, no. 1, pp. 1–6, 2016.

[259] A. M. Beckley, T. G. Brown, and M. A. Alonso, "Full poincaré beams," *Optics express*, vol. 18, no. 10, pp. 10777–10785, 2010.

[260] C. He, J. Chang, Q. Hu, J. Wang, J. Antonello, H. He, S. Liu, J. Lin, B. Dai, D. S. Elson, *et al.*, "Complex vectorial optics through gradient index lens cascades," *Nature communications*, vol. 10, no. 1, pp. 1–8, 2019.

[261] J. Chen, Y. Wang, C. Wan, K. Lu, Y. Liu, and Q. Zhan, "Compact vectorial optical field generator based on a 10-megapixel resolution liquid crystal spatial light modulator," *Optics Communications*, p. 127112, 2021.

[262] H.-J. Wu, H.-R. Yang, C. Rosales-Guzmán, W. Gao, B.-S. Shi, Z.-H. Zhu, *et al.*, "Vectorial nonlinear optics: Type-ii second-harmonic generation driven by spin-orbit-coupled fields," *Physical Review A*, vol. 100, no. 5, p. 053840, 2019.

[263] Y. Tang, K. Li, X. Zhang, J. Deng, G. Li, and E. Brasselet, "Harmonic spin–orbit angular momentum cascade in nonlinear optical crystals," *Nature Photonics*, vol. 14, no. 11, pp. 658–662, 2020.

[264] M. G. Nassiri and E. Brasselet, "Multispectral management of the photon orbital angular momentum," *Physical Review Letters*, vol. 121, no. 21, p. 213901, 2018.

[265] A. Forbes, "Structured light from lasers," *Laser & Photonics Reviews*, vol. 13, no. 11, p. 1900140, 2019.

[266] A. M. Beckley, T. G. Brown, and M. A. Alonso, "Full poincaré beams ii: partial polarization," *Optics express*, vol. 20, no. 9, pp. 9357–9362, 2012.

[267] Z. Ma and S. Ramachandran, "Propagation stability in optical fibers: role of path memory and angular momentum," *Nanophotonics*, vol. 1, no. ahead-of-print, 2020.

[268] D. P. Biss and T. Brown, "Primary aberrations in focused radially polarized vortex beams," *Optics express*, vol. 12, no. 3, pp. 384–393, 2004.

[269] K. S. Youngworth and T. G. Brown, "Focusing of high numerical aperture cylindrical-vector beams," *Optics Express*, vol. 7, no. 2, pp. 77–87, 2000.

[270] F. Bouchard, A. Sit, F. Hufnagel, A. Abbas, Y. Zhang, K. Heshami, R. Fickler, C. Marquardt, G. Leuchs, E. Karimi, *et al.*, "Quantum cryptography with twisted photons through an outdoor underwater channel," *Optics express*, vol. 26, no. 17, pp. 22563–22573, 2018.

[271] Y. Ren, L. Li, Z. Wang, S. M. Kamali, E. Arbabi, A. Arbabi, Z. Zhao, G. Xie, Y. Cao, N. Ahmed, *et al.*, "Orbital angular momentum-based space division

multiplexing for high-capacity underwater optical communications," *Scientific reports*, vol. 6, no. 1, pp. 1–10, 2016.

[272] K. H. Kagalwala, G. Di Giuseppe, A. F. Abouraddy, and B. E. Saleh, "Bell's measure in classical optical coherence," *Nature Photonics*, vol. 7, no. 1, pp. 72–78, 2013.

[273] X.-F. Qian and J. Eberly, "Entanglement and classical polarization states," *Optics Letters*, vol. 36, no. 20, pp. 4110–4112, 2011.

[274] B. Ndagano, B. Perez-Garcia, F. S. Roux, M. McLaren, C. Rosales-Guzman, Y. Zhang, O. Mouane, R. I. Hernandez-Aranda, T. Konrad, and A. Forbes, "Characterizing quantum channels with non-separable states of classical light," *Nature Physics*, vol. 13, no. 4, pp. 397–402, 2017.

[275] P. Vaity, J. Banerji, and R. Singh, "Measuring the topological charge of an optical vortex by using a tilted convex lens," *Physics Letters A*, vol. 377, pp. 1154–1156, jun 2013.

[276] H. Hu, D. Luo, C. Pan, Y. Qin, Y. Zhang, D. Wei, H. Chen, H. Gao, and F. Li, "Collapse of hybrid vector beam in rb atomic vapor," *Optics Letters*, vol. 46, no. 11, pp. 2614–2617, 2021.

[277] H. J. Meyer, S. Mamani, and R. R. Alfano, "Steady-state stimulated raman generation and filamentation using complex vector vortex beams," *Applied Optics*, vol. 59, no. 21, pp. 6245–6251, 2020.

[278] O. J. Farías, V. D'ambrosio, C. Taballione, F. Bisesto, S. Slussarenko, L. Aolita, L. Marrucci, S. P. Walborn, and F. Sciarrino, "Resilience of hybrid optical angular momentum qubits to turbulence," *Scientific reports*, vol. 5, no. 1, pp. 1–5, 2015.

[279] B. Ndagano and A. Forbes, "Entanglement distillation by hong-ou-mandel interference with orbital angular momentum states," *APL Photonics*, vol. 4, no. 1, p. 016103, 2019.

[280] A. Einstein, B. Podolsky, and N. Rosen, "Can quantum-mechanical description of physical reality be considered complete?," *Physical Review*, vol. 47, pp. 777–780, May 1935.

[281] L. Hardy, "Nonlocality for two particles without inequalities for almost all entangled states," *Physical Review Letters*, vol. 71, pp. 1665–1668, Sep 1993.

[282] A. J. Leggett, "Nonlocal hidden-variable theories and quantum mechanics: An incompatibility theorem," *Foundations of Physics*, vol. 33, pp. 1469–1493, Oct 2003.

[283] A. K. Ekert, "Quantum cryptography based on bell's theorem," *Physical Review Letters*, vol. 67, pp. 661–663, Aug 1991.

[284] T. Jennewein, C. Simon, G. Weihs, H. Weinfurter, and A. Zeilinger, "Quantum cryptography with entangled photons," *Physical Review Letters*, vol. 84, pp. 4729–4732, May 2000.

[285] C. H. Bennett, G. Brassard, C. Crépeau, R. Jozsa, A. Peres, and W. K. Wootters, "Teleporting an unknown quantum state via dual classical and einstein-podolsky-rosen channels," *Physical Review Letters*, vol. 70, pp. 1895–1899, Mar 1993.

[286] D. Bouwmeester, J.-W. Pan, K. Mattle, M. Eibl, H. Weinfurter, and A. Zeilinger, "Experimental quantum teleportation," *Nature*, vol. 390, pp. 575––579, 1997.

[287] M. Riebe, H. Häffner, C. F. Roos, W. Hänsel, J. Benhelm, G. P. T. Lancaster, T. W. Körber, C. Becher, F. Schmidt-Kaler, D. F. V. James, and R. Blatt, "Deterministic quantum teleportation with atoms," *Nature*, vol. 429, pp. 734––737, 2004.

[288] M. D. Barrett, J. Chiaverini, T. Schaetz, J. Britton, W. M. Itano, J. D. Jost, E. Knill, C. Langer, D. Leibfried, R. Ozeri, and D. J. Wineland, "Deterministic quantum teleportation of atomic qubits," *Nature*, vol. 429, pp. 737—739, 2004.

[289] R. Ursin, T. Jennewein, M. Aspelmeyer, R. Kaltenbaek, M. Lindenthal, P. Walther, and A. Zeilinger, "Quantum teleportation across the danube," *Nature*, vol. 430, p. 849, 2004.

[290] C. H. Bennett and S. J. Wiesner, "Communication via one- and two-particle operators on einstein-podolsky-rosen states," *Physical Review Letters*, vol. 69, pp. 2881–2884, Nov 1992.

[291] Z. Shadman, H. Kampermann, C. Macchiavello, and D. Bruß, "Optimal super dense coding over noisy quantum channels," *New Journal of Physics*, vol. 12, no. 7, p. 073042, 2010.

[292] T. B. Pittman, Y. H. Shih, D. V. Strekalov, and A. V. Sergienko, "Optical imaging by means of two-photon quantum entanglement," *Physical Review A*, vol. 52, pp. R3429–R3432, Nov 1995.

[293] J. H. Shapiro, "Computational ghost imaging," *Physical Review A*, vol. 78, p. 061802, Dec 2008.

[294] D. Deutsch and A. Ekert, "Quantum computation," *Physics World*, vol. 11, no. 3, pp. 47–53, 1998.

[295] P. Walther, K. J. Resch, T. Rudolph, E. Schenck, H. Weinfurter, V. Vedral, M. Aspelmeyer, and A. Zeilinger, "Experimental one-way quantum computing," *Nature*, vol. 434, pp. 169—176, 2005.

[296] R. Prevedel, P. Walther, F. Tiefenbacher, P. Böhi, R. Kaltenbaek, T. Jennewein, and A. Zeilinger, "High-speed linear optics quantum computing using active feed-forward," *Nature*, vol. 445, pp. 65—69, 2007.

[297] J. Yin, Y. Cao, Y.-H. Li, S.-K. Liao, L. Zhang, J.-G. Ren, W.-Q. Cai, W.-Y. Liu, B. Li, H. Dai, G.-B. Li, Q.-M. Lu, Y.-H. Gong, Y. Xu, S.-L. Li, F.-Z. Li, Y.-Y. Yin, Z.-Q. Jiang, M. Li, J.-J. Jia, G. Ren, D. He, Y.-L. Zhou, X.-X. Zhang, N. Wang, X. Chang, Z.-C. Zhu, N.-L. Liu, Y.-A. Chen, C.-Y. Lu, R. Shu, C.-Z.

Peng, J.-Y. Wang, and J.-W. Pan, "Satellite-based entanglement distribution over 1200 kilometers," *Science*, vol. 356, no. 6343, pp. 1140–1144, 2017.

[298] H. Hübel, M. R. Vanner, T. Lederer, B. Blauensteiner, T. Lorünser, A. Poppe, and A. Zeilinger, "High-fidelity transmission of polarization encoded qubits from an entangled source over 100 km of fiber," *Optics Express*, vol. 15, pp. 7853–7862, Jun 2007.

[299] S. Wengerowsky, S. K. Joshi, F. Steinlechner, J. R. Zichi, B. Liu, T. Scheidl, S. M. Dobrovolskiy, R. van der Molen, J. W. Los, V. Zwiller, *et al.*, "Passively stable distribution of polarisation entanglement over 192 km of deployed optical fibre," *arXiv preprint arXiv:1907.04864*, 2019.

[300] N. J. Cerf, M. Bourennane, A. Karlsson, and N. Gisin, "Security of quantum key distribution using d-level systems," *Physical Review Letters*, vol. 88, p. 127902, Mar 2002.

[301] D.-S. Ding, W. Zhang, S. Shi, Z.-Y. Zhou, Y. Li, B.-S. Shi, and G.-C. Guo, "High-dimensional entanglement between distant atomic-ensemble memories," *Light: Sci. Appl.* , vol. 5, no. 10, p. e16157, 2016.

[302] J. D. Franson, "Bell inequality for position and time," *Physical Review Letters*, vol. 62, pp. 2205–2208, May 1989.

[303] R. T. Thew, A. Acín, H. Zbinden, and N. Gisin, "Bell-type test of energy-time entangled qutrits," *Physical Review Letters*, vol. 93, p. 010503, Jul 2004.

[304] T. Zhong, H. Zhou, R. D. Horansky, C. Lee, V. B. Verma, A. E. Lita, A. Restelli, J. C. Bienfang, R. P. Mirin, T. Gerrits, *et al.*, "Photon-efficient quantum key distribution using time–energy entanglement with high-dimensional encoding," *New Journal of Physics*, vol. 17, no. 2, p. 022002, 2015.

[305] T. Ikuta and H. Takesue, "Four-dimensional entanglement distribution over 100 km," *Sci. Rep.* , vol. 8, no. 1, p. 817, 2018.

[306] C. Lee, D. Bunandar, M. Pavlovich, M. Grein, R. Murphy, S. Hamilton, D. Englund, and P. B. Dixon, "High-dimensional Entanglement Distribution and Einstein-Podolsky-Rosen Steering Over Deployed Fiber," in *2018 Conference on Lasers and Electro-Optics (CLEO)*, pp. 1–2, IEEE, 2018.

[307] P. Imany, J. A. Jaramillo-Villegas, J. M. Lukens, M. S. Alshaykh, O. D. Odele, D. E. Leaird, M. Qi, and A. M. Weiner, "Deterministic optical quantum logic with multiple high-dimensional degrees of freedom in a single photon," *arXiv preprint arXiv:1805.04410*, 2018.

[308] S. Ramelow, L. Ratschbacher, A. Fedrizzi, N. K. Langford, and A. Zeilinger, "Discrete tunable color entanglement," *Physical Review Letters*, vol. 103, p. 253601, Dec 2009.

[309] G. Molina-Terriza, J. P. Torres, and L. Torner, "Twisted photons," *Nature Physics*, vol. 3, p. 305, 2007.

[310] M. Krenn, M. Malik, M. Erhard, and A. Zeilinger, "Orbital angular momentum of photons and the entanglement of laguerre–gaussian modes," *Philosophical Transactions of the Royal Society of London A: Mathematical, Physical and Engineering Sciences*, vol. 375, no. 2087, 2017.

[311] M. Erhard, R. Fickler, M. Krenn, and A. Zeilinger, "Twisted photons: new quantum perspectives in high dimensions," *Light: Science & Applications*, vol. 7, p. 17146, 2018.

[312] W. Löffler, T. G. Euser, E. R. Eliel, M. Scharrer, P. S. J. Russell, and J. P. Woerdman, "Fiber transport of spatially entangled photons," *Physical Review Letters*, vol. 106, p. 240505, Jun 2011.

[313] Y. Kang, J. Ko, S. M. Lee, S.-K. Choi, B. Y. Kim, and H. S. Park, "Measurement of the entanglement between photonic spatial modes in optical fibers," *Physical Review Letters*, vol. 109, p. 020502, Jul 2012.

[314] D. Cozzolino, D. Bacco, B. Da Lio, K. Ingerslev, Y. Ding, K. Dalgaard, P. Kristensen, M. Galili, K. Rottwitt, S. Ramachandran, *et al.*, "Orbital angular momentum states enabling fiber-based high-dimensional quantum communication," *Physical Review Applied*, vol. 11, no. 6, p. 064058, 2019.

[315] M. P. J. Lavery, M. M. Abadi, R. Bauer, G. Brambilla, L. Cheng, M. A. Cox, A. Dudley, A. D. Ellis, N. K. Fontaine, A. E. Kelly, C. Marquardt, S. Matlhane, B. Ndagano, F. Petruccione, R. Slavík, F. Romanato, C. Rosales-Guzmán, F. S. Roux, K. Roux, J. Wang, and A. Forbes, "Tackling Africa's digital divide," *Nature Photonics*, vol. 12, pp. 249–252, 2018.

[316] M. Caleffi, A. S. Cacciapuoti, and G. Bianchi, "Quantum internet: from communication to distributed computing!," *arXiv preprint arXiv:1805.04360*, 2018.

[317] A. S. Cacciapuoti, M. Caleffi, F. Tafuri, F. S. Cataliotti, S. Gherardini, and G. Bianchi, "Quantum internet: networking challenges in distributed quantum computing," *arXiv preprint arXiv:1810.08421*, 2018.

[318] L. Allen, M. W. Beijersbergen, R. J. C. Spreeuw, and J. P. Woerdman, "Orbital angular momentum of light and the transformation of laguerre-gaussian laser modes," *Physical Review A*, vol. 45, pp. 8185–8189, Jun 1992.

[319] R. Jozsa, "Fidelity for mixed quantum states," *Journal of Modern Optics*, vol. 41, no. 12, pp. 2315–2323, 1994.

[320] D. F. James, P. G. Kwiat, W. J. Munro, and A. G. White, "On the measurement of qubits," in *Asymptotic Theory Of Quantum Statistical Inference: Selected Papers*, pp. 509–538, World Scientific, 2005.

[321] J. F. Clauser, M. A. Horne, A. Shimony, and R. A. Holt, "Proposed experiment to test local hidden-variable theories," *Physical Review Letters*, vol. 23, no. 15, p. 880, 1969.

[322] S. P. Walborn, M. O. T. Cunha, S. Pádua, and C. H. Monken, "Double-slit quantum eraser," *Physical Review A*, vol. 65, p. 033818, 2002.

[323] G. Ruffato, M. Girardi, M. Massari, E. Mafakheri, B. Sephton, P. Capaldo, A. Forbes, and F. Romanato, "A compact diffractive sorter for high-resolution demultiplexing of orbital angular momentum beams," *Sci Rep*, vol. 8, no. 1, p. 10248, 2018.

[324] J. Calsamiglia, "Generalized measurements by linear elements," *Physical Review A*, vol. 65, no. 3, p. 030301, 2002.

[325] Y. Zhang, M. Agnew, T. Roger, F. S. Roux, T. Konrad, D. Faccio, J. Leach, and A. Forbes, "Simultaneous entanglement swapping of multiple orbital angular momentum states of light," *Nature Communications*, vol. 8, no. 1, p. 632, 2017.

[326] M. Erhard, M. Malik, and A. Zeilinger, "A quantum router for high-dimensional entanglement," *Quantum Science and Technology*, vol. 2, no. 1, p. 014001, 2017.

[327] F.-G. Deng, B.-C. Ren, and X.-H. Li, "Quantum hyperentanglement and its applications in quantum information processing," *Science bulletin*, vol. 62, no. 1, pp. 46–68, 2017.

[328] J. T. Barreiro, T.-C. Wei, and P. G. Kwiat, "Beating the channel capacity limit for linear photonic superdense coding," *Nature physics*, vol. 4, no. 4, pp. 282–286, 2008.

[329] M. Agnew, J. Leach, M. McLaren, F. S. Roux, and R. W. Boyd, "Tomography of the quantum state of photons entangled in high dimensions," *Physical Review A*, vol. 84, p. 062101, 2011.

[330] J. Bavaresco, N. H. Valencia, C. Klöckl, M. Pivoluska, P. Erker, N. Friis, M. Malik, and M. Huber, "Measurements in two bases are sufficient for certifying high-dimensional entanglement," *Nature Physics*, pp. 1745–2481, 2018.

[331] M. Rambach, M. Qaryan, M. Kewming, C. Ferrie, A. G. White, and J. Romero, "Robust and efficient high-dimensional quantum state tomography," *Physical Review Letters*, vol. 126, no. 10, p. 100402, 2021.

[332] A. Vaziri, G. Weihs, and A. Zeilinger, "Experimental two-photon, three-dimensional entanglement for quantum communication," *Physical Review Letters*, vol. 89, no. 24, p. 240401, 2002.

[333] J. Pors, S. Oemrawsingh, A. Aiello, M. Van Exter, E. Eliel, J. Woerdman, *et al.*, "Shannon dimensionality of quantum channels and its application to photon entanglement," *Physical Review Letters*, vol. 101, no. 12, p. 120502, 2008.

[334] J. Pinnell, V. Rodríguez-Fajardo, and A. Forbes, "Probing the limits of orbital angular momentum generation and detection with spatial light modulators," *Journal of Optics-nouvelle Revue D Optique*, vol. 23, no. 1, p. 015602, 2020.

[335] M. Krenn, M. Huber, R. Fickler, R. Lapkiewicz, S. Ramelow, and A. Zeilinger, "Generation and confirmation of a (100× 100)-dimensional entangled quantum system," *Proceedings of the National Academy of Sciences*, vol. 111, no. 17, pp. 6243–6247, 2014.

[336] J. Leach, E. Bolduc, D. J. Gauthier, and R. W. Boyd, "Secure information capacity of photons entangled in many dimensions," *Physical Review A*, vol. 85, no. 6, p. 060304, 2012.

[337] C. Wang, F.-G. Deng, Y.-S. Li, X.-S. Liu, and G. L. Long, "Quantum secure direct communication with high-dimension quantum superdense coding," *Physical Review A*, vol. 71, no. 4, p. 044305, 2005.

[338] N. Bornman, M. Agnew, F. Zhu, A. Vallés, A. Forbes, and J. Leach, "Ghost imaging using entanglement-swapped photons," *npj Quantum Inf*, vol. 5, no. 1, pp. 1–6, 2019.

[339] F. Steinlechner, S. Ecker, M. Fink, B. Liu, J. Bavaresco, M. Huber, T. Scheidl, and R. Ursin, "Distribution of high-dimensional entanglement via an intra-city free-space link," *Nature Communications*, vol. 8, p. 15971, 2017.

[340] Y. Zhang, F. S. Roux, T. Konrad, M. Agnew, J. Leach, and A. Forbes, "Engineering two-photon high-dimensional states through quantum interference," *Science advances*, vol. 2, no. 2, p. e1501165, 2016.

[341] J. Liu, I. Nape, Q. Wang, A. Vallés, J. Wang, and A. Forbes, "Multidimensional entanglement transport through single-mode fiber," *Science advances*, vol. 6, no. 4, p. eaay0837, 2020.

[342] H. Cao, S.-C. Gao, C. Zhang, J. Wang, D.-Y. He, B.-H. Liu, Z.-W. Zhou, Y.-J. Chen, Z.-H. Li, S.-Y. Yu, *et al.*, "Distribution of high-dimensional orbital angular momentum entanglement over a 1 km few-mode fiber," *Optica*, vol. 7, no. 3, pp. 232–237, 2020.

[343] R. Fickler, R. Lapkiewicz, W. N. Plick, M. Krenn, C. Schaeff, S. Ramelow, and A. Zeilinger, "Quantum entanglement of high angular momenta," *Science*, vol. 338, no. 6107, pp. 640–643, 2012.

[344] R. Fickler, R. Lapkiewicz, M. Huber, M. P. Lavery, M. J. Padgett, and A. Zeilinger, "Interface between path and orbital angular momentum entanglement for high-dimensional photonic quantum information," *Nature communications*, vol. 5, no. 1, pp. 1–6, 2014.

[345] J. B. Götte, S. Franke-Arnold, R. Zambrini, and S. M. Barnett, "Quantum formulation of fractional orbital angular momentum," *J Mod Opt*, vol. 54, no. 12, pp. 1723–1738, 2007.

[346] S. Oemrawsingh, X. Ma, D. Voigt, A. Aiello, E. t. Eliel, J. Woerdman, *et al.*, "Experimental demonstration of fractional orbital angular momentum entanglement of two photons," *Physical Review Letters*, vol. 95, no. 24, p. 240501, 2005.

[347] T. Gregory, P.-A. Moreau, E. Toninelli, and M. J. Padgett, "Imaging through noise with quantum illumination," *Sci Adv*, vol. 6, no. 6, p. eaay2652, 2020.

[348] A. Peres, "Separability criterion for density matrices," *Physical Review Letters*, vol. 77, no. 8, p. 1413, 1996.

[349] P. Horodecki, "Separability criterion and inseparable mixed states with positive partial transposition," *Physics Letters A*, vol. 232, no. 5, pp. 333–339, 1997.

[350] K. G. H. Vollbrecht and M. M. Wolf, "Efficient distillation beyond qubits," *Physical Review A*, vol. 67, no. 1, p. 012303, 2003.

[351] M. Horodecki and P. Horodecki, "Reduction criterion of separability and limits for a class of distillation protocols," *Physical Review A*, vol. 59, no. 6, p. 4206, 1999.

[352] A. K. Ekert, "Quantum cryptography based on Bell's theorem," *Physical Review Letters*, vol. 67, no. 6, p. 661, 1991.

[353] A. A. Klyachko, M. A. Can, S. Binicioğlu, and A. S. Shumovsky, "Simple test for hidden variables in spin-1 systems," *Physical Review Letters*, vol. 101, no. 2, p. 020403, 2008.

[354] R. Lapkiewicz, P. Li, C. Schaeff, N. K. Langford, S. Ramelow, M. Wieśniak, and A. Zeilinger, "Experimental non-classicality of an indivisible quantum system," *Nature*, vol. 474, no. 7352, pp. 490–493, 2011.

[355] J.-Å. Larsson, "Loopholes in bell inequality tests of local realism," *J Phys A: Math Theor*, vol. 47, no. 42, p. 424003, 2014.

[356] H. D. L. Pires, H. C. B. Florijn, and M. P. van Exter, "Measurement of the spiral spectrum of entangled two-photon states," *Physical Review Letters*, vol. 104, p. 020505, 2010.

[357] G. Kulkarni, R. Sahu, O. S. Magaña-Loaiza, R. W. Boyd, and A. K. Jha, "Single-shot measurement of the orbital-angular-momentum spectrum of light," *Nature Communications*, vol. 8, no. 1, pp. 1–8, 2017.

[358] D. L. Fried, "Optical resolution through a randomly inhomogeneous medium for very long and very short exposures," *JOSA*, vol. 56, no. 10, pp. 1372–1379, 1966.

[359] R. Lane, A. Glindemann, and J. Dainty, "Simulation of a kolmogorov phase screen," *Waves in random media*, vol. 2, pp. 209–224, 1992.

[360] B. Ndagano, H. Sroor, M. McLaren, C. Rosales-Guzmán, and A. Forbes, "Beam quality measure for vector beams," *Optics letters*, vol. 41, no. 15, pp. 3407–3410, 2016.

[361] M. Beijersbergen, L. Allen, H. van der Veen, and J. Woerdman, "Astigmatic laser mode converters and transfer of orbital angular momentum," *Optics Communications*, vol. 96, pp. 123–132, feb 1993.

[362] B. P. da Silva, B. Marques, R. Rodrigues, P. S. Ribeiro, and A. Khoury, "Machine-learning recognition of light orbital-angular-momentum superpositions," *Physical Review A*, vol. 103, no. 6, p. 063704, 2021.

[363] S. A. Collins, "Lens-system diffraction integral written in terms of matrix optics," *JOSA*, vol. 60, no. 9, pp. 1168–1177, 1970.

[364] H.-C. Huang, "Various angle periods of parabolic coincidence fringes in violation of the bell inequality with high-dimensional two-photon entanglement," *Physical Review A*, vol. 98, p. 053856, Nov. 2018.